Corrosion Studies of Molten Chloride Salt: Electrochemical Measurements and Forced Flow Loop Tests

Mingyang Zhang

Dissertation submitted to the faculty of the Virginia Polytechnic Institute and State University in partial fulfillment of the requirements for the degree of

Doctor of Philosophy

In

Mechanical Engineering

Jinsuo Zhang, Chair

Li Emily Liu

Wenjun Cai

Danesh Tafti

Lei Zuo

Reza Mirzaeifar

July 27th, 2023

Blacksburg, Virginia

Keywords: Forced convection molten salt loop, Electrochemistry, Flow induced corrosion, Chloride molten salt, Thermal energy storage

Corrosion Studies of Molten Chloride Salt: Electrochemical Measurements and Forced Flow Loop Tests

Mingyang Zhang

ABSTRACT

This study encompasses various aspects of corrosion in chloride molten salt environments, employing electrochemical techniques and a forced convection loop. It explores corrosion thermodynamic properties, electrochemical corrosion kinetics, and flow-induced dynamic corrosion. The study developed a novel electrochemical method for measuring thermodynamic properties of corrosion products and develops a new analysis theory for potentiodynamic polarization data obtained from cathodic diffusion-controlled reactions. Additionally, the design and operation experience of a forced convection chloride molten salt loop is shared. Particularly, the study presents novel findings on the turbulent flow-induced corrosion phenomenon and mechanism of Fe-based alloys in Mg-based chloride molten salt. These outcomes provide valuable insights into the corrosion mechanisms and flow-induced corrosion of Fe-based alloys in chloride molten salt. The results and experiences shared in this paper have implications for the successful implementation of molten salt as an advanced heat transfer fluid and thermal energy storage material in high-temperature applications, benefiting the nuclear and concentrating solar communities.

Corrosion Studies of Molten Chloride Salt: Electrochemical Measurements and Forced Flow Loop Tests

(Mingyang Zhang)

GENERAL AUDIENCE ABSTRACT

This study explores the corrosion behavior of materials chloride molten salt, which is used in advanced energy systems. By using advanced techniques, the researchers investigated how these materials react and corrode in different conditions. They developed new methods to measure the properties of the corrosion products and analyzed how different factors affect the corrosion process. Additionally, they shared their experiences in building and operating a flow loop to simulate these conditions. The study discovered interesting phenomena, such as how the flow of molten salt can cause corrosion in certain types of metals. These findings provide important insights for improving the use of molten salt as a heat transfer fluid and energy storage material in advanced energy technologies.

ACKNOWLEDGMENTS

I would like to express my heartfelt appreciation to my advisor, Dr. Jinsuo Zhang, for providing me with the invaluable opportunity to pursue my Ph.D. studies under his guidance. Dr. Zhang's extensive knowledge of corrosion and his profound understanding of life has truly helped me grow as both an engineer and an individual. Throughout my Ph.D. journey, our frequent conversations were a constant source of inspiration for me. Dr. Zhang consistently encouraged me to think critically and express my ideas freely, fostering an environment of open discussion and learning. His unwavering support and guidance pushed me to practice my skills to the fullest, enabling me to tackle challenges with confidence. Whenever I encountered obstacles, Dr. Zhang always provided me with invaluable suggestions that paved the way for finding solutions. His vast expertise in multiple areas of research motivated me to work harder and strive for excellence in my work. Beyond being my advisor, Dr. Zhang has also become a dear friend in my life, and his encouragement and trust have been instrumental in my Ph.D. journey. I consider myself extremely fortunate to have had Dr. Jinsuo Zhang as my advisor and mentor during my graduate studies. His unwavering support, profound knowledge, and friendship have made a lasting impact on my academic and personal growth, and I am deeply grateful for his mentorship.

My dad Hongliang Zhang and my mum Guojun Yao have always been my pillars of strength, providing me with the emotional support and motivation I needed to pursue my academic goals. Their unconditional love, guidance, and sacrifices have been a driving force behind my achievements, and I am truly grateful for their presence in my life. Their unwavering support has enabled me to overcome challenges and persevere, and I am

forever grateful for their belief in me. I am fortunate to have such loving and supportive parents, and I dedicate my achievements to their unconditional love and support. I express my deepest gratitude to my parents for their unwavering encouragement, love, and sacrifices, which have been instrumental in my Ph.D. journey. Their constant support has been a source of inspiration for me, and I am truly blessed to have them by my side.

I would also like to extend my heartfelt appreciation to my friends, Dr. Ruihao Wang, Dr. Yuqin Li, Dr. Amanda Leong, Nagihan Karakaya, Jaewoo Park, and Xiaoran Wang, for their constant encouragement, understanding, and camaraderie throughout my Ph.D. studies. Their unwavering support, friendship, and positivity have made my academic journey more enjoyable and fulfilling. They have been a constant source of motivation, providing me with emotional support during challenging times, and celebrating my achievements with me. Their presence has been a source of comfort and joy, and I am grateful for their unwavering belief in me. Their friendship has not only enriched my life, but it has also contributed to my personal and professional growth. From late-night study sessions to brainstorming ideas, their input and perspective have been invaluable. Their unwavering encouragement and shared experiences have made my Ph.D. journey more meaningful and memorable. I am deeply thankful to my friends for their unwavering support, laughter, and friendship throughout my Ph.D. studies. Their presence in my life has been a constant source of motivation, and I am grateful for their unwavering belief in me. I cherish the memories we have created together, and I look forward to many more years of friendship and shared adventures.

I would like to express my sincere appreciation to my colleagues, Siheng Ren, Weiqian Zhuo, Qiufeng Yang, Dr. Jianbang Ge, Dr. Shaoqiang Guo, Brent Davis, and Emily Meilus

for their camaraderie, collaboration, and support throughout my Ph.D. studies. I extend my special appreciation to Dr. Brendan Dsouza for providing me with invaluable experience and knowledge on the forced flow loop. His guidance and support in shaping my research direction have been immensely valuable. Their companionship and teamwork have contributed significantly to my research journey, making it a truly enriching experience. They have been my close allies in the pursuit of knowledge, and we have shared countless discussions, experiments, and moments of scientific discovery together. Their willingness to share their expertise, offer feedback, and collaborate has been invaluable in shaping my research and expanding my horizons. Their camaraderie and support have also provided me with a sense of community and belonging in the lab, making it a vibrant and inspiring environment to work in. Whether it was a challenging experiment or a tight deadline, their encouragement and assistance have helped me navigate through tough times and achieve my research goals. I am grateful for the friendships and professional relationships I have developed with my colleagues, and I am fortunate to have had them as colleagues during my Ph.D. studies. I would like to extend my heartfelt thanks to my colleagues for their unwavering support, collaboration, and friendship, which have enriched my academic journey in countless ways.

I would like to acknowledge the funding support of the U.S. Department of Energy's Office of Energy Efficiency and Renewable Energy (EERE) under Solar Energy Technologies Office (SETO) Agreement Number DE-EE0008380, and Prof. Zhang's Virginia Tech Startup funding.

Table of Contents

Table of Figures

Chapter I INTRODUCTION

I.1. Background

The escalating issue of energy consumption and its detrimental impact on greenhouse gas emissions presents a formidable global challenge. Despite concerted efforts by governments to address the root causes of global warming, carbon dioxide emissions from energy and industrial activities have surged by 60% since the United Nations ratified the Framework Convention on Climate Change in 1992. According to a report by the International Energy Agency (IEA), global energy consumption has risen by 26.3% from 2005 to 2019, with electricity accounting for 19.7% of total energy consumption in 2019[1,2]. The demand for electricity continues to outstrip other energy sources on an annual basis. Electricity is a secondary form of energy that is converted from primary sources through mechanical energy systems. While coal remains the predominant source for electricity generation presently, there is a growing trend towards renewable and clean energy sources. It is projected that renewables will constitute nearly 90% of electricity generation in the United States by 2050, with nuclear, solar, wind, and hydroelectric power plants at the forefront of this transition. Consequently, the development of renewable energy sources has become increasingly compelling.

Nuclear and solar energy are projected to play pivotal roles in future electricity generation among sustainable energy sources. Over the past several decades, extensive research has been conducted since the 1950s to develop more secure and efficient nuclear and solar power plants. For Nuclear

energy, one notable development is the proposal of using molten salts as fuel and coolant in these reactors, with significant progress made in the past 10 years in many countries. The origins of molten salt reactor (MSR) concepts can be traced back to the molten salt reactor experiments (MSRE) conducted at ORNL in the 1960s[3-5]. The MSRE[5] successfully demonstrated the MSR concept, operating for over 15,424 hours without incident. Despite funding diversion, interest in MSR technology has been rekindled in recent years as a next-gen reactor concept[6]. The advantages of molten salt reactors can be categorized into three aspects: sustainability of the fuel cycle, economics, and safety[7].

One key benefit of molten salt reactors is the use of liquid fuel, which allows for online fission product removal and fuel refueling, thereby increasing fuel efficiency. Economically, the ability to refuel online enables continuous electricity generation without the need for reactor shutdowns, making MSRs more economically viable. Additionally, molten salts can operate at much higher temperatures and have lower vapor pressure compared to traditional water coolants, resulting in higher thermal efficiency of electricity generation and smaller containment vessels, which can further enhance profitability.

Safety is a critical consideration in nuclear power plants, given the historical incidents such as Fukushima and Chernobyl disasters. Molten salt reactors have inherent safety features, as they require very low excess fuel due to their refuellable nature. This minimizes the risk of shifts in reactor vessel geometry and power spikes. Furthermore, since the fuel and coolant are operated at lower pressure, any leak of fuel and coolant would not result in hazardous expulsions. Molten salt is generally not highly reactive to the environment, mitigating the risk of hydrogen explosions or

sodium fires that have been associated with other types of reactors using water or sodium as coolant. The unique feature of liquid fuel reactors is that the fuel can drain out of the core in case of emergencies, further enhancing safety measures.

In the selection of liquid fuel for molten salt reactors, several criteria have been defined by researchers. The elements in the liquid fuel should have low capture cross sections and high solubility of fissile (e.g., ^{235}U, ^{233}U, or ^{239}Pu) and/or fertile (e.g., ^{232}Th) materials. The liquid fuel should also be compatible with, or less aggressive towards, structural materials. Additionally, it should be thermally stable at operating temperatures and radiolytically stable under in-core conditions[3,8,9]. Various fluoride and chloride salts have been considered for use as liquid fuel and coolant in molten salt reactors. Fluoride salts, such as LiF, NaF, and BeF_2, have been found to be relatively thermally and radiolytically stable, and among them, only BeF_2 and ^{7}LiF remain as preferred diluent candidates due to their nuclear properties, stability, and corrosivity[10]. Other systems, such as NaF-BeF_2 system[11], LiF-NaF-BeF_2 system[12,13], NaF-ZrF_4 system, LiF-NaF-KF system, LiF-NaF-ZrF_4 system, and some chloride systems[14-16], have also been studied as potential fuel and coolant options.

In recent years, further research has been conducted to evaluate the suitability of different fuel salt options by considering factors such as melting temperature, boiling temperature, neutron capture cross-section, partial vapor pressure, heat capacity, thermal conductivity, toxicity, cost, and the possibility of effective regeneration[17-19]. These studies contribute to the ongoing efforts in selecting the most suitable liquid fuel for molten salt reactors by taking into account various technical, safety, and economic considerations.

For solar energy, molten salt is commonly used as a heat transfer fluid and thermal energy storage medium in Concentrated Solar Power (CSP) systems, where the thermal stability of the molten salt is crucial for efficient operation[20-22]. In CSP systems, a binary mixture of 60% $NaNO_3$ and 40% KNO_3 by weight is commonly used, and the mixture is maintained within a temperature range of 290°C to 565°C between the cool and hot storage tanks[23,24]. Several studies have given the thermophysical properties of solar nitrate salts, including viscosity, density, specific heat capacity, and thermal diffusivity, up to temperatures of about 620°C[25-29].

However, the next generation of CSP systems aim for higher power cycle efficiency, operation at temperatures higher than 700°C, therefore, chloride molten salts are considered promising candidates for high-temperature CSP applications due to their favorable thermophysical properties for heat transfer fluid and thermal energy storage medium[30]. Additionally, chloride molten salts have the potential for lower costs compared to other types of molten salts. For example, $MgCl_2$/KCl/NaCl has a cost of less than $0.35/kg, compared to carbonate mixtures ($1.3-$2.5/kg) and traditional nitrite mixtures ($0.5-$0.8/kg)[30]. The lower cost of chloride molten salts makes them an attractive option for next-generation CSP systems, where higher operating temperatures may be required to achieve increased power cycle efficiency.

Material degradation is one of the significant challenges associated with utilizing molten salt in both nuclear and solar power plants, and it is influenced by the chemistry of the molten salt and the properties of containment vessel materials[31-34]. The redox potentials of fuel components, corrosion products, and fission products in molten salt have been summarized by Guo et al.[31]. From the charts, it can be observed that the salt mixture itself is not corrosive. However, fission

reactions, generation of transmutation products, and contamination of the salt with metal ions or other oxidizing impurities can affect the redox potential and corrosion behavior of the materials[33].

To control the redox potential and mitigate material degradation, online methods such as redox potential control have been proposed. The principle of redox potential control is to maintain the potential range of the salt lower than the redox potential of the most susceptible corrosion elements in the containment vessel[35]. Purification of the salt, adjusting the cover gas partial pressure, adding reacting metals, and introducing soluble redox buffers are some of the methods used for redox potential control[36-39]. Electrochemical and optical spectroscopy studies are typical methods used to measure the redox potential and kinetic data of species of interest in molten salt[35]. Based on existing experience and databases, redox potential control has been demonstrated as a practical method to adjust the salt chemistry and mitigate material degradation in molten salt systems used in nuclear and solar power plants.

The selection of vessel materials for storing and operating molten salt at high temperatures, typically in the range of 650°C to 800°C, is a challenging aspect of molten salt reactor design for long-lived nuclear or solar power plants. The development and investigation of suitable materials started around the same time as the concept of molten salt reactors was proposed. One of the first materials developed for use with molten fluoride salts was a nickel-based alloy such as Hastelloy N which was developed at Oak Ridge National Laboratory (ORNL)[40]. In recent years, several alloys derived from Hastelloy N have been studied to address some of the issues identified in molten salt applications[41].

Table I-1 and Table I-2 summarizes the worldwide development of Hastelloy N, along with some other nickel and cobalt-based superalloys that have been developed and tested for molten salt applications[41]. Nickel and cobalt-based alloys are preferred due to their excellent physical properties and corrosion resistance. However, the high cost of nickel and cobalt due to metal reserves and demand from the battery industry makes building power plants out of superalloys economically challenging. As a result, research on the compatibility of molten salts with iron-based stainless steel has been actively pursued[42-44].

Surface treatment techniques have also been explored as a method to increase the corrosion resistance of metallic materials and reduce the cost of power plant construction. Carburization[45] and boronization[46] are two examples of surface treatment technologies. These methods involve forming unique stable compounds of the bulk metal with carbon or boron on the metal surface to increase corrosion resistance while preserving the mechanical properties of the material.

In summary, the selection of vessel materials for molten salt applications is a challenging aspect of molten salt reactor design, and various materials and surface treatment techniques have been investigated to address issues such as corrosion resistance and cost-effectiveness.

Table I-1 Chemistry of alloys that have been investigated for MSR structural applications[41].

Element	Ni	Cr	Mo	Ti	Fe	Mn	Nb	Si	Al	W
Hastelloy N US	Bal.	7.52	16.28	0.26	3.97	0.52	-	0.5	0.26	0.06
Hastelloy NM US	Bal.	7.3	13.6	0.5-2.0	<0.1	0.14	-	<0.01	-	-
HN80M-VI Russia	82	7.61	12.2	0.001	0.28	0.22	1.48	0.040	0.038	0.21
HN80MTY Russia	82	6.81	13.2	0.93	0.15	0.013	0.01	0.040	1.12	-
HN80MTW Russia	77	7	10	1.7	-	-	-	-	-	6
MONICR Czech Rep	Bal.	6.85	15.8	0.026	2.27	0.037	<0.01	0.13	0.02	0.16
GH3535 China	Bal.	6.88	15.9	-	4.1	0.49	0.01	1.01	0.88	-
EM-721 France	68.8	5.7	0.07	0.13	0.05	0.086	-	0.065	0.08	25.2

Table I-2 Chemistry of nickel and cobalt -based super alloys.

Element	Inconel 625	Inconel 718	A-286	188 alloy	L605
Ni	58	50-55	24-27	22	10
Cr	20-23	17-21	13.5-16	22	20
Mo	8-10	2.80-3.30	1-1.4	-	-
Fe	5	Bal.	Bal.	3	< 3
Mn	0.5	< 0.35	< 2	1.25	1.5
Nb	3.15-4.15	4.75-5.50	-	-	-
Ti	0.4	0.65-1.15	1.9-2.35	-	-
Si	0.5	< 0.35	< 1	0.35	< 0.4
Al	0.4	0.20-0.80	< 0.35	-	-
Co	1	< 1.00	-	Bal.	Bal.
Cu	-	< 0.3	-	-	-
W	-	-	-	14	15
B	-	< 0.006	0.003-0.01	0.015	-
C	0.1	< 0.08	0.08	-	0.1
P	0.01	< 0.015	0.025		< 0.04
V	-	-	0.1-0.5		-
S	0.1	< 0.015	0.025		< 0.03
La	-	-	-	0.03	-

In academia, the databases on molten salt corrosion have largely been compiled from small-scale capsule or crucible setups under static conditions. In such static environments, the corrosion parameters such as its kinetics are influenced by factors such as the contact area to salt volume ratio and the solubility limit of corrosion products, which eventually reach equilibrium. However, it is important to note that the corrosion behavior in flowing molten salt environments, such as in molten salt reactors or concentrating solar power receivers, may not always follow the same equilibrium behavior[47]. In power plant applications, where structures are exposed to flowing molten salt conditions, the corrosion process is influenced by the fluid dynamic parameters of the

molten salt, including flow conditions, attacking effects from insoluble impurities, and mass transfer effects of impurities and corrosion products.

There have been some thermal convection loop tests using molten fluoride salts reported by Oak Ridge National Laboratory (ORNL) over 50 years ago[48,49], and forced convection molten salt loop tests have been announced by Brookhaven National Laboratory, ORNL, and the University of Wisconsin[50-52]. However, corrosion results from forced convection loops are not readily available due to the significant expenses associated with building and operating these loops, as well as compatibility challenges with critical components such as valves, flanges, pumps, and sealants. It should be noted that all the flowing tests conducted in forced convection loop so far have used fluoride fluid medium. Therefore, there is a need to develop chloride flow systems for corrosion testing of candidate alloys that have been selected through static testing.

I.2. Significance of the problem

The corrosion of materials in molten salt environments is a significant problem with broad implications for various industries and applications, including nuclear energy, concentrating solar power, and other high-temperature processes. Comprehending and addressing molten salt corrosion is of utmost importance to ensure the secure and effective functioning of equipment and structures that are exposed to molten salt environments.

In the context of nuclear energy, molten salt corrosion can pose challenges to the integrity and durability of materials used in molten salt reactors (MSRs), which are a promising type of advanced nuclear reactor technology. MSRs use liquid fuel in the form of molten salts as both the

fuel and the coolant, and materials exposed to these harsh environments must withstand high temperatures, radiation levels and corrosion of the molten salts. Corrosion of materials in MSRs can result in material degradation, reduced performance, and potential safety concerns, which can limit the viability and deployment of MSR technology.

Similarly, in concentrating solar power (CSP) systems, molten salts are used as a heat transfer medium to transport and/or store thermal energy, and materials used in CSP receivers and heat exchangers are exposed to high-temperature molten salt environments. Corrosion of materials in CSP systems can impact the efficiency and reliability of the system, leading to reduced performance, increased maintenance costs, and potential safety risks.

Moreover, molten salt corrosion has implications beyond nuclear energy and CSP. It is also relevant to other high-temperature industrial processes, such as in metallurgy, chemical processing, and thermal and chemical energy storage. In these applications, corrosion of materials can lead to equipment failure, reduced productivity, and increased costs.

Therefore, understanding the fundamental mechanisms of molten salt corrosion, developing effective corrosion mitigation strategies, and obtaining reliable data from realistic operational conditions, such as flowing molten salt environments, are important for various industries and applications, and can contribute to the advancement and safe deployment of molten salt-based technologies.

I.3. Problem Statement

While there have been numerous corrosion studies conducted in static conditions using fluoride salts, there is a lack of comprehensive data for chloride salts, which are also candidates for nuclear fuel and/or coolant and CSP heat transfer and thermal storage applications. Additionally, there is a dearth of corrosion data from flowing molten salt environments, such as forced convection loops and thermal convection loops, which are more representative of real-world operating conditions in power plants and other industrial processes.

The lack of corrosion data for chloride salts and flowing conditions poses several challenges. Firstly, it limits the understanding of the corrosion behavior of materials in these environments, which can impede the development of effective corrosion mitigation strategies. Secondly, it hinders the selection and qualification of suitable materials for use in chloride salt systems and flowing molten salt environments, which can result in uncertainties and risks in the design and operation of related equipment and structures. Thirdly, it restricts the ability to accurately predict the performance and lifetime of materials in chloride salt systems and flowing molten salt environments, which can impact the safety, reliability, and cost-effectiveness of molten salt-based technologies.

Addressing the data shortage in corrosion studies for chloride salts and flowing conditions is critical for advancing the understanding of corrosion mechanisms, developing effective corrosion mitigation techniques, and ensuring the safe and reliable operation of equipment and structures exposed to these environments. This requires dedicated research efforts, including experimental

studies, data collection, and data sharing, in order to generate comprehensive and reliable corrosion data for chloride salts and flowing molten salt conditions. Such data can inform materials selection, design criteria, and operational guidelines, and contribute to the development and deployment of molten salt-based technologies with improved performance, durability, and safety.

I.4. Research hypotheses

Hypothesis 1: The thermodynamic properties of Ni, Fe, and Cr corrosion products in chloride salt systems differ from those in other salt systems, such as fluoride salt and nitrate salt, due to differences in salt chemistry, thermodynamics, and transport properties.

Hypothesis 2: Flowing conditions, such as forced convection and thermal convection, have a significant impact on the corrosion behavior of materials in molten salt environments, because of flow velocity that leads to convection of mass transfer.

Hypothesis 3: The corrosion rates and mechanisms of materials in chloride salt systems and flowing molten salt environments are influenced by various factors, including alloy composition, temperature, salt chemistry, flow velocity.

Hypothesis 4: Developing chloride flow systems for corrosion testing of candidate alloys will provide valuable insights into the corrosion behavior of materials in chloride salt systems under realistic flowing conditions.

Chapter II LITERATURE REVIEW

II.1. Coolant salt chemistry, selection, and application in MSR & CSP

Molten salts have become a crucial component in various industrial engineering applications, particularly in those involving high-temperature fluidic systems. These salts are utilized as working fluids for a wide range of high-temperature processing applications, such as acting as a catalyst and fluid reaction bed, as well as a heat transfer medium for coal gasification[53,54]. Additionally, they are used as a pyro-processing fluid for metal production[55,56], a means of separating unclear waste[57-60], and as an electrolyte in advanced thermal batteries[61,62]. The focus of this dissertation, however, is their application in Molten Salt Reactors (MSR) and Concentrated Solar Power (CSP) systems, where they are proposed to be as heat transfer fluids (HTF) and thermal energy storage (TES) salts.

Molten salt refers to an inorganic salt or mixture of salts that is normally solid at room temperature and atmosphere pressure but can become liquid at high temperatures. The choice of salt depends on the specific application and environment. For instance, in CSP plants, molten salt working fluids must have a lower freezing point to prevent salt from freezing in the tubing. Currently, a eutectic mixture of sodium nitrate and potassium nitrate, known as "Solar Salt," is used in commercial systems. Solar salt has a melting point of approximately 236 °C. Similarly, in Molten Salt Reactors (MSRs), the primary molten salt must not only be stability at high temperatures, but also possess desirable neutronic and radiation stability properties. Generally, we will consider molten salts' thermal-physical properties such as melting point, boiling point, vapor pressure,

density, thermal conductivity, specific heat capacity and viscosity, and molten salts' chemistry such as solubility, thermal stability and corrosivity.

Molten chloride salts are considered one of the most promising TES and HTF materials for next-generation molten salt technology due to their high thermal stability and low costs. Several research groups have conducted selection and optimization of promising chloride salt mixtures for the next generation of molten salt technology by reviewing the literature or conducting measurements. As shown in Table II-1, chloride mixtures have high thermal stability (greater than 800°C), comparable thermo-physical properties, but potentially much lower prices. Regarding the thermos-physical properties and material price, the interested chloride salts include LiCl, $MgCl_2$, $CaCl_2$, $ZnCl_2$, $BaCl_2$, $AlCl_3$, $SrCl_2$, NaCl, and KCl.

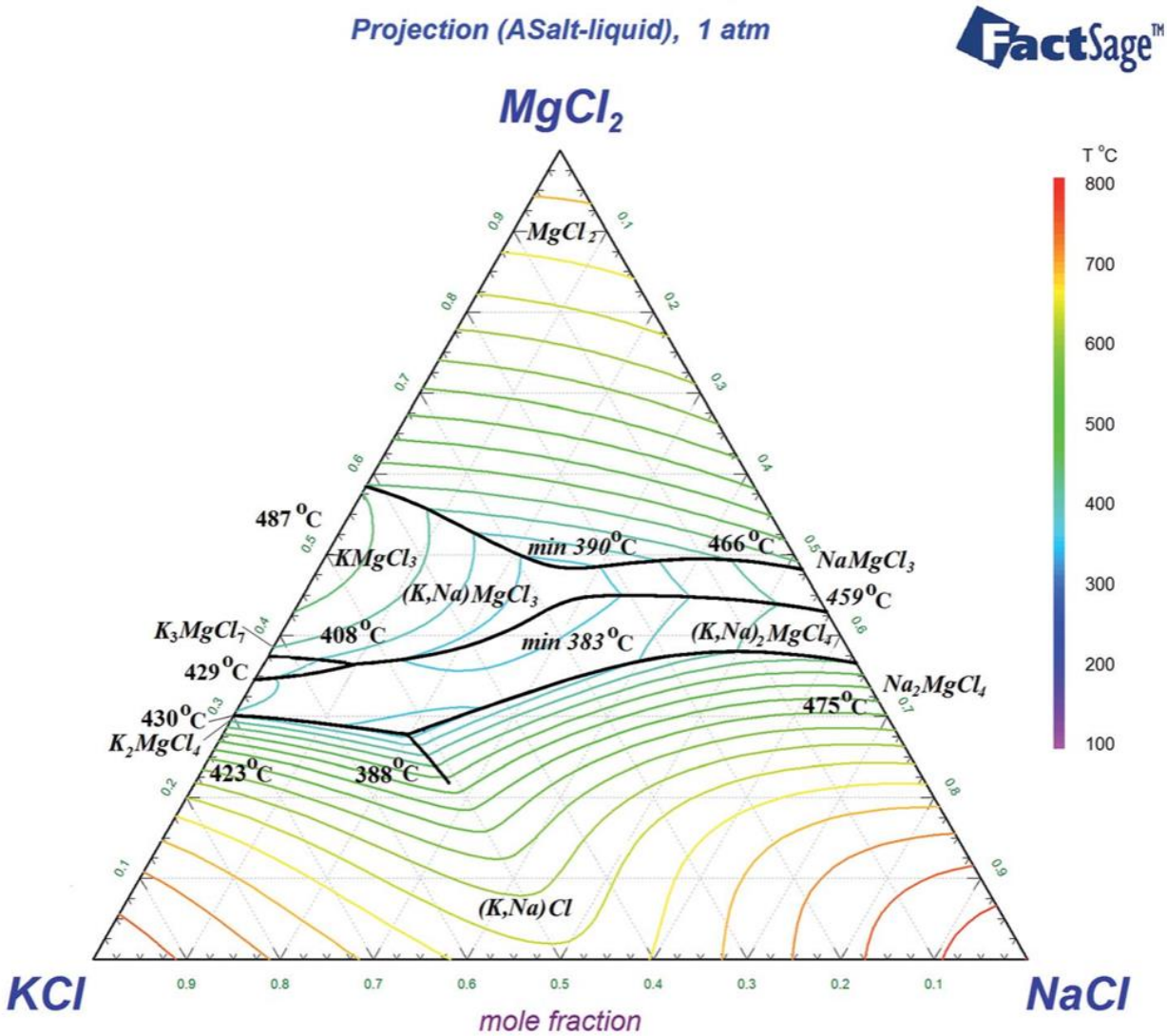

Figure II-1 Liquidus projection of the ternary halide salts (KCl, NaCl and $MgCl_2$) system[63].

Ding et al.[64] provided an overview of the properties of single salts and binary salt mixtures, highlighting that alkali metal chloride salts such as KCl and NaCl offer high heat capacities, low vapor pressures at high temperatures, weak hygroscopic properties, and affordable prices, although their high melting temperatures pose a challenge. To expand the operational temperature range, the melting temperatures of single alkali metal chloride salts can be significantly reduced through mixing with alkaline earth metal chlorides (e.g., $MgCl_2$, $CaCl_2$, $SrCl_2$) or other metal chlorides such as $ZnCl_2$ and $AlCl_3$. However, salts based on $ZnCl_2$ and $AlCl_3$, although having lower melting temperatures than other candidates, are not favored for next-generation MSR/CSP development due to their high vapor pressures at a temperature above 720 ^{o}C which can be an operation temperature of an advanced MSR and CSP. Instead, salt mixtures containing NaCl, KCl, $CaCl_2$, and $MgCl_2$ have shown promising properties. Among them, KCl–$MgCl_2$ has a relatively low melting temperature (426 °C), low vapor pressures at high temperatures, and low material costs. The addition of inexpensive NaCl to this mixture could further lower the melting temperature, reduce costs, and increase heat capacity.

Since the 1920s, researchers have conducted experimental and simulation studies to determine the eutectic composition and thermophysical properties of the $MgCl_2$-KCl-NaCl molten salt mixture. Leung et al.[63] (2015) reported a detailed phase diagram, Figure II-1, of the NaCl, KCl, and $MgCl_2$ system, which included a melting temperature as low as 383°C estimated by FactSage software with compositions of 27.5$MgCl_2$ – 52.5KCl– 20NaCl (mol.%), 44.7 $MgCl_2$ – 25.8 KCl – 29.4 NaCl (mol.%). Two eutectic points were found at the liquidus boundary with similar melting temperatures. Thermophysical properties for more than ten different eutectic compositions of the

$MgCl_2$-KCl-NaCl molten salt mixture were summarized in Table II-2, with experimental melting temperatures ranging from 380-390°C and specific heat capacities measured around 1 $kJ \cdot kg^{-1} \cdot K^{-1}$ at 700°C. However, vapor pressure measurements of the $MgCl_2$-KCl-NaCl system varied greatly in accuracy, with Wang[65] reporting 10 kPa and Villada et al.[66] reporting 1 kPa at 800°C. Therefore, vapor pressure measurement techniques need to be optimized to obtain consistent and reliable results. Despite the slight dependence on eutectic composition, the thermophysical properties of the mixture were generally consistent. In 2019, the National Renewable Energy Laboratory (NREL) selected the eutectic composition $MgCl_2$-KCl-NaCl (44.7/25.8/29.4 mole%) as a candidate for third generation CSP (Gen. III CSP) plants for HTF and TES salt[67]. In this dissertation, we investigate the NREL composition in both CSP and MSR application, which is referred to as Magnak salt in this dissertation.

Table II-1 Properties and prices of molten salts as TES/HTF in CSP[68].

Composition (wt%)	Melting Point (°C)	Thermal Stability Limit (°C)	Density ($g \cdot cm^{-3}$)	Heat Capacity ($kJ \cdot kg^{-1} \cdot K^{-1}$)	Price ($US\ \$ \cdot kg^{-1}$)
KNO_3-$NaNO_3$ (40/60)	240[a]	530-565[a]	~1.8[a] (400 °C)	~1.5[a] (400 °C)	0.5[c]
KNO_3-$NaNO_3$-$NaNO_2$ (53/35/33)	142[a]	450-540[a]	~1.8[a] (400 °C)	1.5[a] (400 °C)	0.9[c]
Li_2CO_3-K_2CO_3-Na_2CO_3 (32/35/33)	397[a]	>650[a]	2.0[a] (700 °C)	1.9[a] (700 °C)	~1.3[c]
KF-LiF-NaF (59/29/12)	454[a]	>700[a]	2.0[a] (700 °C)	1.9[a] (700 °C)	>2[f]
$ZnCl_2$-KCl-NaCl (68.6/23.9/7.5)	204[c]	850[c]	2.0[b] (600 °C)	0.8 [c] (300-600 °C)	0.8[e]
$MgCl_2$-KCl-NaCl (68.2/17.8/14)	380[d]	>800[e]	1.7[b] (600 °C)	~1.0 [b] (500-800 °C)	<0.35[e]
$CaCl_2$-NaCl–KCl (66.0-27.5–6.5)	504	850	1.8[g] (800 °C)	~0.80[g]	

[a] refers to the Ref[69]. [b] refers to the Ref[70]. [c] refers to the Ref[71]. [d] refers to the Ref[72]. [e] refers to the Ref[30]. [f] refers to the Ref[68]. G refers to Ref[73]

Table II-2 Eutectic compositions and thermos-physical properties of $MgCl_2$–KCl–NaCl from literature.

	$MgCl_2$	KCl	NaCl	Melting Point (°C)	Vapor pressure (kPa)	Heat Capacity ($kJ \cdot kg^{-1} \cdot K^{-1}$)
mol % wt %	49 58.7	18.5 17.4	32.5 23.9	385[74]		
mol % wt %	45.4 55	21.6 20.5	33 24.5	385[75] 383[76] 387[76]	0.07 (800 °C)	1.01 (400 °C) 1.18[76] (455-600 °C)
mol % wt %	47.1 56.5	22.7 21.3	30.2 22.2	385[77]		
mol % wt %	44.7 53.9	25.8 24.4	29.4 21.8	385[67]		~1.03[66] (420-800 °C)
mol % wt %	47.1 56.5	22.7 21.3	30.2 22.2	385.4[66]		1.04[66] (420-800 °C)
mol % wt %	46.5 56	22.2 20.9	31.3 23.1	385[66]	1[66] (804 °C)	
mol % wt %	40 48.59	32.5 30.91	27.5 20.5	383[65]	~10[65] (800 °C)	1.04-0.99[65] (600-750 °C)
mol % wt %	47.9 57.39	21.2 19.89	30.9 22.72	390[65]	~ 8[65] (800 °C)	1.01-0.94[65] (600-750 °C)
mol % wt %	44.36 53.37	27.25 25.67	28.39 20.96	382[65]	~10[65] (800 °C)	1.07-1[65] (600-750 °C)
mol % wt %	60 68.2	20 14.0	20 17.8	380[72]		~1[70] (500-800 °C)

II.2. Molten salt corrosion mechanism

II.2.1. Static state corrosion mechanism

Despite its promising cost and thermophysical properties, the commercial application of Magnak salt as a HTF and TES salt for third generation CSPs is hindered by its strong corrosivity towards structural materials, especially metallic materials. In recent years, extensive studies have been conducted on the interaction of metal materials with the $MgCl_2$–KCl–NaCl system[78-82], and several review papers have focused on the corrosion mechanism in chloride molten salt[31,66,68,83]. While pure Magnak salt does not corrode metal materials significantly due to the limited dissolution concentration of metallic corrosion products[35], it is well-established that the corrosion of metal in chloride salt is mainly driven by non-metallic impurities such as H_2O, HCl, O_2, or Cl_2. The hygroscopic nature of $MgCl_2$ in the Magnak salt can easily combine with moisture in the air to form hydrates, increasing its corrosivity. Therefore, investigations on the purification of $MgCl_2$-based salts are essential for commercialization. Recent studies at research groups such as German Aerospace Center (DLR), National Renewable Energy Laboratory (NREL), and Shanghai Institute of Applied Physics, Chinese Academy of Sciences (SINAP-CAS) have confirmed that $MgOH^+$ is the primary corrosive impurity in the molten $MgCl_2$-KCl-NaCl salt due to its high solubility and thermal stability[68]. Figure II-2 is the schematic of corrosion mechanism of alloy in Magnak salt at static state. It is important to note that MgOHCl is a byproduct of thermal treatment and dissolves in the molten salt due to its high solubility, as expressed in Equation II-1 and Equation II-2. However, it is thermally stable up to around 555°C and gradually decomposes to MgO precipitates and HCl gas as expressed in Equation II-3.

The following are decomposition pathways of anhydrous $MgCl_2$ in the presence of moisture[67]:

$$MgCl_2 \cdot 2H_2O \rightarrow MgOHCl + HCl(g) + H_2O, \text{ T=182 ºC} \qquad \textbf{Equation II-1}$$

$$MgCl_2 \cdot H_2O \rightarrow MgOHCl + HCl(g), \text{ T=350 ºC} \qquad \textbf{Equation II-2}$$

$$MgOHCl \rightarrow MgO(s) + HCl(g), \text{ T=554 ºC} \qquad \textbf{Equation II-3}$$

Similar to aqueous solutions, the principle of corrosion in chloride molten salt is an electrochemical process. Bell et al. (2019) proposed that the molten salt solution can be classified as either acidic or basic depending on the oxide ion concentration, based on the Lux-Flood acid-base model[84]. This approach can be useful in identifying the corrosion pathways in the molten salts. According to Bell et al.'s theory, Magnak salt can be defined as an acidic molten salt due to the low concentration of O^{2-} formed from impurity sources. Consequently, the corrosion products (metal oxides) dissociate to form O^{2-} and metal ions (M^{n+}), which then dissolve into the salt. The detailed process is illustrated in Figure II-3. Therefore, unlike in aqueous solutions, the formation of a passive metal oxide layer to protect the metal is not stable in molten salt solutions.

Under static state conditions, as illustrated Figure II-2, the corrosion process is governed by the rate of diffusion of corrosive impurities to the interface, the rate of corrosion reactions, the rate of diffusion of alloying elements to the interface, and the rate of dissolution of corrosion products into the salt. In an ideal situation where the bulk salt is infinite, the impurities continuously dissolve into the salt system, and the metal is thick enough, the thickness of the porous corrosion layer will

continue to grow with a decreasing rate, and eventually stop growth as the layer becomes thicker. But in reality, once the corrosion products saturated the bulk salt, the corrosion stopped.

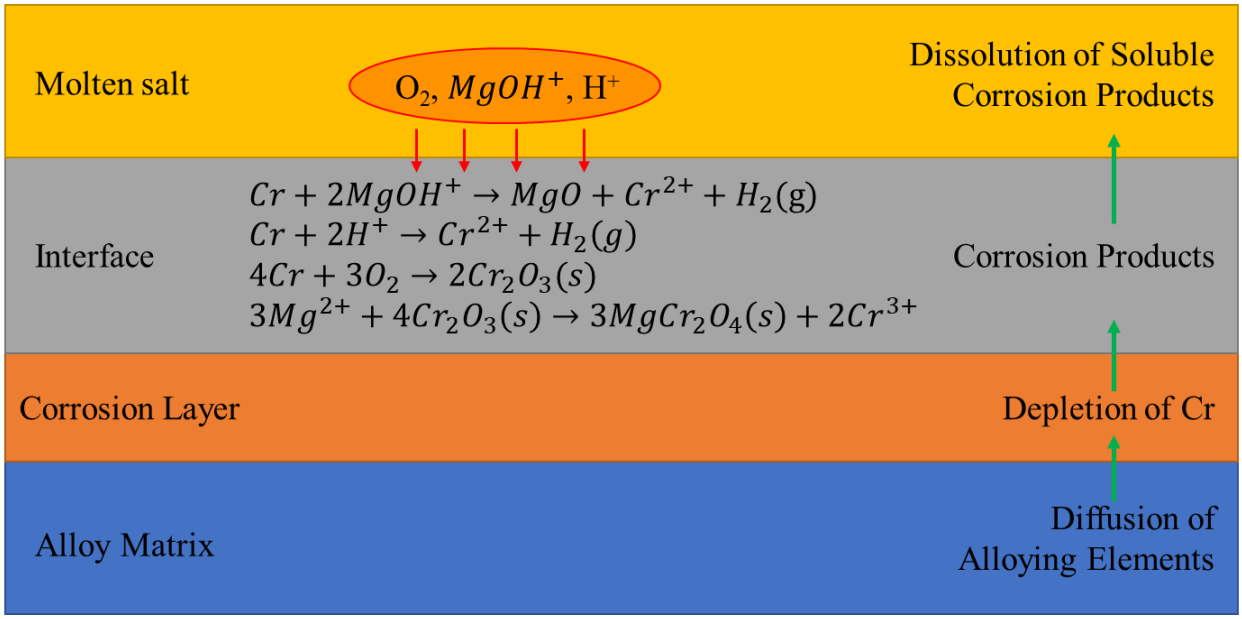

Figure II-2 Schematic of corrosion mechanism of alloy in Magnak salt at static state. (Reproduce from[68,85,86])

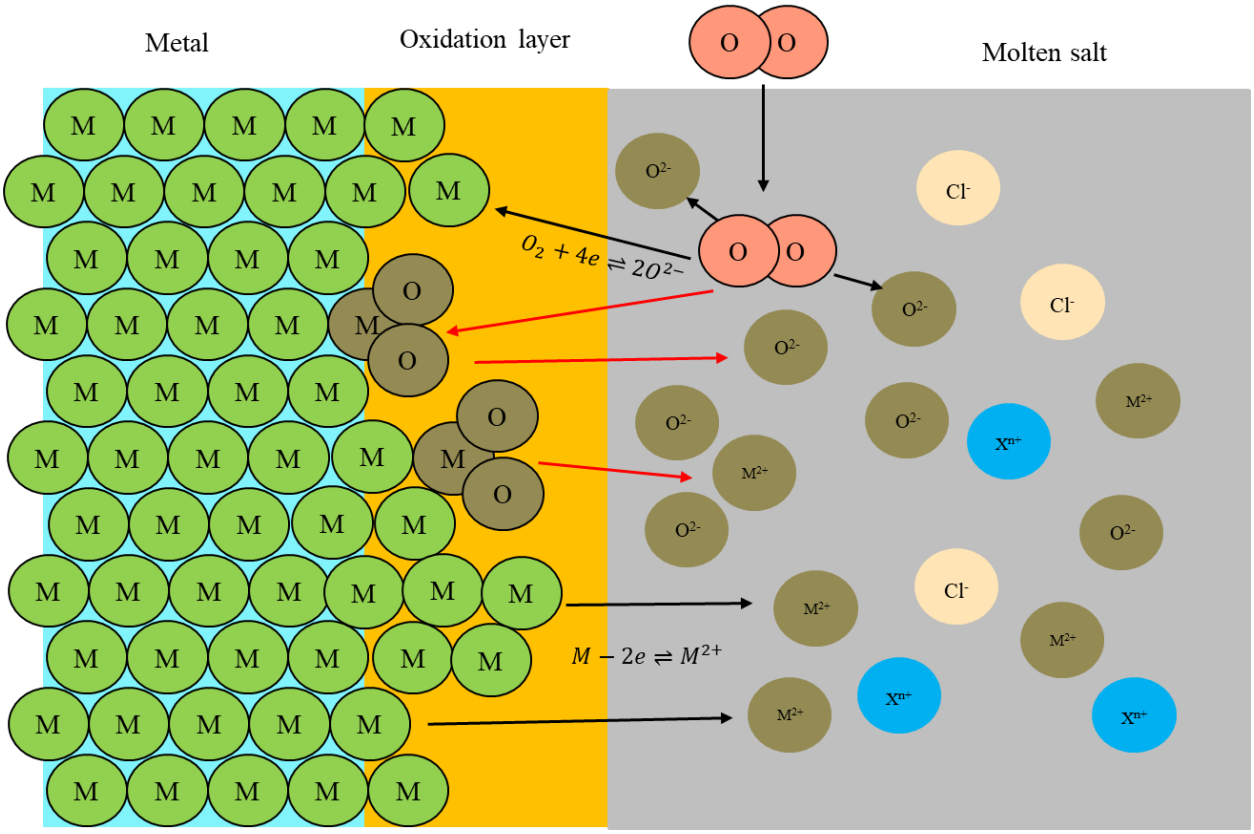

Figure II-3 Corrosion mechanism for acidic Magnak salt.

II.2.2. Dynamic corrosion mechanism

The corrosion studies in static conditions do not account for other influential factors such as temperature gradient effects and flow-effects[85]. Figure II-4 illustrated the flow induced corrosion process. Initially the corrosion process is dominated by impurities, then the corrosion happens at a lower and constant rate driven by thermal gradient. The flow factors include but not limited to, temperature gradient, flow velocity, flow viscosity, and pressure gradient[87]. Different from the static corrosion, the flow induced corrosion can be governed by one of rates of or a combined rate

of mass transfer of corrosive impurities to the interface, the rate of corrosion reactions, and the rate of diffusion of alloying elements to the interface, the rate of erosion, and the rate of mass transportation.

II.2.2.1.Temperature effects

All the governing rates mentioned above are temperature-dependent, and a higher temperature leads to higher rates, resulting in a higher corrosion rate. In a closed loop with a temperature gradient, corrosion will continuously occur in the hot leg due to the precipitation of corrosion products in the cold leg, and the corrosion product will never saturate the salt. Figure II-4 demonstrates that once the system reaches equilibrium, the temperature gradient becomes the major factor affecting corrosion. Even for loops with the same highest temperature and other hydraulic parameters, corrosion rates can vary if the loops are operated under different streamwise temperature profiles[88].

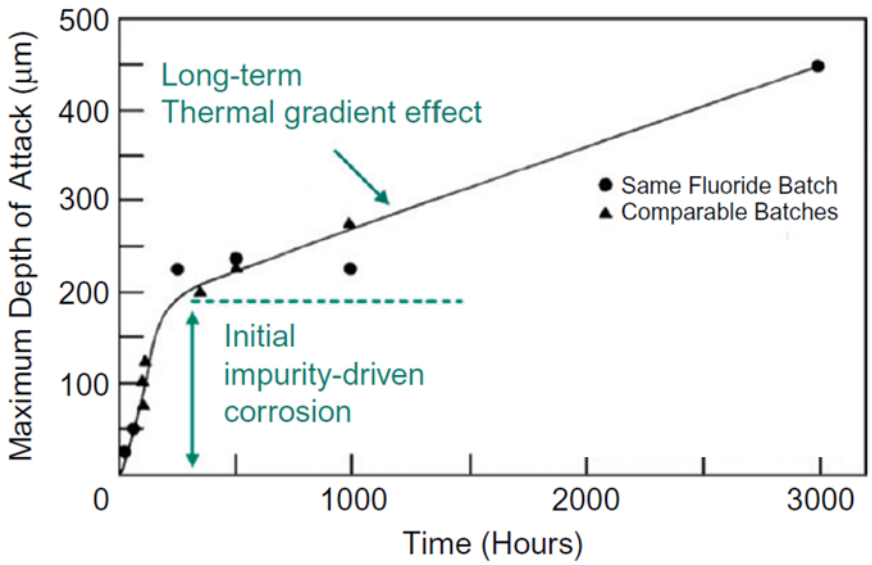

Figure II-4 Depth of corrosion attack in Inconel 600 in natural convection molten fluoride salt as a function of exposure time[89].

II.2.2.2.Mass transfer effects

II.2.2.2.1. Isothermal flowing molten salt system.

Under static conditions, the transport of corrosion products from the interface to the bulk salt occurs solely through diffusion. However, under flow conditions, both diffusion and convection can contribute to the transport of corrosion products from the interface to the bulk salt. The flow velocity plays a key role in determining the degree of convection[90]. The effects of flow velocity on single-phase flow in liquid lead isothermal system is summarized by Zhang and Li[88].

II.2.2.2.2. Non-isothermal flowing molten salt system.

In a non-isothermal flowing molten salt system, as previously discussed in section II.2.2.1, the temperature gradient plays a crucial role in corrosion when a non-isothermal loop reaches equilibrium. In this scenario, corrosion products dissolve into the stream at high temperature regions and precipitate out at low temperature regions in the form of metal or corrosion products. Zhang and Li[88] outlined three phenomena of corrosion product deposition in liquid metal, which can also be applicable in the molten salt system. Depending on the case, the precipitated corrosion products may accelerate or inhibit the corrosion in high temperature regions.

II.2.3. Corrosion types in molten salt

II.2.3.1. Pitting corrosion

Pitting corrosion refers to the localized attack of metal or metal elements, resulting in the formation of pits, holes, or voids due to corrosion. This form of corrosion commonly occurs in molten salt environments where unstable alloy elements are dissolved, resulting in a porous surface. Pitting corrosion is hazardous as it is challenging to detect and predict when it will occur, making it difficult to design against the formation of pits. ASTM-G46[91] defines various types of pits, including uniform, wide, shallow, narrow, or deep, which perforate the metal's wall thickness. Figure II-5. illustrates the pitting surface of HAYNES 230 alloy in KCl-$MgCl_2$-NaCl salt. Pit-induced fatigue and stress corrosion cracking (SCC) are responsible for several failures. Fatigue occurs when repetitive loads weaken a material, while SCC presents itself as a crack that grows due to a combination of stress and a corrosive environment, usually resulting from high stresses in the pits. Since the oxide scale is not stable in molten salt, the pitting corrosion mechanisms should

be different from these in aqueous corrosion in which the pits can be re-passivated by new oxide scale formation.

II.2.3.2. Galvanic corrosion

Galvanic corrosion occurs when two dissimilar metals in an electrolyte solution undergo an electrochemical process, with one being less corrosion resistant than the other. The less corrosion resistant metal serves as the anode, while the more corrosion resistant metal acts as the cathode. The two metals, when in contact with an electrolyte solution, create a closed circuit, allowing electrons to flow between them. In a study by Wang et al.[92], galvanic corrosion testing was performed on pure metals in fluoride molten salt. Guo et al.[31] summarized the galvanic series in both chloride and fluoride molten salt. During scientific research to study the alloy corrosion performance under specific conditions, galvanic corrosion must be avoided or minimized.

II.2.3.3. Intergranular corrosion

Intergranular corrosion (IGC) refers to a type of localized corrosion that occurs at and near grain boundaries (GB). This corrosion leads to the disintegration of the metal alloy and a loss of its strength. IGC can occur due to impurities present at the GBs and depletion or enrichment of alloying elements in the GB region. For instance, in stainless steel, the formation of chromium carbide at the GB regions results in sensitization, leading to IGC[93]. This phenomenon is also observed in molten salt environments, as depicted in Figure II-6. There are numerous reports in the literature of IGC in alloys in molten salt. In both chloride and fluoride salt mixtures, Cr is the

most easily dissolvable element into the salt. Researchers have found that Cr can dissolve along the GB in bulk alloy near the surface. Subsequently, Mo or Nb is enriched at the GD[31,46,89,94,95].

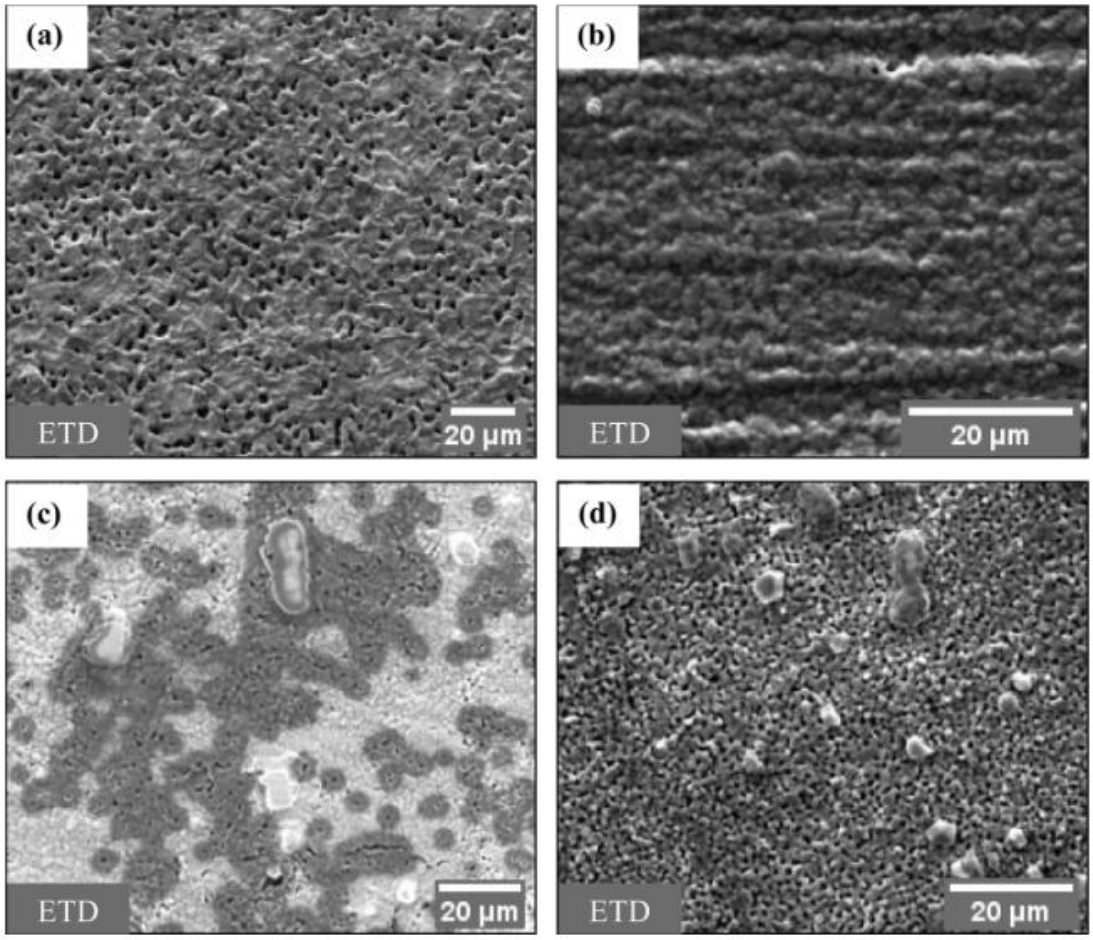

Figure II-5 SEM surface images of HAYNES® 230® alloy after exposure to molten KCl-$MgCl_2$-NaCl salt at 800 ˚C for 100 h. (a) HP salt purified without Mg. (b) HP salt purified with Mg. (c) ICL salt not purified. (d) ICL salt purified with Mg. D'Souza et al.[96].

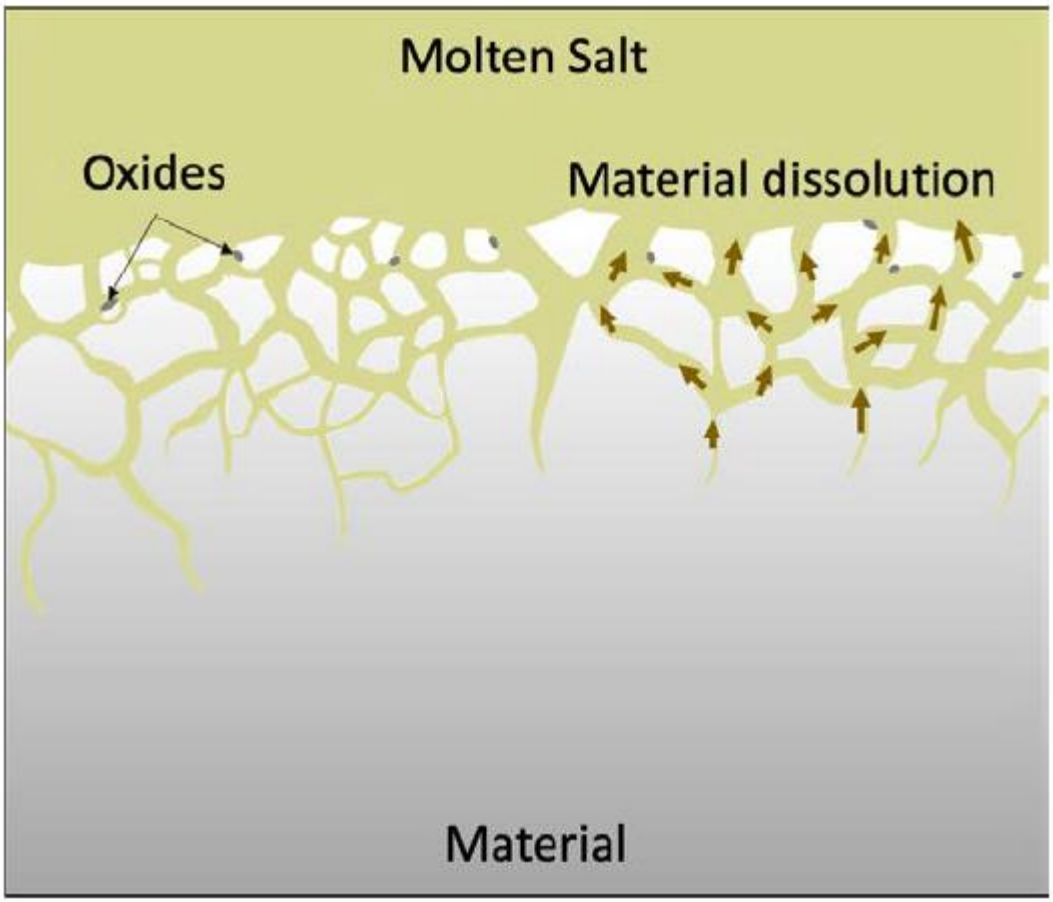

Figure II-6 IGC mechanism in molten salt. Leong[97].

II.2.3.4.Erosion corrosion

Erosion corrosion (EC) refers to the accelerated form of metal corrosion that occurs due to the relative movement between metal surfaces and a corrosive medium. The corrosive medium can take many forms, such as fluids (e.g., water or solutions with suspension), organics, liquid metals, or molten salt. The metal surface becomes damaged due to mechanical or hydraulic wear or abrasion caused by the medium's flow. Failures due to EC can occur unexpectedly and in a

relatively short time, particularly if the previous corrosion evaluations were conducted under static conditions or if the effects of erosion were not taken into account. In molten salt, especially chloride salt, the metal surface is not protected by corrosion products, and EC occurs immediately when induced by the flow. Increased velocity typically results in increased EC. While EC effects have been studied extensively in liquid metals for TES and HTF applications, no reports are available for molten salt environments. Figure II-7 depicts the EC mechanism of an alloy in Pb-Bi, but it will differ in molten salt due to the lack of corrosion product protection. Molten salt EC will be discussed in section IV.4.3.

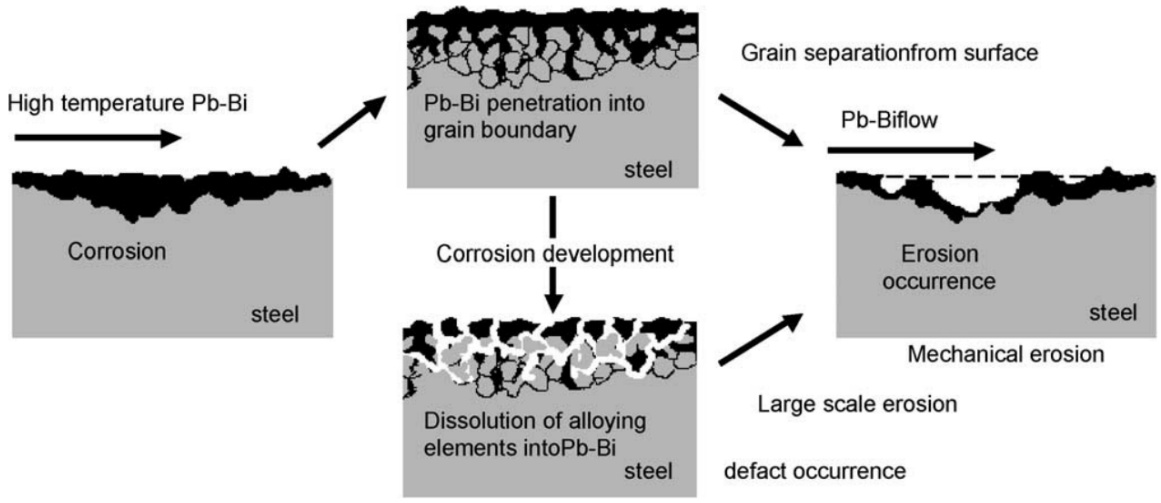

Figure II-7 Schematic of alloy EC mechanism in Pb-Bi. Kondo et al.[98].

II.3. Electrochemical measurement methods

Electrochemistry is a field of physical chemistry that focuses on the connection between measurable electrical potential difference and identifiable chemical changes. It examines how a specific chemical change can lead to an outcome of potential difference, or vice versa[99]. In electrochemical studies, measurements are performed using an electrochemical cell comprising two or more electrodes, along with electronic circuitry for controlling and measuring the current and potential. Electrochemical measurements serve as a highly effective tool for quantifying and monitoring the corrosion process in molten salt systems.

II.3.1. Electrochemical cell

II.3.1.1.Two-electrode electrochemical cells

Two-electrode electrochemical cells (TWEC), also known as galvanic cells, are the simplest setup for electrochemical experiments. This configuration consists of a working electrode (WE), where the desired chemical reactions take place, and a counter electrode (CE), which completes the cell. In TWEC, the current-carrying electrodes are also utilized for sensing measurements. Two-electrode setups are employed in specific cases. Firstly, they are used when measuring the overall cell voltage is crucial, as in electrochemical energy devices such as batteries, fuel cells, and supercapacitors. Secondly, they are suitable when the counter electrode potential is expected to remain stable throughout the experiment. This is typically observed in systems with low currents, short timescales, and a well-matched counter electrode. For instance, a micro working electrode paired with a larger silver counter electrode can be used in such cases.

II.3.1.2.Three-electrode electrochemical cell

The three-electrode electrochemical cell (THEC) is composed of a working electrode (WE), a counter electrode (CE), and a reference electrode (RE). The RE serves as a reference point for

measuring and controlling the potential of the WE, with no significant current passing through it. The primary function of the RE is to maintain a stable potential, which ideally only relies on temperature. In practical terms, a small or negligible amount of current may pass through the RE to complete the circuit. However, the potential drop resulting from the solution resistance between the WE and RE is minimal. The potential gradients in a THEC system are illustrated in Figure II-8. This characteristic enables the THEC to provide more precise control and measurement of the WE potential. Due to this advantage, the three-electrode configuration is the most commonly employed setup in electrochemical experiments.

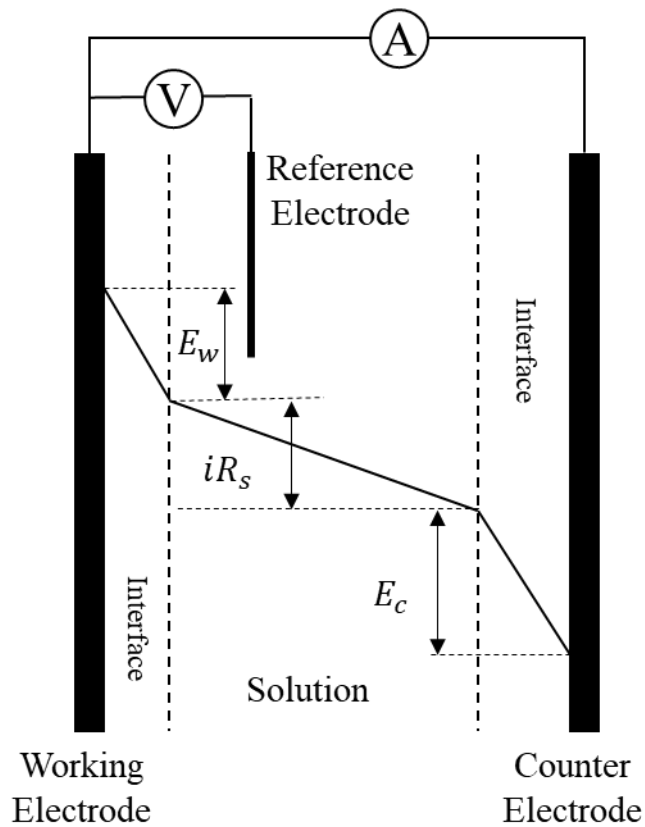

Figure II-8 Schematic of potential gradients in a THEC system.$\boldsymbol{E_w}$ and $\boldsymbol{E_c}$ are the potential change at the working and counter electrode interfaces. $\boldsymbol{iR_s}$ is the potential change caused by the solution resistance.

II.3.2. Electrochemical experiments

The objective of an experiment is to gather valuable information about a system's thermodynamic and kinetic properties by analyzing excitation and response functions, as well as utilizing appropriate models. In the case of an electrochemical system, the focus is on investigating the electrochemical behavior of the working electrode (WE) by manipulating specific variables within the cell and observing corresponding changes in other variables. Several parameters are of significance in an electrochemical cell, including:

- System Temperature: The temperature at which the electrochemical system operates is an essential parameter that influences the kinetics and thermodynamics of the electrochemical processes.
- Working Electrode Variables: Variables related to the working electrode, such as its material composition, surface condition, geometry, and surface area, play a crucial role in determining the electrochemical behavior and responses.
- Solution Variables: Various factors related to the bulk solutions are important, including the choice of solvent, its concentration, the presence of impurities, and any other relevant chemical species.

II.3.2.1. Reaction mechanism near the working electrode surface

Figure II-9. illustrates the mechanism of reactions occurring on the surface of an inert working electrode (WE). The process begins with the transport of reactants from the bulk solution to the region near the electrode surface. In this region, the half redox reaction takes place, involving either oxidation or reduction of the reactants. During the electron transfer process, electrons are

either absorbed onto or desorbed from the electrode surface as part of the redox reaction. At steady state conditions, the electron transfer occurs through the electrode, bridging between the reactants and products, rather than through a chemical reaction in the bulk solution. The changes in potential or current resulting from these electron transfer events can be detected and measured using external devices, allowing for the analysis and characterization of the electrochemical system.

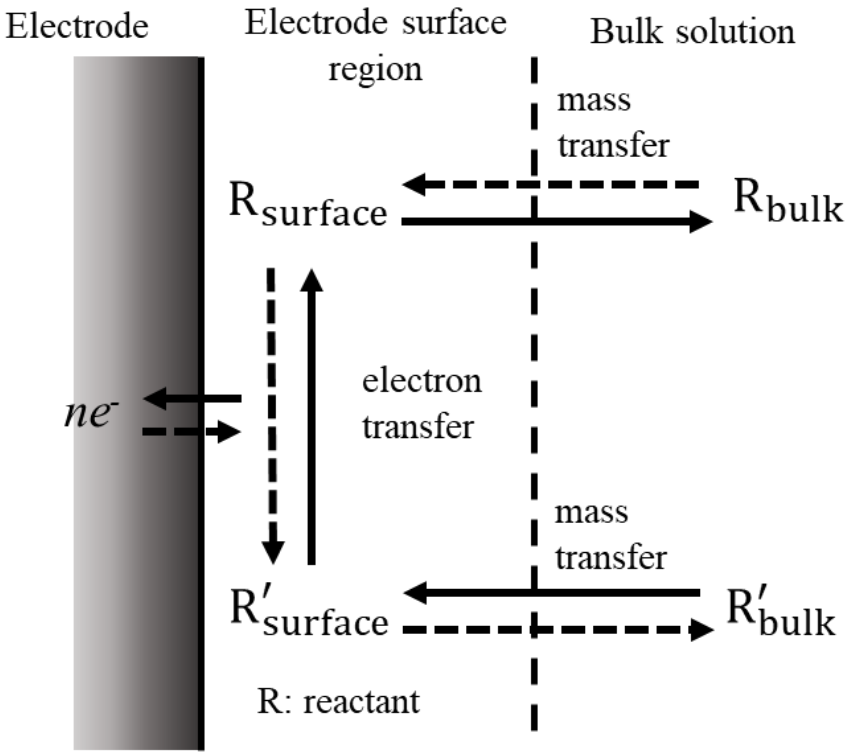

Figure II-9 Reaction and the pathway near the inert working electrode surface for soluble-soluble reactions.

In corrosion testing, the working electrode typically consists of a sample rather than an inert material. Figure II-10 depicts the mechanism of electrochemical corrosion testing. The electrochemical corrosion process involves not only the transportation of solution species between the bulk solution and the electrode interface but also the mass transfer of metal elements between

the bulk electrode and the electrode surface. Similarly, all electron transfer processes occur through the electrode.

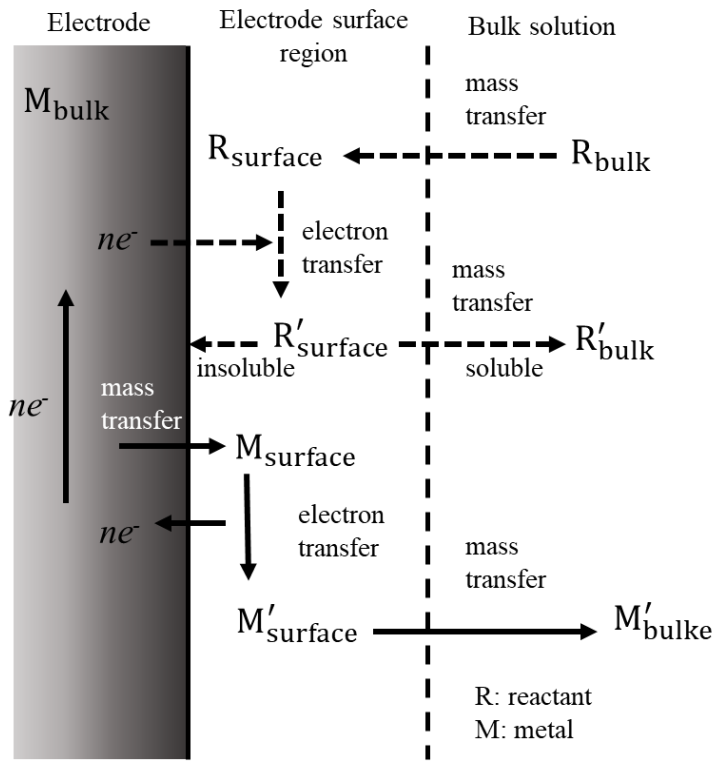

Figure II-10 Reaction and the pathway near the corrosion sample surface.

II.3.2.2.Thermodynamic property measurement method

In electrochemical experiments, potentials are typically measured relative to a stable reference electrode, allowing researchers to focus on the working electrode where the reactions take place. In the case of molten salt solutions, the commonly used reference electrode is the AgCl/Ag electrode, which consists of an Ag wire immersed in an AgCl-containing salt and separated from the main electrolyte by an ion-conductive membrane such as quartz, alumina, borosilicate glass, or glass-bonded mullite. However, the potential of this reference electrode (compared to the Cl^2/Cl^-

reference) requires additional measurement due to the uncertain activity of AgCl dissolved in the salt. In the 1950s, Yang et al.[100] conducted pioneering research on the equilibrium potential of the AgCl/Ag redox couple in LiCl-KCl molten salt at various temperatures and concentrations using a two-electrode cell configuration: Ag(s)|AgCl in molten salt|Cl_2(g)|graphite. This method and the data obtained by Yang et al. gained wide acceptance, to the extent that some studies[101-103] directly extrapolated the redox potential of 1 wt% AgCl from Yang's dataset without conducting further experimental measurements.

Subsequent studies[100,104-107] have measured the potential of the AgCl/Ag redox couple in molten chloride salts under various conditions, involving different salts or experimental setups. Shirai et al.[108], for instance, reported the equilibrium potential of the AgCl/Ag redox couple in LiCl-KCl eutectic over a concentration range of 0.01 mol% to 20 mol%. Their results exhibited significant deviations from those of Yang et al., even within the similar concentration range of AgCl. This discrepancy might be attributed to the variable Ag^+ concentration of the Ag^+/AgCl reference electrode during the electrochemical measurements. In a recent study by Yoon et al.[109], the redox potential at lower AgCl mole fractions (X=0.0043 and X=0.00039) in LiCl-KCl eutectic melt was investigated using a three-electrode electrochemical cell with chlorine gas injected into the salt. Their results showed good agreement with Yang's data, providing further support for Yang's findings.

Since the redox potential is an important thermodynamic data that can be used to predict the corrosion reactions, measurements of redox potential of metal ions in Magnak chloride salt are essential. Traditionally, redox potential is measured in a suitable galvanic cell or a double

concentration cell by using emf method [104,105,110,111]. In those cases, an independent chlorine source must be supplied to establish a chlorine electrode, which makes it difficult to assemble the setup in a glovebox. To simplify the experimental setup and improve operational safety, some researchers [112-115] have developed a three-electrode electrochemical cell that uses a real reference electrode (e.g. AgCl/Ag) to measure redox potential, but the application is very limited. For example, it cannot measure the redox potential of a major component of the salt, such as the Mg ions in Magnak chloride. A new method has been developed in our previous study to address this limitation. With a metal reference electrode, the behavior of the chlorine formation on a graphite working electrode was recorded, which simplifies redox potential measurement [116]. However, our previous experimental setup is only suitable for cations that have a single valence state, such as Ag(I), Mg(II), and Ni(II). For metals with more than one stable valence state, such as Cr (Cr(II), Cr(III))[36], the electrolysis process of chlorine is accompanied by the oxidation state change of cations, which makes the cation concentration in the bulk salt unpredictable. In this studies, we proposed a solution to overcome the limitations of the previous setup.

II.3.2.3.Electrochemical corrosion measurement method

Electrochemical corrosion measurement methods are widely used to evaluate the corrosion behavior of metals and alloys under corrosive environments[117,118]. These methods involve the application of electrochemical techniques to assess the rate and extent of corrosion processes occurring at the metal-electrolyte interface[119-121]. One of the commonly used electrochemical corrosion measurement methods is known as potentiodynamic polarization (PD) measurement[122].

Potentiodynamic polarization measurement is a valuable tool for evaluating the corrosion behavior of materials in molten salt environments. It provides crucial data for materials selection, corrosion mitigation strategies, and the development of new materials[95,123-125]. Advanced characterization techniques such as in-situ electrochemical impedance spectroscopy (EIS)[126-128] coupled with potentiodynamic polarization measurements have provided insights into the film formation and breakdown processes. Most corrosion studies of structural alloys in molten salts have been performed using long-term (up to a few thousand hours) static capsule or flow-loop tests followed by characterization of near surface regions of the samples[47]. Despite the challenges associated with the high-temperature and corrosive nature of molten salts, recent advancements in experimental techniques and materials design have expanded our understanding of corrosion mechanisms, paving the way for improved materials performance in these challenging environments.

II.4. Force and Natural convection study

II.4.1. Forced convection molten salt loop experience

The Molten Salt Reactor (MSR) concept has been identified as a promising next-generation advanced nuclear reactors[129]. Molten salt advanced features make molten salt an exceptional heat transfer fluid. Over the past few decades, numerous studies have been conducted to understand the chemistries, physical properties, and thermodynamic properties of different salts in both fluoride and chloride form. However, most databases on molten salt corrosion have been compiled from small-scale capsule or crucible setups under static conditions. In such scenarios, the corrosion process is influenced by factors such as the contact area to salt volume ratio and the solubility limit

of corrosion products, which ultimately reach equilibrium. Nonetheless, it is impossible to apply the results from static tests to explain the corrosion behavior in flowing molten salt environments, such as in the coolant system of MSRs or CSP which may not always follow the same equilibrium behavior[47]. In power plant applications, where structures are exposed to flowing molten salt conditions, the corrosion process is influenced by fluid dynamic parameters.

Conducting corrosion tests under flowing molten salt is of utmost importance, as it simulates as it simulates real- or near-real- world conditions in which structures are exposed to molten salt. The significance of this type of testing was initially demonstrated by the Oak Ridge National Laboratory (ORNL) in the 1950s, during the Aircraft Reactor Experiment (ARE) and Molten Salt Reactor Experiment (MSRE) programs, where molten salt was used as a heat transfer fluid in nuclear reactor applications. ORNL built and operated several nature convection loops (NCL) and force convection loops (FCL) between the 1950s and 1970s, to study the material compatibility of various molten salt[48,49]. Unfortunately, the study of molten salt loops (MSL) came to a sudden halt with the termination of the MSRE program.

In recent years, a few MSLs have been constructed and operated by Chinese[130], Russian[131], Japanese[132], and U.S[133,134] groups. However, from the limited MSL publications available, NCL studies dominate due to their simple structure and ease of operation. FCL investigations are scarce due to the significant expenses associated with building and operating these loops, as well as compatibility challenges with critical components such as valves, flanges, pumps, and sealants.

In 1998, the Tohoku University and National Institute for Fusion Science in Japan constructed a FCL to study the heat transfer properties of molten salt using Flibe as a coolant. However, due to the high melting point of Flibe, the Japanese group never used it and instead used a simulant, heat transfer salt (HTS) which is a Hitec salt (KNO_3: $NaNO_2$: $NaNO_3$, 53-40-7 mol%) eutectic salt with a lower melting point. The group reported various findings including HTS melting sound phenomena, HTS invasion into gas line incident, HTS residuals at some welding joints phenomena, and un-uniform pipe heating phenomena[132]. The heat transfer test of the Japanese MSL was completed in 2007, using HTS at a temperature of 200 ^{o}C[135,136].

In 2010, Sabharwall et al.[52] published a report on the FCL experiments. The report provided a detailed design of the FCL for fluoride salts (FLiNaK) and magnesium chloride salts ($MgCl_2$-KCl) and suggested four different molten salt flow measurement methods including GE Ultrasonic Flow meter, Bundle waveguide transducers, Foxboro vortex flow meters, and UW customized thermal flow meters. The report also discussed different kinds of seals, pressure drop measurement methods, different jointing implemented by UW, and bellow valves for flow controlling. Sabharwall et al. provided a comprehensive design lesson on FCL, but did not include any operational reports of the FCL[52]. In the same year, Sohal et al. proposed a conceptual design of forces convection molten salt heat transfer testing loop[137].

In a 2014 publication, Yoder Jr. et al.[138] reported on the construction of a forced convection liquid salt test loop at the ORNL. The loop is capable of circulating FLiNaK salt and operating at temperatures up to 700°C and has been specifically designed to support the FHR concept by facilitating thermal, fluid, and component testing necessary for the development of this reactor

design. However, the authors noted that they were only in the initial stages of conducting material compatibility tests under static conditions at the time of their report.

Arora et al.[139] (2021) conducted a study on the development of advanced flow and temperature measurements in an FCL operating at 600°C. Their research was funded to advance the understanding of measuring thermal-hydraulic parameters in FLiNaK. They employed the FLEXIM ultrasonic flowmeter and NaK-filled pressure sensor to measure flow rate and validate the ultrasonic flowmeter readings within a broad range of flow rates. Additionally, they confirmed the practicality of using Optical Fiber Distributed Temperature Sensors (OFDTS) in MSL environments.

In 2023, Head et al.[140] published their experience testing an FCL, similar in construction to the FCL developed by Arora et al.[139], but using a eutectic mixture of Hitec molten salt at a temperature of 200°C. The purpose of their reactor was to serve as a test bed for fluoride salt MSR technologies, specifically in the areas of instrumentation, reactor component development, and online monitoring of salt and system chemistry. The paper describes in detail the components of the FCL, including the pump, sump tank, heater, cover gas system, and trace heating system. While they gained valuable experience in MSL operations, the duration of their testing period was short, and the operation temperature was low.

It is worth noting that the majority of MSL tests conducted to date have focused on fluoride salt. Despite several FCLs having been tested or operated in the past 25 years, none have been able to match the achievements of ORNL in the 1970s, with significantly lower operation temperatures

and durations. This study aims to share our experiences and lessons learned from our three long-term tests, lasting 50, 80, and 100 hours, on an FCL utilizing Magnak salt[35] ($MgCl_2$-KCl-NaCl) at 650°C, including design modifications and operational procedures.

II.4.2. Flow induced corrosion in molten salt

In the real world, flow-induced or dynamic corrosions are more complex than static corrosion cases. This complexity arises due to the involvement of forced mass transfer processes, which require considering additional parameters such as temperature gradients, flow velocities, and fluid hydraulic properties. As a result, the results obtained from static corrosion tests may not accurately represent the conditions experienced in flow-induced corrosion environments. However, static corrosion tests are still valuable and cost-effective as an initial step in material selection before proceeding to expensive dynamic corrosion tests. The most commonly used dynamic corrosion facilities include rotating cylinder electrodes on crucible scales, which have been extensively utilized in aqueous solutions[141-146]. However, these facilities are rarely found in molten salt corrosion condition[147]. Other widely employed options for dynamic corrosion studies are natural convection corrosion loops (NCL) and forced convection corrosion loops (FCL). The recent literature review is focused on the available data regarding the NCL and FCL in molten salt environment.

The majority of molten salt corrosion research can be traced back to the 1950s at Oak Ridge National Laboratory (ORNL). In the early stages of the Aircraft Reactor Experiment (ARE), static and seesaw tests revealed that nickel-based alloys and austenitic stainless steels exhibited

promising corrosion resistance in molten salt fluoride[148-150]. Subsequent tests were conducted on these alloys in NCL, where one loop leg was heated while another was cooled to achieve a flow velocity ranging from two to six feet per minute (fpm) at temperatures ranging from 1300 to 1500 degrees Fahrenheit. In a 1957 report, it was observed that molten fluorides caused subsurface voids in Inconel. Chemical analyses of the molten fluorides indicated a decrease in iron and nickel content and an increase in chromium content. Severe chromium loss occurred in the loop leg. The formation of voids was attributed to chromium oxidation, oxide removal from the material surface, and chromium diffusion within the bulk materials. It is worth noting that the voids beneath the surface were empty and did not connect to the surface. Furthermore, the voids tended to agglomerate and increase in size with time and/or temperature. Figure II-4 presents the results of other NCL experiments[151].

The ARE program successfully implemented FCL to conduct corrosion experiments. Apart from materials, the tested parameters included corrosion time, temperature, the ratio of structure-material-surface area to the volume of salt, and flow velocity. It was found that the maximum depth of attack was proportional to the operating time. Since the loop itself served as the corrosion specimen, the temperature at the wall-salt interface was a crucial factor. Notably, even after 1000 or more hours of recirculation, the salt in the cold leg did not reach equilibrium, and corrosion continued in both the hot and cold legs. The mass transfer attack was limited to a small region near the point of highest wall temperature. The ratio of structure-material-surface area to the volume of salt played a significant role in determining the depth of attack in the hot region, with a larger ratio

resulting in less attack depth. A comparison between NCL and FCL results indicated that the effect of flow velocity was minor, but this conclusion is not solid since only three data points available[151].

During the development of the Molten Salt Reactor Experiment (MSRE), corrosion characterization of fluoride salts was extensively studied. In March 1960, an important report was issued regarding the corrosion behavior of nickel-based alloys, specifically INOR-8 and Inconel, in a LiF-BeF_2-UF_4 (62-37-1 mole%) FCL. The FCL design and operation were reported later than the results presented by Crowley et al.[152]. The results for INOR-8 showed that after 5000 hours of operation, corrosion in the loop leg had ceased, and all the couples exhibited a corrosion band approximately 25 to 50 μm thick. Below the band, recrystallized fine grains were observed. In the case of Inconel, FCL experiments were conducted using three different salts: LiF-BeF_2-UF_4 (62-37-1 mole%), NaF-LiF-KF (11.5-46.5-42 mole%), and LiF-BeF_2-UF_4 (60-36-4 mole%). Severe corrosion occurred in the heated regions, while significantly less corrosion was observed in the unheated and cold legs. Interestingly, no deposits were observed in the cold legs. Similar to the findings in the ARE program, chromium dissolution was identified as the primary cause of material corrosion[153].

The MSRE research spanned the 1960s, with the reactor being constructed in 1964 and achieving criticality in 1965. After four years of operation, the reactor was shut down in 1969. However, the investigation into material compatibility continued until 1976. Following the reactor shutdown, the research focus shifted towards developing an alloy that could withstand irradiation and grain boundary embrittlement caused by tellurium[49,154,155]. In the MSRE report of 1975, corrosion results of SS316, Hastelloy N, and Inconel in fuel salt, coolant salt, and blanket salt were presented. The

experiments utilized both natural convection loops (NCL) and forced convection loops (FCL). The results consistently showed relatively low corrosion rates, typically around 25 μm. Notably, even with the higher flow rates in the FCL, the corrosion rate did not increase significantly compared to NCL results[156].

After a hiatus of 40 years, the study of flow-induced corrosion in high-temperature molten salts has regained attention within the research community. However, the focus has primarily been on natural convection loop (NCL) corrosion experiments. Raiman et al.[134] conducted a corrosion investigation on 316H in FLiNaK salt, operating for 1000 hours at 650°C. Similarly, Kelleher et al.[133] reported NCL work ranging from a few hours to over 10,000 hours but in NaCl-$MgCl_2$ and $MgCl_2$-NaCl-KCl salt. Unlike fluoride salt corrosion, the chloride salt corrosion experiments not only observed chromium dissolution layers and voids but also encountered instances of intergranular cracking. Kelleher et al.'s work provided a comprehensive examination of material compatibility with chloride salt in NCL, thus paving the way for future forced convection loop (FCL) tests. In this article, we will present our corrosion studies of SS316 and A709 in an FCL utilizing Magnak salt.

Chapter III EXPERIMENTAL METHOD

III.1. Thermodynamic properties measurement

III.1.1. Redox potential measurement method development

The experimental setup used is illustrated in Figure III-1. The following chemicals with high purity levels were purchased: anhydrous LiCl (>99%), anhydrous KCl (>99%), and AgCl (99.999%) from Sigma Aldrich. A reference electrode and a counter electrode were made from 1 mm diameter silver wires (99.999% purity, Alfa Aesar). A working electrode was made from a 3.05 mm diameter graphite rod (99.9995% purity, Alfa Aesar), with the tip end section roughened using 120-grade sandpaper to absorb and store the produced chlorine. The electrodes were connected to a potentiostat instrument (Gamry Interface 1000) for electrochemical tests. The heating instrument was a muffle furnace equipped with a digital single setpoint temperature controller. The furnace exhibited ±7.8 °C uniformity and ±0.3°C stability at 1000°C. The experiments were conducted in an Argon (>99.999% purity) filled glovebox (PureLab HE 4-glove 1950mm, Inert), maintaining oxygen and moisture levels lower than 5 ppm.

To prepare the eutectic salt (45wt% LiCl, 55wt% KCl), high purity anhydrous LiCl and KCl were weighed using a high precision digital balance (MS 105DU Mettler Toledo) and mixed (~50 g). The mixture was loaded into an alumina crucible and heated at 300 ℃ in the furnace for at least 8 hours to remove residual moisture from the salt. A heating rate of 3°C/min was set to avoid thermal

expansion of the alumina crucible and safety dish. The salt was then heated to the target working temperature and kept in the furnace for 8 hours to stabilize the system. AgCl was added to the alumina crucible in the desired amount, and the temperature was maintained for several additional hours before the electrochemical experiments were conducted.

In this experiment, the formation of chlorine gas at the graphite working electrode surface was achieved through either chronopotentiometry or potentiodynamic scan methods, instead of direct injection of chlorine gas into the system, which is inconvenient from an experimental standpoint, as explained earlier. This required unique constant current values (ranging from 0.012 A/cm^2 to

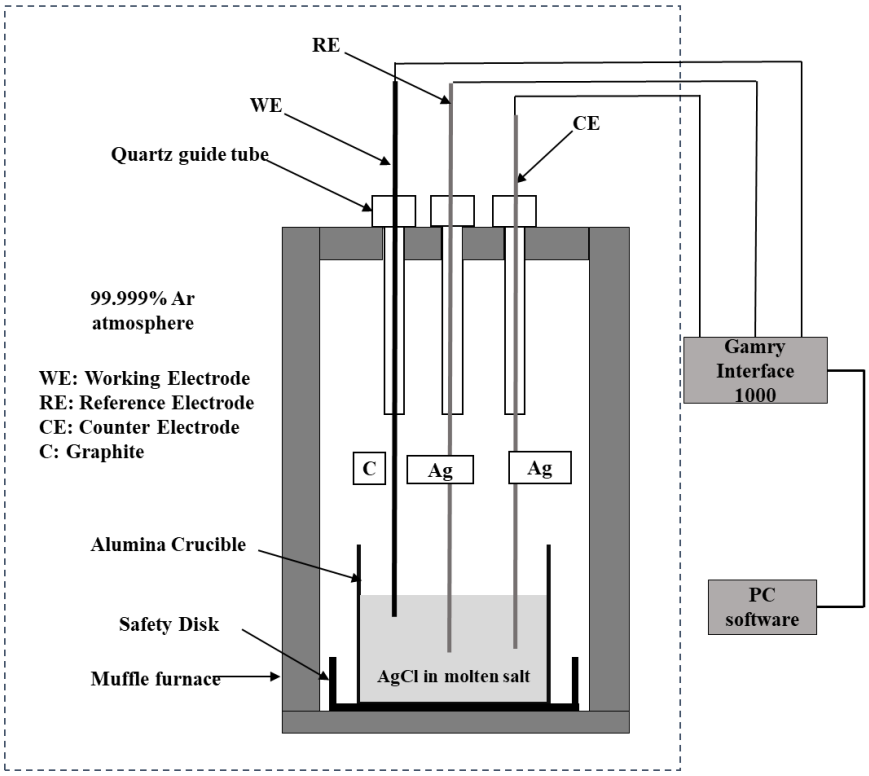

Figure III-1 Schematic drawing of the three-electrode electrochemical cell.

0.03 A/cm^2) for chronopotentiometry and scan rates (ranging from 50 mV/s to 250 mV/s) for the potentiodynamic scan, which will be described later. The equilibrium potential of the graphite working electrode was measured with an Ag wire serving as a reference electrode, and it corresponds to the potential of the Cl_2/Cl^- couple versus the Ag^+/Ag reference couple. As sufficient chlorine gas is produced at the graphite electrode using these two techniques and the system is saturated with chlorine ions, the activities of Cl_2 and Cl^- are assumed to be unity, and the potential of the working electrode is fixed. Activity coefficient calculations are then performed.

III.1.2. Redox potential measurement in Magnak salt

To conduct the electrochemical experiments, a three-electrode electrochemical cell was constructed using a working electrode (WE), a counter electrode (CE), and a metal reference electrode (RE), as shown in Figure III-2. In the magnesium and chromium tests, both the WE and CE were graphite rods with a 3.05 mm diameter and 99.9995% purity. In the nickel test, a 3 mm Ni rod was used as the CE. The immersion surface area of the CE was over four times greater than that of the WE. The surface areas of the WE and CE were determined by measuring the immersion length and diameter of the electrode after the experiment. Two different types of REs were used for different element experiments. In the chromium test, a Cr metal reference electrolyte was contained in a one-end closed, alumina tube with a 4.78 mm inner diameter and a 6.35 mm outer diameter (McDanel Advance Ceramic Technologies, 99.8%). The closed-end was polished to a wall thickness of about 0.40 mm or less. For the nickel and magnesium tests, the metal references were directly exposed to the salt matrices. However, since the melting point of magnesium is lower than the operating temperature and magnesium has a lower density compared to the salt matrices,

a test fixture was designed for the magnesium test, as shown in Figure III-3 (a). The outer alumina tube used was the same as the chromium test, but a hole was drilled near the closed end instead of polishing. An open-end tube with an OD of 3.96 mm and an ID of 2.39 mm was then inserted into the bottom of the alumina tube. At the center of the fixture is a 1 mm diameter tungsten rod, which is used as an extension wire to make the liquid magnesium connectable. Three electrodes were connected to a Gamry workstation (Interface 1000), which was controlled and monitored by a PC using its software.

To prepare the Magnak salt mixture, a total of 50g of anhydrous $MgCl_2$ (99%, American Element), KCl (>99%, Sigma-Aldrich), and NaCl (>99.5%, Sigma-Aldrich) were weighed using a high-precision digital balance (MS 105DU Mettle Toledo) in a 100ml high-form alumina crucible (AdValue Technology). As chloride salts, especially $MgCl_2$, are hygroscopic and can absorb moisture to form hydrates during transportation, a thermal purification procedure of the mixed salt powder was developed based on Vidal and Klammer's report[67]. The temperature profile of the furnace (FB1315M, HOGENTOGLER&CO.INC) and operations are shown in Figure III-4 . The long holding time and stirring operation were designed to help release hydrates.

III.1.2.1. Chromium tests

For the electrochemical experiments, 0.3g of Magnak reference electrolyte was mixed well in the alumina tube with the desired amount of $CrCl_2$ (Sigma-Aldrich, 99.9%). The tube was inserted into the furnace, but it was hanging above the bulk salt at the beginning of the thermal purification procedure. After stabilization at 873 K for 8 hours, samples of both the RE salt and bulk salt were collected for further Inductively Coupled Plasma Mass Spectrometry (ICP-MS) concentration

analysis. The tube was then immersed in the salt, and a chromium rod (99.95%, American Element) with a 2.54 mm diameter was inserted into the reference electrolyte to establish an equilibrium Cr(II)/Cr couple. After 4 to 5 hours, CP tests were performed gradually with a 50 K temperature gradient from 873 K to 1073 K.

III.1.2.2. Nickel tests

In this experiment, a desired amount of $NiCl_2$ (98%, Sigma-Aldrich) was added to the bulk salt. As nickel ion has only one stable valence in the molten salt, the alumina tube used in the chromium test was not necessary, as shown in a previous study[116]. During the CP test, the concentration of $NiCl_2$ did not change, as confirmed by ICP-MS results. The experimental setup was the same as in the previous study[116], with a 3.2 mm diameter Ni-RE rod (99%, Alfa Aesar) exposed to the bulk salt. The CE was the same material as the RE. The heating procedure was the same as before. To verify the results, two independent experiments were carried out at different temperature ranges with the same $NiCl_2$ concentration. One experiment was conducted from 773 K to 973 K, and the other was conducted from 873 K to 1073 K. More details are discussed below.

III.1.2.3.Magnesium tests

For the magnesium experiment, a magnesium ball (99.99%, Amazon) weighing 0.176g was added to the tube as shown in Figure III-3.(a). This weight was calculated based on liquid Mg density data reported by McGonigal et al.[157]. The weight ensured that, in the liquid state, the Mg was higher than the hole but lower than the bulk salt after immersing the RE into the bulk salt. Firstly, the tube with solid Mg was inserted into the furnace without touching the pre-prepared bulk salt

and heated to 1023 K at a heating rate of 3 K/min to ensure that the Mg was melted, which is higher than Mg's melting point of 823 K. Secondly, the two-end open alumina tube was inserted into the liquid Mg to be in contact with the bottom of the outer tube, then a W rod was inserted into the two-end open tube to touch the liquid Mg. Finally, the RE was inserted into the bulk salt. At this time, because liquid Mg has strong surface tension, it blocked the hole on the outer tube instead of flowing out. Even though the density of Mg is much smaller than the density of salt, the bulk salt would not flow into the tube due to high surface tension[158]. The schematic explanation of Mg RE is shown in Figure III-3.(b). After the experiments, no Mg metal was found in the salt, and no salt was found in the RE alumina tube, indicating that there was no mass exchange between liquid Mg and molten salt through the hole. The experiments were performed at a temperature gradient of 25 K from 1023 K to 1073 K. Then it was cooled to 923 K and reheated to 998 K with a temperature gradient of 25 K. All operations were carried out in a high purity Argon (99.997%) filled glovebox (Inert), which maintained the moisture lower than 0.5 ppm and oxygen lower than 0.1 ppm. After inserting the CE and WE, CP tests were performed. After the test, samples of the reference electrolyte and bulk salt were collected for further ICP-MS concentration determination.

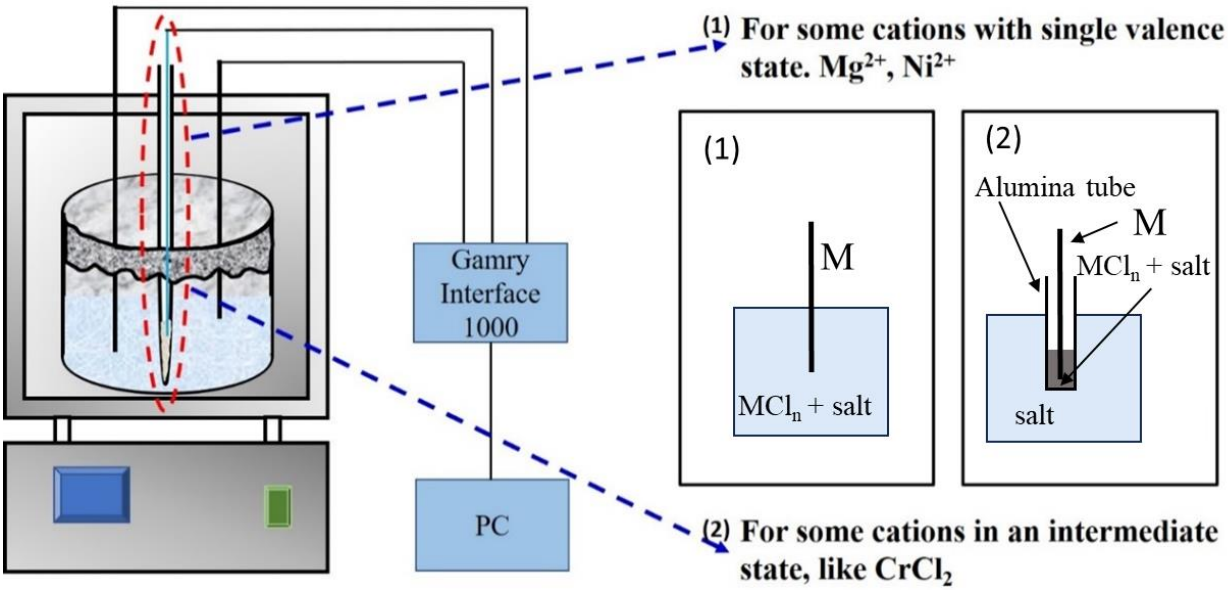

Figure III-2 Schematic of experimental setup three-electrode electrochemical cell (1) metal reference for single valence state cations, (2) metal reference with alumina membrane for cations in an intermediate state.

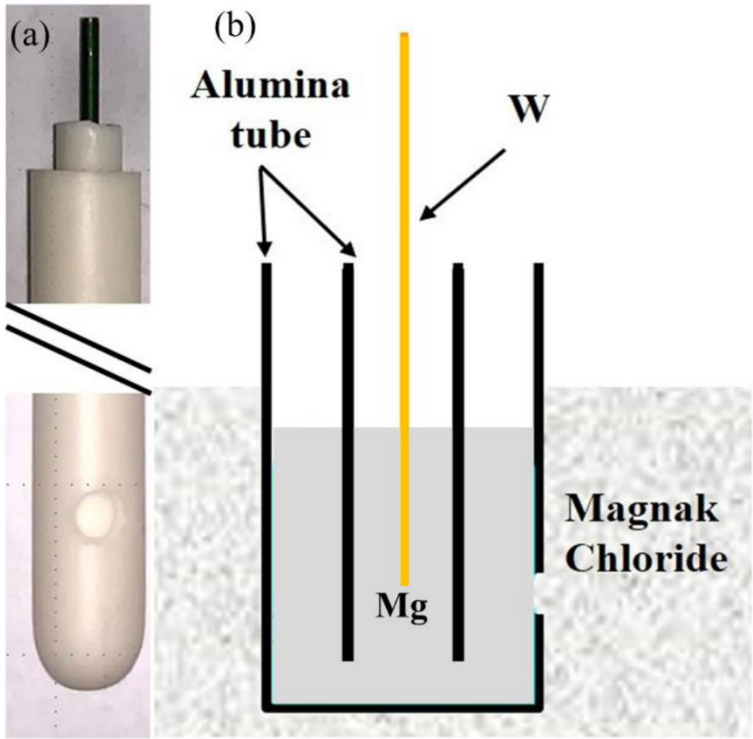

Figure III-3 (a) Design of liquid magnesium electrode. (b) schematic of liquid magnesium in the alumina container.

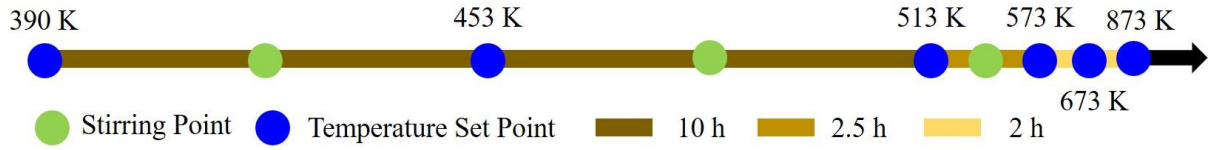

Figure III-4 The thermal purification profile and operations timeline.

III.2. Electrochemical corrosion study in Magnak salt

The electrochemical corrosion test was conducted within a glove box filled with pure argon gas, ensuring an oxygen level of 15 parts per million (ppm) and a moisture level of 2.3 ppm. To assess

the corrosion potential, corrosion rate, and surface conditions of the sample, a three-electrode electrochemical setup was employed. This setup facilitated measurements through various techniques, including conduction potentiodynamic scan (PD), electrochemical impedance spectroscopy (EIS), open circuit potential (OCP), and cyclic voltammetry scan (CV) during the initial 10-hour immersion period.

The salt mixture (Magnak) used in the experiment was composed of $MgCl_2$-KCl-NaCl in mole percentages of 44.7%, 25.8%, and 29.4% respectively. The individual chloride salts, $MgCl_2$, KCl, and NaCl, were separately purchased from Thermo Fisher Scientific with a purity of 99%. Prior to conducting the experiments, the salts were stored in ambient conditions. It should be noted that chloride salts have hygroscopic properties, which means they tend to absorb moisture during shipping and storage.

To mitigate the moisture content, the salts were transferred into a glove box and subjected to separate thermal purification processes using alumina crucibles at a temperature of 200 °C for over 24 hours. During this step, the moisture and oxygen levels within the glove box were monitored and observed increasing then return to their original values. A total of 70 grams of heat-treated salts were accurately weighed using a high-precision digital balance (MS 105DU Mettle Toledo) and physically mixed in a 100 ml high-form alumina crucible (MSE Supplies). The mixture was then subjected to a thermal purification process following a method developed by our lab. The process involved heating the mixture to 500 °C and allowing it to settle for at least 5 hours before gently pouring it onto a pure nickel plate to rapidly cool and solidify the salt. It is important to note

that during this process, some insoluble particles settled at the bottom of the crucible, and caution should be exercised to avoid pouring out the precipitates.

After this step, approximately 60 grams of the quenched salt were obtained. Subsequently, a clean alumina crucible was used to melt approximately 120 grams of the thermally purified Magnak salt at 500 °C. Following that, 10-15 wt% magnesium balls (99.99% purity, sourced from Amazon) were added to the salt. The magnesium balls were cleaned using a 0.5 mole/L HNO_3 solution for 30-60 seconds, followed by rinsing with deionized water and ethanol, and vacuum drying. The system was then heated at a rate of 3 °C/min until reaching 800 °C, where it was held isothermally for 2 hours. Afterward, the system was cooled down to 550 °C, and the remaining magnesium was separated from the salt. It should be noted that the magnesium typically maintained a spherical shape, but occasionally merged into larger balls or formed individual smaller balls. The chemically purified salt was allowed to settle for at least 8 hours at 550 °C to allow the precipitation of MgO. The same quenching process as before was employed, and approximately 100-105 grams of chemically purified salt were collected. The O and H analysis were conducted to the chemical purified salt, to determine the impurity contain.

Three batches of thermally purified salts were prepared and labeled as A, B, and C. The details of the test matrix can be found in Table III-1. The materials investigated in this study include Ni (99%, Alfa Aesar by thermo fisher scientific), Fe (99%), and Cr (99.95%, American Elements). Additionally, two alloys, namely SS316 and A709, were studied. The chemical compositions of these alloys are provided in Table III-2. Except for the A709 samples, all other materials were in rod shape. The A709 samples, on the other hand, were in plate shape with dimensions of 3 mm

width and 1.5 mm thickness. The immersion depth of the samples was measured after the experiments were conducted. Before the experiments, all sample surfaces underwent a polishing process using SiC sandpaper with gradually increasing grit sizes from 240 to 1200. Following the polishing step, the samples were stored in the glovebox.

Table III-1 Electrochemical corrosion tests matrix.

Batches	Sub-Batches	Sample Material	Magnak salt weight (g)	Temperature (°C)		
A	A1	Ni	30	600	650	700
	A2	Fe	30	600	650	700
	A3	Cr	30	600	650	700
B	B1	A709	30		600	
	B2	A709	30		650	
	B3	A709	30		700	
C	C1	SS316	30		600	
	C2	SS316	30		650	
	C3	SS316	30		700	

Table III-2 Chemical composition of SS316 and A709.

Elements	Cr	Ni	Fe	Mn	Mo	Si	Nb	Ti
A709	19.93	24.98	Bal.	0.91	1.51	0.44	0.2	0.04
SS316	18-20	11-14	Bal.	1-2.5	2-3	0.3-0.65	_	_

Elements	Cu	N	C	P	B	S
A709		0.148	0.066	0.014	0.0045	-
SS316	0.75	_	0.03	0.03	_	0.03

Figure III-6 illustrates the arrangement of electrochemical tests conducted in this study. One of the objectives of this research was to determine the corrosion potentials of pure metals and alloys in Magnak salt, therefore careful consideration was given to the design of the reference electrode (RE) section. In the current study, a magnesium (Mg) metal reference electrode, modified based on our previous work[35], was utilized. The Mg RE was prepared using the same acid-treated Mg balls employed in the chemical purification process.

To fabricate the Mg reference electrode, 0.37 grams of Mg balls were placed in a cleaned alumina tube, and the temperature gradually increased to 700 °C. Subsequently, a 1 mm tungsten rod was inserted into the tube, and the system was allowed to cool naturally. This entire Mg electrode fabrication process was performed within the glovebox. Finally, the aluminum tube was broken, and the Mg electrode was acid cleaned, followed by rinsing with deionized water and ethanol. The image of the Mg electrode can be seen in Figure III-5. The Mg reference electrode also incorporated an alumina tube with a 1 mm hole drilled at the bottom. This hole allowed the salt to flow into the tube and made contact with the Mg electrode while slowing down the diffusion process of corrosion products towards the Mg electrode.

The experimental procedures for the electrochemical corrosion study of pure metals and alloys differ, as indicated in Table III-1. The sub-batch salts are separated from the same chemically purified batches to ensure that the sub-batch salts have similar conditions, especially in terms of impurities. For the study of pure metals, electrochemical corrosion experiments were conducted at three different temperatures gradually increasing from 600 to 700 °C. The procedure involved ramp heating a 30 g sub-batch salt in an alumina crucible at a rate of 5 °C/min until reaching 600

°C. At this temperature, ICP-MS samples were collected, and CV scan was performed using a tungsten electrode before switching to corrosion specimens. Once the corrosion specimens were set up, an OCP measurement was performed for 1 hour, followed by a PD scan in the positive direction at a rate of 2 mV/s[124] within a scan window of ±0.25 V relative to the OCP. To ensure consistency and avoid introducing excess corrosion products into the molten salt for the subsequent tests, a carefully selected scan rate was applied during the experimentation process. The chosen scan rate was designed to minimize the amount of corrosion products released into the melt. The temperature was then increased to 650 °C, and the same procedure was repeated with a new set of corrosion samples.

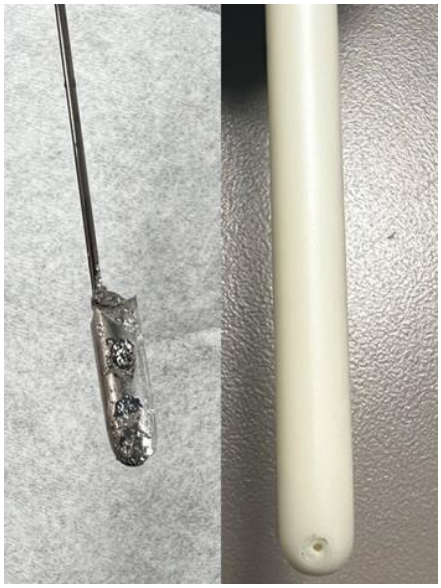

Figure III-5 Pictures of Mg reference electrode (Left) and Mg reference container (Right).

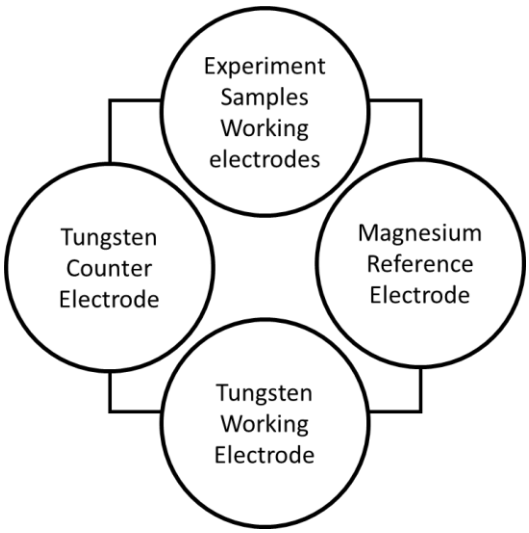

Figure III-6 Top view of the electrochemical corrosion tests setup.

III.3. Forced convection molten sate loop design and experience

A forced convection molten salt loop was designed and constructed in Nuclear Material and Fuel Cycle Center at Virginia Tech. The loop consists of an SS316 auxiliary tank, an SS316 storage tank, a centrifugal sump-type pump system, an SS316 loop, a vertical sample insertion column, an SS316 drain line, a cover gas and pressurizing system, heater zones on tanks, trace heating system for all pipes, and temperature and flow measurement system. This section will give details of each system.

III.3.1. Auxiliary tank

The auxiliary tank serves as both a reservoir and purification tank and is constructed of 316 stainless steels. The tank is comprised of a cylindrical body, an ellipsoidal bottom, and a flat flange lid that are welded to ensure a proper seal. Its inner diameter measures 16 inches, outer diameter

16.5 inches, and depth 8.5 inches. With a total capacity of 1800 cu.-inch, the auxiliary tank can hold up to 1190 cu.-inch of liquid salt and 610 cu.-inch of cover gas. A 1-inch schedule 160, SS316 pipe is welded to the center of the ellipsoidal bottom to serve as the connection point to the storage tank. The powder-salt loading port measures 2.5 inches and is located on the lid. Seven 0.5 inches FNPT ports are present, serving as the cover gas port, exhaust port, pressure transducer port, thermowell port, and three purging ports. The tank bottom also features a 0.5-inch SS316 tubing underneath the purging port, enabling flushing of the powder or liquid salt for purification.

III.3.2. Pump and storage tank

The storage tank functions as a critical component in the molten salt circulation loop system. Once the salt is purified in the auxiliary tank, it is transferred to the storage tank in preparation for operation. The storage tank shares similar specifications with the auxiliary tank, consisting of an SS316 cylindrical body with an SS316 ellipsoidal bottom. It features an inner diameter of 12.4 inches, a depth of 15.5 inches, and a wall thickness of 0.25 inches. The total volume of the storage tank amounts to 1950 cu.-inch. At the top of the storage tank, there is a 1-inch thick SS316 flange with an inner diameter of 12.5 inches and an outer diameter of 17.5 inches. This flange is used to connect to the sump pump system. To ensure a reliable seal, both the pump and storage tank flanges are equipped with concentric grooves and sealed with a metallic gasket from Flexitallic that covers the entire surface. It is noteworthy that we have encountered no issues with this setup during our operations.

The centrifugal pump used for the molten salt circulation is fabricated entirely from SS316, ensuring its durability and resistance to corrosion. It is driven by a 3-phase variable frequency motor with a maximum power rating of 3 HP. The motor is connected to the pump via a chain coupling, which effectively eliminates shaft vibration and efficiently transmits torque. To address the potential impact of thermal expansion on the dynamic balance of the shaft, a shaft with a diameter of 1.5 inches is utilized, extending along a length of 30 inches. Moreover, in consideration of the high operating temperature of the system, the pump shaft bearings and supports are cooled using an industrial fan, as the bearing grease cannot exceed 260 ^{o}C to maintain optimal performance. For reference, the pump system drawing is illustrated in Figure III-9, providing a visual representation of the pump and its components.

One of the primary concerns in a molten salt loop system is the seal around the shaft, as leakage can result in air diffusing into the system and causing the salt to become aggressive. To address this concern, a stuffing box is designed for the shaft seal, as depicted in Figure III-7. The stuffing box is composed of five components: an SS316 seal box, an SS316 lid, an SS316 flange, a metallic raising surface gasket, and a pack of graphite seals. The gasket is compressed between the box and flange using only four 3/8 inch SS316 bolts, with the compression force being limited. Concentric grooves are fabricated on the flange and stuffing box surfaces to enhance the sealing performance. Furthermore, a customized raising-surface metallic gasket from Flexitallic is utilized to reduce the contact surface area and increase the compression pressure, ensuring a tight seal. Three layers of die-formed graphite seal sets, in Figure III-8, obtained from American Seal and Packing, are installed in the orientation illustrated in the figure and then compressed with the lid by tightening

the four bolts. The die-formed graphite seal is a hard-solid ring at room temperature but becomes softer as the temperature increases, making it an ideal material for working with the rotating shaft to provide a seal with minimal friction. However, it is important to note that graphite material is not suitable for use in an oxidizing environment above 500 ^{o}C, and as a result, the pump flange cannot be thermally isolated to prevent material failure. Proper care and monitoring of the stuffing box and graphite seals are crucial to ensure effective sealing in the molten salt loop system.

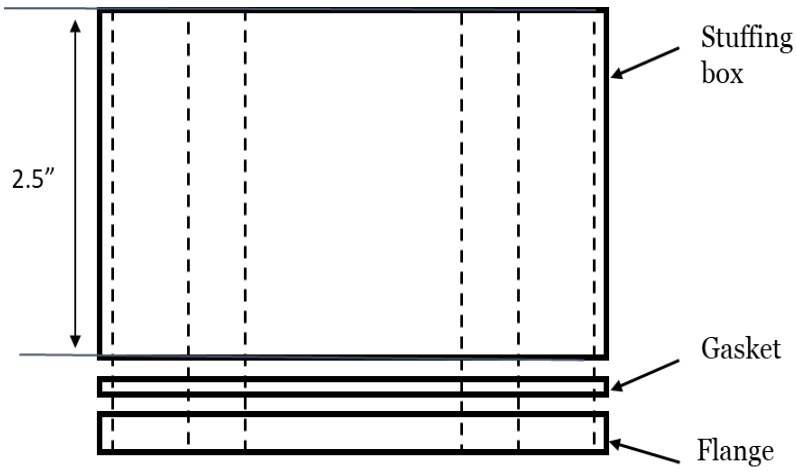

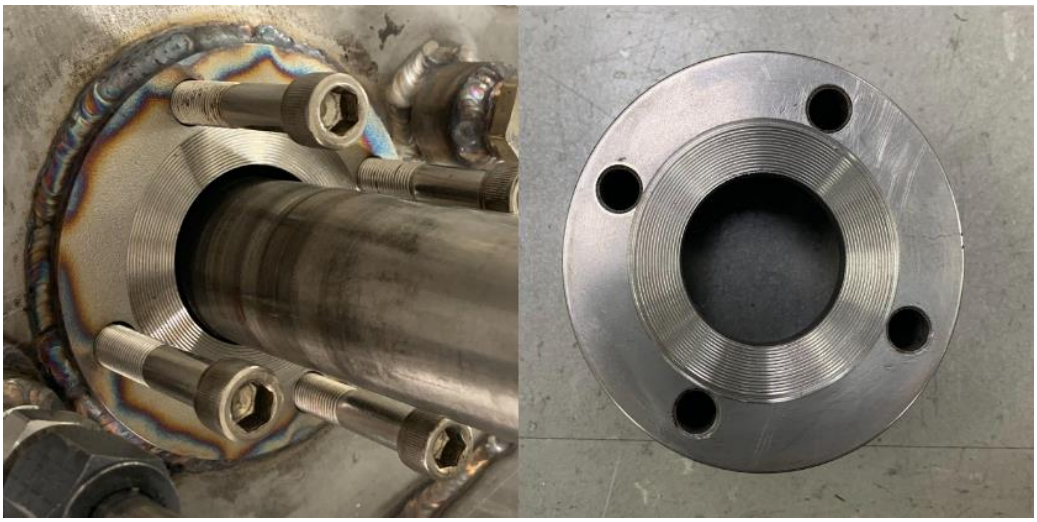

Figure III-7 Stuffing box design and real pictures.

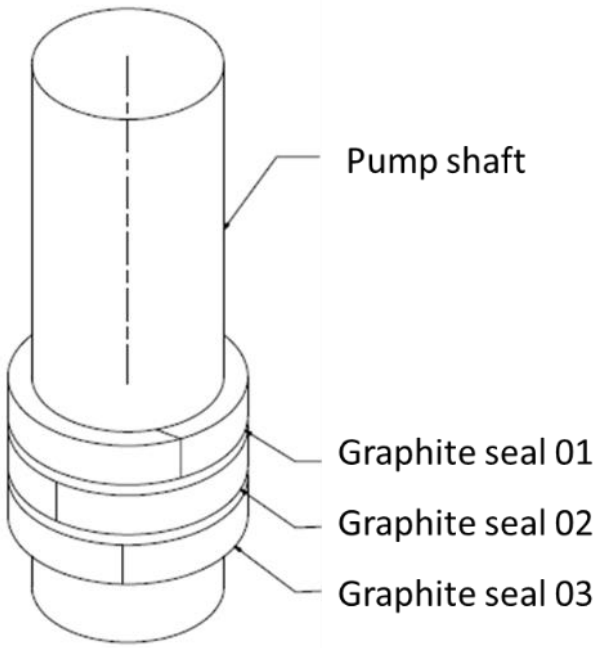

Figure III-8 Illustration of Graphite seal pack.

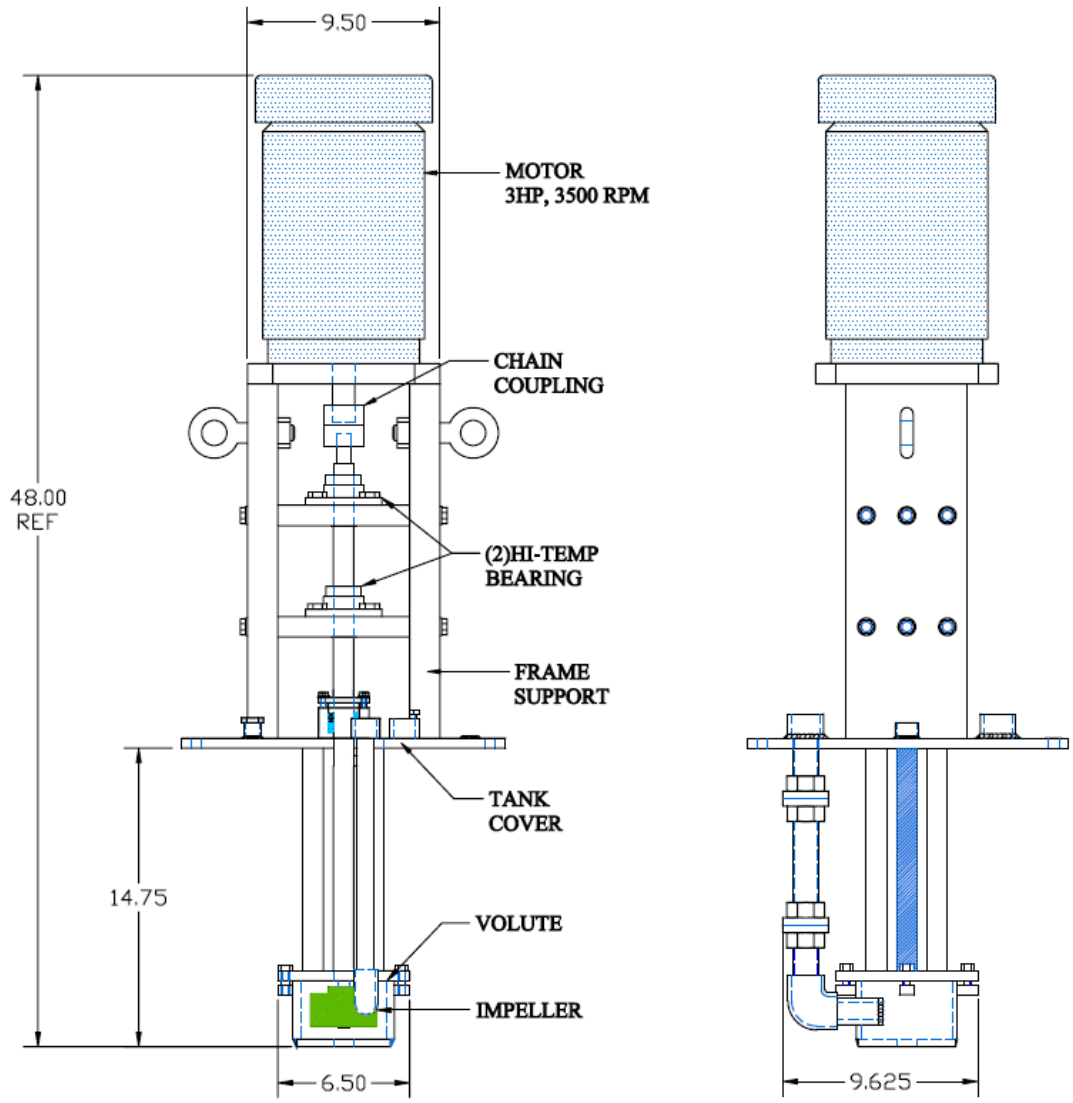

Figure III-9 Drawing of the pump system. Unit: inch.

III.3.3. Loop and test column

The loop body of the molten salt loop system, shown in Figure III-10, consists of four main parts: a 17 ft long closed circuit, a 6.5 ft long salt supply line, a 2 ft long drain line, and a 2 ft long vertical

test column associated with the closed circuit. All of these components are made of schedule 160, 1-inch SS316 seamless pipe with a 1.3125 inches outer diameter (OD) and a 0.815 inches inner diameter (ID). The salt flow in the system is controlled by several high-temperature ball valves that were ordered from Gosco Valves. However, issues were encountered with the valves during application, particularly with regards to leaks. All other connections between the pipes and valves were welded using both the socket and butt weld connection methods at different joint locations to ensure a reliable seal. No issues were encountered with the welding seals. Prior to changing all connections to welding, flange connections with metallic gasket combinations were tested for portability reasons. While flanges worked well at room temperature and the system passed the argon gas leak test at 500 ^{o}C, all flanges failed after recirculating the salt at 600 ^{o}C. As a result, it was decided to weld all joints to ensure a reliable and leak-free connection between the pipes and valves in the molten salt loop system.

The supply line and drain line facilitate the transportation of salt between the auxiliary and storage tanks, with valves regulating the flow direction. Upon termination of the operation, the salt is drained back to the auxiliary tank. However, due to the imperfect assembly of the storage tank, which includes a pump and stuffing box seal at ambient temperature, there is visible leakage observed around the shaft. Furthermore, the solidification and re-melting of the salt may result in detrimental effects on the shaft and impeller, potentially leading to pump failure.

The test column is located vertically at the far end of the circulation loop, and the flow direction is bottom-up to avoid bubble formation. The sample fixture insertion port is at the top of the test column and is sealed with two class 300 raising surface flanges and a metallic gasket. Since the

gasket does not directly contact the salt, this is the only location where the flange is used. The design of the SS316 sample fixture, Figure III-11, is complex due to the large length and diameter ratio of the bottom part, making it difficult to make it perfectly straight. The fixture is welded to the bottom of the thermowell flange, and six individual samples can be installed on the sample holder, which is designed to prevent any contact between the samples and the holders. To achieve this, an alumina tube covers the sample holder surface, and two layers of alumina spacers are sandwiched between the samples. Thermal expansion is also a concern, as the sample fixture assembly is assembled at room temperature. Therefore, before heating the system, all components are compressed by a tightened nut. As the temperature reaches the operating temperature, the thermal expansion difference between the alumina and SS316 creates a 1 mm gap. When exposed to the flowing salt, the unexpected jumping of the samples may cause the alumina isolators to fail. To prevent this, four Nimonic 900 spring washers are used to overcome the thermal expansion effect. The final assembly is shown in Figure III-12.

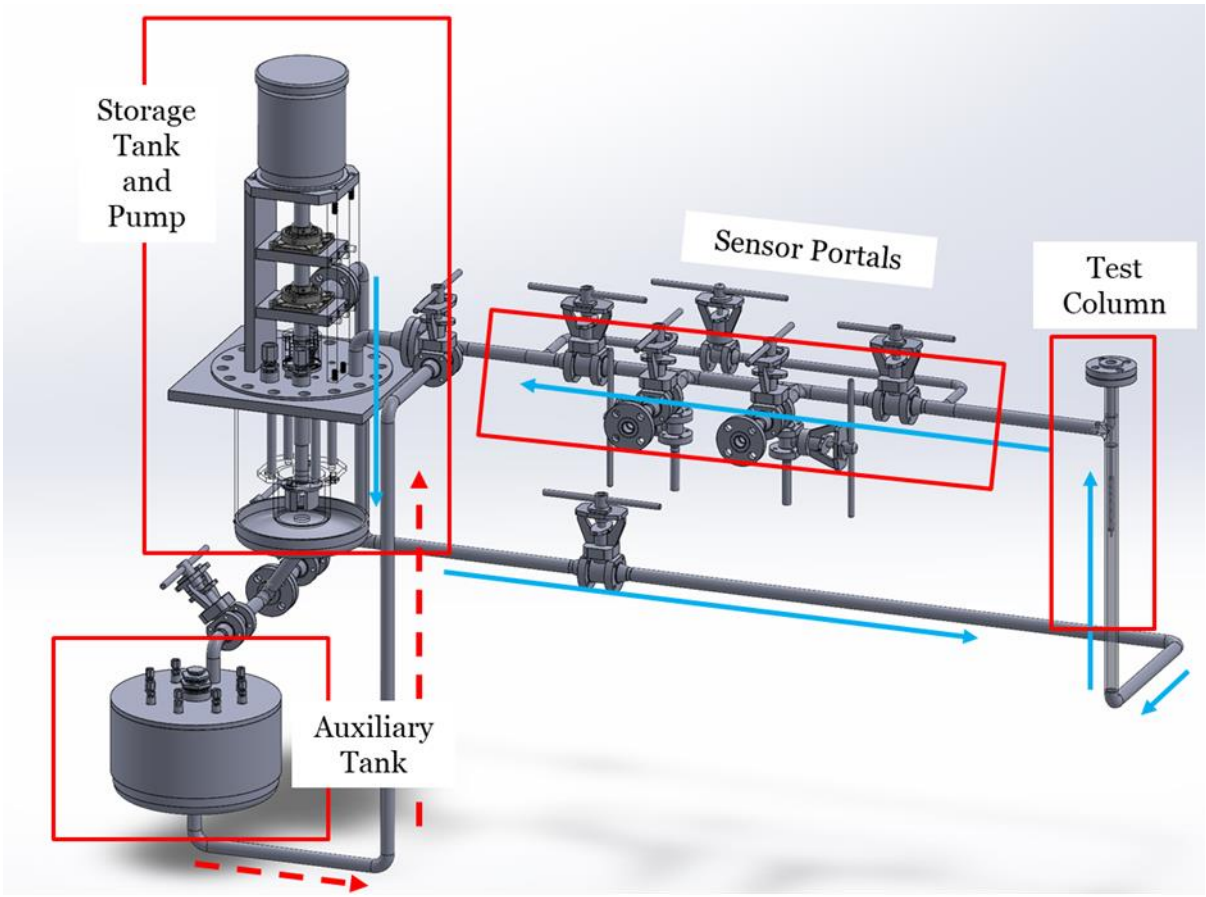

Figure III-10 3D drawings of the initial loop design.

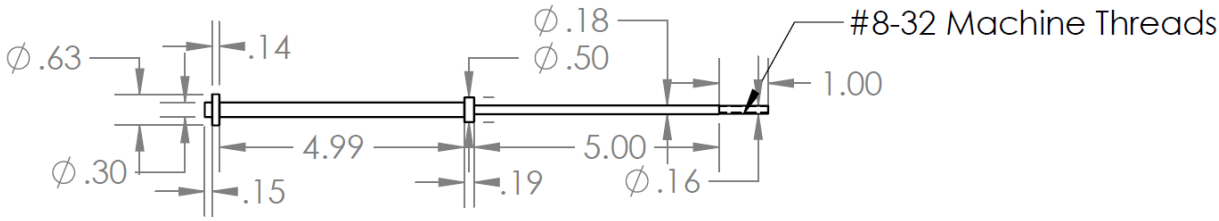

Figure III-11 Detailed sample holder drawing and dimensions. Unit: inch.

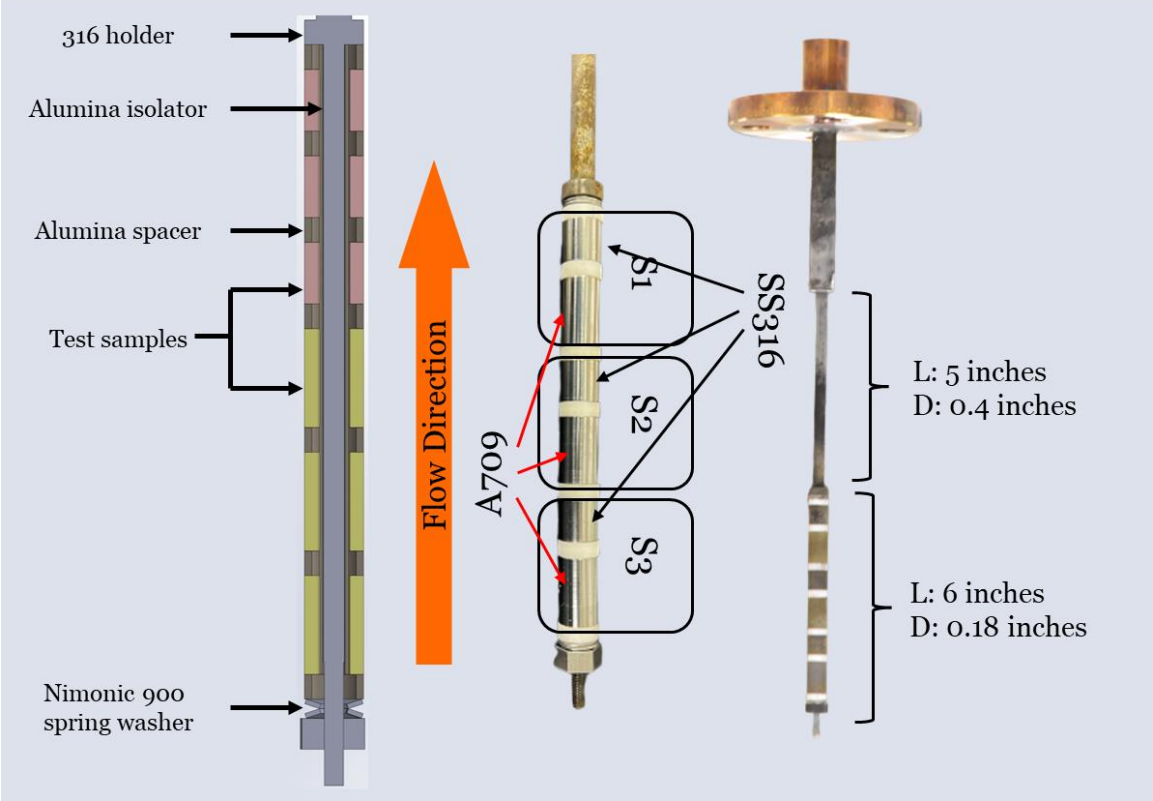

Figure III-12 Sample assembly overview. Left: sample assembly cross-section demonstration. Mid: sample assembly before test. Right: sample assembly after 100 hours test.

III.3.4. Gas system

The gas system is established by connecting an ultra-high purity argon gas source. The gas system within the loop serves four primary functions. Firstly, it is utilized for purification purging purposes. Secondly, it is employed for pressurizing the system to facilitate the transport of liquid salt between the auxiliary and storage tanks. Thirdly, it is used to establish cover gas in both the auxiliary and storage tanks during operation, and fourthly, it is utilized to drive the salt in the loop back to the tank when the pump is stopped, in order to prevent accidental flow of salt into the loop

prior to restarting the pump. The ultra-high purity argon gas is supplied from a standard gas cylinder with a maximum output pressure of 2500 psi. A pressure regulator is employed to reduce the pressure to within 30 psi, and the argon gas then passes through a flow meter before being distributed to the respective sections of the system.

III.3.5. Heating and isolation system

Three distinct heating zones have been incorporated into the design of this loop. The first heating zone is specifically intended to maintain the liquid salt within the storage tank at the desired temperature. To achieve this, six clamp heaters with a power rating of 1500W and operating at 240 VAC are utilized. These heaters are capable of reaching temperatures of up to 760 ^{o}C and are controlled by a high-limit thermocouple (TC) positioned beneath the heater, as well as a TC immersed directly into the salt.

Similarly, the second heating zone is responsible for regulating the temperature of the auxiliary tank. It employs the same configuration as the first heating zone, consisting of six clamp heaters with a power rating of 1500W and operating at 240 VAC. These heaters are also capable of reaching temperatures of up to 760 ^{o}C and are controlled by a high-limit TC positioned beneath the heater, as well as a TC immersed in the salt.

The third heating zone, referred to as the trace heating zone, is utilized to heat all the pipes within the system before the salt is introduced into them. For this purpose, tape heaters from Omega Engineering are utilized, with a power density of 13 W/in^2 and operating at 240 VAC. These heaters are capable of reaching temperatures of up to 760 ^{o}C. The total power rating for the trace

heating in the circulation loop is 10,000 W, with 6500 W designated for heating the lines between the auxiliary and storage tanks.

The clamp heaters installed on the two tanks have been performing satisfactorily, as there have been no issues with leaks or salt moisture on the tank surface. However, the tape heaters, which utilize fiberglass insulation, have experienced some challenges. The color of the fiberglass insulation changes from brown (when new) to white after being exposed to temperatures of 650 ^{o}C or higher. Additionally, after heating to 700 ^{o}C, the fiberglass insulation becomes brittle and difficult to move, even with gentle handling. This poses a risk of the insulation breaking and losing its effectiveness, particularly if the loop is accidentally impacted, potentially resulting in a short circuit.

Furthermore, the tape heaters are wrapped around valves or welding joints, which are areas with a high risk of leaks. If the fiberglass insulation becomes wet with salt, it can lead to heater failure. The most concerning issue is that before a heater short circuit occurs and burns a fuse, the salt-wetted fiberglass may come into contact with the heating element and loop, allowing current to flow into the salt and leading to electrolysis of the salt, which can result in chlorine-related hazards.

The clamp and tape heaters are in direct contact with the surfaces of the tanks and pipes. To provide insulation and protect against heat loss, a layer of half-inch ceramic fiber blanket with a high purity grade of 8 lb is installed on the outer surface of the heaters. This is followed by a one-inch thick customized isothermal jacket that covers the thermal blanket. Another layer of one-inch thick ceramic fiber blanket with a high purity grade of 8 lb is then applied to cover the jacket. The

outermost layer consists of a half-inch thick ceramic fiber blanket with one side coated with aluminum foil, which serves to minimize the risk of fiber and dust hazards. Even during operation at temperatures as high as 650 ^{o}C, the final outer surface temperature of the insulation is maintained at around 50 ^{o}C.

III.3.6. Temperature and flow measure system

Temperature is measured and monitored by 18 K-type probe and surface thermocouples (TC). Three probe-type TCs are immersed into auxiliary tank, storage tank, and the test column with thermowell to monitor the salt temperature. Four surface TCs are below the heaters to avoid heater overheat, two for the tanks' heaters, two for the tape pipes' heaters. Twelve pipe clamp surface TCs distributed along the loops. All three probe TCs are calibrated before installation. However, the clamp TCs are ordered from different venders and the high-temperature leads are too short. They are not calibrated.

A non-intrusive ultrasonic flowmeter manufactured by FLEXIM was used to measure the flow rate. The largest attraction of non-intrusive measurement is the high accuracy and not leaks risk. The measurement is achieved by mounting two wave injectors on the special treated pipe outer surface in 180 degrees. The ultrasonic flow meter operates by alternately transmitting and receiving a burst of ultrasound between the two transducers by measuring the transit time that it takes for sound to travel between the two transducers in both directions, shown in Figure III-13. The difference in the transit time measured is directly proportional to the velocity of the liquid in the pipe. The basic theory is Doppler effect of the ultrasound frequency caused by the flow

properties, such as temperature, density, viscosity, and suspended particulates. The properties we use are reported by Wang et al, which is shown in Table III-3.

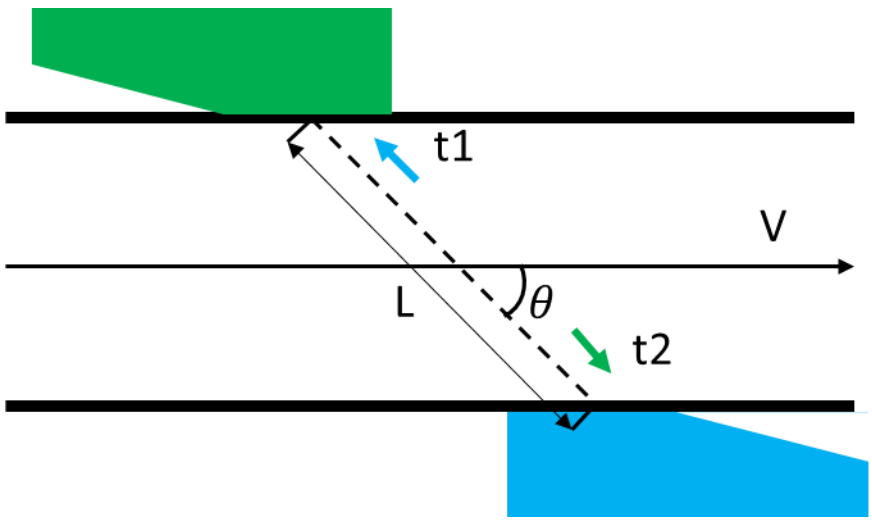

Figure III-13 Illustration of the principle of ultrasonic flow meter.

Table III-3 Ternary chloride molten salt density and viscosity for NaCl-KCl-$MgCl_2$ (Mole:28.39%-27.25%-44.36%)[65].

Temperature ℃	Density (kg/m^3) $\rho = 1993.38 - 0.55663 * T(℃)$	Viscosity (cP) $\ln \mu = \frac{1102.42}{T\ (K)} - 0.1525$
600	1659.402	3.035
650	1631.571	2.835
700	1603.739	2.666
750	1575.908	2.522

III.3.7. Seals

In various locations, different seal technologies are utilized. In the case of the VT loop system, we have implemented copper paste seals, flange seals, welding seal, metallic gasket seals, and graphite seal.

Copper paste seal: the copper paste seal is applied to the compression fitting threads, which are directly connected to the two tanks on the lid but are not exposed to the salt. These fittings are primarily utilized on the gas line, and the highest measured temperature on these fittings is approximately 600 ^{o}C. We have not encountered any issues with the copper paste seal, and all connections are able to be disassembled for maintenance and repair purposes.

Flange and rigid metallic gasket (FRG): In the VT FCMSL application, the FRG assembly is used for the pipe connections and sample assembly insertion, and a similar setup to provide seal of the stuffing box. The rigid metallic gasket used is the Flexpro Style ZA model, which is ordered from Flexitallic. This gasket is designed for smooth or raise surface flanges and consists of a serrated solid metal core, a losing outer ring, and 0.02” thick facing materials, as shown in Figure III-14. In our application, the facing material is Thermiculite® 845, which can withstand temperatures of up to 982 ^{o}C. The core material is SS316, and the SS316 loose outer ring is made of a pre-weld half ring. All flanges in the current design are SS316 Class 300 raised surface flanges for 1” pipe, and four 5/8” B8M bolts are tightened to 90 ft-lbs at room temperatures. The torque is 20 ft-lbs higher than the requirement of ANSI B16.21-78, considering thermal expansion and yield strength at operation temperature of 650 ^{o}C.

Based on operational experience, the FRG assembly performs well in the test column section and the stuffing box seal at temperatures of around 450 ^{o}C to 500 ^{o}C. Most importantly, it is extended out of the loop, and the salt does not infiltrate the gasket. Post-test gaskets are shown in Figure III-15. However, all the FRG assemblies in the loop leak. Failed gaskets are shown in Figure III-15 top picture, with the facing material disappeared, and the pre-weld outer ring separated. One of the reasons for this failure is that the B8M grade bolts are not suitable for this high-temperature application, as their yield strength is only rated up to 425 ^{o}C. As the temperature increases, the compression pressure is not sufficient to provide a seal. Another reason is that the Thermiculite® 845 material is not compatible with the flow, as it dissolved into the salt, leading to leaks.

To address these issues, several suggestions can be made. Firstly, the flanges could use a male and female design. Secondly, testing the compatibility of Thermiculite® 845 with chloride molten salt could be performed. Thirdly, bolt materials such as Nimonic and Inconel alloys could be considered as potential improvements.

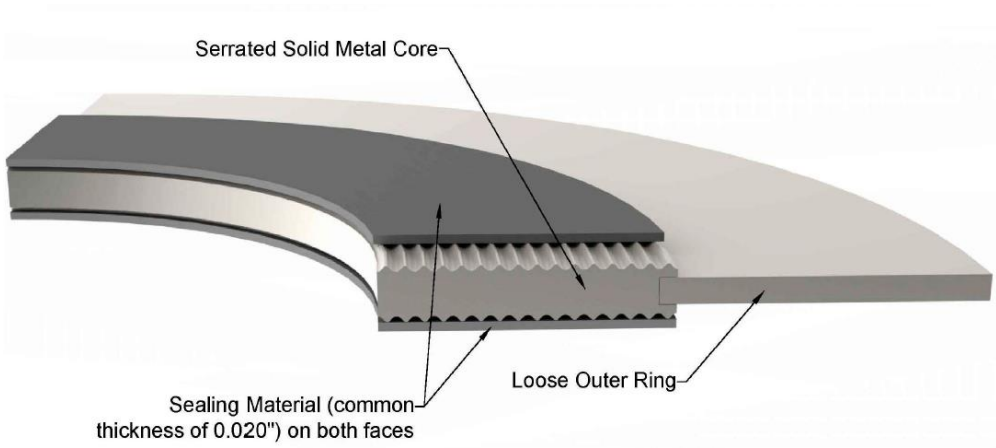

Figure III-14 Profile of Flexpro style ZA gasket, * from Flexitallic document.

Figure III-15 Pictures of post-test gaskets. Top: The gasket exposed to the salt. Bottom: the gasket does not contact salt.

Flange and metallic full-face gasket (FFG): In the VT FCMSL application, the storage tank lid seal utilizes the (FFG) assembly. The FFG assembly is applied because the lid of the storage tank is designed to be opened for pump maintenance purposes. The FFG assembly in this application is made from Thermiculite® 815 Tanged Sheet Material and is custom ordered from Flexitallic.

The FFG assembly has a size of 12.50” ID x 17.50” OD x .125” thick with (16) 1.125” Bolt Holes on a 15.50” Bolt Circle. The gasket is sandwiched between two flanges, whose surfaces are concentrically serrated to provide a tight seal. It is important to note that the FFG assembly does not come in contact with the salt, and we have not encountered any issues with the FFG assembly during operation.

Graphite seal: In the VT loop application, the graphite seal is applied in the stuffing box to provide a shaft seal. The assembly and function are discussed before. We have not encountered any issues with it.

Welding seal: In the VT loop application, all the connections on the loop body, except for the flanges and ball valves, are created using Tungsten Inert Gas (TIG) welding. There are two types of connections used, including pipe-to-pipe butt welding and pipe-to-fitting socket welding connections. Although the welding experts were careful during the welding process, we found that the welding quality cannot be guaranteed without radiograph technology. We conducted pressure tests using argon gas at room temperature and at 500 ^{o}C, as well as water tests at room temperature, and found that some joints still leaked when operate molten salt at 650 ^{o}C. Despite the occasional leak issues, we believe that TIG welding remains the most reliable method available for this application.

To address the welding quality issue, we recommend conducting very detailed radiograph analysis of the welding joints and developing monitoring techniques for the welding joints during

operation. This approach will ensure that the welding quality is consistently high and help prevent any potential leaks from occurring in the future.

III.3.8. Valves

Two types of valves are utilized in the VT FCMSL system: Gosco Valves' 2-way ball valves for salt control and ValvTechnology's 2-way heavy-duty ball valves for chemical gas control. The 2-way heavy-duty ball valves are installed on each gas line near the loop. Originally designed to handle CCl_4 gas for chlorination purification of the new salt, they were only used for thermal purification under argon flow due to toxicity concerns. Based on our operational experience, we recommend installing a check valve on each gas line, and each line should have a separate gas source to maintain pressure.

However, the Gosco Valves' ball valves are not compatible with the chloride salt, and during operation, all valves leaked. We were compelled to reduce the number of valves from eight to three. Interestingly, the valves exposed to flowing molten salt at the opening condition leaked much faster than those exposed to the flowing molten salt at the closing condition. In both cases, salt was observed on the valve outer surface, particularly at the valve bottom. Salt penetrated the seals and caused severe corrosion on the metal parts, which accelerated the leaks. We also investigated thermal shock as a possible reason for the leaks, but preheating did not prevent them.

Based on our experience with molten salt operation, the combination of gasket and flange seal has a high risk of failure. However, this does not mean that the existing design does not work if it is fully immersed into molten salt. Leakage is inevitable if the assembled parts keep exposing to the

flow of molten salt. The problem worsens due to the oxidizing of critical parts. Therefore, if the valve body could be covered or if all the connections are welded, the valve lifetime could be increased. Additionally, the valve stem should be as long as possible. The leaked salt itself would solidify at the further end of the valve body around the stem to provide a seal. After turning off the valve, the main flow is cut, and the temperature goes down. There is no way to reopen the valve without pre-heating. Thus, the valve designer should also consider the heating element design for the valve.

III.4. Forced convection molten salt loop tests

III.4.1. General experimental conditions

In this study, three flow induced corrosion tests were conducted on SS 316 and A709 alloys in the FCL. The specific procedures followed in these tests are discussed in detail in section IV.4. The tests were assigned the numbers FCL-50, FCL-80, and FCL-100 for reference purposes. he construction of the specimens' fixture, which was used to hold the samples during the tests, is described in section III.3.3. The flow direction was set from S3 to S1, with the flow moving from bottom to top, perpendicular to the ground. This arrangement was chosen to ensure that the flow filled the pipe and made full contact with the samples, thereby preventing the formation of any voids or gaps. It is important to note that due to the ongoing development of the FCL operation process and the lack of prior experience, the conditions of the specimens were not identical for all tests. The flow conditions of each test is listed in Table III-4. This section provides a detailed account of the experimental conditions for each of the three tests, highlighting any variations or

unique aspects observed. The post-test samples are cut vertically, Figure III-16, and the outer (facing to the flow) and inner (facing to the fixture) surfaces were examined by using SEM, respectively. In order to differentiate the post-test samples, the dimensions of the samples were specified as follows: The OD of the samples measures 0.5 inches, while the ID measures 0.27 inches. The length of the SS316 sample is 0.5 inches, while the A709 sample measures 0.8 inches in length.

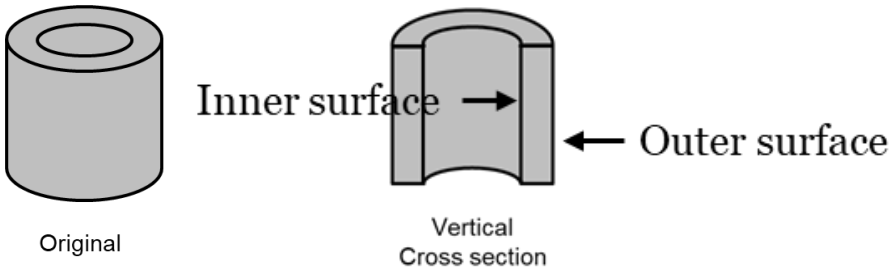

Figure III-16 FCL post-test samples preparation.

III.4.2. FCL-50: 50 hours forced convection loop test

The FCL-50 test marked the successful circulation of salt for the first time. Prior to the salt circulation, the samples were installed in the test column and remained there for a period of seven months. During this time, the samples underwent multiple cycles of heating and cooling, ranging from room temperature to 700°C.

For FCL-50, all the outer surfaces of the samples were polished using SiC paper with a gradient from 400 to 1000. After polishing, the samples were cleaned using an ultra-sonic machine with DI water. The temperature within the test column was maintained at 650°C. During the test, the pump

speed was set to a range of 1900 to 2000 rpm, and the flow velocity was measured using the FLEXIM ultrasonic flowmeter, which recorded a reading of 0.5 m/s.

The FCL-50 test was terminated when leakage was observed at the flanges. Following the termination of the test, the entire sample fixture was immersed in DI water to dissolve any residual salt that may have penetrated into the gaps between the samples. This process was accompanied by the use of an ultrasonic machine. Subsequently, the samples were dried and mounted into epoxy. It is worth mentioning that the FCL-50 samples were intentionally not cleaned thoroughly in order to observe the behavior of the salt on their surfaces. As a result, the weight change of the FCL-50 samples was not obtained for analysis.

III.4.3. FCL-80: 80 hours forced convection loop test

The FCL-80 test was conducted after addressing the leakage issue that occurred in FCL-50. To resolve this problem, the flanges were replaced with welding joints. Additionally, the chain coupling between the motor and shaft was upgraded to improve alignment, and the rubber pad between the ultrasound sensor and metal fixture was upgraded to a high-temperature paste suitable for the high-temperature application.

In FCL-80, the samples were installed as received from the machine shop and underwent only ultrasonic cleaning. The temperature within the test column was maintained at 650°C. During the test, the pump speed was set to 2400 rpm, and the flow velocity was measured using the FLEXIM ultrasonic flowmeter, which recorded a reading of 1.25 m/s. The FCL-80 test was terminated due to a chlorine electrolysis accident. After shutting down the loop, it was discovered that a pipe had

completely broken at one of the welding joints located at the original flange position. The details of these accidents can be found in section IV.3.4 of this dissertation. It is important to note that the salt used in FCL-80 was the same as in FCL-50, but with an additional bubbling purification process in the auxiliary tank for one hour, using high-purity argon. The post-test samples underwent the same process as in FCL-50 for further analysis and evaluation.

III.4.4. FCL-100: 100 hours forced convection loop test

The operation procedures for the tests became more refined and mature after the FCL-80 test. The FCL-100 test was conducted immediately after replacing the broken pipe. It is important to note that in FCL-100, the salt did not be refreshed or replaced, even if it became contaminated. The pre-test sample preparation for FCL-100 was identical to that of FCL-80. No severe leakage was observed during the test, but there was salt penetration at the valve. The termination of the test occurred due to chloride electrolysis, similar to what happened in FCL-80. The salt penetrated from the valves creeped along the heater glass fiber insulation, resulting in short circuits in the further operation heaters.

Following the test, the post-test specimens underwent thorough cleaning to obtain the weight change of the samples and perform surface characterization. The samples were then mounted into epoxy for cross-section characterization, allowing for a detailed analysis of their internal structures and properties.

Table III-4 Summary of flow conditions of FCL tests.

	Meter velocity m/s	Flow rate $m^3/s \times 10^{-4}$	Loop Re	Test column velocity m/s	Test column Re
FCL-50	0.5	1.68	5657	0.8	3690
FCL-80	1.25	4.21	14892	2	9225
FCL-100	1.25	4.21	14892	2	9225

Chapter IV RESULTS AND DISCUSSIONS

IV.1. Thermodynamic properties measurement

IV.1.1. Redox potential measurement method development

Gonzalez et al.[22] found that impurities like oxygen and moisture can lead to the formation of unexpected hydroxides during heating, resulting in a complex reaction mechanism. Prior to measurements, cyclic voltammetry (CV) was performed on the blank salt. The results, depicted in Figure IV-1 showed no redox peaks except for alkali metal, indicating the absence of impurities in the blank salt.

For CP tests, during each experiment, a positive and constant current was applied in step function form. Then the potential of the working electrode was monitored as a function of time. The application of a positive current produced chlorine on the working electrode. Since this molten salt system is full of molten chlorine ions, the effect of mass transfer (both diffusion and migration) at low current density is regarded as negligible. Therefore, any changes in overpotential in the cell are ascribable to the kinetics of the reaction. More to this point, this overpotential at the electrode is proportional to the small current density applied on the working electrode based on the Butler-Volmer equation[159]. This means that the overpotential should be small enough. Meanwhile, if the applied current density is too small, insufficient chlorine gas on the working electrode surface will

be produced, which will lead to an unstable potential plateau. Due to the low solubility of chlorine gas in molten LiCl-KCl salt, the activity of Cl_2 gas could be considered as one at the electrode[160]. In this study, the applied current density was selected from 0.012 A/cm^2 to 0.030 A/cm^2 with sufficient chlorine gas generated on the working electrode.

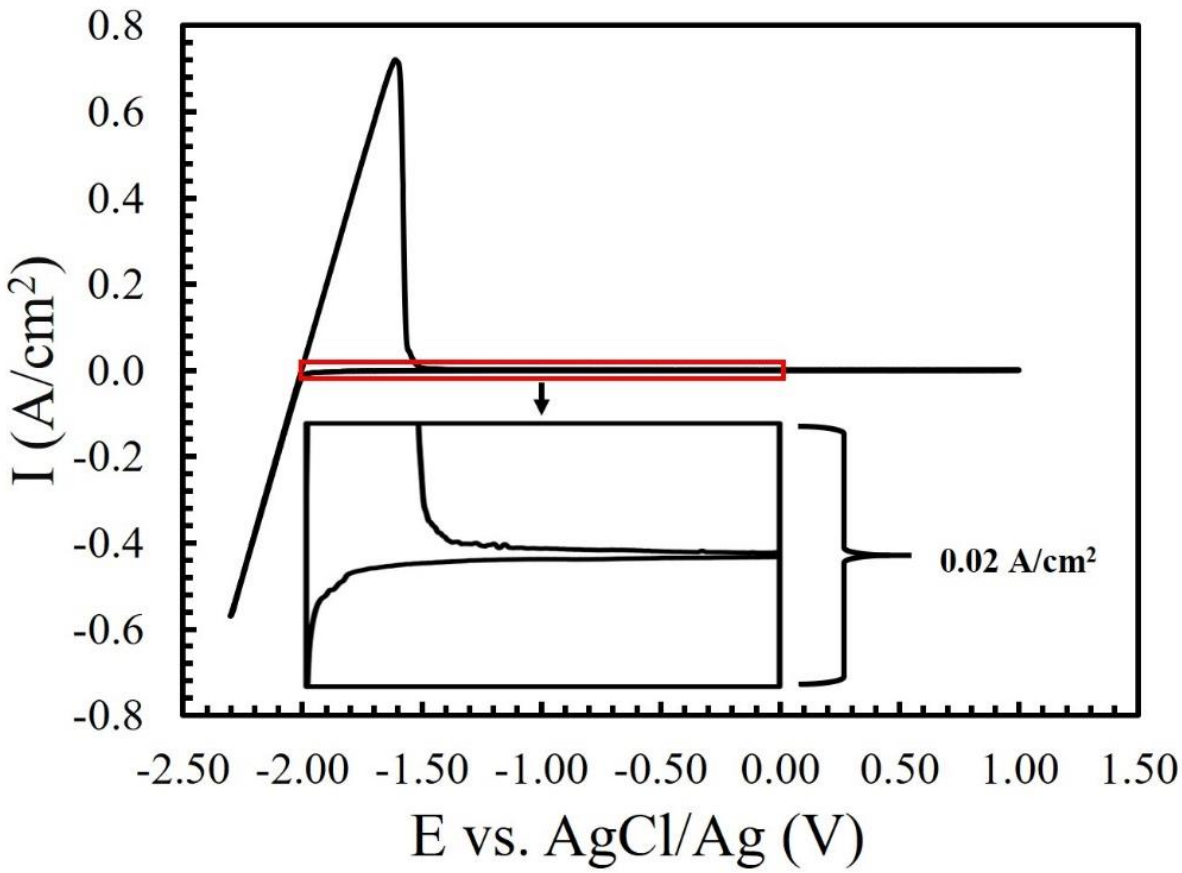

Figure IV-1 Cyclic voltammetry curve for the blank molten LiCl-KCl salt at 723 K. WE: Tungsten, CE: Graphite, RE: 10 wt% AgCl in LiCl-KCl and Ag wire contained in Pyrex tube. Scan rate: 1mV/s.

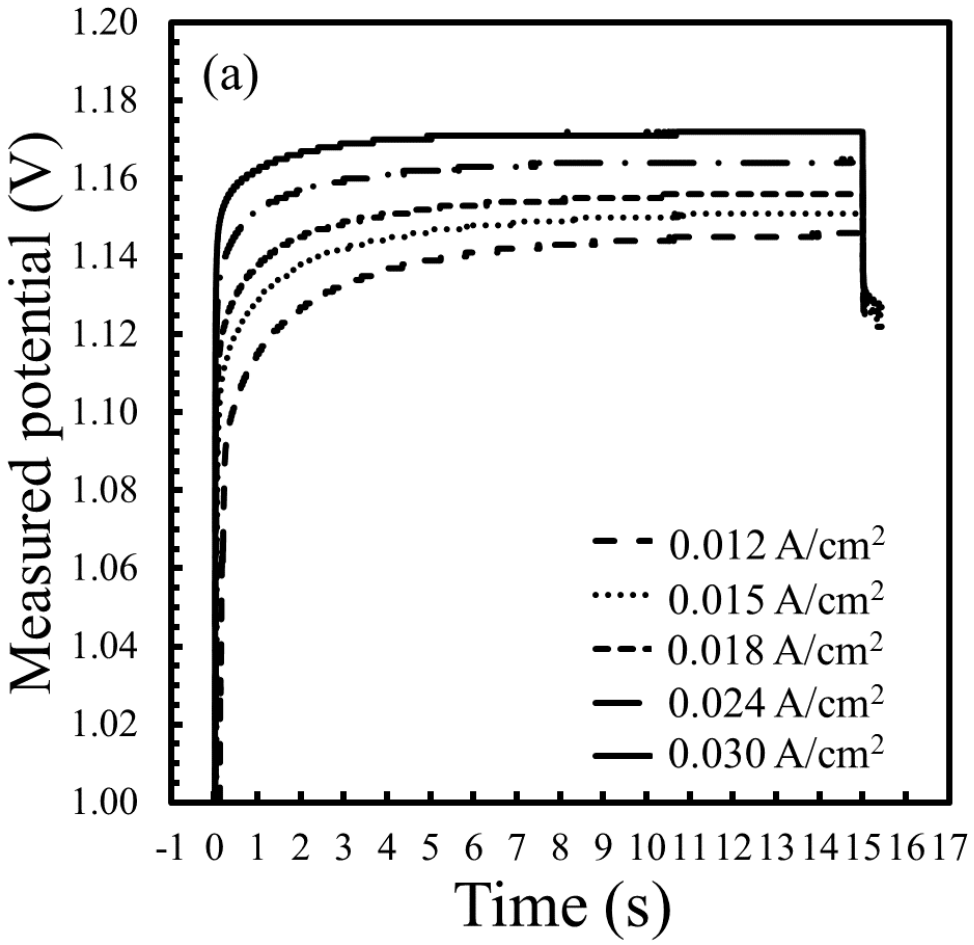
(a)
Measured potential (V)
1.20
1.18
1.16
1.14
1.12
1.10
1.08
1.06
1.04
1.02
1.00
-1 0 1 2 3 4 5 6 7 8 9 10 11 12 13 14 15 16 17
Time (s)
0.012 A/cm2
0.015 A/cm2
0.018 A/cm2
0.024 A/cm2
0.030 A/cm2

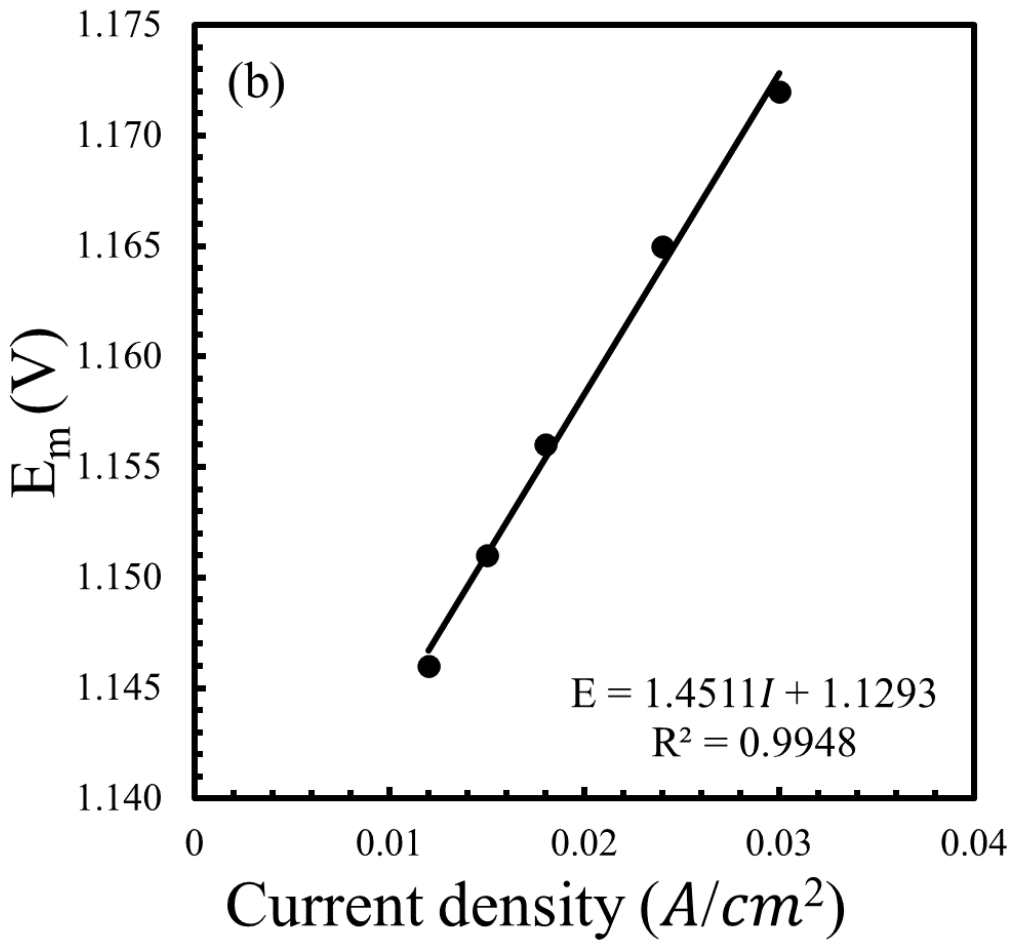

Figure IV-2 (a) Chronopotentiometry curves at different current densities; (b) Linear correlation between applied currents and measured stable potentials with CP method. Working Temp: 748K. Molten salt system: LiCl-KCl-AgCl (X=0.0145). WE is 3-mm graphite rod, RE and CE are 1-mm silver wires.

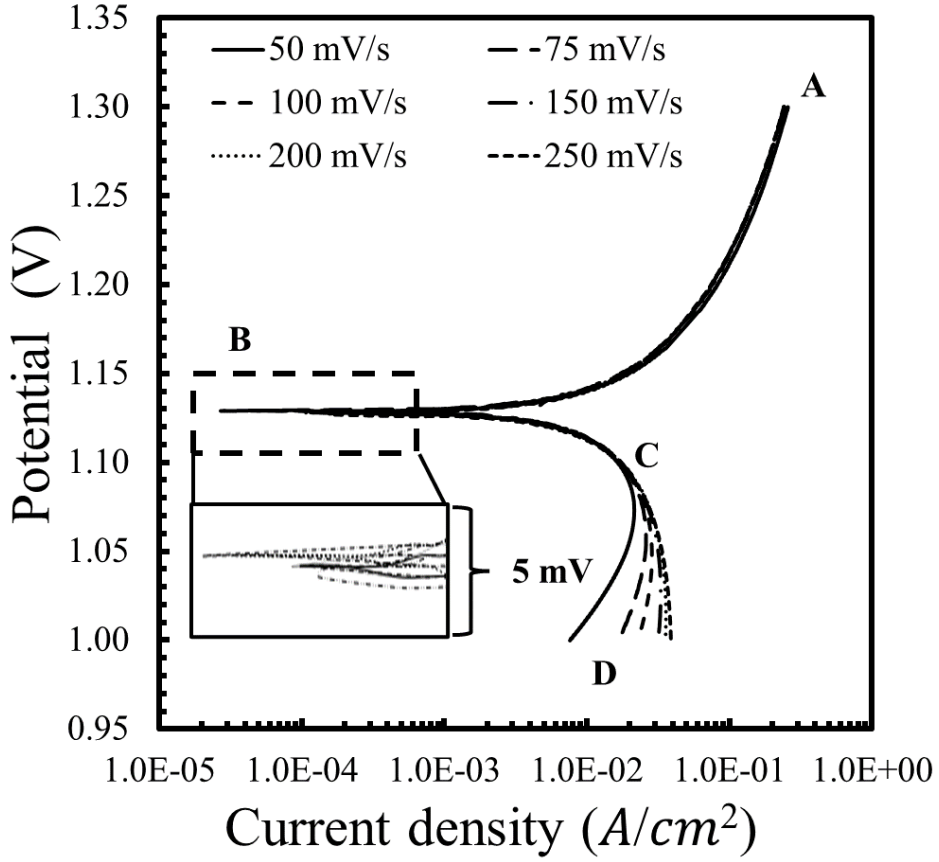

Figure IV-3 Potentiodynamic curves measured at various scan rates and 748 K in LiCl-KCl-AgCl(X=0.0145) molten melt. WE is 3-mm graphite rod, RE and CE are 1-mm silver wires.

The potential-time curves obtained by chronopotentiometry technique at 748 K in the LiCl-KCl-AgCl (mole fraction=0.0145) molten salt are shown in Figure IV-2 (a). In the beginning, the potentials were sharply shifted to positive values due to the decrease in the non-faradaic charging current (or the increase in the faradaic current where the Cl^- was oxidized to Cl_2). After 8 to 10 seconds, stable potential was achieved. Since the mass transfer effect in this system was negligible, showing that the system reached equilibrium potentials. Thus, the measured potential (E_{m}) can be expressed by Equation IV-1, which has all components at unit activity:

$$E_{\mathrm{m}} = Ir + Ir_{\mathrm{ct}} + \left[E^0_{\mathrm{Cl_2/Cl^-}} + \frac{RT}{nF}\ln\left(\frac{a_{\mathrm{Cl_2},s}}{a_{\mathrm{Cl^-},s}}\right)\right]_{\mathrm{AgCl/Ag}} \qquad \textbf{Equation IV-1}$$

Where I is the applied current, r is the uncompensated solution resistance, r_{ct} is the charge transfer resistance, $E^0_{\mathrm{Cl_2/Cl^-}}$ is the standard potential of Cl_2/Cl^- couple verse AgCl/Ag, R is the gas constant 8.314 $\mathrm{J{\cdot}K^{-1}{\cdot}mol^{-1}}$, T is the temperature in Kelvin, n is the charge transfer number, F is the Faraday constant 96485 $\mathrm{s{\cdot}A{\cdot}mol^{-1}}$, $a_{\mathrm{Cl_2},s}$ and $a_{\mathrm{Cl^-},s}$ are the activity of Cl_2 and Cl^- at the working electrode surface, respectively. The third term on the right-hand side could be eliminated since $a_{\mathrm{Cl_2},s}$ and $a_{\mathrm{Cl^-},s}$ are at unit activity. Moreover, the standard potential of Cl_2/Cl^- verse AgCl/Ag equals to the negative value of the redox potential of AgCl/Ag verse standard chlorine reference. Hence, Equation IV-1 can be written as

$$E_{\mathrm{m}} = Ir + Ir_{\mathrm{ct}} - \left[E'_{\mathrm{AgCl/Ag}}\right]_{\mathrm{Cl_2/Cl^-}} \qquad \textbf{Equation IV-2}$$

Where $E'_{\mathrm{AgCl/Ag}}$ is the redox potential of AgCl/Ag verse standard chlorine reference redox couple, which is defined as:

$$E'_{\mathrm{AgCl/Ag}} = E^0_{\mathrm{AgCl/Ag}} + \frac{RT}{F}\ln\left(\gamma_{\mathrm{AgCl}}\right) + \frac{RT}{F}\ln\left(X_{\mathrm{AgCl}}\right) \qquad \textbf{Equation IV-3}$$

Where $E^0_{\mathrm{AgCl/Ag}}$ is the standard potential of AgCl/Ag couple, γ_{AgCl} is the activity coefficient of AgCl, X_{AgCl} is the concentration of AgCl in mole fraction. Thus, the formal potential ($E^{0\prime}_{\mathrm{AgCl/Ag}}$) is:

$$E^{0\prime}_{\mathrm{AgCl/Ag}} = E^0_{\mathrm{AgCl/Ag}} + \frac{RT}{F}\ln\left(\gamma_{\mathrm{AgCl}}\right) \qquad \textbf{Equation IV-4}$$

The equilibrium potentials at different current densities and the corresponding linear correlation in the LiCl-KCl-AgCl (X=0.0145) eutectic salt are shown in Figure IV-2 (b). The extrapolated line intersects the Y-axis at a value of 1.1293 where the current equal to zero and then the effects of solution resistance and charge transfer resistance can be eliminated. Thus, the negative value (-1.1293 V) of this intercept is the redox potential of AgCl/Ag with respect to Cl_2/Cl^- reference redox.

Another method is the potentiodynamic scan of which the potential starts from a potential positive enough to generate sufficient chlorine gas first, moves in a negative direction with a certain scan rate and usually stops at a value negative than the equilibrium potential of the redox couple to be studied. The typical polarization curves in LiCl-KCl-AgCl(X=0.0145) eutectic salt at 748 K with different scan rates are illustrated in Figure IV-3. A typical scan started from point A and progressed in the negative direction until termination at point D. In region A to B for the Cl_2/Cl^- redox couple, the domain reaction is the anodic reaction: $\mathrm{Cl^- - e \rightarrow 0.5Cl_2}$ at the electrode while from B to D the main reaction is the cathodic reaction: $\mathrm{0.5Cl_2 + e \rightarrow Cl^-}$. The chlorine gas in cathodic reaction actually comes from the gas evolved in the anodic area. Since the generated chlorine is limited, the current drastically reduced to zero after point C. Therefore, this method requires a proper scan rate not too fast so that ensures a sufficient amount of chlorine and not to slow so that keeps the generated chlorine gas remain at the electrode. Six different scan rates from 50 mV/s to 250 mV were selected in our experiments. The equilibrium potential was located at point B, where the anodic and cathodic reaction on the electrode surface reaches an equilibrium and the current equals to zero (this point is very hard to get experimentally). The potential ranged from 1.3 V to 1V, which was determined by the equilibrium potential and current density limitation of the potentiostat instrumentation (maximum $1A/cm^2$). The measured equilibrium potentials were slightly shifting, which should be related to the small charging currents caused by scan rates. In this scan rate interval, the changes in equilibrium potential are less than 3mV, which shows strong stability. Therefore, the average values were used in the current study. The redox potential of AgCl/Ag with respect to Cl_2/Cl^- reference redox is equal to the negative value (-1.1283 V) of the

measured potential at point B, which is almost the same as the value (-1.1293 V) from CP method. These two methods show perfect consistency with each other. It should be noted that for PD method under different conditions (either temperatures or concentrations), the stable equilibrium potentials were commonly achieved with a scan rate higher than 100 mV/s or 150 mV/s. The vibration in potential with various scan rates for all results was within 3 mV.

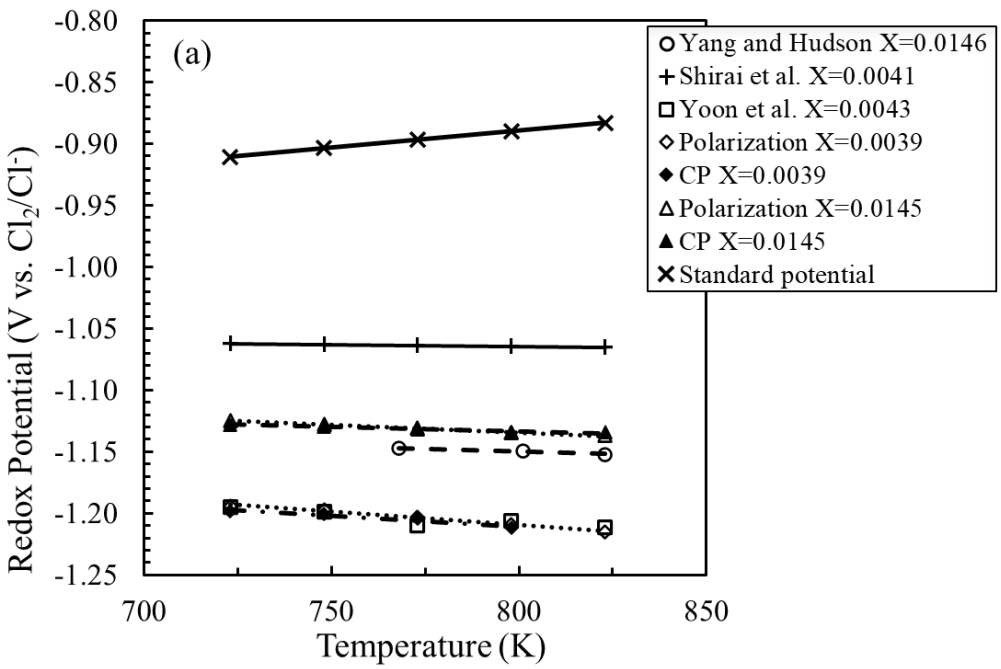

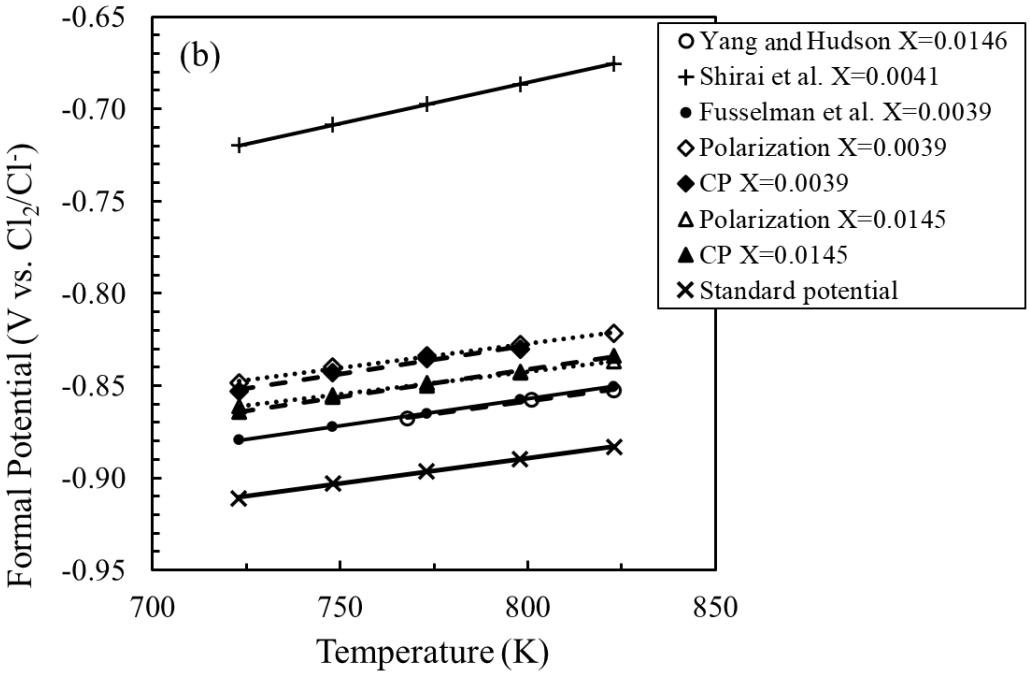

Figure IV-4 (a) Temperature dependence of equilibrium potentials with different concentration of AgCl; (b) Temperature dependence of formal potentials measured by chronopotentiometry and potentiodynamic scan technique for AgCl/Ag in LiCl-KCl molten melt. WE is 3-mm graphite rod, RE and CE are 1-mm silver wires. (Yang and Hudson[100] , Shirai et al.[108]. , Yoon et al.[109], Fusselman et al.[101])

Temperature dependence of the equilibrium potentials of AgCl/Ag measured with CP and PD scan techniques are shown in

Figure IV-4 (a). As can be seen, these two methods give almost the same results under the same condition. The differences in the measured redox potential of Ag/AgCl between these two methods are less than 3 mV. Moreover, in order to validate these two methods, the concentration (X=0.0145) similar to Yang and Hudson[100] was carried out. The redox potentials measured using current techniques are ~15mV higher than Yang and Hudson's data[100] in the whole temperature interval. The uncertainty of the system led to a deviation of the results. This 2% difference is considered to be acceptable. In addition, the results obtained from mole fraction of X=0.0039 were in well consistent with Yoon et al.[109] and much lower than the redox potential of AgCl/Ag at a mole fraction of 0.0041 reported by Shirai[108]. However, the results from Shirai was even much higher than that of AgCl/Ag at the mole reaction of 0.00146 by Yang and Hudson[100], which implies that these abnormal results may come from the experimental disturbances such as potential drop caused by Pyrex tube.

Figure IV-4 (b) shows the temperature dependence of the formal potentials of AgCl/Ag redox couple. The formal potentials of AgCl are slightly higher than that of Yang and Hudson's[100] at the concentration of X=0.0145, which is regarded as the experimental uncertainty as discussed earlier. The formal potential $E_{\mathrm{AgCl}}^{0'}$ at X=0.0145 (3.75 wt%) can be expressed as follow:

$$E^{0'}_{\mathrm{AgCl/Ag}} = -1.037 + 0.000244T \qquad \textbf{Equation IV-5}$$

And the formal potential of concentration of X=0.0039 (1 wt%) is represented as

$$E^{0'}_{\mathrm{AgCl/Ag}} = -1.038 + 0.000264T \qquad \textbf{Equation IV-6}$$

The formal potential of AgCl/Ag in the mole fraction of AgCl at 0.0039 by Fusselman et al.[101], widely accepted by other researchers, was actually derived with the activity coefficients obtained by Yang and Hudson[100] at the concentration of X=0.0146. Fusselman et al.[101] made a simple assumption that the activity coefficient was constant at the diluted condition and thus the formal potential of AgCl/Ag is independent of the molt fraction. As can be seen from

Figure IV-4 (b), the formal potential by Fusselman et al.[101] at X=0.0039 is equal to that from Yang and Hudson[100] at X=0.0146. However, the activity coefficients at different mole fractions are quite different based on the present study (Table IV-1). The formal potentials at the concentration of X=0.0041 by Shirai[108]show a large deviation from all the results as mentioned earlier. Commonly, the dissolved AgCl behaves like a regular solution, with positive AgCl activity coefficient deviation from Raoult's law[100].

Figure IV-4 (b) shows that all the experimental data at those concentrations are more positive than the standard formation potential $E^{0}_{\mathrm{AgCl/Ag}}$ $(\mathrm{vs.\,Cl_2/Cl^-})$, which can be calculated based on the

thermodynamic expression ($\Delta G^0 = -nFE^0$) of the reaction: AgCl = Ag + 0.5Cl_2. All the standard Gibbs energies of this reaction at various temperatures could be obtained in previous studies[109,161].

Table IV-1 Calculated activity coefficient of AgCl by using the supercooled free energy of formation.

Mole fraction of AgCl	723K	748K	773K	798K	823K
0.0039	2.638	2.618	2.516	2.406	2.318
0.0145	2.148	2.065	2.010	1.934	1.905

Table IV-1 shows the activity coefficients of AgCl in the range from 1.905 to 2.638 under various conditions calculated by Equation IV-3, and the results are in consistent with the data set by Yang and Hudson[100]. Even though the measured potentials of the AgCl/Ag couple from Yoon et al.[109] are almost the same as that of the present study, the activity coefficients of AgCl in AgCl-LiCl-KCl system given in their study ranged from 0.0012 to 1.19. Furthermore, the thermodynamic form could be obtained by rearrangement of Equation IV-4 with Nernst equation ($\Delta G^0 = -nFE^0$):

$$\Delta G^{0'}_{\mathrm{AgCl/Ag}} = \Delta G^0_{\mathrm{AgCl/Ag}} + RT\ln(\gamma) \qquad \textbf{Equation IV-7}$$

Where $\Delta G^{0'}_{AgCl/Ag}$ is the formal Gibbs free energy, $\Delta G^0_{\mathrm{AgCl/Ag}}$ is the standard Gibbs free energy of the reaction. It should be noted that E^0 only represents the reaction potential of $\mathrm{AgCl} = \mathrm{Ag} + 0.5\mathrm{Cl_2}$, not $E^0_{AgCl/Ag}$ when rearranging this transformation. The second term on the right-hand side

of is the excess Gibbs free energy ΔG^{ex}, which only depends on temperature and shows a linear correlation with each other.

$$\Delta G^{\mathrm{ex}} = \mathrm{A} + \mathrm{B}T \qquad \textbf{Equation IV-8}$$

Combining Equation IV-7 and Equation IV-8, the correlation between temperature and activity coefficient is shown as

$$\ln(\gamma) = \frac{\mathrm{A}}{\mathrm{R}}\frac{1}{T} + \frac{\mathrm{B}}{R} \qquad \textbf{Equation IV-9}$$

The values of the constants A and B in Equation IV-8 and Equation IV-9 equal to 6326.12 J and -0.45 J/K in the mole fraction of X=0.0039, and equal to 6322.80 J and -2.28 J/K in the mole fraction of X = 0.0145, respectively. It seems that the more dilute of the AgCl in LiCl-KCl solvent is, the higher activity coefficient of AgCl is. At all concentrations, the activity coefficient of AgCl becomes smaller with the increasing working temperature. Thus, with these two methods, one can easily obtain accurate, reliable performance on the measurement of the formal potentials as well as activities of redox couples at various conditions in high-temperature molten chlorides, which is of great importance to molten salt electrochemistry.

IV.1.2. Redox potential measurement in Magnak salt

Figure IV-5 shows a CV curve obtained at 873 K using a chromium (II)/chromium redox couple as the reference electrode in Magnak chloride after inserting all the electrodes. The left peak

corresponds to the Mg (II)/Mg reaction and the right peak corresponds to the Cl_2/Cl^- reaction. No impurity peaks were detected in this scanning window, indicating that the purification process was successful. As current redox potential measurement methods do not require the current density, the y-axis is labeled as current instead of current density. Before the CP test at each temperature, a CV test was performed to check for any leaks in the reference electrode container. ICP-MS results confirmed that the types and concentrations of components in the bulk and reference electrolytes remained unchanged before and after the test. In this work, four concentrations of $CrCl_2$ were tested with mole fractions X=0.0044, 0.0102, 0.0190, and 0.0293. Three concentrations of NiCl2 with X=0.0061, X=0.0184, and X=0.0296 were gradually added into the bulk salt. To minimize experimental error, two individual Magnak chloride salts were prepared with final $MgCl_2$ concentrations of X=0.3993 and X=0.4587.

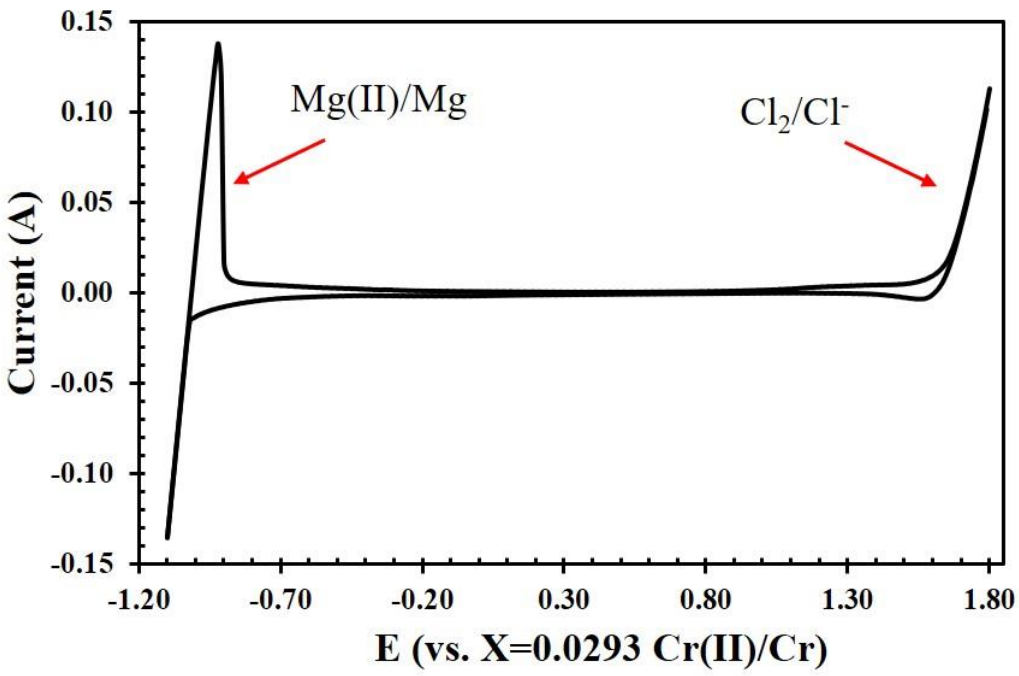

Figure IV-5 Cyclic voltammetry curve of clean Magnak chloride mixture at 873 K, the scan rate is 150mV/s. WE: C, CE: C.

Figure IV-6 demonstrates an example of the typical CP data curve and analytical data. A positive current was applied during the CP test and the potential between WE and RE with time was monitored. After 5s current pulse, the current was reduced to zero. Because of the applied positive current, the WE worked as an anode, where the oxidation reaction occurred during the current pulse. The only species that can release electron in the bulk salt was chloride ions, which means that the reaction on the WE surface is the formation of chlorine. Meanwhile, during the current pulse, the measured potential was the total of chlorine potential on WE, solution resistance (r),

and some potential change across the WE and solution interface ($\delta(I)$), as shown in Figure IV-6.(a). Thus, the measured potential E_m was defined as

$$E_m = \left(E^0_{Cl_2} + \frac{RT}{nF}\ln\left(\frac{a_{Cl_2}}{a_{Cl^-}}\right)\right)_{Cr^{2+}(X=x)/Cr} + Ir + \delta(I) \qquad \textbf{Equation IV-10}$$

, where $E^0_{Cl_2}$ is the standard potential of Cl_2, R=3.814 J·K^{-1}mol^{-1} is the gas constant, T is the temperature in Kelvin, n=1 is the electron transfer number of chlorine formation, F= 96485 s·A·mol^{-1} is the Faraday constant, a_{Cl_2} and a_{Cl^-} are the activity of Cl_2 on the WE surface and Cl^- in the bulk solution. The sum of the last two terms on the right-hand side is the so-called overpotential η. As reported by Bard and Faulkner [162], when overpotential is small enough, the Butler–Volmer equation can be simplified as $i = i_0\frac{nF}{RT}\eta$, where I is proportional to η. Theoretically, the better results can be achieved by reducing the applied current. However, when the current is too small, the potential oscillates violently. The reason is that chlorine gas not uniformly generates on the WE. Experimentally, when the overpotential is ranging from 40 mV to 100 mV, the linear relationship between applied current and overpotential is ideal. The data points in Figure IV-6.(b) are the average of the last 3 seconds of the measured potential. Linear correlation is then applied to the data and extrapolated to $I = 0$, where the effects of the last two terms have been eliminated.

$$E_{m(I=0)} = \left(E^0_{Cl_2} + \frac{RT}{nF}\ln\left(\frac{a_{Cl_2}}{a_{Cl^-}}\right)\right)_{Cr^{2+}(X=x)/Cr} \qquad \textbf{Equation IV-11}$$

Since the chloride salt is full of Cl^- and the generated chlorine gas is pure, the activity of Cl^- and Cl_2 are considered as a unity. Thus, the value of $E_{m(I=0)}$ is the standard chlorine formation potential relates to the potential of Cr^{2+}/Cr reference. In other words, the negative value of $E_{m(I=0)}$ is the Cr^{2+}/Cr redox potential related to the potential of standard chlorine.

$$-E_{m(I=0)} = (E_{red})_{Cl_2/Cl^-}$$ **Equation IV-12**

$$E_{red} = E^0_{Cr^{2+}/Cr} + \frac{RT}{nF}\ln(\frac{a_{Cr^{2+}}}{a_{Cr}})$$ **Equation IV-13**

In Equation IV-13, E_{red} is the redox potential of $\mathrm{Cr(II)/Cr}$ couple in Magnak chloride, $E^0_{Cr^{2+}/Cr}$ is the supercooled standard formation potential of $CrCl_2$. The value is calculated based on the data reported by Barin [163] using the method reported in Bagri's dissertation [164]. n =2 is the transferred electron number. $a_{Cr^{2+}}$ is the activity of $CrCl_2$ in Magnak chloride, and a_{Cr} is the activity of the metal rod equal to one. Equation IV-13 can be rewritten as

$$E_{red} = E^f_{Cr^{2+}/Cr} + \frac{RT}{nF}\ln(X)$$ **Equation IV-14**

, where $E^f_{Cr^{2+}/Cr}$ is the formal potential of $\mathrm{Cr(II)/Cr}$ in Magnak chloride. It is expressed as

$$E^f_{Cr^{2+}/Cr} = E^0_{Cr^{2+}/Cr} + \frac{RT}{nF}\ln(\gamma)$$ **Equation IV-15**

The X and γ in Equation IV-14 and Equation IV-15 refer to the concentration and activity coefficient of $CrCl_2$ in the Magnak chloride.

Redox potential and formal potential of four different concentrations of $CrCl_2$ at different temperatures are presented in Figure IV-7. The redox potential increases with increasing temperature and $CrCl_2$ concentration. Since at a high temperature the random thermal motions of the ions overcome some of the electrostatic repulsions between like ions to make the solution more ideal, the activity at the same concentration increases. An increase in concentration at the same temperature also increases activity. Figure IV-7.(b) indicates that the formal potential is independent of the concentration; in other words, at these four tested concentrations the activity coefficient is the same at the same temperature. The red line is the fitted linear correlation of the formal potential, given in equation form as

$$E^{f}_{Cr^{2+}/Cr} = -2.127 + 7.041 \times 10^{-4}T \qquad \textbf{Equation IV-16}$$

, where T is the temperature in Kelvin. As shown in Figure IV-7.(b), all the data are within an error of $\pm 0.7\%$.

The mark (1) and (2) in Figure IV-8 refer to two independent experiments with the same $NiCl_2$ concentration X=0.0061 but different test temperature range. In the temperature range of 873 K to 973 K, the potential data shows great agreement with each other. The reproducible results confirmed the reliability of the CP method in the study of redox potential. The expression of the fitting correlation in Figure IV-8.(b) is expressed in Equation IV-17.

$$E^{f}_{Ni^{2+}/Ni} = -1.385 + 6.020 \times 10^{-4}T \qquad \textbf{Equation IV-17}$$

The error bar, in this case, is $\pm 0.1\%$.

The final concentration of the Magnak determined by ICP-MS test, in mole fraction is $MgCl_2$ X=0.4587, KCl X=0.2432, NaCl X=0.2981. Another $MgCl_2$ concentration X=0.3993 was measured due to the preparation error, potential results are shown in Figure IV-9 (triangle). These two results are similar. This is due to the redox potential difference caused by the concentration difference being less than the experimental uncertainty. The formal potential of Mg(II)/Mg (X=0.4587) can be used for the future study, the equation is given as bellow

$$E^{f}_{Mg^{2+}/Mg} = -3.289 + 7.501 \times 10^{-4}T \qquad \textbf{Equation IV-18}$$

Once the formal potential of Mg, Cr, and Ni were obtained, activity coefficients of $MgCl_2$, $CrCl_2$, and $NiCl_2$ were calculated by utilizing supercooled standard potential and Equation IV-16 and Equation IV-18. Results are shown in Table IV-2. The $MgCl_2$ activity coefficient is about 3 times larger than the results reported by Neil et al. [165], in a similar salt composition but slightly different composition ratio. They used a MgBi binary alloy as the electrode and induced the activity of Mg in MgBi(l) alloy during the analysis. The data they used was measured from a different molten salt system, which could be the root of the difference in the activity coefficient. Thus, the database they used increased their experimental errors. For the Mg test, the W rod was pulled out 10 mm (the total immerge length is about 16 mm), assuming that the bulk salt flowed into the alumina tube and liquid Mg was floating on it. The results were the same as W rod touching the bottom of

alumina tube, which means that the potential on RE is the redox potential of Mg(II)/Mg couple and that no salt flows into RE as mentioned before. After the test there no visible solid sale in the tube as well.

The Mg(II)/Mg redox potential and the formal potentials of Ni(II)/Ni and Cr(II)/Cr are plotted in Figure IV-9. Since $MgCl_2$ is one of the components of the salt mixture, it has only one concentration and redox potential; and at the tested concentration, the form potentials of $NiCl_2$ and $CrCl_2$ are independent of their concentrations. Therefore, formal potential is best used to represent their potential. For a pure metal (Ni or Cr) immersed in a pure Magnak chloride mixture, corrosion will happen. From Equation IV-14 the value of redox potential of Ni(II)/Ni and Cr(II)/Cr are very negative at the beginning because there are no metal cations in the solution. The metal will be corroded until the concentration of dissolved Ni(II) or Cr(II) reaches the equilibrium level at which $E_{red}^{Ni(II)\,/Ni\ or\ Cr(II)/Cr} = E_{red}^{Mg(II)\,/Mg}$. Employing Equation IV-14 and Equation IV-15, the limited dissolution concentration (X_L) was calculated and shown in Table IV-3. As X_L of Ni(II) and Cr(II) are both very small as shown in the table, therefore, it is reasonable to conclude that pure Magnak chloride is not considered corrosive to these two metals. The magnitude order of $X_L(NiCl_2)$ is much smaller than $X_L(CrCl_2)$, which indicates that Ni has higher corrosion resistance compared to Cr.

Table IV-2 Activity coefficient and supercooled standard potential.

	Temperature K	Activity coefficient γ	Supercooled standard potential V
$CrCl_2$	873	0.1622	-1.4439
X=0.0044	923	0.2577	-1.4232
X=0.0102	973	0.3906	-1.4025
X=0.0190	1023	0.5696	-1.3819
X=0.0293	1073	0.8003	-1.3612
$MgCl_2$	923	0.2499	-2.5453
X= 0.4587	948	0.3418	-2.5310
	973	0.3803	-2.5168
	998	0.3983	-2.5024
	1023	0.4671	-2.4881
	1048	0.5377	-2.4738
	1073	0.5640	-2.4595
$NiCl_2$	773	0.0281	-0.8007
X=0.0061	823	0.0469	-0.7810
X=0.0184	873	0.0737	-0.7614
X=0.0296	923	0.1103	-0.7417
	973	0.1585	-0.7220
	1023	0.2197	-0.7024
	1073	0.2954	-0.6827

Table IV-3 Limited dissolution concentration of $NiCl_2$ and $CrCl_2$ in Magnak chloride salt.

Temperature K	$X_L(NiCl_2)$	$X_L(CrCl_2)$
873	1.4725×10^{-21}	5.1421×10^{-14}
923	2.2862×10^{-20}	2.7403×10^{-13}
973	2.6776×10^{-19}	1.2297×10^{-12}
1023	2.4656×10^{-18}	4.7647×10^{-12}
1073	1.8461×10^{-17}	1.6273×10^{-11}

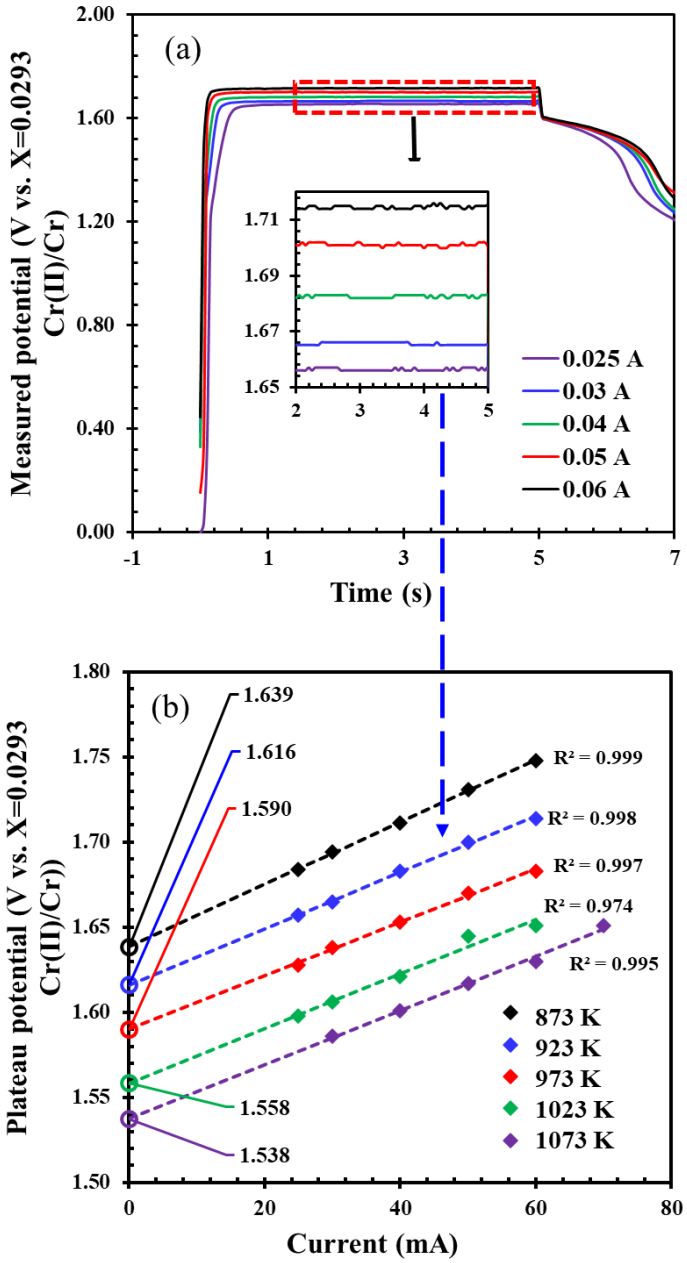

Figure IV-6 CP curve with different currents at 923 K and the analytical data for different temperatures in X=0.0293 $CrCl_2$ in Magnak chloride.

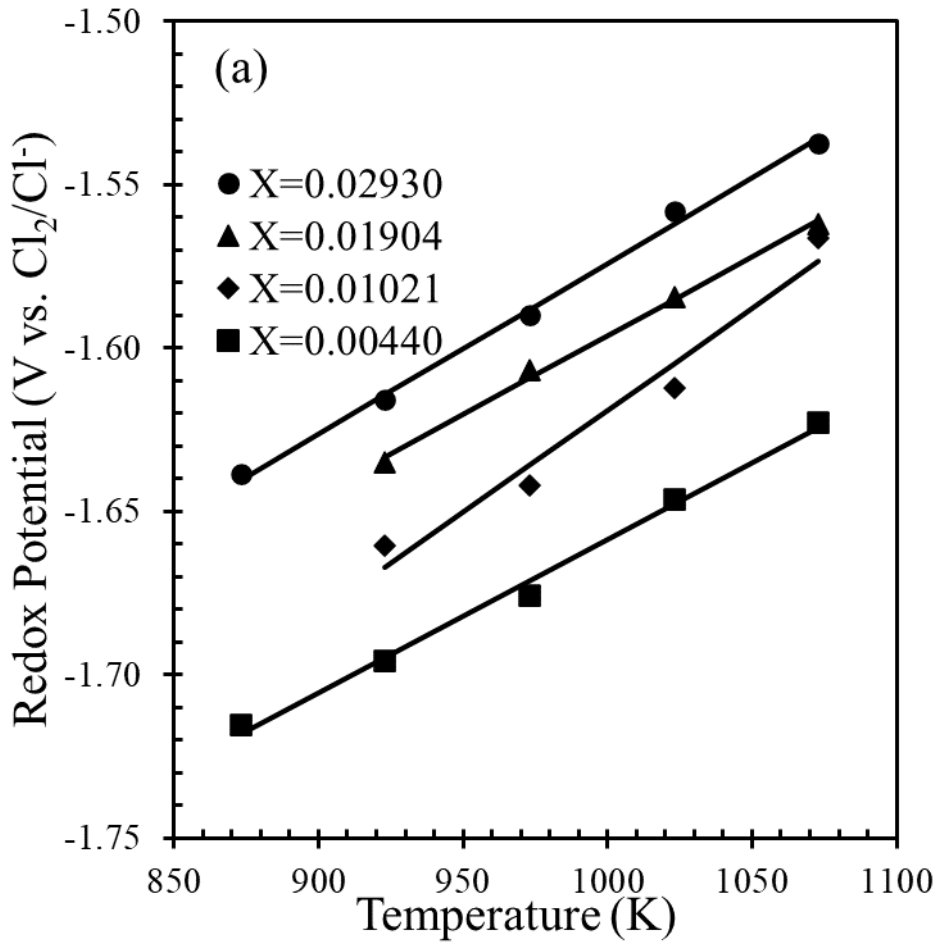
(a)
X=0.02930
X=0.01904
X=0.01021
X=0.00440
Redox Potential (V vs. Cl2/Cl-)
Temperature (K)
-1.50
-1.55
-1.60
-1.65
-1.70
-1.75
850
900
950
1000
1050
1100

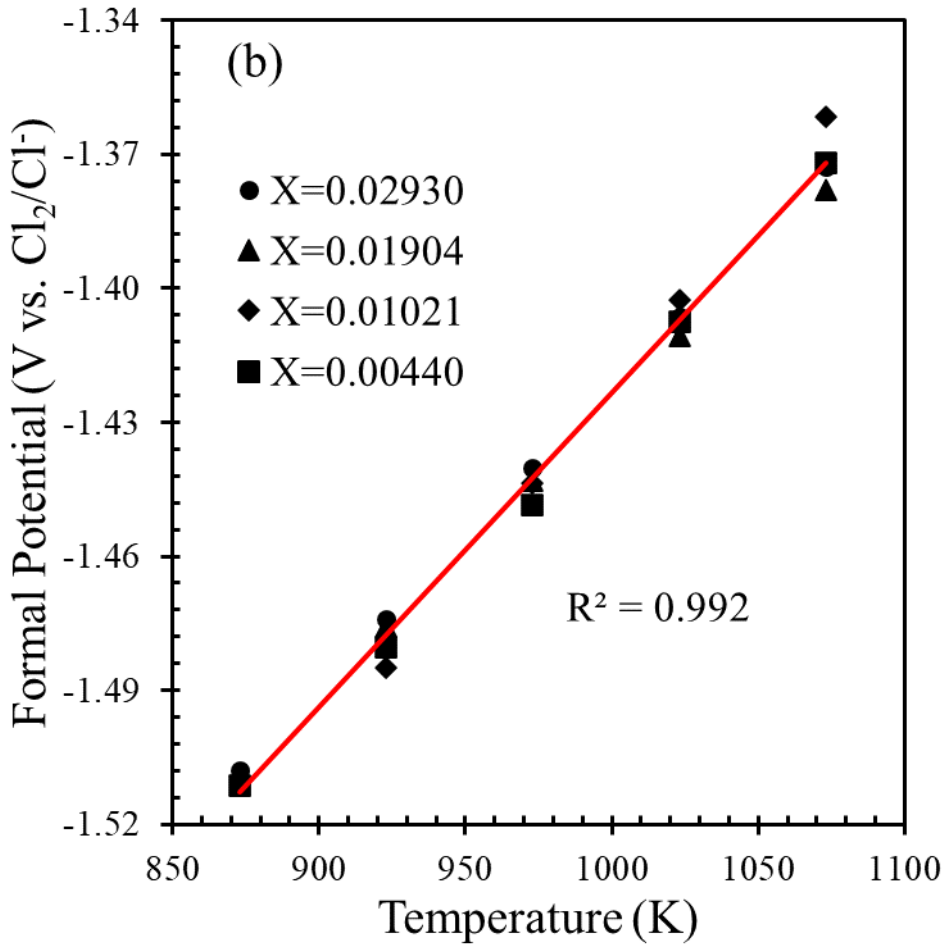

Figure IV-7 Redox potential and formal potential of four $CrCl_2$ concentrations in Magnak chloride, the red line in (b) is the fitted linear relation.

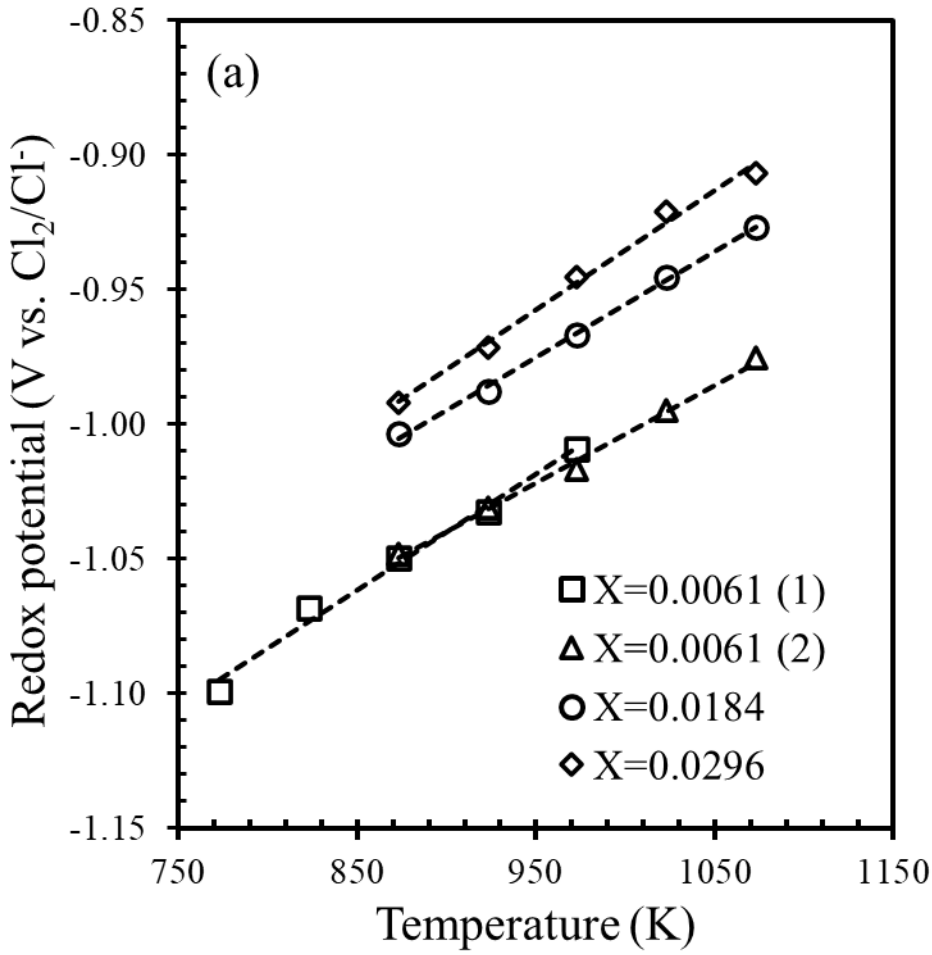
(a)
Redox potential (V vs. Cl_2/Cl^-)
-0.85
-0.90
-0.95
-1.00
-1.05
-1.10
-1.15
750
850
950
1050
1150
Temperature (K)
X=0.0061 (1)
X=0.0061 (2)
X=0.0184
X=0.0296

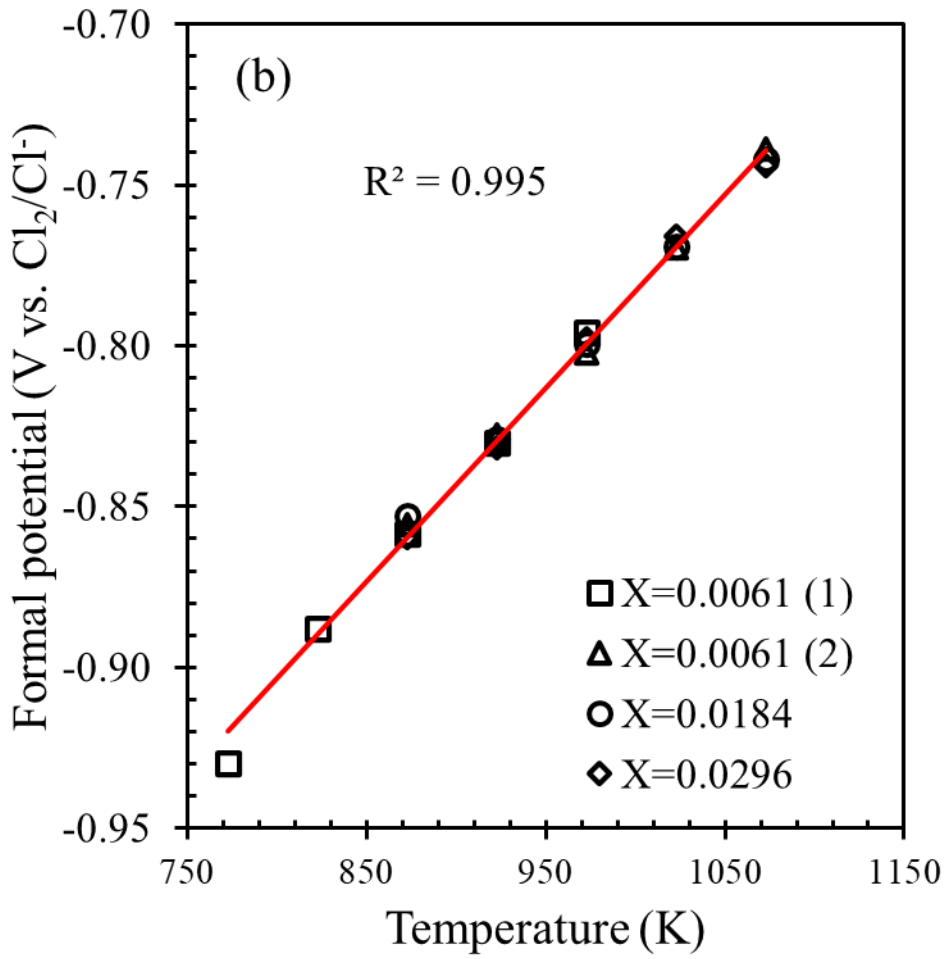

Figure IV-8 Redox potential and formal potential of three $NiCl_2$ concentrations in Magnak chloride, the red line in (b) is the fitted linear relation. (1) and (2) refer to two independent experiments.

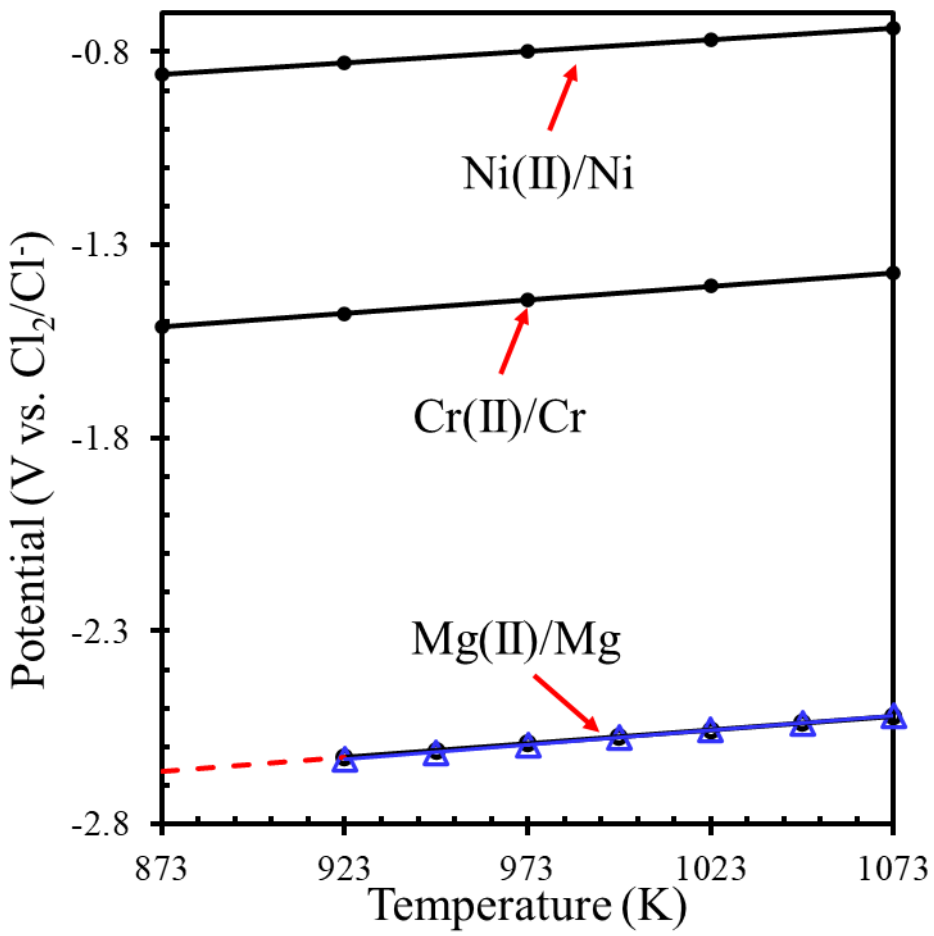

Figure IV-9 Comparison of Mg (II) / Mg redox potential and Cr (II) / Cr and Ni(II) / Ni formal potential in Magnak chloride.

IV.1.3. Sub-Conclusion

In conclusion, this study focused on developing chronopotentiometry and potentiodynamic polarization techniques to measure the redox potentials by using Ag^+/Ag to Cl_2/Cl^- redox couple in LiCl-KCl eutectic melt. The measurements were conducted at different mole fractions of AgCl and temperatures ranging from 723 K to 823 K. The formal potentials and activity coefficients

were calculated based on these measurements, yielding results that aligned well with previous studies.

The obtained results were considered reliable, with a deviation of less than 2% compared to reported values when chlorine gas injection was not involved. Moreover, the study presented a new correlation between formal potential and temperature for AgCl mole fractions of 0.0039 and 0.0145. The calculated activity coefficients of AgCl ranged from 1.905 to 2.638, and a relationship between temperature and the activity coefficient was proposed.

Furthermore, this paper introduced an innovative and precise method for measuring redox potential in chloride molten salt without the need for a thermodynamic reference electrode. The use of an alumina container as an ion membrane enabled measurements of the Cr(II)/Cr redox potential, and the setup was demonstrated to be universal, allowing for testing with various chloride salts. Additionally, a novel design of a liquid Mg reference electrode was reported, enabling the use of pure Mg instead of MgBi alloy.

The study extended its scope to investigate the redox potentials of $MgCl_2$, $NiCl_2$, and $CrCl_2$ in the temperature range of 873 K to 1073 K. Activity coefficients were calculated using supercooled standard potential, and empirical expressions for the formal potential were derived. The results indicated that Ni exhibited higher corrosion resistance compared to Cr in Magnak chloride salt. Moreover, the limited dissolution concentration of $NiCl_2$ and $CrCl_2$ suggested that pure Magnak chloride salt, free from corrosive impurities like moisture, would not corrode Ni and Cr metals.

IV.2. Electrochemical corrosion test of pure metal and alloys in Magnak salt

IV.2.1. Electrochemical corrosion test of pure metal

The chemical purification of Magnak salt to eliminate MgOHCl has been extensively discussed by Zhao and Vidal[166]. According to their report, thermal purification did not affect the content of MgOHCl. However, the introduction of Mg metal significantly reduced the MgOHCl content to 0.11 wt%. In our current study, we analyzed the purified salt using the CV, ICP-MS methods, and O&H analyzer.

Figure IV-10 illustrates the CV curves of each sub-batch of salt before immersing the testing samples at 600°C, with a scan rate of 100 mV/s. The prominent peaks observed at the right end correspond to the redox reaction of the Mg(II)/Mg couple. Since the reference electrode (RE) reaction is the same and the potential of the Mg(II) reduction reaction remains constant across batches and temperatures, it occurs at a potential equal to zero. This stability provided by the Mg RE ensures consistent potential measurements. The scanning potential range is fixed between -0.025 V and 2 V. The upper limit is restricted due to the generation of chlorine gas. Within this scanning window, one impurity peak was detected in the range of 1-1.25 V vs. Mg^{2+}/Mg. Additionally, the ICP results do not indicate the presence of any metallic impurities, suggesting that the impurity likely belongs to the non-metallic category. The O&H analysis of the purified salt indicates that the average hydrogen content is approximately 127 $\pm$ 3 ppm, and the average oxygen content is approximately 66 $\pm$ 22 ppm. These findings suggest that the impurity content is very low in the salt, however they still play a crucial role as corrosive agents. Reflecting on the

CV scan results in Figure IV-10, it's evident that the oxidation peaks' potential (1) is more negative than that of the reduction peaks (2), indicating distinct reaction origins for these peaks. According to Kanzaki and Takahashi's[167] calculations, peak (1) corresponds to the reaction of $2O^{2-} - 4e^{-} \rightarrow O_2$, possessing a standard potential of -1.173 V vs. Cl_2/Cl^-. On the other hand, peak (2) corresponds to the reaction of $2H^{+} + 2e^{-} \rightarrow H_2$, with a standard potential of -1.016 V vs. Cl_2/Cl^-. Both O_2 and H_2 are released from the system, resulting in the absence of discernible reverse peaks.

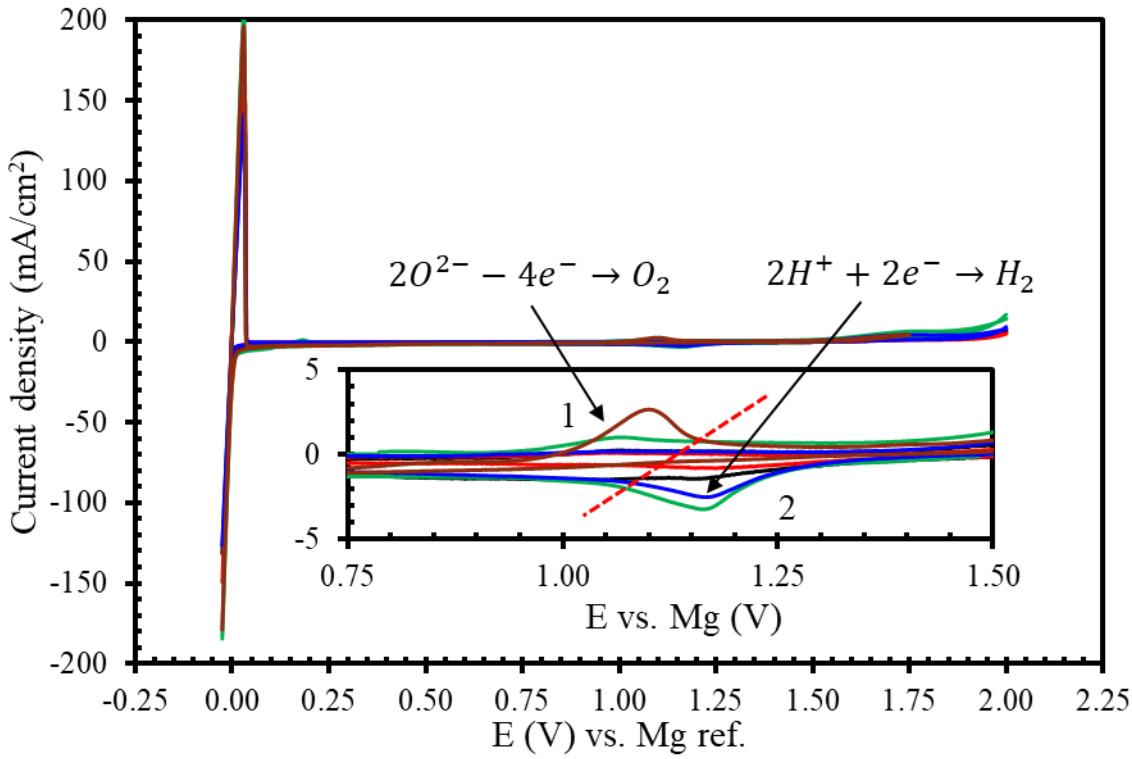

Figure IV-10 Cyclic Voltammetry scans of each sub-batch salt at 600 °C the scan rate is 100 mV/s, the WE is tungsten, the RE is Mg metal, and CE is tungsten.

The CV scan and ICP-MS results indicate the presence of minor impurities in the chemically purified Magnak salt. Prior to conducting the PD scan, a one-hour OCP scan was performed to monitor the system's equilibrium. Figure IV-11 presents the OCP results of Fe at different temperatures. Overall, as the immersion time increases, the OCP of the metal specimens also increases. This phenomenon can be attributed to the thermodynamic mechanism of corrosion, as depicted in Equation IV-19.

$$R_M + R_{im} \rightleftharpoons P_M + P_{im}$$ **Equation IV-19**

Where R_M refers to the metal element, R_{im} refers to the impurity oxidants, P_M refers to the oxidation state of metal element, and P_{im} refers to the reduction state of impurities.

Corrosion of a metal specimen occurs upon contact with the salt, and thermodynamically, there is an infinitely large EMF driving the reaction in Equation IV-19 forward. As the corrosion process progresses, corrosion products and impurity reduction products accumulate in the salt system. However, the impurity contaminants in the salt are assumed to remain constant due to the equilibrium of oxygen or moisture between the overlying gas and the salt. Theoretically, the EMF required to drive Equation IV-19 forward should increase over time until reaching a stable potential. The OCP results in Figure IV-11 indicate that after one hour of stabilization, the OCP change is very small. However, it is important to note that the corrosion process will continue, and the OCP will keep increasing as corrosion is an ongoing phenomenon.

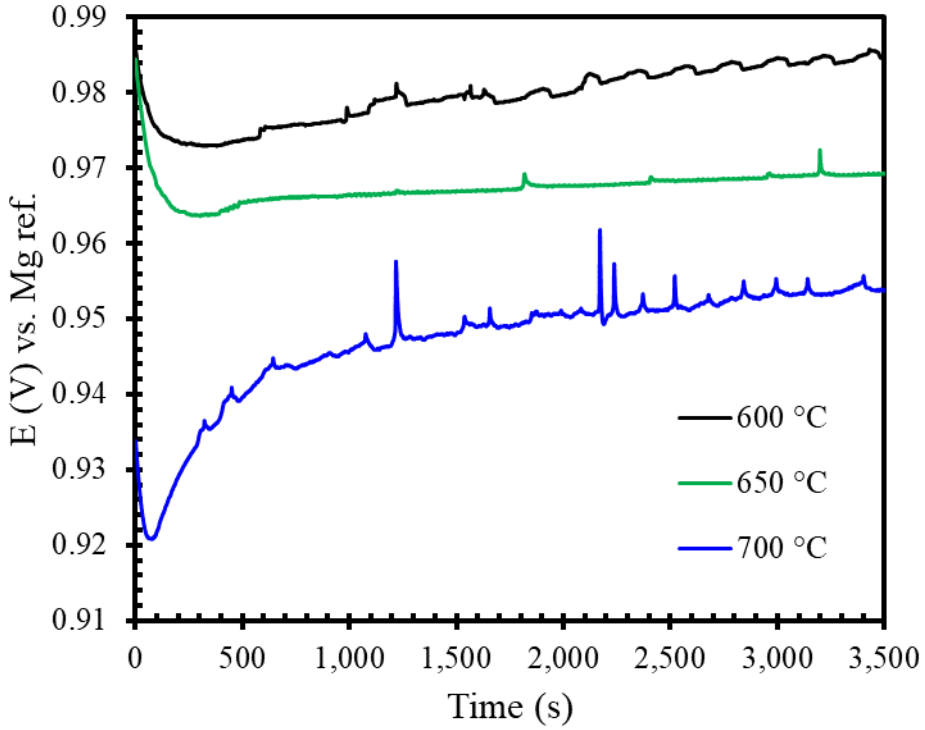

Figure IV-11 One-hour OCP curve of pure Fe sample before conducting PD scan. WE: iron, RE: magnesium, CE: tungsten.

Following the OCP measurement, a PD scan was performed in the range of ±0.25 V around the OCP with a scan rate of 2 mV/s. Figure IV-12 (a)-(c) illustrates the PD curves of pure metals at different temperatures. The PD scan was conducted from the negative potential to the positive potential direction with respect to the OCP. As described in the previous section, corrosion continued to occur for an hour, introducing corrosion products into the salt. This is why the PD current is initially higher and rapidly drops within the first 10-15 mV of the sweep. Once the corrosion products near the working electrode (WE) surface are consumed, the cathodic current is dominated by the reduction of impurities. An interesting observation can be made in Figure IV-12

(a) and (b), where the cathodic current density slopes of Fe and Cr are very similar within the approximately range of -0.2V to -0.1V scan window. This similarity is attributed to the cathodic current being limited by the diffusion of impurities in the salt. While progressing favorably from approximately -0.1 V towards the OCP, the impact of the anodic current becomes increasingly noteworthy. For instance, the oxidation current of Fe becomes notable compared to the reduction current of impurities. Eventually, the anodic current balances with the cathodic current, resulting in the total current equal to zero. After the balance point, the anodic current begins to dominate the PD current. Ni's PD curve differs from Fe and Cr as it exhibits a typical Tafel curve.

The illustration of the minor impurity-controlled PD curves is depicted in Figure IV-12 (d), which is drawn based on Figure IV-12 (a) to (c) and the slope data from Table IV-4. In Figure IV-12 (d), the curve colors represent different temperatures. Taking the 600°C curves as an example, the top curve represents the cathodic PD curve of impurities, which always has a higher Nernst potential ($E_{impurity}$) than the metals. The Nerst potential is describes in Equation IV-20, as the a_{jo} and a_{jr} are unknown, so the real E_j is hard to be determined accurately.

$$E_j = E_j^s + \frac{RT}{nF}\ln\left(\frac{a_{jo}}{a_{jr}}\right) \qquad \textbf{Equation IV-20}$$

In Equation IV-20, j represents the impurity, Fe, Ni and Cr. E_j represents the Nernst potential of j. E_j^s refers to the standard potential of j. And a_{jo} and a_{jr} represents the activity of j's oxidation state and reduction state.

As the overpotential increases in the negative direction further away from $E_{impurity}$, the cathodic current of impurities is controlled by the activation of the reduction reaction at the beginning, referred to as the activation control region. As the overpotential continues to increase, the supply of impurities near the electrode surface becomes limited by their diffusion from the bulk salt, resulting in a region where the cathodic current remains constant with increasing overpotential. This region is called the diffusion control region. On the other hand, the PD curves of Ni, Fe, and Cr only exhibit anodic curves, which are plotted gradually as a dashed line with two dots, a dashed line with one dot, and a solid black dashed line, respectively. It is worth noting that at 600°C, the PD curves of Fe and Cr fall into the impurity diffusion control region, while Ni falls into the impurity activation control region. It should be pointed out that the experimental curves in (a) to (c) represent the mixed current of impurity cathodic current and metal anodic current, which are represented by the purple color.

Taking the Cr curve as an example, the PD scan was conducted from point A to point D. In the A to B region, where the potential is lower than the E_{cr}, the corrosion PD curve is dominated by impurity's cathodic current. After point B, the Cr anodic current begins to counterbalance the impurity cathodic current and equals it at point C. The potential at point C is known as the Cr corrosion potential of the Magnak salt. From point C to point D, the Cr anodic current gains more weight in the overall PD current, and after point D, the impurity's cathodic current becomes negligible. Clearly, in the impurity diffusion control region, the Tafel fitting is not suitable for fitting the corrosion PD curve and obtaining the corrosion current. In this study, the E vs. $Log\ |i|$ fitting of the -0.2 to -0.1 V overpotential region is used to determine the impurity diffusion-

controlled corrosion current. As the temperature rises, the diffusion rate of impurities also increases, leading to a broader activation zone and a shorter diffusion control zone. Consequently, at 700°C, the slope of the Fe corrosion curve approaches the slope value of Ni. The corrosion current density of each metal is presented in Table IV-4. In Figure IV-12 (d), the Nernst potentials of all species may either increase or decrease with increasing temperatures. However, it is essential to note that this does not impact the overall conclusion. For illustration purposes, the decreasing case in (d) was employed to explain the observed phenomena.

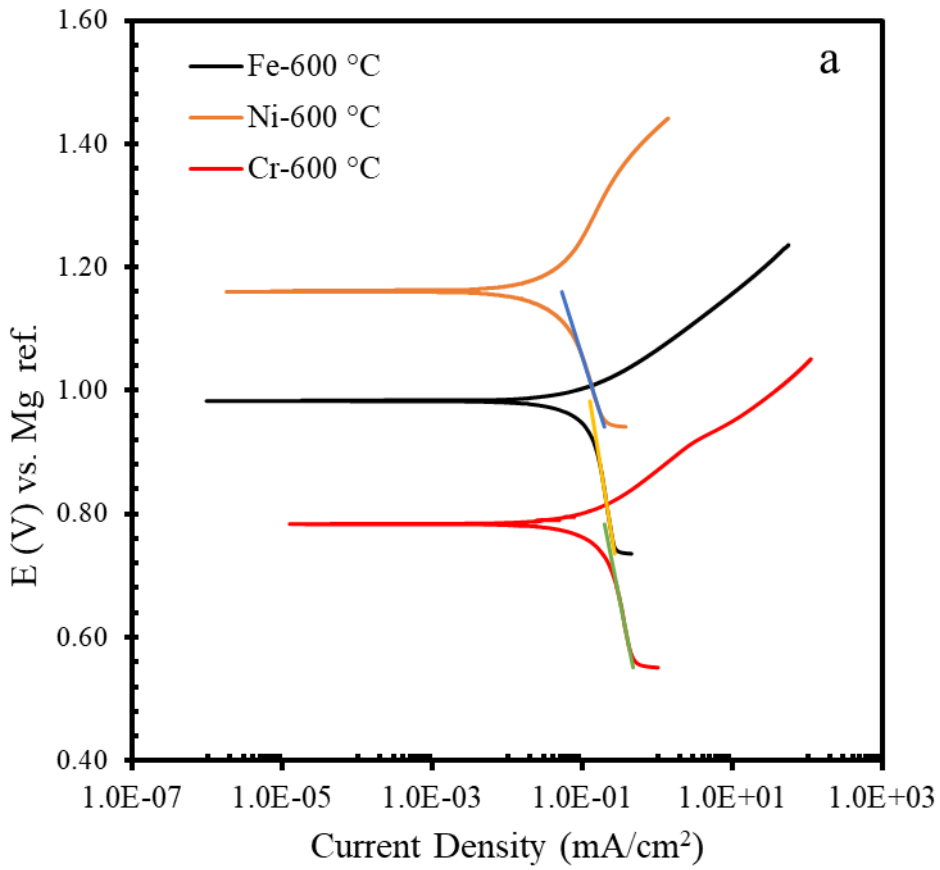

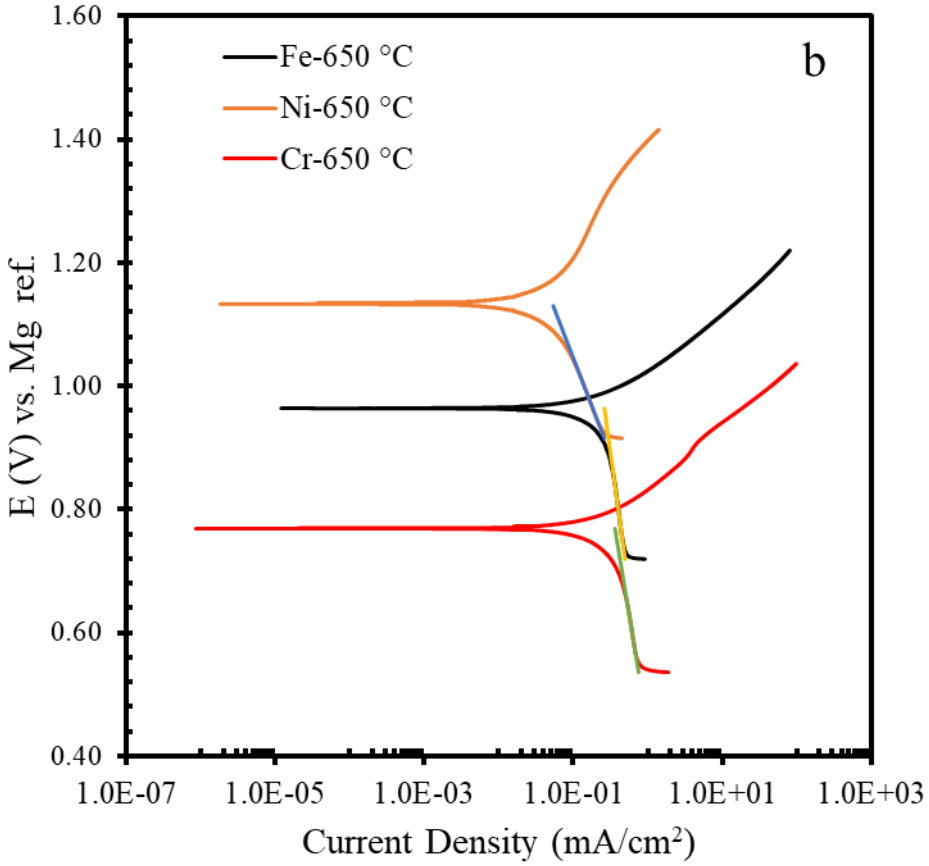
b
Fe-650 °C
Ni-650 °C
Cr-650 °C
E (V) vs. Mg ref.
1.60
1.40
1.20
1.00
0.80
0.60
0.40
1.0E-07
1.0E-05
1.0E-03
1.0E-01
1.0E+01
1.0E+03
Current Density (mA/cm²)

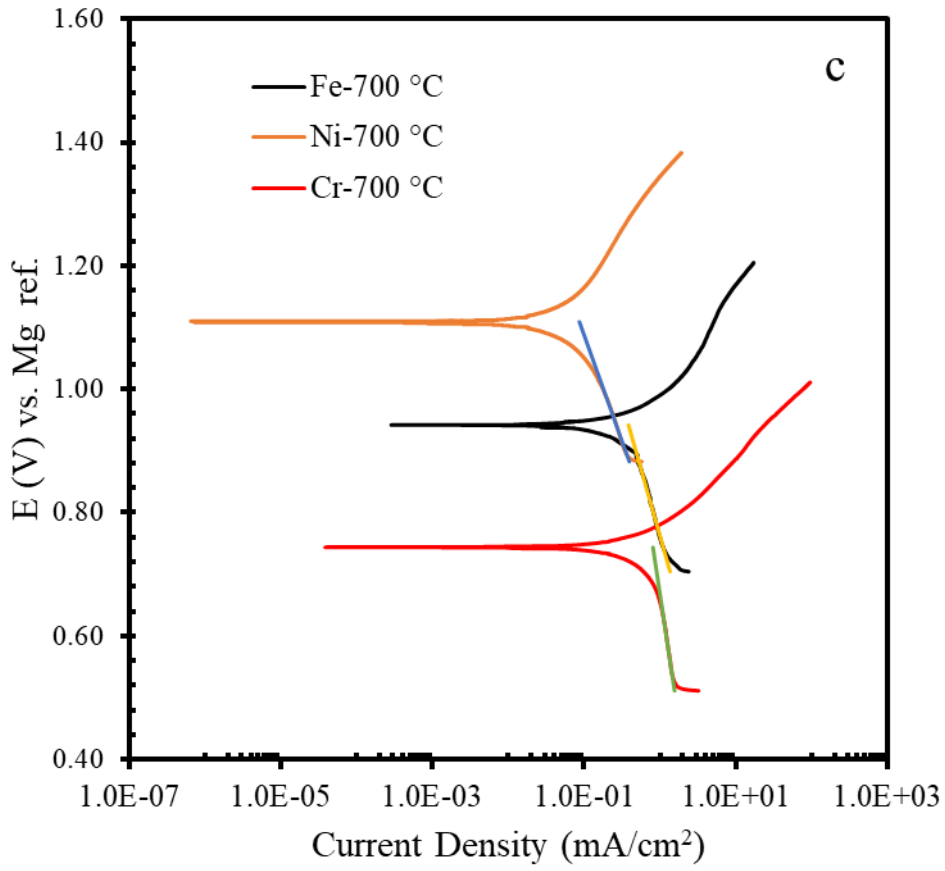
c
Fe-700 °C
Ni-700 °C
Cr-700 °C
1.60
1.40
1.20
1.00
0.80
0.60
0.40
E (V) vs. Mg ref.
1.0E-07
1.0E-05
1.0E-03
1.0E-01
1.0E+01
1.0E+03
Current Density (mA/cm2)

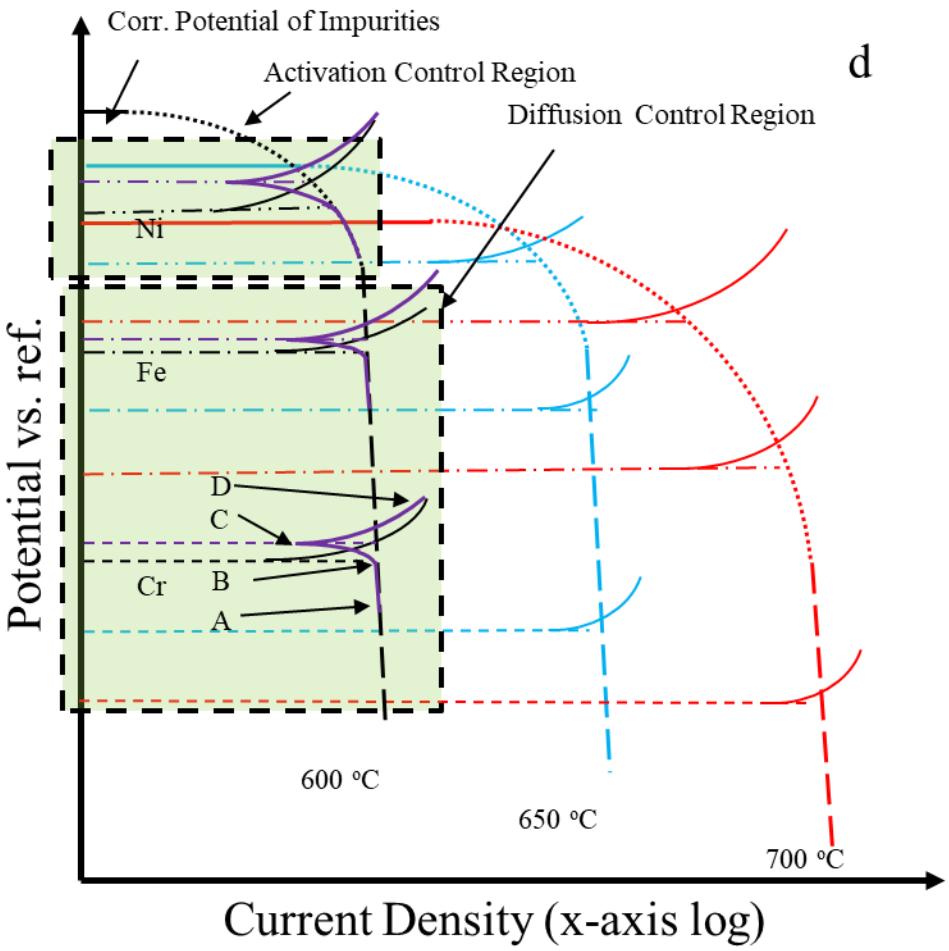

Figure IV-12 Potentiodynamic scan of pure metals in Magnak salt at (a) 600 °C, (b) 650 °C, (c) 700 °C. (d) Illustration of the PD curve driven by impurities.

Table IV-4 Summary of cathodic slope and corrosion current density.

Temp. °C	Samples	Slope $\boldsymbol{\beta_c}$ V/decade	$\boldsymbol{i_{corr}^{PD}}$ mA/cm^2	i_{corr}^{OCP} mA/cm^2	$i_{corr}^{PD} - i_{corr}^{OCP}$ mA/cm^2	$\frac{i_{corr}^{PD} - i_{corr}^{OCP}}{i_{corr}^{OCP}}$ %
600	Fe	0.7505	0.1256	0.1248	0.0008	0.6155
	Ni	0.3853	0.0528	0.0444	0.0084	18.9230
	Cr	0.6104	0.1965	0.1842	0.0123	6.7034
	SS316	0.4347	0.1240	0.1147	0.0093	8.0935
	A709	0.2846	0.1484	0.1371	0.0113	8.2041
650	Fe	0.8766	0.2616	0.2581	0.0034	1.3220
	Ni	0.3130	0.0525	0.0403	0.0122	30.3215
	Cr	0.7327	0.3626	0.3442	0.0184	5.3552
	SS316	0.5533	0.2605	0.2426	0.0179	7.3779
	A709	0.3074	0.2924	0.2772	0.0152	5.4862
700	Fe	0.4823	0.4161	0.3907	0.0254	6.5047
	Ni	0.3439	0.0861	0.0748	0.0113	15.0971
	Cr	0.8193	0.8079	0.7696	0.0383	4.9822
	SS316	0.3598	0.4942	0.4433	0.0508	11.4642
	A709	0.3746	0.5197	0.4677	0.0520	11.1276

The corrosion potentials of the materials were determined using both the OCP method and the PD scan method at different temperatures are listed in Table IV-5. The corrosion potential represents the potential at which corrosion occurs in a corrosive environment, and the OCP method is commonly used to measure the corrosion potential of a material[168]. However, in some systems, the OCP method may require a long stabilization time. Consequently, electrochemical methods, such as PD scans, have been developed to measure the corrosion potential more efficiently.

In the present study, the corrosion potentials obtained from the OCP method ($\boldsymbol{E_{corr}^{OCP}}$) were consistently found to be more positive than the corrosion potentials obtained from the PD scans

($\boldsymbol{E_{corr}^{PD}}$). Assis et al.[169] described this phenomenon as being attributed to the large initial reduction potential that disrupts the passive layer, resulting in a switch to a more negative potential in aqueous solutions. However, this explanation may not be applicable in molten salt environments due to the instability of the corrosion layer. Furthermore, Zhang et al.[122] pointed out that Assis et al.'s theory could not explain why the $\boldsymbol{E_{corr}^{PD}}$ shifts further to negative potentials as the PD scan rate increases in aqueous solutions. Brad and Faulkner discussed the impact of double-layer capacitance in a potential sweep experiment, where a charging current density ($\boldsymbol{i_{charging}}$) proportional to the product of the scan rate and interface capacitance is always present. The faradic current density ($\boldsymbol{i_f}$) is measured based on the charging current density[170]. In the case of a PD scan, the peak of the polarization curve occurs when the total current density ($\boldsymbol{i}$) equals zero.

$$i^{PD} = i_{charging} + i_f = i_{charging} + i_a + i_c \qquad \textbf{Equation IV-21}$$

In Equation IV-21, i_c and i_a refer to the cathodic current density and anodic current density. At the open circuit potential there is no charging current involved, resulting in a total current of zero. This means the Faradic current is zero, or equivalently, the cathodic current equals the anodic current. However, in the case of a positive potential scan, the positive charge stored in the interface capacitor continues to increase. This implies that electrons are being forced from the electrode to the interface by the external power source. Consequently, the charging current flows in the same direction as the anodic current during a positive scan. As a result, a lower E_{corr}^{PD} is required to achieve a total current density of zero compared to E_{corr}^{OCP}.

In the case of a negative potential scan, the direction of potential shift is reversed. It should be noted that a higher scan rate leads to a larger charging current density and a larger potential shift. In our current experiment, a scan rate of 2 mV/s was employed. The results presented in Table IV-5 indicate that, except for Fe, all other samples exhibited a potential shift ranging from 17-30 mV in the negative direction. This discrepancy was depicted as an error in the Figure IV-16.

Once the potential difference between E_{corr}^{OCP} and E_{corr}^{PD} is known, the corrosion current density, which was previously determined by using the intersection of E_{corr}^{PD} and the cathodic current density, becomes less accurate. Figure IV-13 illustrates the correlation between the OCP corrosion current density and PD corrosion current density. The charge current density influences the PD current density. Within the potential range B to C, since the i_{charge} in the same direction a i_a, it reduces E_{corr}^{OCP} to E_{corr}^{PD}. However, within the potential range of A to B, when i_c is significantly high, the influence of i_a and i_{charge} is minimal. Extending the cathodic fitting line (solid red) in the A to B range allows determination of its intersection with E_{corr}^{OCP}, which, through Equation IV-22, yields the corrosion current density at E_{corr}^{OCP}. Furthermore, within the range of C to E, i_{charge} increases i_{PD}. Beyond point E, both i_c and i_{charge} become inconsequential. Importantly, regardless of whether the cathodic PD curve lies within the impurities' activation zone or diffusion zone, at E_{corr}^{OCP}, the cathodic current density remains lower than the anodic current density. This observation signifies that the cathodic current density corresponds to the i_{corr}^{OCP}. Consequently, the corresponding corrosion current density at $E_{corr}^{OCP}$is calculated and detailed presented in Table IV-4.

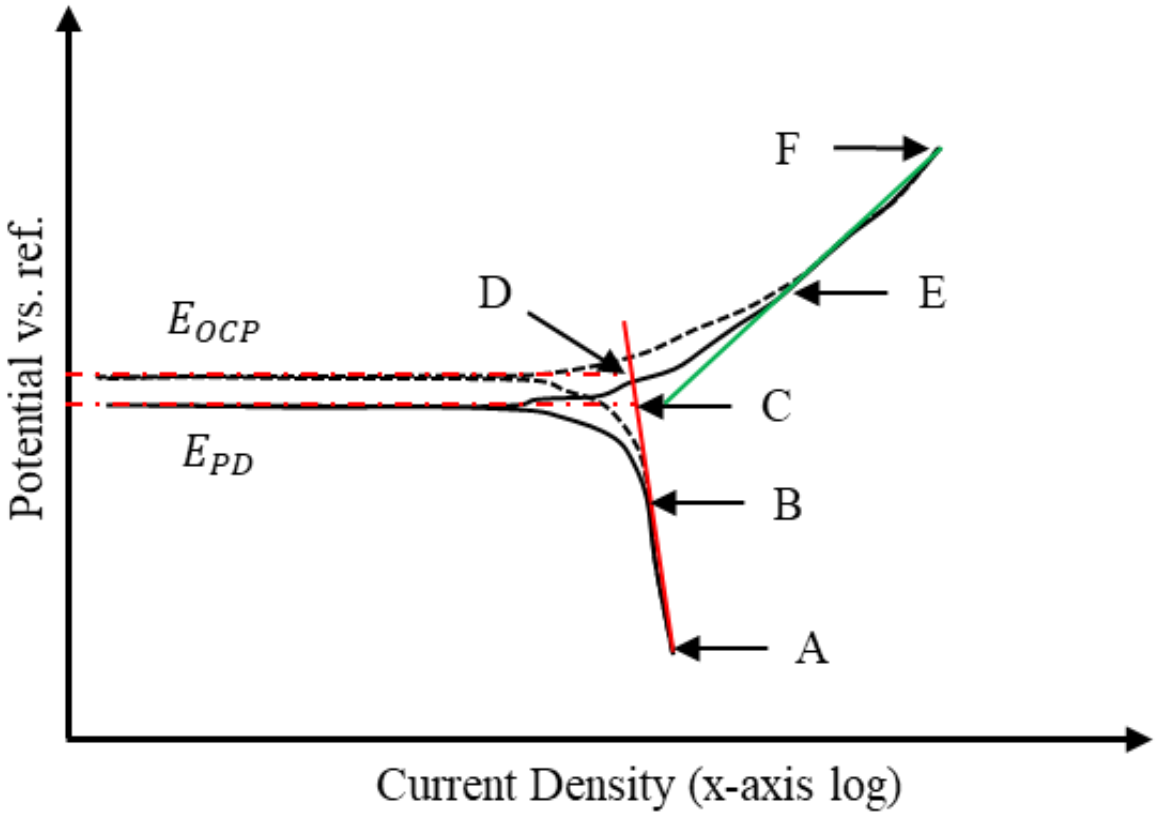

Figure IV-13 Illustration of the correlation between the OCP corrosion current density and PD corrosion current density.

$$\log(|i^{OCP}|) = \log(|i^{PD}|) - \frac{E_{corr}^{OCP} - E_{corr}^{PD}}{\beta_c}$$ **Equation IV-22**

Upon examining the results, it can be observed that the disparity between the corrosion current density obtained from the PD and the OCP for pure Fe and Cr falls within a 10% range compared to the OCP corrosion current density. However, the corrosion current density of Ni exhibits a significant difference, amounting to approximately 20% of its OCP corrosion current density. This

phenomenon arises due to Ni's inherently low current density at both the potential of passivation (PD) and OCP. Consequently, even a slight alteration in current density results in a substantial ratio change.

Table IV-5 Corrosion potentials obtained from OCP and potentiodynamic scans at varying temperatures

Temp. °C	Samples	E_{corr}^{OCP} (V)	E_{corr}^{PD} (V)	$E_{corr}^{OCP} - E_{corr}^{PD}$ (V)
600	Fe	0.985	0.983	0.002
	Ni	1.190	1.161	0.029
	Cr	0.801	0.784	0.017
	A709	0.960 ± 0.004	0.935 ± 0.005	0.025
	SS316	1.011 ± 0.005	0.985 ± 0.004	0.026
650	Fe	0.969	0.964	0.005
	Ni	1.170	1.134	0.036
	Cr	0.786	0.769	0.017
	A709	0.949 ± 0.001	0.922 ± 0.004	0.027
	SS316	0.985 ± 0.003	0.965 ± 0.002	0.020
700	Fe	0.954	0.941	0.013
	Ni	1.130	1.109	0.021
	Cr	0.761	0.744	0.017
	A709	0.918 ± 0.008	0.895 ± 0.005	0.023
	SS316	0.928 ± 0.005	0.906 ± 0.005	0.022

IV.2.2. Electrochemical corrosion test of SS316 and A709

In the case of alloys, the polarization curves obtained through potential scan (PD) exhibit notable differences compared to those of pure metals. Figure IV-14 (a) demonstrates that the alloys' PD curves display a wide noise band instead of a single peak. Both SS316 and A709 alloys exhibit a peak zone in their respective PD curves. Typically, the peak band for SS316 is around 30 mV, while for A709, it is around 20 mV. To enhance the visualization of the data, a smoothing filter

was applied to the current using the Gamry Echem Analyst software. Specifically, a Sacitzky-Golay filter of the fourth order with 16 points was utilized. Figure IV-14 (b) illustrates the three smoothed curves of A709 obtained at 600°C. These curves correspond to three individual A709 samples from the same sub-batch of salt, denoted as S1, S2, and S3. The obtained $\boldsymbol{E_{corr}^{OCP}}$ and $\boldsymbol{E_{corr}^{PD}}$ values from the smoothed curves of the alloys at different temperatures are compiled in Table IV-5. It is worth noting that the standard deviations of the potentials are less than 8 mV, indicating the reliability and repeatability of the potential results. The corrosion potentials determined through the PD method are plotted in Figure IV.15.

In alloys, the Nernst potential, in Equation IV-20, of the majority element, even with the same a_{jo} as the pure metal, shifts positively compared to the Nernst potential of the corresponding pure metal. This shift occurs because the a_{jr} becomes smaller in alloys compared to pure metals. Consequently, even though A709 and SS316 contain Cr, their corrosion potential is significantly higher than that of pure chromium metal. As shown in Figure IV-16, at 600°C and 650°C, SS316 exhibits a higher corrosion potential than pure Fe. However, at 700°C, the corrosion potential of SS316 decreases to lower than Fe. On the other hand, the corrosion potential of A709 remains consistently lower than that of pure iron, with a difference of approximately 50 mV. It is noteworthy that SS316 and A709 demonstrate very similar corrosion potentials at 700°C.

Considering that the E_{corr}^{OCP} of SS316 and A709 is either close to or lower than that of pure Fe, it suggests that the potential scan region in the PD falls within the impurity diffusion control region, as illustrated in Figure IV-12 (d). The PD curves of the first sample of A709, SS316, and pure

metal at different temperatures are shown in Figure IV-15. The reason for presenting the plots based on temperature is that, in an impurity diffusion control scenario, disregarding the effect of impurity cathodic current leads to significant errors when obtaining the corrosion current from either the Tafel or Butler-Volmer equation based on the anodic dissolution. Figure IV-15 (a) and (b) exhibit intriguing cathodic curves within a similar PD scan range. It is observed that SS316 exhibits a higher cathodic current density, whereas A709's cathodic current density is lower when compared to the baseline Fe curve. The cathodic current density of an alloy in the PD can be simplified using Equation IV-23.

$$i_c^{PD} = i_c^{impurity} + i_c^{corrosion\ product} + i_a^{alloy} + i_{charging}$$ **Equation IV-23**

In Equation IV-23, $i_c^{PD}, i_c^{impurity}, and\ i_c^{corrosion\ product}$ represent the total cathodic current density, the cathodic current density resulting from impurities, and the reduction of corrosion products, respectively. The term i_a^{alloy} denotes the current density caused by alloy oxidation, majorly caused by the Cr dissolution. Equation IV-23 can be expressed as Equation IV-24 when i_c^{PD} equals zero.

$$-i_a^{alloy} - i_{charging} = i_c^{impurity} + i_c^{corrosion\ product}$$ **Equation IV-24**

Taking the data at 650°C, as shown in Figure IV-15 (b), as an example, let's assume that the cathodic current density of pure Fe only includes the contribution from impurities ($i_c^{impurity}$), and the contribution from corrosion products ($i_c^{corrosion\ product}$) is negligible. Therefore, the cathodic

curve of impurities (indicated by the purple dashed line) matches the cathodic curve of pure Fe. Consequently, the cathodic current density due to impurities ($i_c^{impurity}$) in the potential range of 0.7 V to 9.8 V vs. Mg is obtained from the data of pure Fe. The green lines (representing Cr in A709) and blue lines (representing Cr in SS316) depict the approximate Nernst potential and cathodic curves of Cr in the respective alloys. In the region from point A to point B, SS316 exhibits a larger cathodic current density compared to $i_c^{impurity}$. This can be attributed to the contribution from corrosion products ($i_c^{corrosion\ product}$), which were introduced during the 1-hour immersion. On the other hand, A709 shows a lower current density compared to $i_c^{impurity}$. The difference between A709 and SS316 lies in the Nernst potential of Cr, meaning that the Nernst potential of Cr in A709 is lower than that in SS316. As a result, the current density caused by Cr oxidation (i_a^{Cr}) starts to play an important role around point A in the polarization diagram (PD) curve of A709. Approximately, i_a^{Cr} starts to have more influence around point B in the PD curve of SS316.

Assuming that at the beginning of the electrochemical corrosion tests, there are fewer corrosion products available to contribute to $i_c^{corrosion\ product}$, the corrosion process is primarily governed by $i_c^{impurity}$, regardless of whether i_a^{Cr} starts to take effect at point A or point B. Therefore, in order to obtain the E_{corr}^{PD} of the alloys in a scenario where impurity diffusion controls the process, it is necessary to use auxiliary data of impurities obtained from pure Fe, rather than fitting the PD curves of the alloys. The calculation is presented in Equation IV-25. The corrosion current density derived from Equation IV-25 is comparatively lower than that determined from the dissolution current density. This suggests that the corrosion process is governed by impurity diffusion.

$$\log(|i^{alloy}|) = \log(|i_{Fe}^{PD}|) - \frac{E_{corr-alloy}^{PD} - E_{corr-Fe}^{PD}}{\beta_{c-Fe}}$$ **Equation IV-25**

Significantly noticeable is the corrosion potential of SS316, which experiences a notable reduction at 700°C in comparison to lower temperatures. Moreover, the net PD cathodic current density at this temperature falls below the impurity diffusion current density. This phenomenon arises because SS316 initiates dissolution at the lower scanning potential, signifying a decline in corrosion resistance. The corrosion current density of the alloys at the open circuit potential was subsequently converted using Equation IV-22. Despite the presence of wide noise in the PD curve, which increases the error associated with the E_{corr}^{PD}, the use of the corrosion correction equation (Equation IV-22) helps mitigate the errors introduced by data smoothing techniques. As a result, the corrosion current density obtained from both E_{corr}^{OCP} and $E_{corr}^{PD}$is provided in Table IV-4.

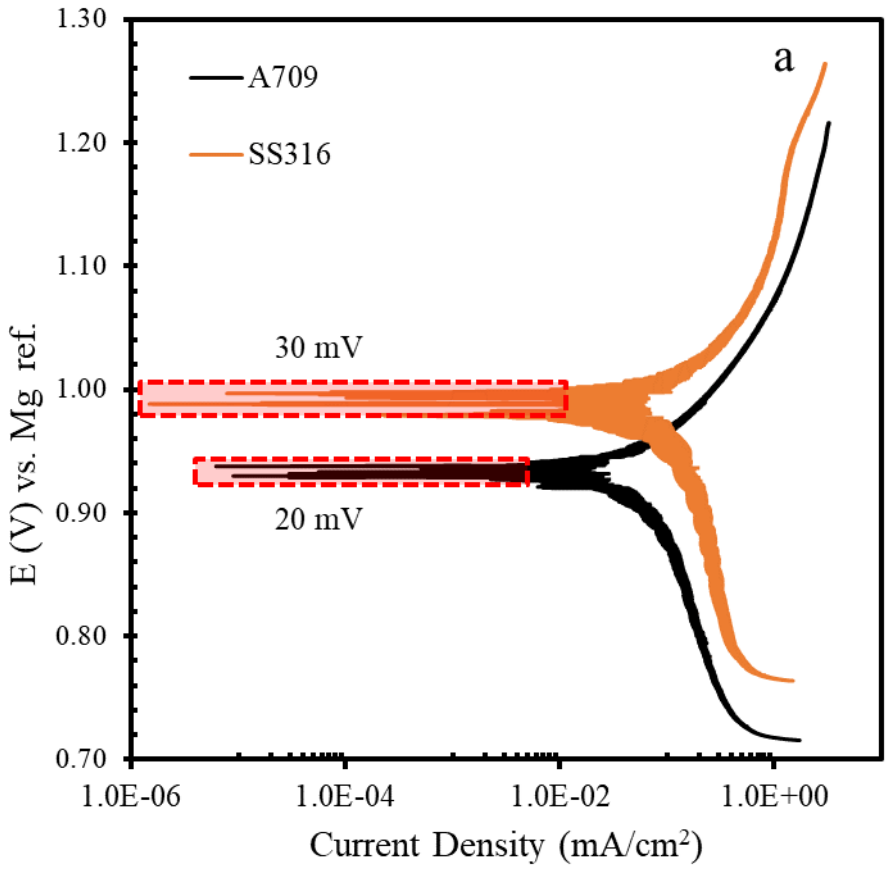
a
A709
SS316
30 mV
20 mV
1.30
1.20
1.10
1.00
0.90
0.80
0.70
E (V) vs. Mg ref.
1.0E-06
1.0E-04
1.0E-02
1.0E+00
Current Density (mA/cm²)

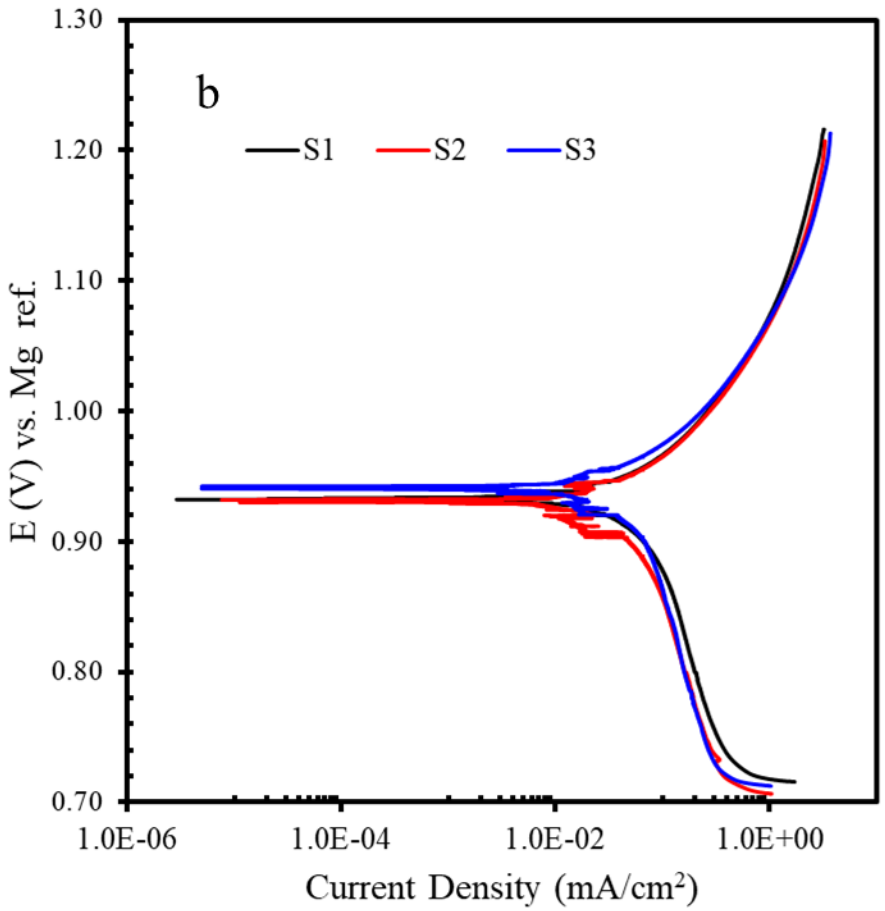

Figure IV-14 Potentiodynamic scan of alloys. (a) Original data of the first sample of SS316 and A709 at 600 ºC. (b) Smoothed PD curves of three A709 samples at 600 ºC.

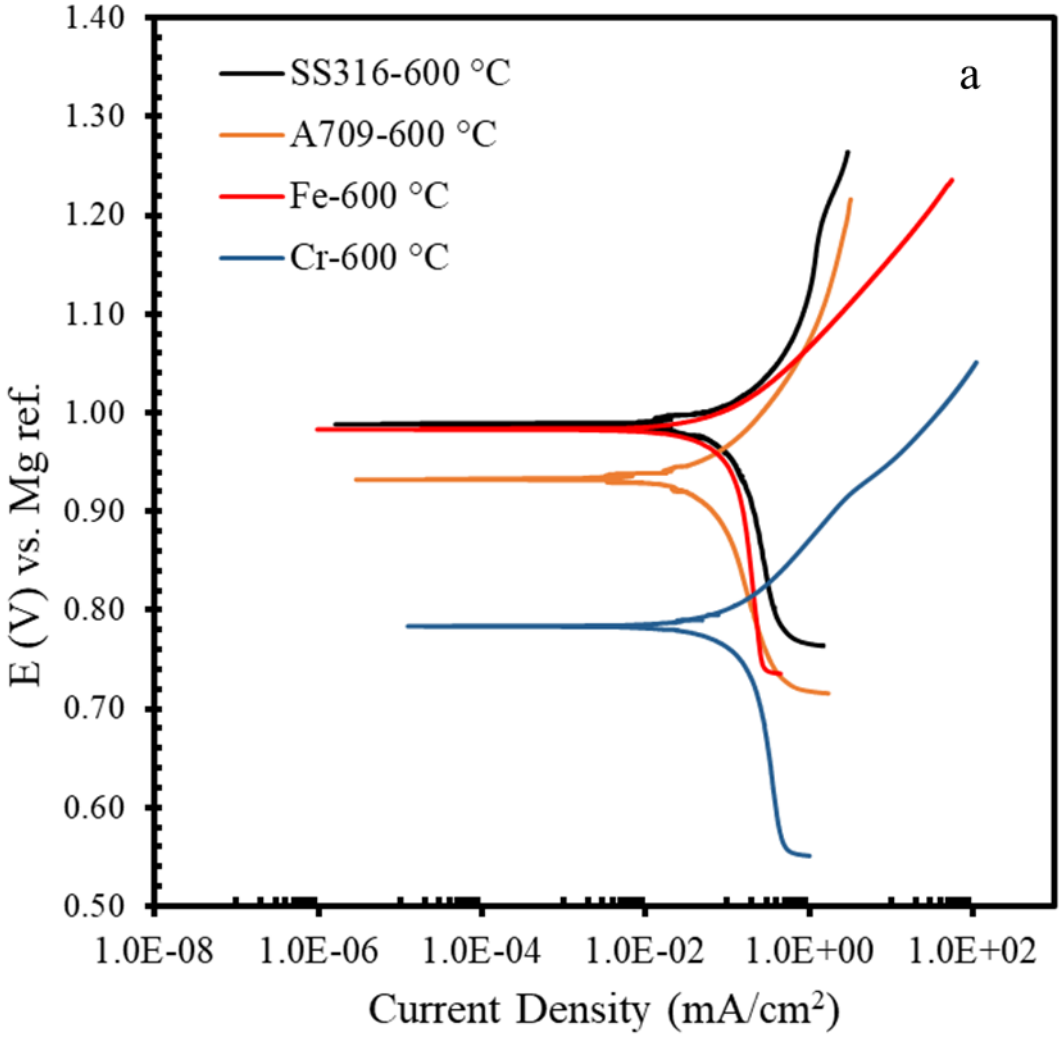
SS316-600 °C
A709-600 °C
Fe-600 °C
Cr-600 °C
a
1.40
1.30
1.20
1.10
1.00
0.90
0.80
0.70
0.60
0.50
E (V) vs. Mg ref.
1.0E-08
1.0E-06
1.0E-04
1.0E-02
1.0E+00
1.0E+02
Current Density (mA/cm²)

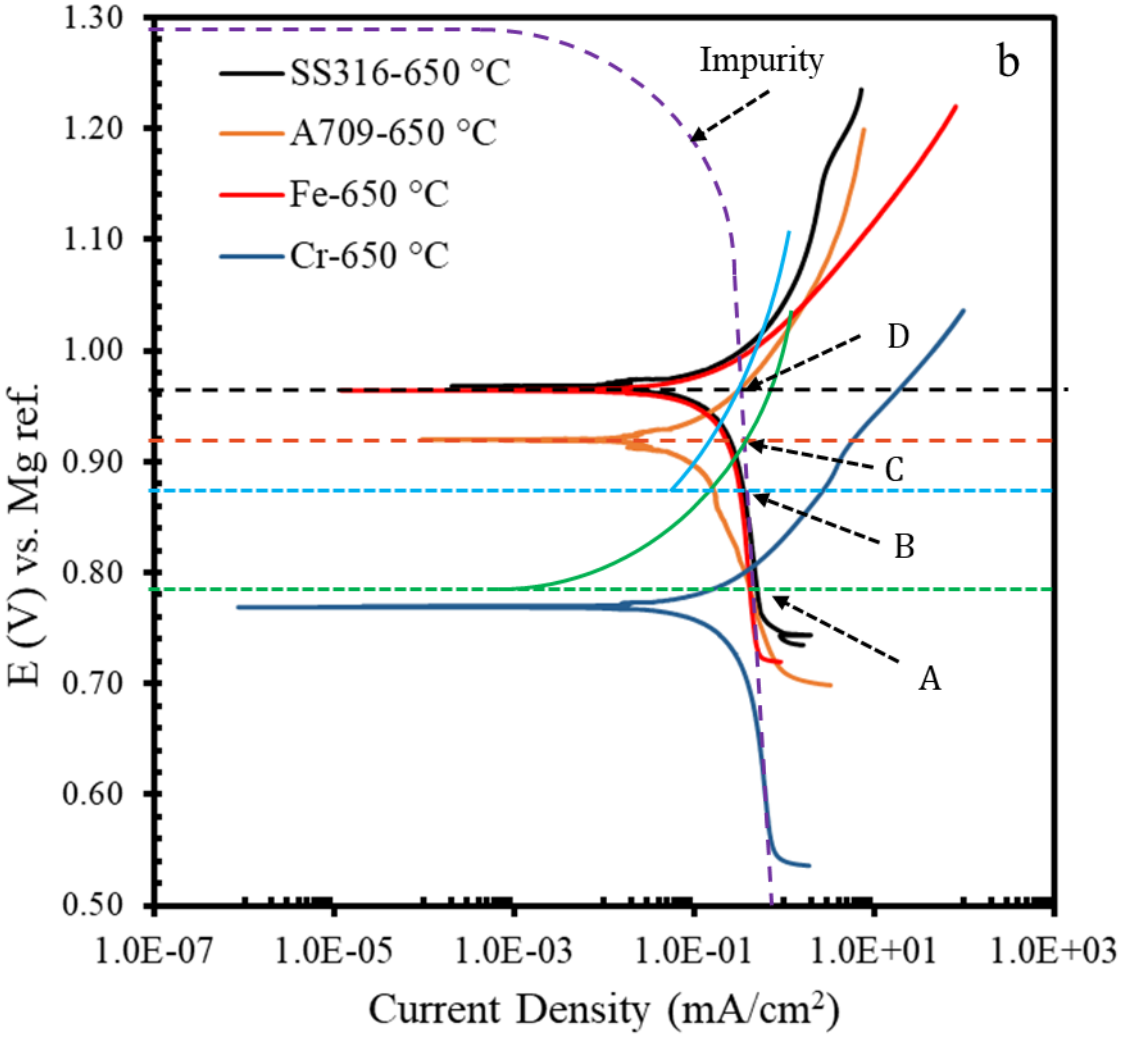
1.30
1.20
1.10
1.00
0.90
0.80
0.70
0.60
0.50
E (V) vs. Mg ref.
1.0E-07
1.0E-05
1.0E-03
1.0E-01
1.0E+01
1.0E+03
Current Density (mA/cm²)
SS316-650 °C
A709-650 °C
Fe-650 °C
Cr-650 °C
Impurity
b
D
C
B
A

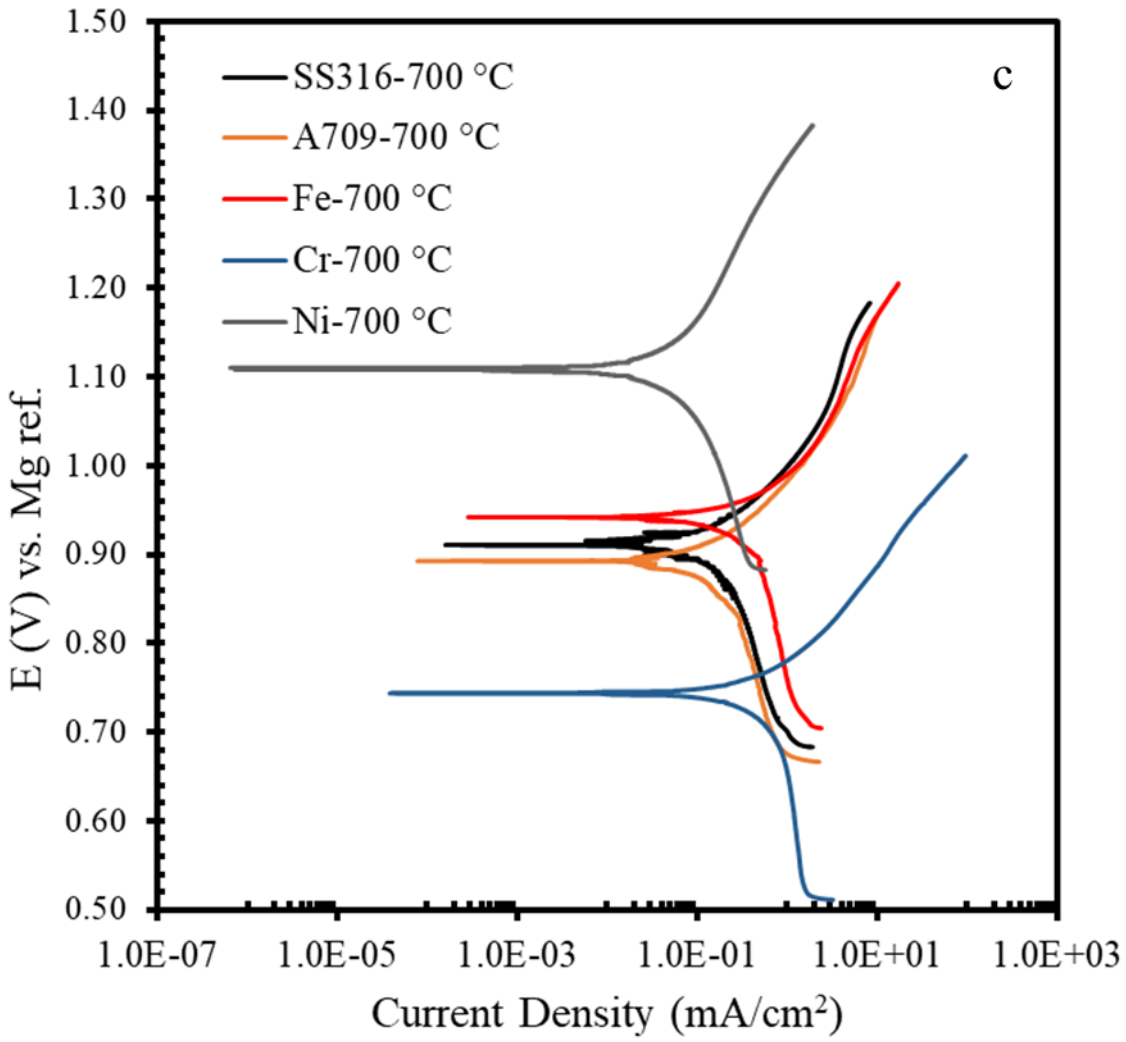

Figure IV-15 The smoothed potentiodynamic scan curves of first sample of A709 and SS316 and pure metal PD curves at various temperatures.

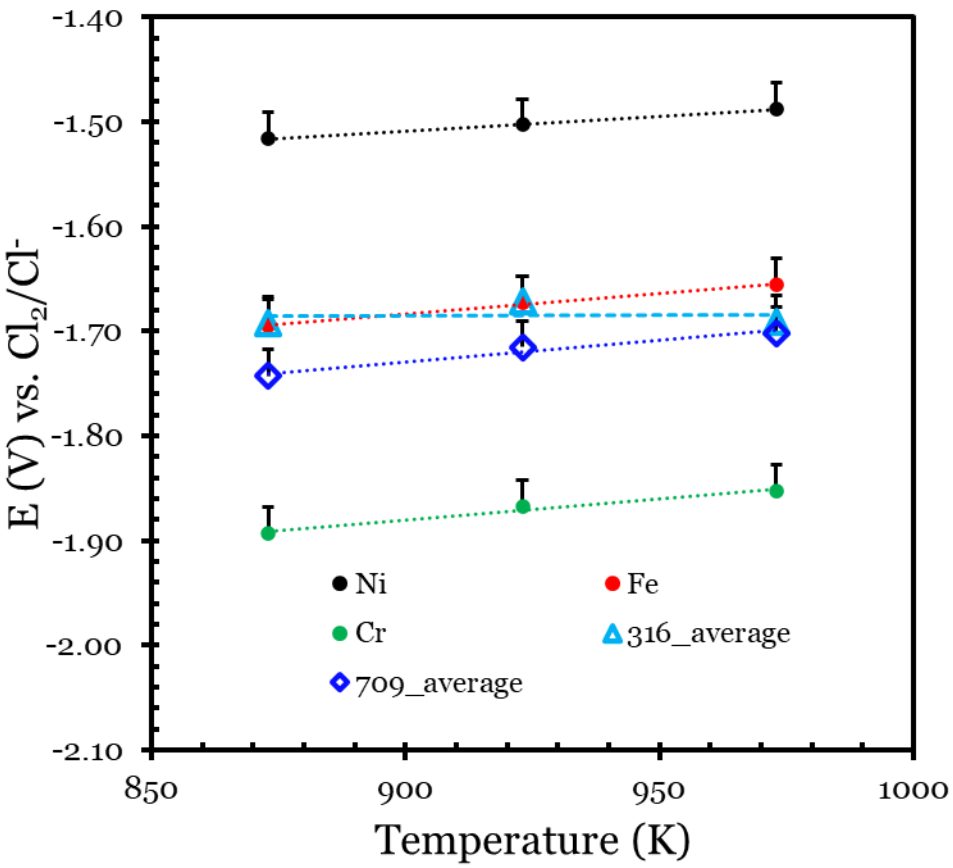

Figure IV-16 Corrosion potential from potentiodynamic scan of pure metal and alloy.

IV.2.3. Sub-Conclusion

In conclusion, the PD polarization tests conducted on pure Fe, pure Cr, pure Ni, A709, and SS316 exposed to chemically purified Magnak chloride molten salt at various temperatures to obtain their corrosion potential and corrosion current density. These results shed light on the electrochemical corrosion process within a low impurity level molten salt environment. The observed corrosion mechanism was found to be diffusion-controlled, predominantly driven by cathodic reactions.

Furthermore, a cathodic controlled PD data analysis procedure was developed to analyze the obtained results. The findings indicate that at temperatures of 600°C and 650°C, SS316 exhibited a higher corrosion potential compared to A709 and slightly higher than pure Fe. However, at 700°C, SS316 demonstrated corrosion potential closer to that of A709 and both were lower than pure Fe, although still higher than pure Cr. Additionally, the corrosion current of SS316 consistently remained lower than that of A709 across all tested temperatures.

For future research, it is recommended to conduct a corrosion study on SS316 and A709 at higher temperatures. While A709 displayed inferior corrosion resistance under the current test conditions, it demonstrated more stable corrosion properties compared to SS316, with the corrosion potential of SS316 increasing as the temperature rose.

IV.3. Lessons Learned from Operation of a Forced Convection Loop Using Chloride Molten Salt

This section describes our experience with loop operations, where we ran the loop three times and gained valuable insights on its execution. The loop operation can be divided into five key steps, namely salt loading, salt purification and pre-melt, salt transportation, salt circulation, and salt drainage.

IV.3.1. Salt loading

As previously mentioned, the ternary salt composition $MgCl_2$-KCl-NaCl is utilized in our process. These salts are acquired individually in powder form and are separately weighed and pre-mixed in a bucket. The mixture is then loaded into the auxiliary tank via a 2" diameter port, using a funnel.

The weighing and loading of the salt are carried out in the ambient environment while wearing appropriate personal protective equipment. Once loaded, the port is sealed with a threaded lid. Since the salts used are non-toxic and non-hazardous, we did not encounter any issues in this step.

However, as the original design utilized the auxiliary tank as both the purification and drain reservoir, we overlooked the density difference between the powder and liquid salt during the loading process. Nonetheless, this presented an opportunity for us to load and purify multiple batches of salt. Our only suggestion in this regard is to consider the initial tank volume design.

IV.3.2. Salt purification and solid salt pre-melt

The initial step in our process is to purify the salt received from the vendor, which is done in the auxiliary (Aux.) tank. The purification process involves thermal purification with argon flow. A total of 40 kg of salt is purified in two separate batches of 25 kg and 15 kg, respectively, filling the Aux. tank to 50-75% capacity with powder salt. An overview of the purification process is presented in Error! Reference source not found.. To begin, the tank is evacuated and refilled with a rgon gas five times to replace the air from the open-air salt loading process. Port 8 is connected to both the argon source and a vacuum pump to facilitate this process. Once the air is sufficiently replaced, the cover gas line is turned off, and the purging and exhaust line is turned on. The inlet argon flow rate is maintained at 5-10 standard cubic feet per hour (SCFH), and the tank pressure is set to 1 psi. The heating system is then activated to gradually heat the salt at a rate of 1 °C per minute. After the salt has melted, it is kept at a temperature of 500 ºC and bubbled with argon flow

at a constant rate for one hour. Once this process is completed, the exhaust line is turned off and the salt is heated to a temperature of 600 ^{o}C for transportation.

Our purification process highlighted the importance of not relying solely on flow rate and pressure during the heating process. As the volume of argon gas in the tank expands with increasing temperature, maintaining a constant flow rate will cause the tank pressure to exceed the designed pressure limit of 15 psi. To prevent this, we manually adjusted the exhaust valve to maintain a pressure of 1 psi. However, we recognize the need for a more automated solution and suggest implementing a back regulator on the exhaust line to regulate the flow and pressure automatically.

We also observed that the powder salt had low thermal conductivity during the purification process. As shown in Figure IV-17, the process TC was inserted into port 6, while the high limit TC was placed between the tank and heater. We noticed that there was a significant delay in the temperature response of the process TC, and there was a large temperature difference between the wall and center of the tank. The control system we used had a built-in automatic ramp heating function, which was not suitable for powder and solid salt. This resulted in overheating of the outer layer of salt. To overcome this issue, we experimented with low constant heating power (3-5%) to achieve a more balanced heating. However, we recognize the need for a more permanent solution. This could involve designing a tank with a taller height and relatively smaller diameter or incorporating an internal heat element to uniformly distribute heat throughout the tank. Another potential solution could be implementing a stirring system to distribute the heat in the powder salt evenly.

We have also noted that the powder form of $MgCl_2$ has a fluffy consistency and small particle size, making it highly susceptible to being blown up. During the purification phase, the tank cover gas is maintained at approximately 2 to 3 inches. The purging flow, which carries the salt powder, predominantly $MgCl_2$, away from the system, causes some of the salt powder to settle at the far end of the exhaust line. To avoid this issue in the future, we suggest using a taller tank or implementing vacuum heating before melting.

The purification process is a one-time operation, and subsequent operations were carried out using solidified salt. One issue we encountered with the solidified salt was its low thermal conductivity. Automated control methods using set point would likely result in overheating the tank. In future designs, this issue should be taken into account, especially when dealing with large batches of molten salt.

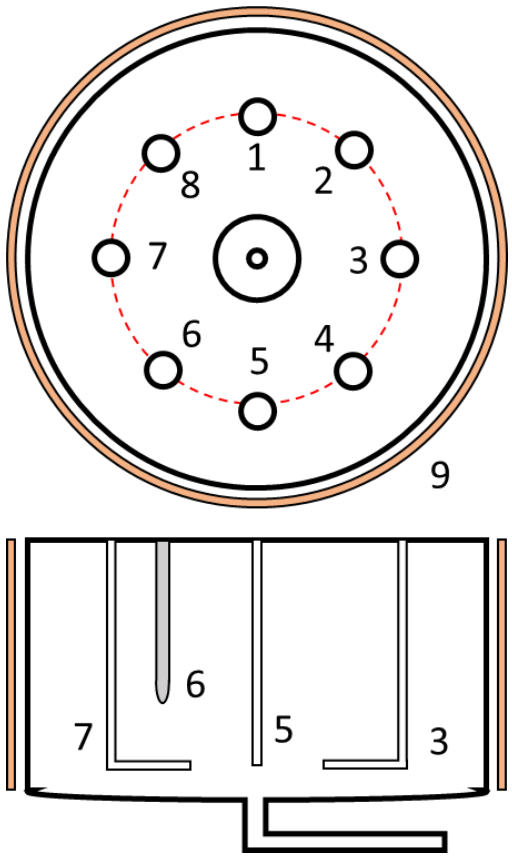

Figure IV-17 Illustration of the purification tank. 1. Drain hole. 2. Pressure transducer port. 3, 5, &7. Purging ports. 4. Exhaust line. 6. Thermal couple port with thermowell. 8. Cover gas line and evacuation line. 9. Heaters.

IV.3.3. Salt transportation

Figure IV-18 illustrates the equipment orientation utilized in the salt transportation process, which involves transferring pre-melted salt from the auxiliary tank to the upper storage tank, with a height difference of approximately 3.5 ft (1.12 m) between the two tanks. The temperature of the salt in the auxiliary tank is maintained at 600 ^{o}C during transportation. To accomplish this, two primary

steps are followed. First, the loop and storage tank gas are exchanged from air to argon atmosphere through evacuation and refill. Second, the storage tank and supply line are heated to 550 ^{o}C, with particular attention given to the valve temperature. As discussed in the valve section, gaps in the valve can allow salt to penetrate and solidify, necessitating preheating of the valve to melt the salt. While a tape heater was used to heat the valve, the valve surface was not uniform, and contact between the heater and valve was less than ideal, requiring more powder input and longer heating time. Due to the difficulty of measuring the valve temperature accurately, a temperature sensor was only installed near the end of the pipe, resulting in a temperature reading at the valve that is much higher than the salt melting point, typically around 600-650 ^{o}C. It should be noted that this valve can be reused multiple times with minimal leaks, as it is only briefly exposed to flowing salt during transportation and is kept closed during salt circulation, with a temperature lower than the main loop at approximately 450-550 ^{o}C. At this stage, the temperature of all equipment shown in Figure IV-23 is over 500 ^{o}C. Despite our efforts to cover all pipes as thoroughly as possible, temperature distribution is uneven in the absence of liquid in the pipe.

The method utilized to transport molten salt between two tanks is pressure-driven, and the pressure required to achieve a certain height can be estimated using the hydraulic head equation, as shown in Equation IV-26.

$$H = pgh$$ **Equation IV-26**

The approximate pressure requirement for this process is 2.6 psi (18 kPa). The initial step involves setting the pressure in the auxiliary tank to 3 psi. Note that when pressurizing the auxiliary tank, the gas line must be the purging line, rather than the cover gas line, to prevent the pressure from forcing the salt back to low-pressure lines, such as the purging line, where it can solidify and potentially damage equipment not designed to handle high temperatures. Alternatively, future designs could have the purging line exit the liquid prior to pressurization.

Next, the storage tank exhaust valve is opened to release the pressure, followed by the ball valve. The pressure difference results in the molten salt being pressed from the auxiliary tank to the storage tank. The flow is adjusted to 15 SCFH while monitoring the pressure in the storage tank to maintain it at 0 psi. The process becomes complicated when the flow rate increases rapidly, reaching the upper limit of the flowmeter. In this situation, the exhaust valve is closed, followed by the ball valve, and the storage tank covering gas valve is opened to maintain the pressure at 1.5-2 psi. Finally, the auxiliary tank is cooled down, and the transportation process is completed.

Figure IV-19 and Figure IV-20 illustrate the images of the auxiliary tank subsequent to the transportation of salt into the storage tank. The salt transfer process was highly effective, as evidenced by the presence of black crystals, which indicate MgO deposition, and minimal salt residue. Furthermore, solidified salt was observed at the salt loading port, likely resulting from the condensation of vapor due to the lower temperature at the port compared to the melting point of salt.

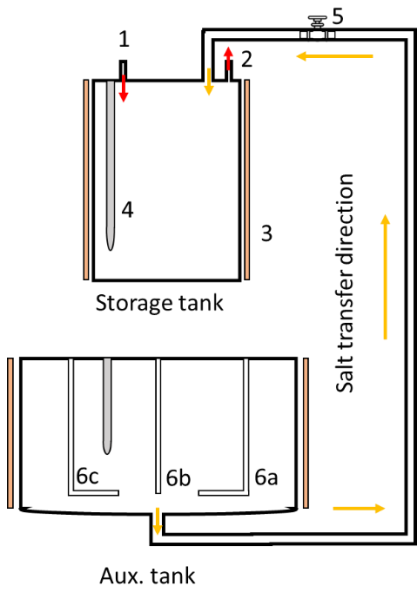

Figure IV-18 Illustration of the salt transportation process. 1.Cover gas inlet. 2. Gas exhaust. 3. Heater. 4 Thermowell. 5. Ball valve. 6. Purging line.

Figure IV-19 Auxiliary tank after first batch of salt transportation.

Figure IV-20 Solidified salt vapor at the auxiliary tank salt loading port.

IV.3.4. Salt circulation

This step may appear to be the most straightforward, but in reality, it is the most challenging one compared to others. The first step involves heating the storage tank to the target temperature of 650 ^{o}C, and the pipes are heated to 550 ^{o}C. During the pipe heating process, it was observed that the temperature distribution was highly non-uniform. Areas without heaters experienced a rapid decrease in temperature, with the lowest temperature on the loop occurring at the flow meter section, which ranged from 300 ^{o}C to 350 ^{o}C due to approximately one foot of the pipe that could not accommodate heaters. The second step requires the opening of ball valve #6 in Figure IV-21 and activating the pump with a frequency of 37.5 Hz. The temperature and flow rate on the loops

must be monitored closely. Once all the TCs show consistent readings, the start-up is considered a success.

Circulating molten salt at 650 ^{o}C through a 17-foot-long pipe is a challenging task, and as expected, leaks were encountered throughout the operation. The first issue that arose was related to the flange connections. Unfortunately, all three flange connections failed, highlighting the unsuitability of applying FRG combinations during the loop design. New materials for gaskets and compression, such as bolts, need to be tested and developed. To address the issue, the flanges were replaced with welded connections.

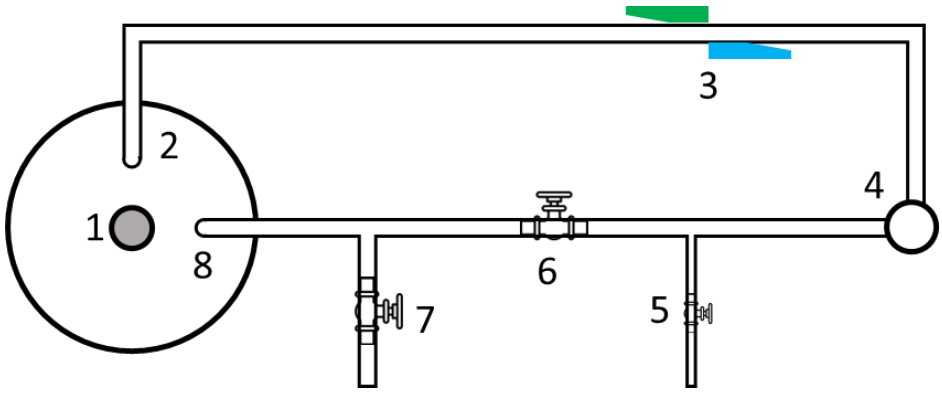

Figure IV-21 Illustration of the salt circulation process. 1. Pump. 2. Outlet. 3. Ultrasonic flow meter. 4. Sample insertion port. 5. Gas ball valve. 6. Loop ball valve, 7 Transportation ball valve. 8. Inlet.

The persistent issue of ball valve leaks has proven to be a significant challenge, requiring considerable effort before a solution was finally found during the final test. To mitigate the risks

associated with these leaks, we have adopted a strategy of disabling power to all valves and any surrounding equipment. Despite our best efforts to isolate the system, we have observed a loss in temperature over the 17-foot pipe, which necessitates the use of pipe heaters to circulate salt and maintain a consistent temperature of 650 ^{o}C in the storage tank. However, we have discovered that this requires a continuous power input of at least 70%, without the help of pipe heaters. Without the use of pipe heaters to increase the temperature of the test column to 650 ^{o}C, there is a high risk of damaging the storage tank heaters, as they will need to work harder to maintain the desired temperature. In theory, the more heat generated by the pipe heaters, the less strain on the storage tank heaters. However, the persistent issue of valve leaks has led to damage to the heaters in the past. The potential danger of this problem was underscored by a severe accident caused by a short circuit, which led to the electrolysis of chloride salt. This event will be discussed further in subsequent sections. To minimize the risk of further accidents, we have chosen to only use the pipe heaters located before and at the test column to supplement the heating of the test column and maintain its temperature at 650 ^{o}C.

As previously noted, one of the potential hazards associated with operating a large-scale molten salt loop is the occurrence of chlorine electrolysis resulting from a heater short circuit. Our team has unfortunately experienced this failure on two separate occasions. Following several hours of loop operation, a noxious odor was detected, and subsequently, heat failure was observed. The odor was extremely potent and caused significant irritation. Our colleagues provided the following feedback:

"It smelled like an indoor chlorine pool but in a higher concentration. My throat and nostrils were irritated a bit in the few minutes I was in the lab Saturday afternoon with no mask. I was able to be in the lab for an hour or so with no issues after getting the respirator with filters for acid gas and organic vapor. My cough went away the next day. I don't think it had any lasting affects for me anyway."

"Firstly, I smelled like acid, probably the HCl is closer to the smell I got. My nostrils and my eyes felt burning after like 10 min exposure. The next day, instead of a burning feeling, the smell was more similar to NH_3 and it was harder to breathe even in a couple of minutes. I felt that my throat was not handling it well. I used a face mask, so when I was out of the lab, I didn't have any cough."

Fortuitously, both incidents occurred over the weekend when the building was unoccupied. Upon recognizing that the odor could not be mitigated, and that additional heaters and temperature controllers had failed, we promptly shut down the loop. We also observed the presence of a green coating on the equipment adjacent to the loop, likely indicating corrosion from chlorine gas.

IV.3.4.1.Accident #1:

The initial incident occurred approximately 40 hours into the molten salt loop's operation, at which point a strong and unpleasant odor became apparent. We attempted to mitigate the issue by shutting off all pipe heaters to halt electrolysis and increasing ventilation, but these measures proved ineffective. After 40 additional hours, the odor intensified, and we made the decision to shut down the loop. Upon disassembling the leak section, we observed a significant accumulation of yellow substance on the white insulation, likely a gas byproduct. Interestingly, a complete failure of one

welding joint was also detected, with the pipe separating into two sections and salt leaking out. Pictures are shown in Figure IV-22. Notably, the flow meter did not detect any flow rate change, demonstrating the potential benefits of using molten salt to address coolant loss incidents in boiling water reactors. The welding joint failure was attributed to both stress and electrolysis. Specifically, the stress was induced by the modification of the flange, resulting in imperfect alignment during the online portable welding process. After force electrochemical corrosion occurred, the weakest part ultimately broke. Importantly, the leak did not originate from the broken section. Rather, we observed an unexpected small leak at the outlet, which resulted in a short circuit of the heater and converted the loop into an electrolysis pool. Although the welding filler material was SS 316, which is the same as pipe material, the uniform structure and morphology made it susceptible to corrosion. When combined with stress, this led to joint failure. This accident let us know the endangerment of the heater short circuit.

IV.3.4.2. Accident #2:

The first incident served as a valuable lesson. While a leak is a potential hazard, it was not as dangerous as a short circuit between the heater and the loop. The team was aware that ball valve #6 was prone to leakage. To mitigate this risk, only three pipe heaters were activated between the ultrasonic flow meter and sample insertion port, and their condition was closely monitored. The system functioned smoothly and without any detectable odor for 90 hours until a broken and short-circuited heater caused a distinct odor to reappear. Upon investigation, one of the heaters was found to be the source of the issue. The salt that leaked from ball valve #6 spread and wet the

heaters along the pipe. Electrolysis occurred once the salt reached the heater at the sample insertion port end after 90 hours. The system was ultimately shut down at the 100-hour mark.

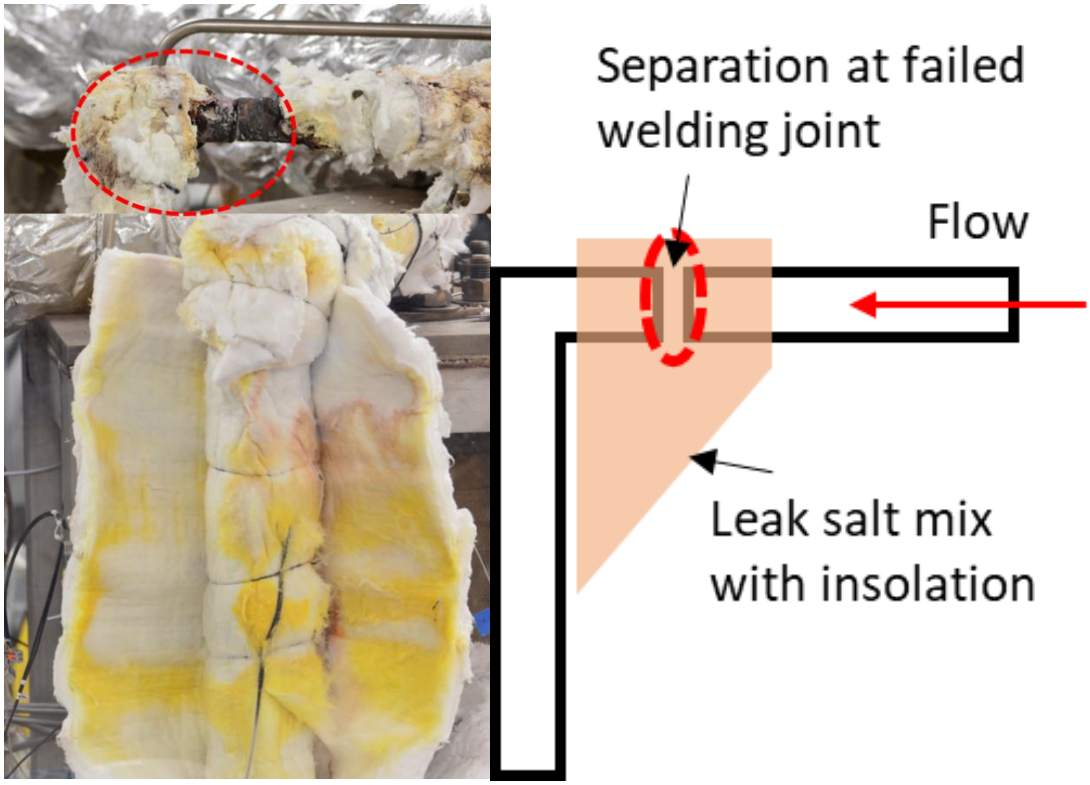

Figure IV-22 accident #1 Images of the chlorine electrolysis and electrochemical corrosion failure at one of the welding joints.

IV.3.4.3.Vapor issue

One observation made during the operation was the solidification of vapor at the gas inlet line and exhaust line. This was evident from Figure IV-20, which showed that the salt solidified at the top of the tank due to lower temperatures caused by inadequate insulation. Under normal operation, the exhaust line was closed, and the gas inlet line had a constant flow rate of 1.5 SCFH (0.7 L/min)

through a half-inch tube. The constant flow rate is because of the shaft leak. The observed incident was that while the inlet pressure remained unchanged, both the flow rate and tank pressure decreased, indicating a blockage in the inlet line. To address this issue, we used a torch to heat the inlet port and a hammer to knock the tube, allowing the solidified salt to fall and restoring normal flow and pressure in the tank. Subsequently, we closely monitored the pressure and inlet flow rate to maintain the proper functioning of the covering gas system.

IV.3.4.4.Temperature

Figure IV-23 depicts the temperature profile of the loop body and storage tank during the day of salt circulation. The process value (PV) and high limit (HL) value of the storage tank are illustrated in red and black lines, respectively. Prior to the circulation, the temperatures of the storage tank exhibit constant variation, which can be attributed to the delayed response between heating and PV-TC. Notably, the PV temperature lags behind the HL temperature by three minutes due to the limitations of TC readers in our system.

At point A, the salt transportation TCs were plugged into the thermocouple adapters, resulting in a temperature drop. At point B, the loop heaters commenced operation to heat up the pipes, revealing non-uniform temperature distribution in the empty pipe. Subsequently, at point C, the overall temperature of the pipe rose above 300 ^{o}C, and increasing the heating power did not effectively raise the temperature of the low temperature section. Therefore, we raised the salt temperature from 550 ^{o}C to 600 ^{o}C to prevent salt solidification in the low temperature section.

Since the loop heaters are controlled by a single heating zone, they are turned off during the period from C to D to prevent overheating. At point D, the pump was turned on with a power setting of 37.5 Hz, establishing a flow rate of 1.25 m/s. Notably, all the TCs merged with the salt temperature once the circulation was established. Subsequently, the salt in the storage tank gradually heated up to the target temperature of 650 ^{o}C. After point D, the working heaters were the storage tank heaters and three pipe heaters at the test column.

After point E, the system reached an equilibrium state characterized by constant flow rate, temperature, and heating power. It should be noted that, except for the storage PV-TC and test column TC, all other TCs are surface thermocouples. From the figure after point E, the temperatures settled into two groups, namely 650 ^{o}C and 600 ^{o}C. This discrepancy is attributed to the fact that the TCs were obtained from different brands and vendors after several modifications, and the distance to the storage tank also affects the temperature, with lower temperatures observed further away. If the test column heaters are turned off, the test column temperature will decrease to 630 ^{o}C. However, due to inadequate calibration of the TCs, the temperature change in the loop according to the location cannot be accurately determined.

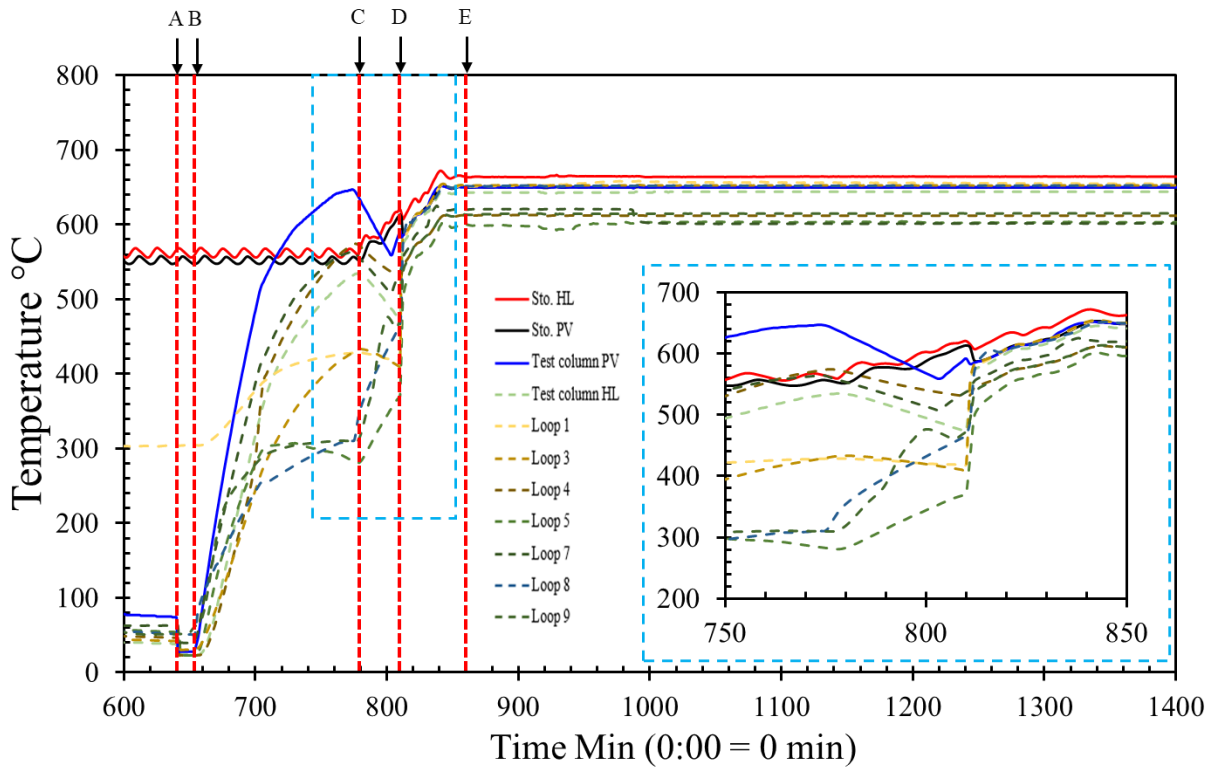

Figure IV-23 Temperature profile of the loop body and storage tank on the day of salt circulation. Red line: storage tank process temperature. Black line: storage tank high-limit temperature. Blue line: test column temperature. Other color dashed line: loop body temperature.

IV.3.5. Salt drainage

The process of salt drainage occurs after each salt circulation, or in case of incidents requiring the loop to be shut down. This is facilitated by the use of an auxiliary tank, which provides a reliable seal. The first step in the drainage process involves pushing the salt in the pipe back to the storage tank. To achieve this, the pump is shut down, the cover gas line is closed, and the exhaust line of the storage tank is opened, as shown in Figure IV-21. Next, ball valve #6 is quickly closed, and gas valve #5 is opened. This allows the pressure to push the salt in the opposite direction of

circulation, back to the storage tank. Once this is done, valve #5 and the storage tank vent line in Figure IV-21 are turned off, and the cover gas system is opened.

Subsequently, the drain line, drain valve #3, and auxiliary tank, as illustrated in Figure IV-24, are heated up. Valve #3 is turned on when the tank temperature reaches above 500°C. Before turning on valve #3, the auxiliary vent line is opened. This allows the salt to be driven by the pressure of the cover gas and gravity, draining from the storage tank to the auxiliary tank. After the salt has been drained, valve #3 and the auxiliary exhaust line are turned off. The final step in the process is to turn off all heater power, allowing the system to naturally cool to room temperature. It is important to note that the auxiliary tank gas system should be kept on avoiding the formation of negative pressure in the tank due to the shrinking gas volume as the temperature decreases. It is also worth mentioning that we have not encountered any incidents during the drainage process, apart from minor leakage in valve #3.

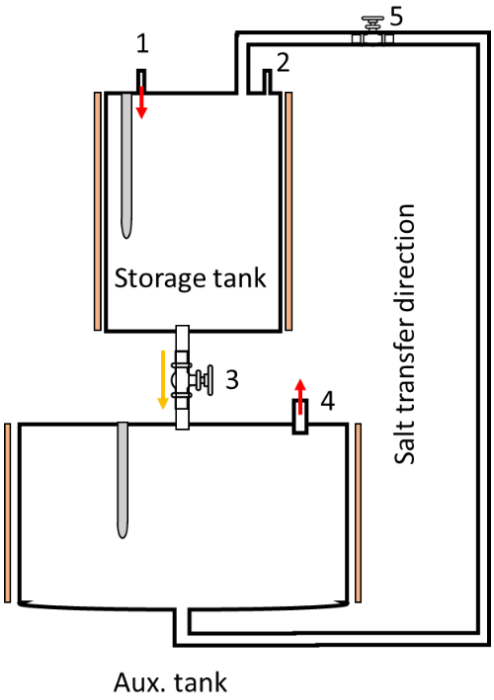

Figure IV-24 Illustration of the salt drainage process. 1. Storage tank covering gas line. 2. Storage tank exhaust line. 3 Drain line ball valve. 4. Auxiliary exhaust line.

IV.3.6. Sub-Conclusion

In conclusion, the construction and operation of a forced convection chloride molten salt corrosion test loop at the Nuclear Material and Fuel Cycle Center at Virginia Tech have significantly advanced our understanding of material compatibility in a molten chloride environment. Throughout this paper, we have addressed the design experience and challenges faced during the development of the test loop components, as well as the operational experiences gained from using the chloride salt loop. Through our operational experience, we have confirmed the advantages of using molten salt as a coolant, which effectively reduces the risk of coolant leaks. The self-sealing

properties of the molten salt slow down or even stop leaks at points of rupture. However, it is important to be cautious about the potential electrolysis of the chloride salt, as the current heating source for the test loop is electricity, which may generate hazardous gases. One of the most significant challenges identified during the operation of the molten salt loop for high-temperature applications is the implementation of effective seal techniques for the connections and valves. Given the demanding conditions, ensuring reliable and durable seals remains a crucial aspect that requires careful consideration and innovation.

The future work is the analysis of corrosion samples, which will contribute to a deeper understanding of the behavior of selected materials under flow-induced conditions. This knowledge will be invaluable for future research and development endeavors in the field. Overall, the construction and operation of the forced convection chloride molten salt corrosion test loop have provided significant insights into material compatibility in molten chloride environments, paving the way for further advancements in this area of study.

IV.4. Forced convection molten salt loop tests

IV.4.1. Corrosion behavior of SS316 in chloride FCL

This section provides a summary of the flow-induced corrosion (FIC) of SS316, which is a Fe-based alloy commonly used in high-temperature applications. The corrosion behavior and mechanisms of SS316 in molten salt have been a subject of interest for researchers. However, previous corrosion studies were primarily limited to capsule and static corrosion tests[171,172]. Despite molten salts' unfavorable thermodynamic conditions for corroding the major elements in

the alloys (such as chlorides or fluorides), corrosion is driven by oxidizing impurities. The BED/SEM inner and outer cross-section images of SS316 sample in FCL test is illustrated in Figure IV-25. In the case of our loop salt tests, the impurities (moisture and oxygen) were not monitored for each test and there were leakages because of valves or pipe broken, therefore, comparing different tests is not meaningful.

The images in Figure IV-26 on the left displays the result of outer cross-section EDS mapping for SS316 in test FCL-50. Notably, a very thin depletion layer of Cr was detected on the outer surface of the sample, accompanied by numerous cracks and intergranular attacks. This cracking phenomenon beneath the steel surface was unique to the FCL-50 test and can be attributed to repeated heating during the operational procedure's development. It is also worth mentioning that the loss of Cr and Fe occurred at the surface area along the cracks/grain boundaries and did not penetrate the bulk material. The presence of Mg residues along the cracks or grain boundaries indicates that the salt invaded the material through the cracks formed during heating. The deepest cracks measured over 70 μm after 50 hours of testing, while the Cr dissolution layer apart from the crack was only about 2-3 μm for MSL-50-SS316-1, and 4-5 μm, shown in Figure IV-27 (a1) and ((b1).

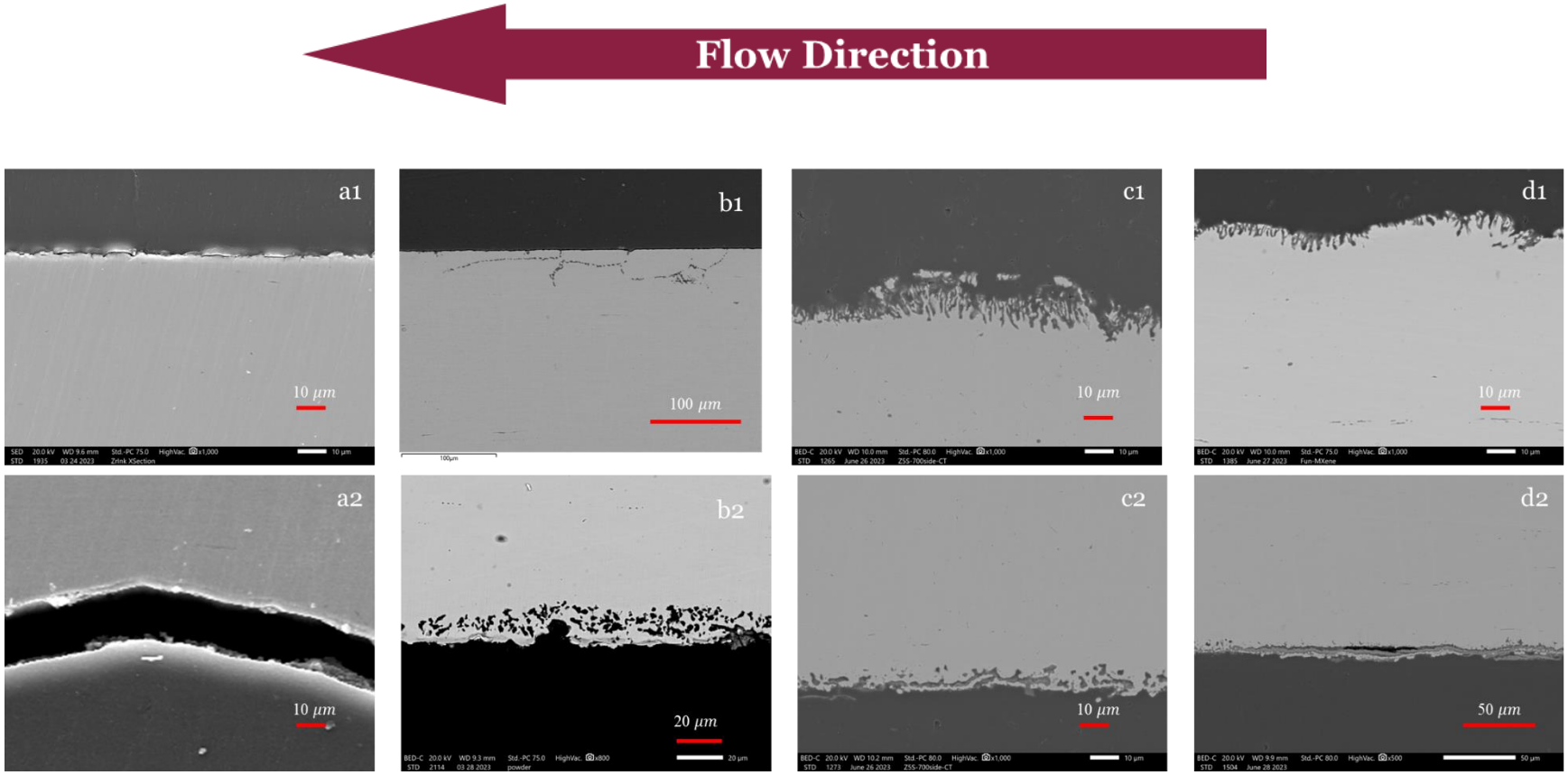
Flow Direction
a1
10 μm
b1
100 μm
c1
10 μm
d1
10 μm
a2
10 μm
b2
20 μm
c2
10 μm
d2
50 μm

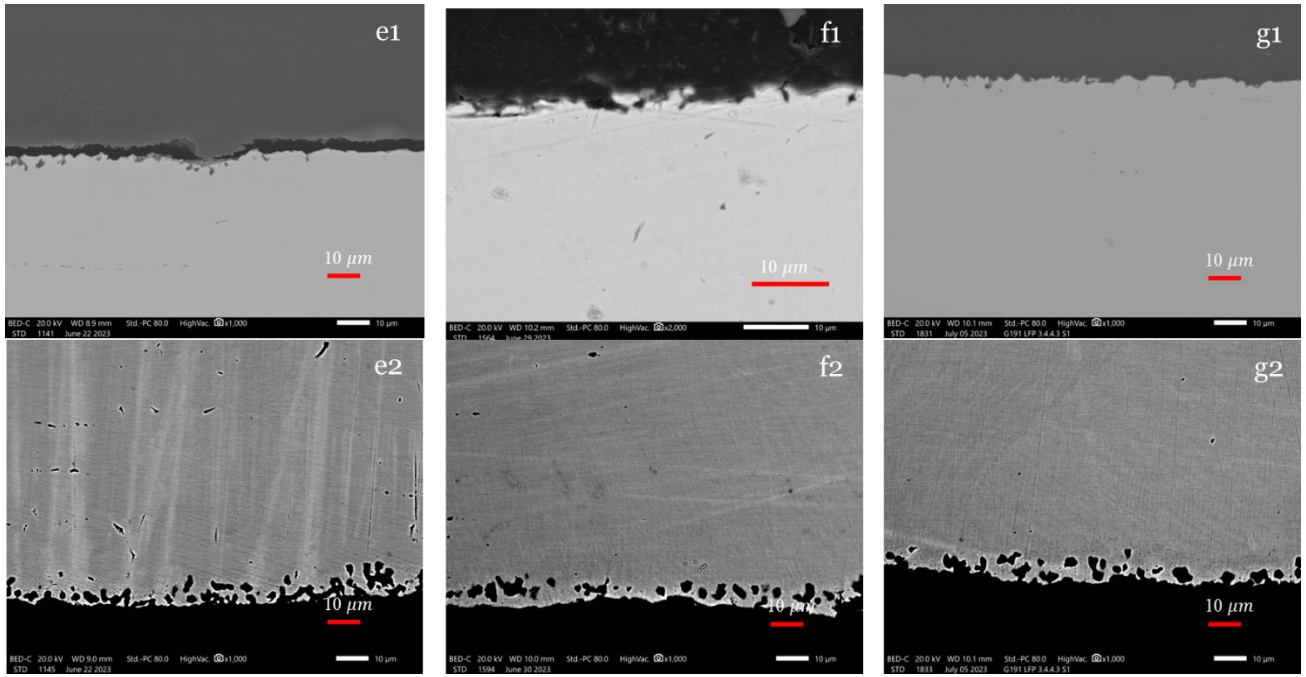

Figure IV-25 BED/SEM inner and outer cross-section images of SS316 sample in FCL test. (a) As received sample. (b) FCL-50-SS316. (c) FCL-80-SS316-S1. (d) FCL-80-SS316-S3. (e) FCL-100-SS316-S1. (f) FCL-100-SS316-S2. (g) FCL-100-SS316-S3.

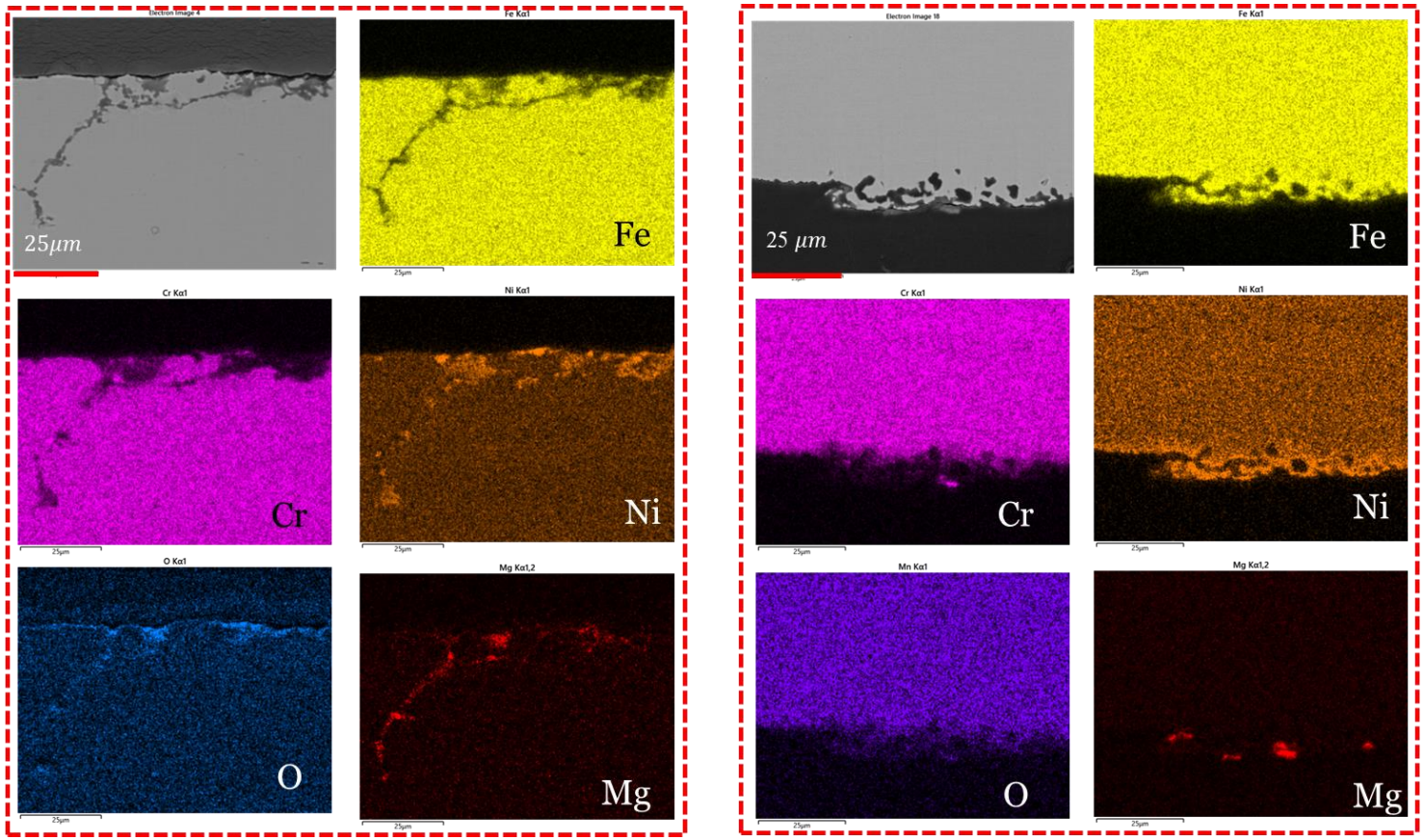

Figure IV-26 BSE/EDS cross-sectional true mapping of SS316 exposed in FCL-50 test. (left) Outer surface facing the flow. (right) Inner surface without flow.

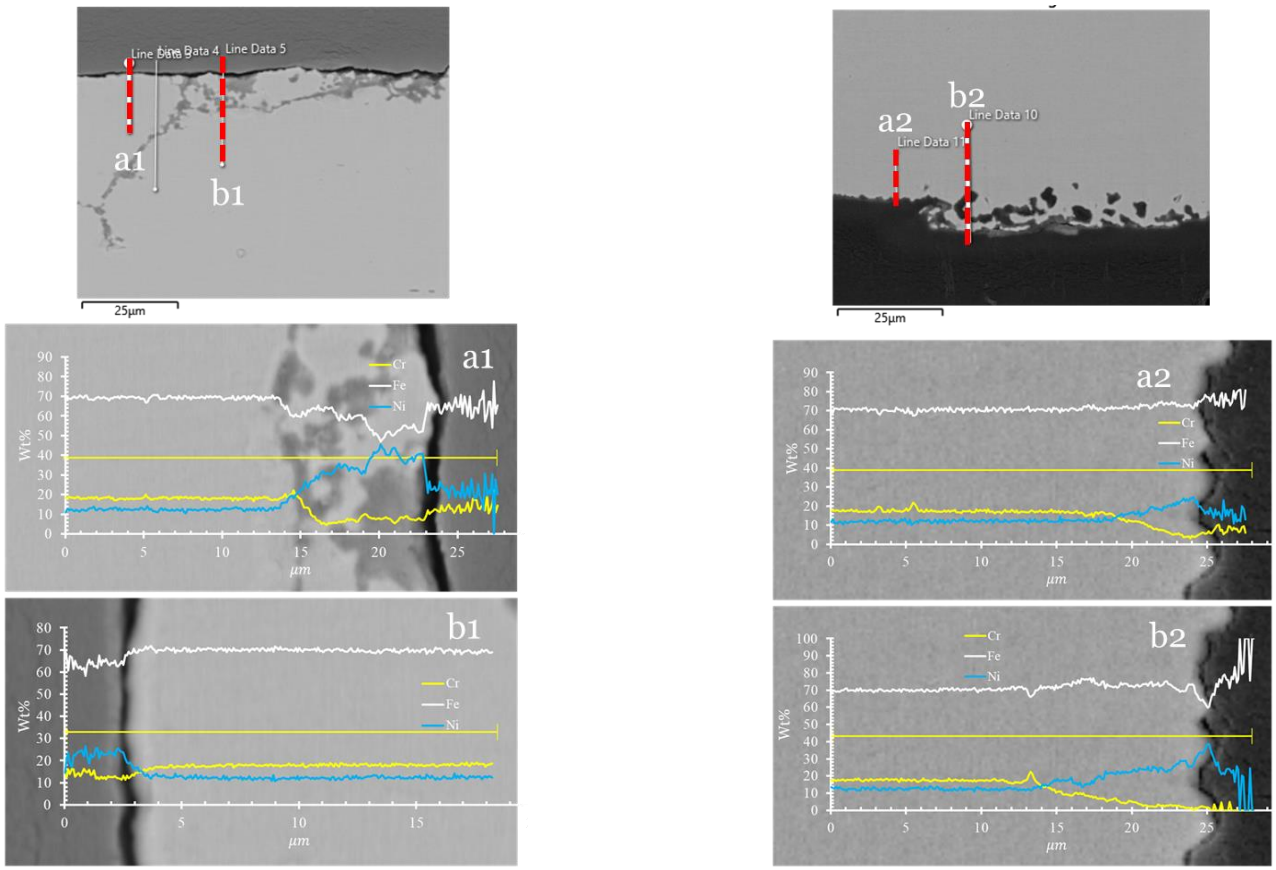

Figure IV-27 EDS line scan data of SS316 surface exposed in FCL-50 test. (a1) & (b1) Outer surface facing the flow. (a2) & (b2) Inner surface without flow.

We observed that the inner surface of the sample, where the flow was negligible, but also contacted with the salt, displaying static corrosion characteristics. Figure IV-25 (b2) illustrates the BSE-SEM images of the inner surface of MSL-50-SS316-S3. The original surface was reminding and vaccines or void forming under the surface due to Cr depletion. It is important to note that no cracks were observed in the cross-section of the inner surface. Because the inner surface experienced compression stress different from the outer surfer where underwent tension stress during heating. This finding further supports the notion that the attack on the outer surface is caused by the heating and cooling cycles. Based on the SED mapping and SED line scan results, Figure IV-26 (right) and Figure IV-46 (a2) and (b2), the inner corrosion layer primarily experienced significant Cr depletion, minor Fe depletion, and Ni enrichment. The corrosion layer thickness measured approximately 4-5 μm for MSL-50-SS316-S1 and 12-16 μm for MSL-50-SS316-S3.

Figure IV-28 (a) illustrates the outer cross-section EDS mapping results of SS316 in test FCL-80, which experienced an unexpected pipe break incident. The duration of the pipe break is unknown. It is evident that the corrosion in FCL-80 is much more severe compared to FCL-50, as a highly uneven surface with distinct dissolution layers of Cr and Fe is observed. The original surface is damaged, and the presence of cavities on the surface is attributed to particle removal by the flowing salt. An interesting observation in Figure VII-1 (b) is the separation of the corrosion layer or Cr depletion layer from the bulk material, with the right end connected to the bulk (possibly with other connections not visible). EDS mapping reveals that corrosion only occurred in the top layer

and abruptly ceased at the separation line, perhaps it was the grain boundary. Figure IV-28 (a) represent FCL-800-SS316-S3, demonstrating a uniformly corroded layer and clear evidence of material dissolution. All the cavities or voids are open to the surface. However, Ni enrichment is observed along the corrosion layer in the EDS mapping, indicating that the primary mechanism of flow-induced corrosion is the dissolution of Cr and Fe. The corrosion layer thickness for MSL-80-SS316-S1 and MSL-80-SS316-S3 is approximately 5-9 μm and 4-6 μm, respectively.

The inner cross-section characterization is presented in Figure IV-28 (b). Similar to the results of FCL-50 inner surface, a uniform static corrosion pattern is observed. However, there is evidence of Cr-enriched layers that consistently coexist with MgO residue, as shown in Figure IV-29. According to one study, the presence of MgO residue is attributed to the decomposition of $MgOH^+$ at high temperatures[173]. However, it could not explain the coexist phenomenon. EDS point analysis in the present study suggests that Cr is embedded into the MgO layer in its metallic form rather than as an ion. Contrary to our observations, Thorp et al.[174] reported that chromium tends to be present in MgO as Cr^{3+} in the form of $MgCr_2O_4$. Ding et al.[86] also observed the formation of $MgCr_2O_4$ on the alloy surfaces within the $MgCl_2$/KCl/NaCl (60/20/20 mol%) environment through XRD analysis. Given that the EDS point scans only provide elemental information, leaving out the precise composition details, it is strongly plausible that the observed coexisting Cr-Mg-O layer corresponds to $MgCr_2O_4$. It is important to note that the $MgCr_2O_4$ layer forms along the surface or beneath the Cr depletion layer. It can be observed that in some areas, the $MgCr_2O_4$ layer is continuous. The inner cross-section Cr depletion layer thickness for MSL-80-SS316-S1 and MSL-80-SS316-S3 is approximately 12-15 μm and 5-10 μm, respectively.

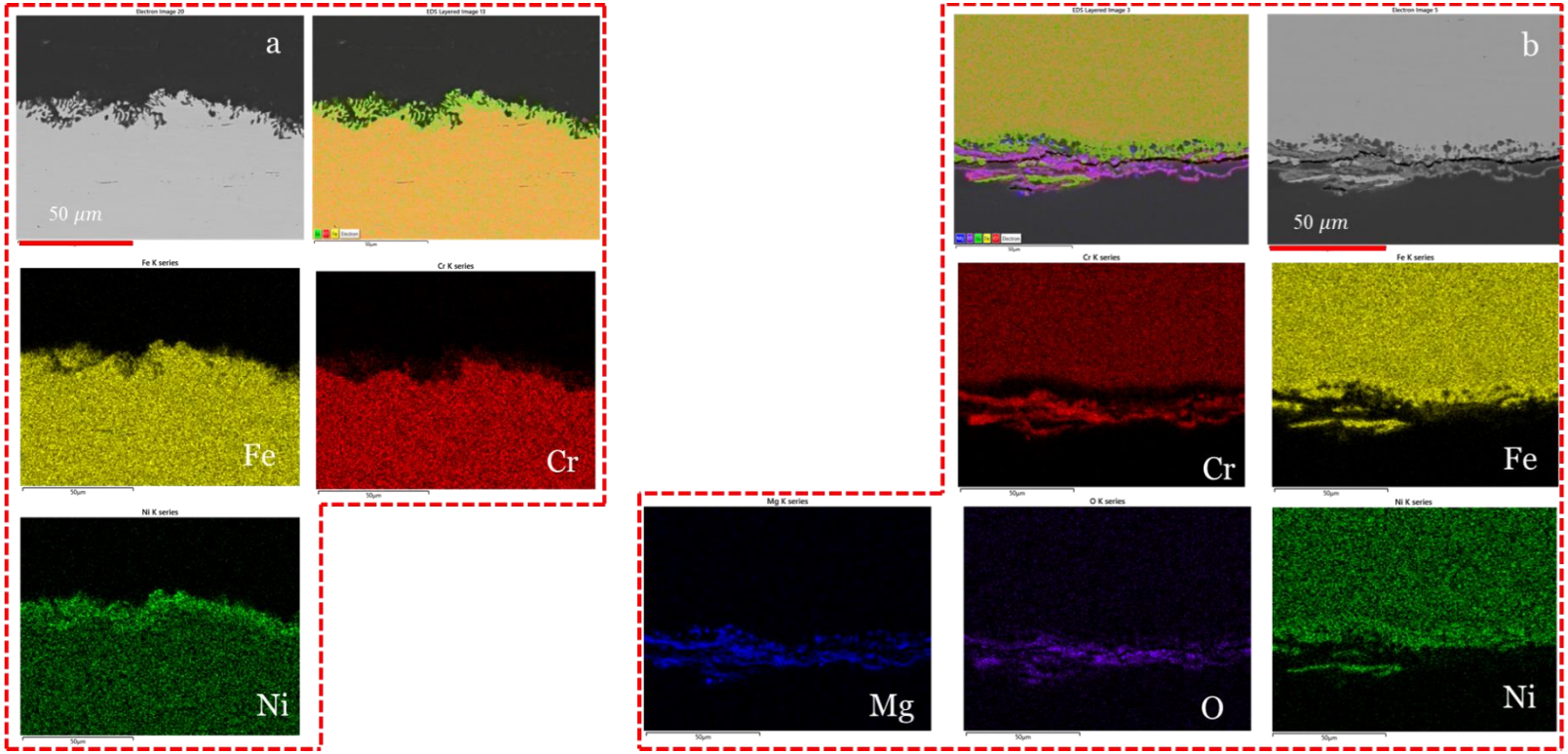

Figure IV-28 BSE/EDS cross-sectional true mapping of SS316 exposed in FCL-80 test. (a) Outer surface facing the flow. (b) Inner surface without flow.

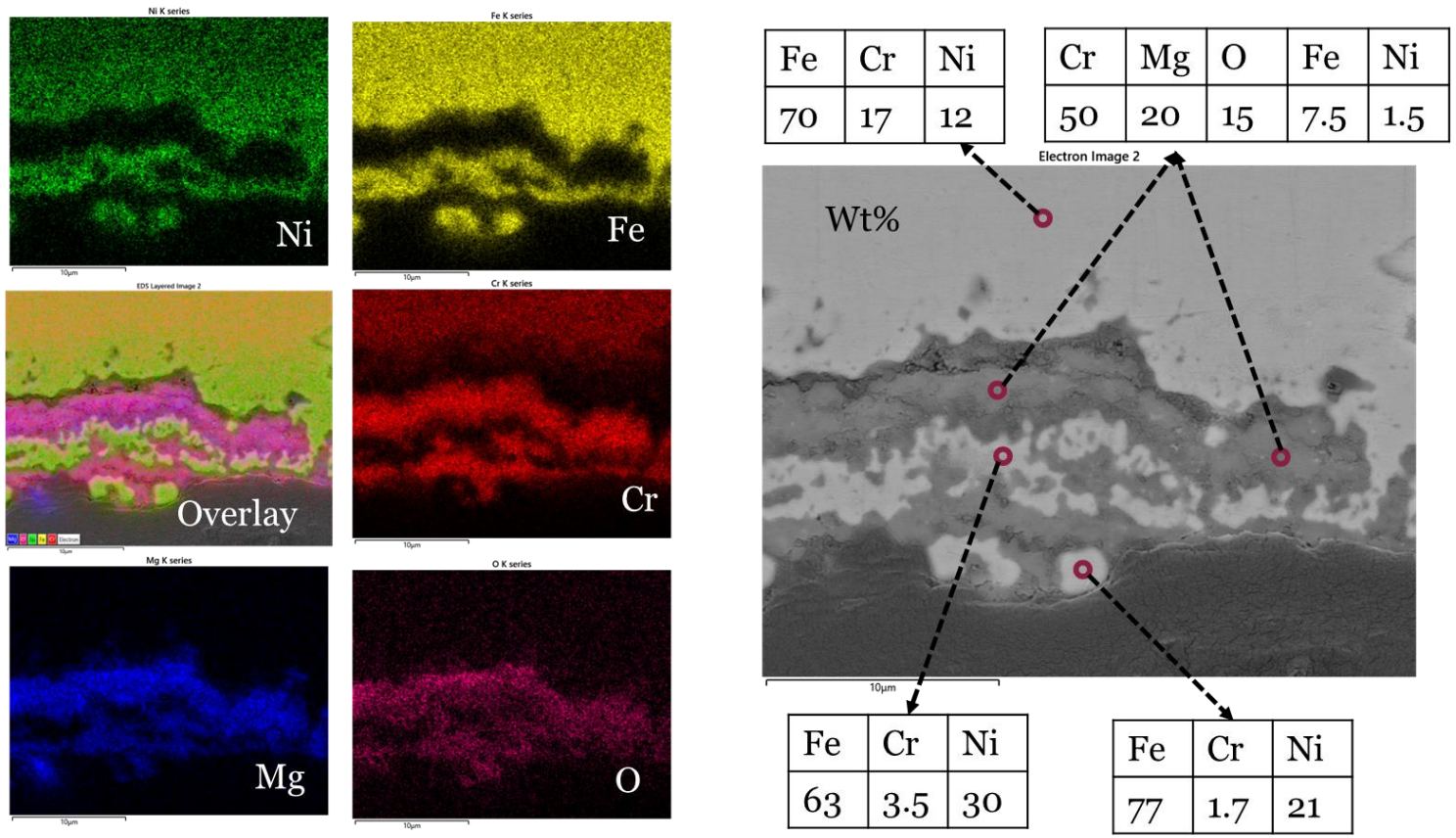

Figure IV-29 BSE/EDS mapping and point spectrum of the MgO-Cr coexisting layer on FCL-80-SS316 inner surface.

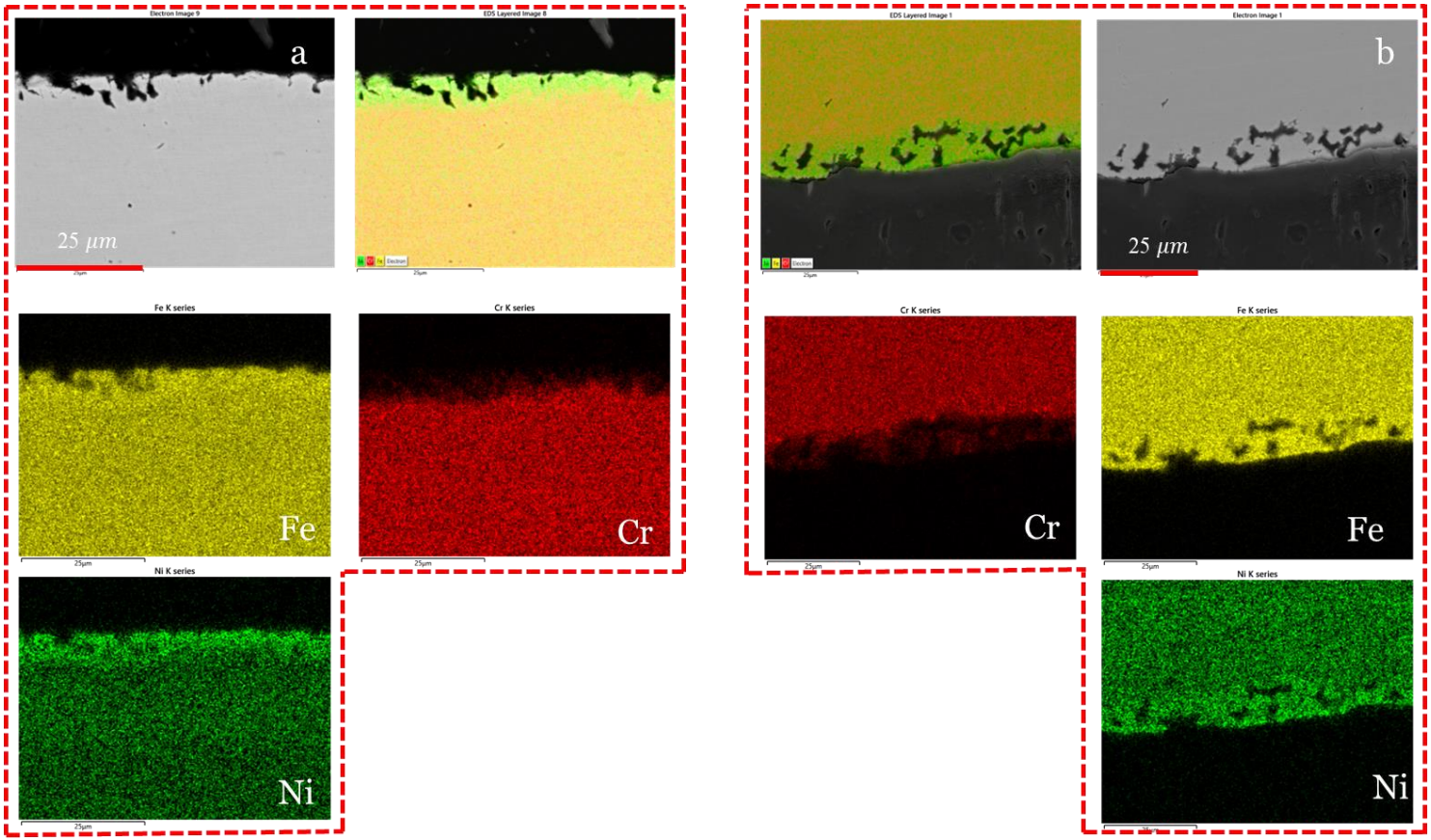

Figure IV-30 BSE/EDS cross-sectional true mapping of SS316 exposed in FCL-100 test. (a) Outer surface facing the flow. (b) Inner surface without flow.

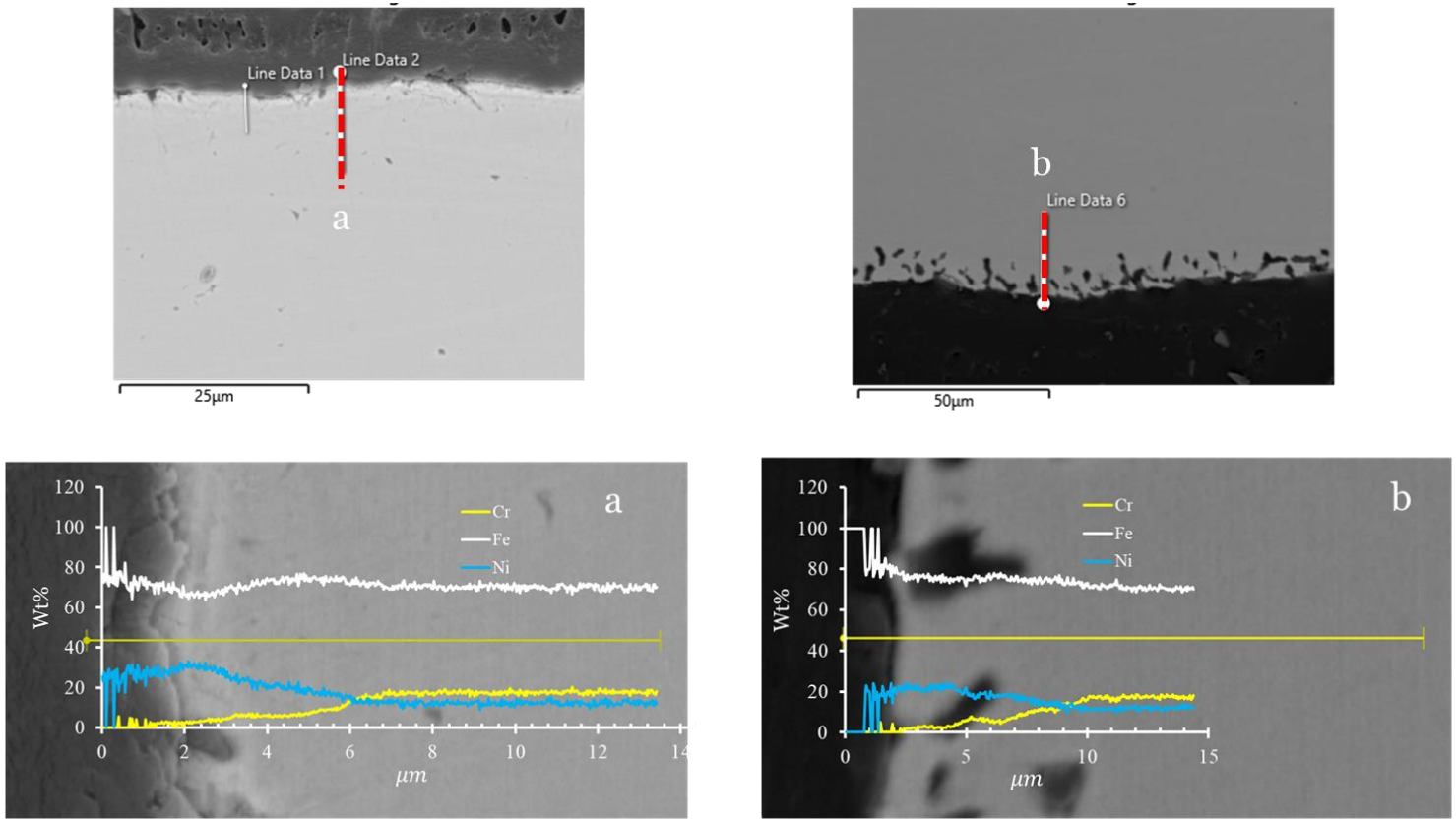

Figure IV-31 EDS line scan data of SS316 surface exposed in FCL-100 test. (a) Outer surface facing the flow. (b) Inner surface without flow.

Figure IV-30 (a) and Figure IV-31 (a) depict the outer cross-section EDS mapping and EDS line scan results of SS316 in test FCL-100. In the FCL-100 test, the experimental conditions were well controlled, and no significant accidents occurred except for a heater short circuit incident lasting less than 5 hours. The SEM results of the outer surface shows that the Cr depletion layer is measured approximately 4-8 μm. Although the overall surface appears intact, it is difficult to determine if it is the original surface. Conversely, the inner surfaces exhibited more severe corrosion, as demonstrated in Figure IV-30 (b) and Figure IV-31 (b). The inner corrosion thickness is ranging from 5-14 μm. One possible explanation for this phenomenon is surface removal by corrosion or/and erosion, and it is worth noting that the outer surface, specifically the Ni-enriched Fe-Ni layer, was evenly peeled off.

The Cr depletion layer thickness of SS316 in FCL tests are summarized in Table IV-6. Interestingly, despite the severe appearance of corrosion on the outer surface as observed in the SEM images, the Cr depletion layer is thinner than that of the inner surface. This finding strongly supports the occurrence of surface removal by flow-induced either erosion or corrosion.

Table IV-6. Cr depletion layer thickness of SS316 in FCL tests.

Unit μm	MSL-50-S1	MSL-50-S3	MSL-80-S1	MSL-80-S3	MSL-100-S1	MSL-100-S2	MSL-100-S3
Inner	4-5	12-16	12-15	5-10	7-14	8-12	5-13
Outer	2-3	4.5-5	5-9	4-6	4-7	5-6	5-8

IV.4.2. Corrosion behavior of A709 in chloride FCL

This section summarizes the results of A709 in FCL tests. Figure IV-32 displays BED/SEM images of the outer and inner cross-sections of A709 samples before and after the FIC tests. The inner surface exhibits similar corrosion phenomena as observed in the results for SS316, displaying a typical static corrosion layer. On the other hand, the FIC on the outer surface varies depending on the experimental conditions. We can also note that grain boundaries are formed across the entire cross-section. Overall, the corrosion of A709 is more severe compared to SS316 at the same testing conditions.

Figure IV-33 (a) illustrated the outer cross-section EDS mappings of test FCL-50. Despite the relatively short duration of the test, Intergranular grain boundary corrosion is observed. Cr depletion primarily occurs around the grain boundaries. It is worth noting that the corrosions occur along the grain boundaries and in the grains sandwich between the boundaries. More SEM results are shown in Figure VII-5, all the images indicate a discontinuous corrosion attack similar as FCL-50-SS316. In the examined region shown in Figure VII-5 (c), corrosion has not even occurred. In contrast to SS316, the outer surface of A709 exhibits a Cr-MgO layer, as depicted in Figure VII-5 (d). Combining the EDS mapping with line scan data, Figure IV-34 (a), the overall outer corrosion depths for FCL-50-A709-S1 and FCL-50-A709-S3 are approximately 2-5 μm and 3-10 μm, respectively. Figure IV-33 (b) and Figure IV-34 (b) present the EDS mapping and line scan results of the inner cross-section of test FCL-50-A709. At the inner surface, a uniform corrosion layer

with a thickness of 25-30 μm is observed. The presence of cavities and voids within the corrosion layer is attributed to Cr depletion. The EDS/SEM mapping reveals enrichment of both Fe and Ni in the corrosion layer. Additionally, residual MgO is detected within the Cr depletion layer.

Figure IV-35 provides clear evidence of the corrosion mechanism of A709. Obvious intergranular corrosion was observed on both outer and inner sample surface. Figure IV-36 illustrates the details of flow induced intergranular corrosion on A709. The EDS mapping reveals that Cr depletion initially occurs along the grain boundaries, followed by the depletion of Cr within the grains. As shown in Figure IV-32 (a3), the presence of chromium-rich grain boundaries in the pretest samples exacerbated the depletion of chromium along these grain boundaries. Interestingly, it is observed that the depletion of Cr in the grains is more prominent once the boundaries are dissolved. Subsequently, the Ni-Fe alloy becomes less stable, resulting in the consuming of Fe in the Fe-Ni corrosion layer. Near the surface, a thick-porous Fe-Ni layer without Cr, followed by a denser region with a significant depletion of Cr was observed, as illustrated in Figure IV-36. As demonstrated in Figure IV-33 (a) and Figure IV-35 (a), a discontinuous chromium oxide layer is observed on the outer surface. This is because in the molten salt the chromium oxidation layer is not stable and can easily dissolve in to the salt[171]. However, under the flow condition, it is challenging to determine whether the disappearance of the chromium oxide layer is due to dissolution first or being peeled off by the flow first then dissolution. The depth of the flow-induced corrosion layer for FCL-80-A709-S1 is in the range of 7-16 μm, while for FCL-80-A709-S3, it is in the range of 25-40 μm.

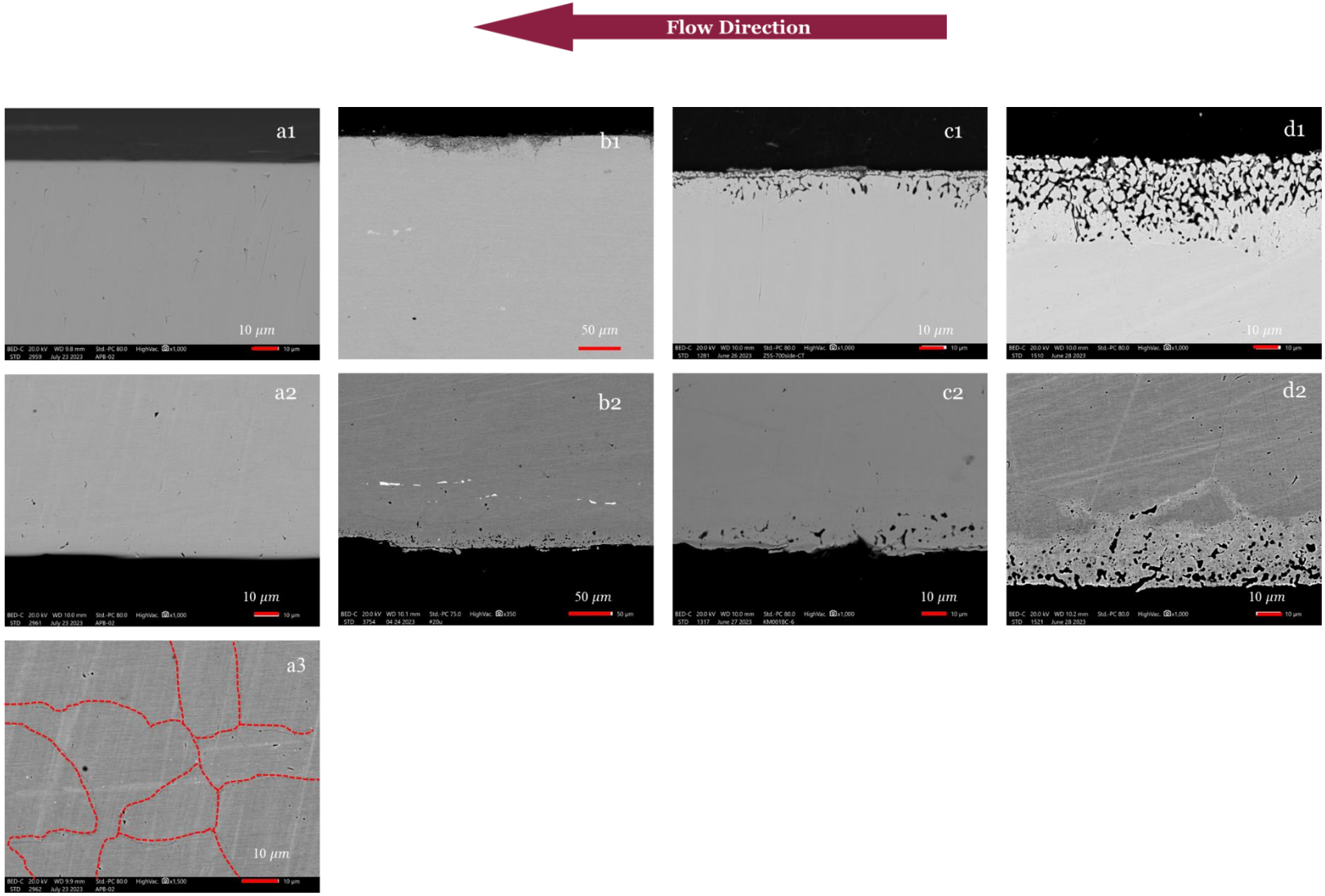
Flow Direction
a1
10 μm
b1
50 μm
c1
10 μm
d1
10 μm
a2
10 μm
b2
50 μm
c2
10 μm
d2
10 μm
a3
10 μm

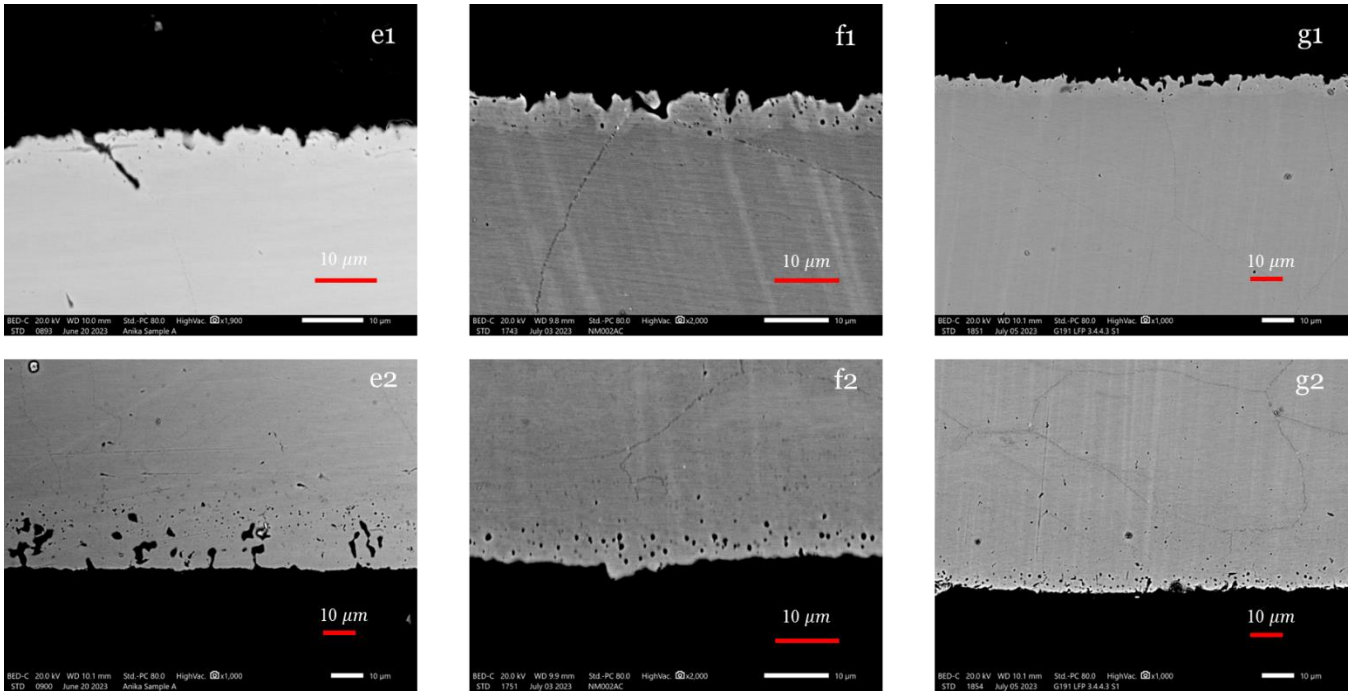

Figure IV-32 BED/SEM inner and outer cross-section images of A709 sample in FCL test. (a) As received sample. (b) FCL-50-A709. (c) FCL-80-A709-S1. (d) FCL-80-A709-S3. (e) FCL-100-A709-S1. (f) FCL-100-A709-S2. (g) FCL-100-A709-S3.

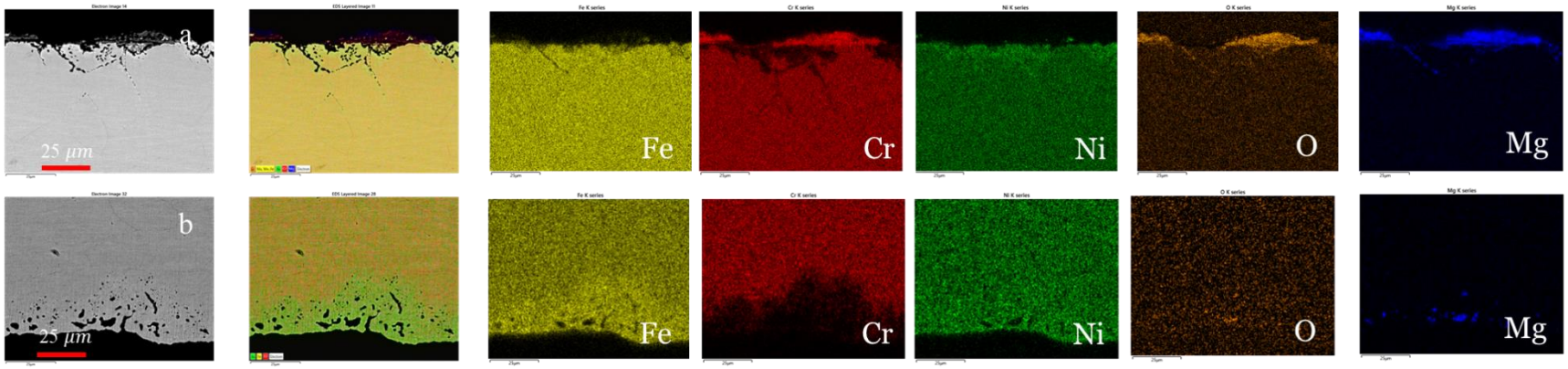

Figure IV-33 BSE/EDS cross-sectional true mapping of A709 exposed in FCL-50 test. (a) Outer surface facing the flow. (b) Inner surface without flow.

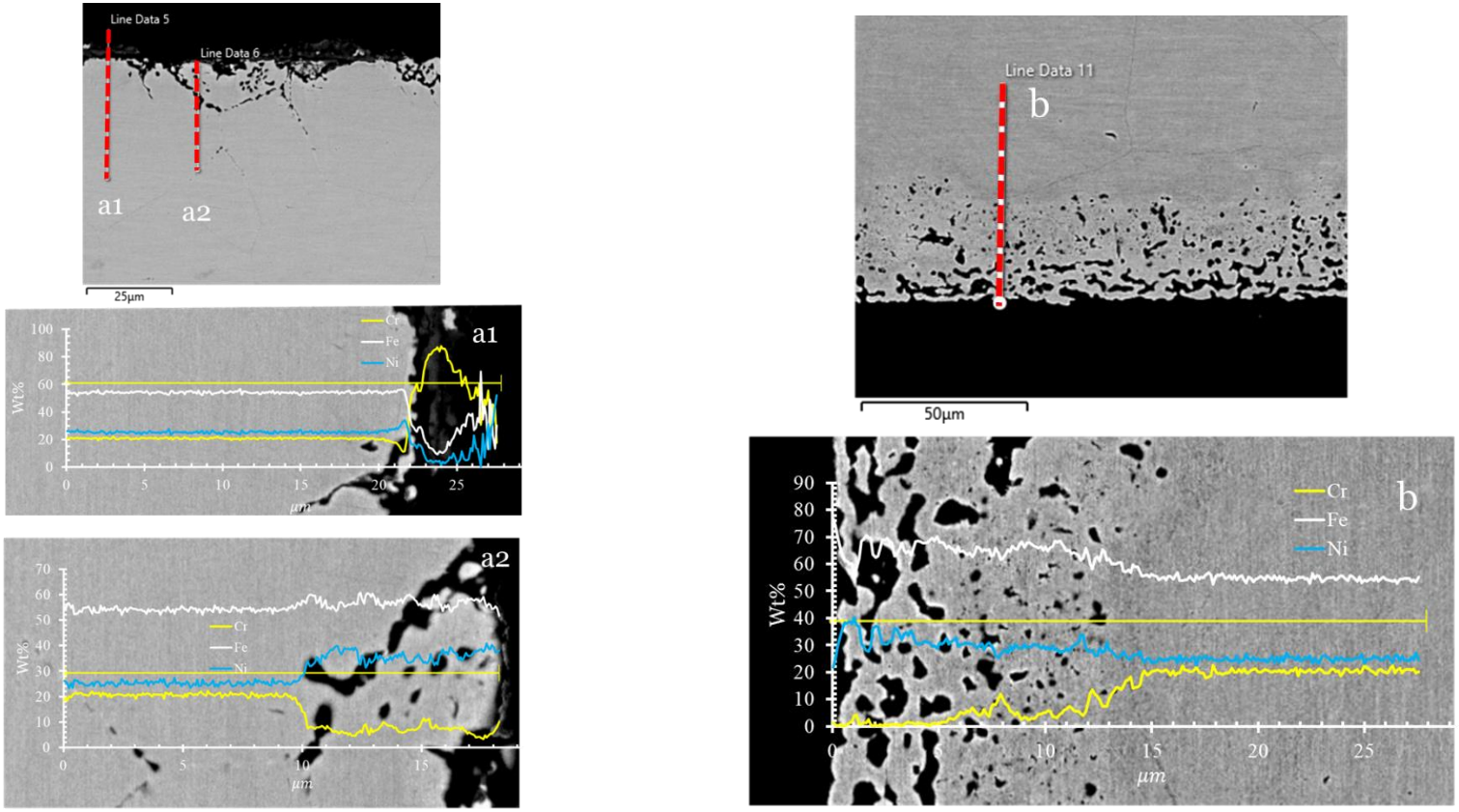

Figure IV-34 EDS line scan data of A709 surface exposed in FCL-50 test. (a1) & (a2) Outer surface facing the flow. (b) Inner surface without flow.

The SEM mapping depicted in Figure IV-35 (b) offers valuable insights into the contrast between FIC and static corrosion. The inner corrosion layer exhibits a notably more uniform distribution compared to the outer corrosion layer, and it appears denser as well. These observations suggest that the corrosion reaction at the inner surface is relatively subdued, enabling Cr diffusion to facilitate the reaction without excessive consumption of Fe. The corrosion depth of the inner surface for FCL-80-A709-S1 ranges from 15-20 μm, while for FCL-80-A709-S3, it ranges from 30-35 μm. It is noteworthy that the FCL-80-A709-S3 sample is the only one with an outer corrosion layer thicker than the inner layer.

Figure IV-37 illustrate the general corrosion characteristics of A709 under FIC and static corrosion during the FCL-100 test. In order to comprehend Figure IV-37 (a), it is necessary to combine the low magnification SEM images presented in Figure IV-32 (e1) to (g1). It is evident that the post-test outer surface differs from the original surface, displaying grooves and cavities along its texture. This is further supported by the intact nature of the inner surfaces where static corrosion occurs, as depicted in Figure IV-32 (e2) to (g2), suggesting their authenticity as the original surfaces.

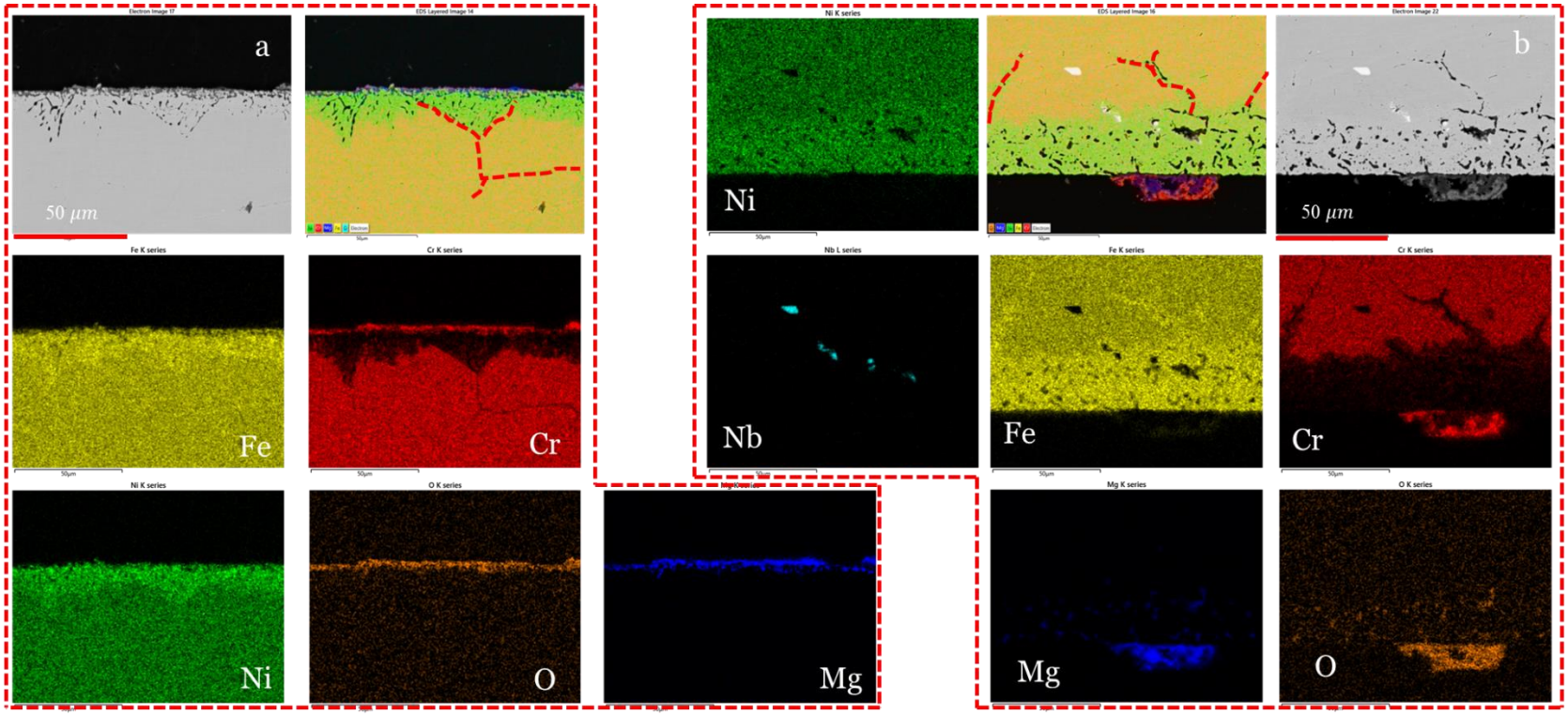

Figure IV-35 BSE/EDS cross-sectional true mapping of A709 exposed in FCL-80 test. (a) Outer surface facing the flow. (b) Inner surface without flow.

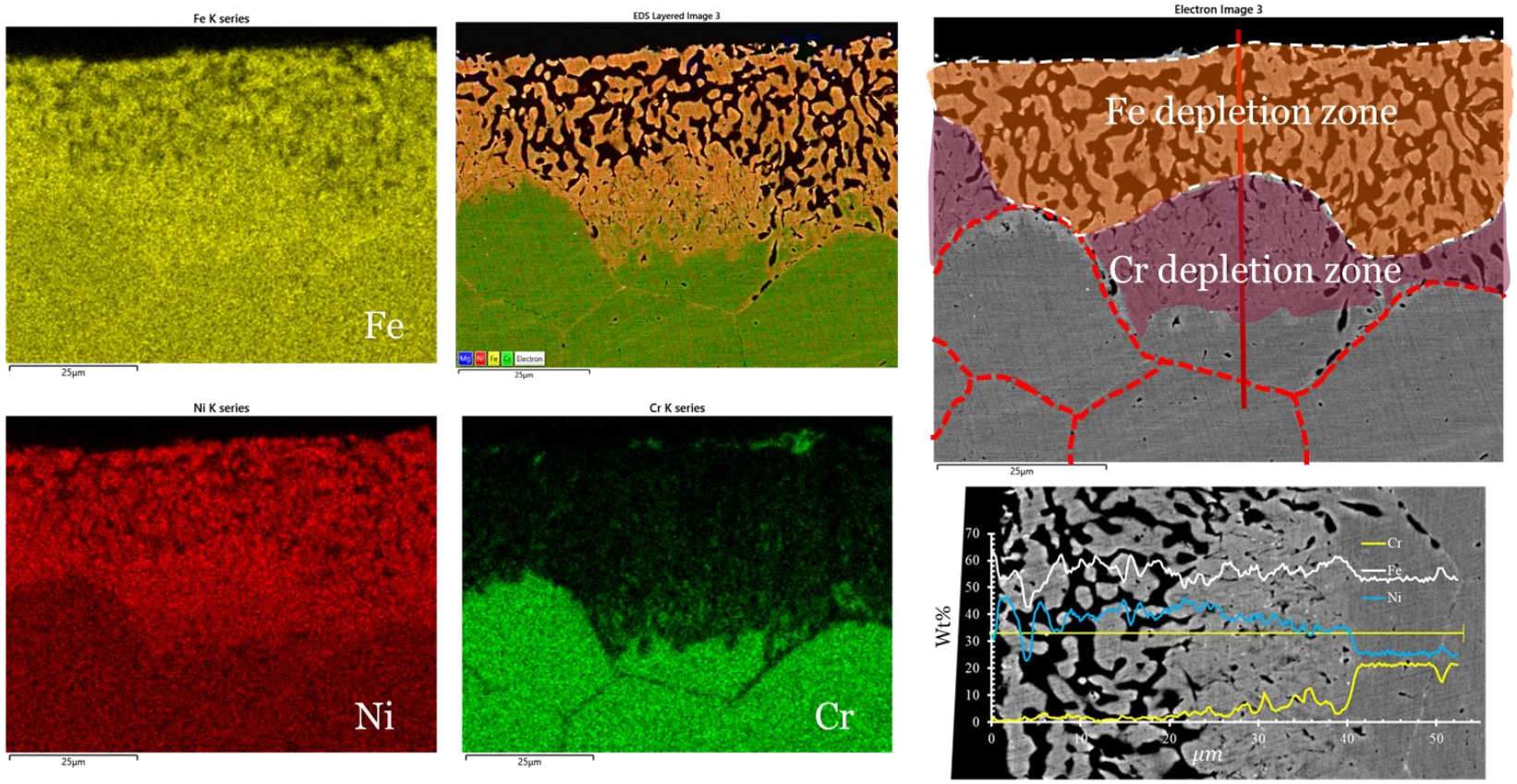

Figure IV-36 BSE/EDS mapping and line scan of the outer surface of sample FCL-80-A709-S3.

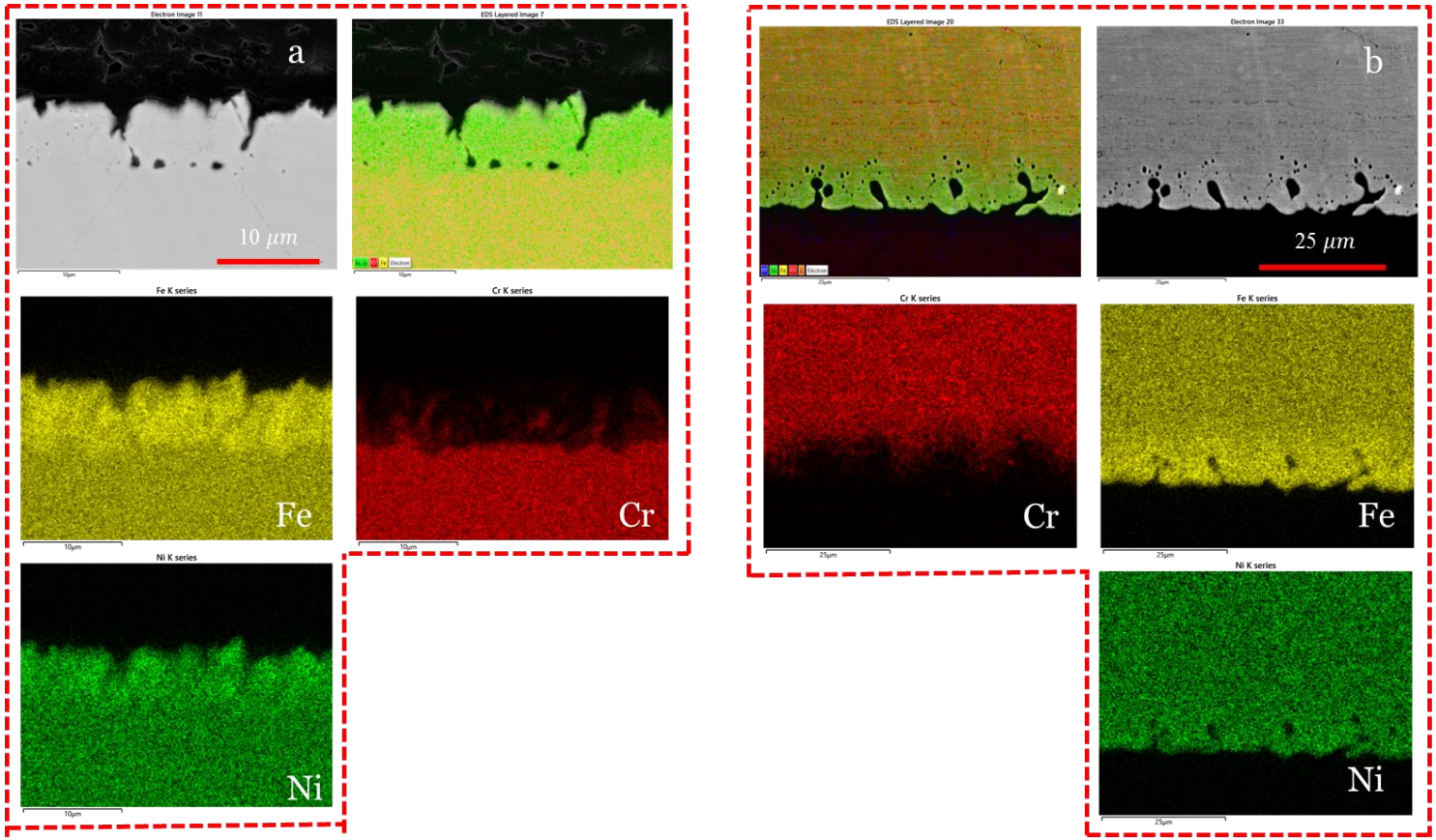

Figure IV-37 BSE/EDS cross-sectional true mapping of A709 exposed in FCL-100 test. (a) Outer surface facing the flow. (b) Inner surface without flow.

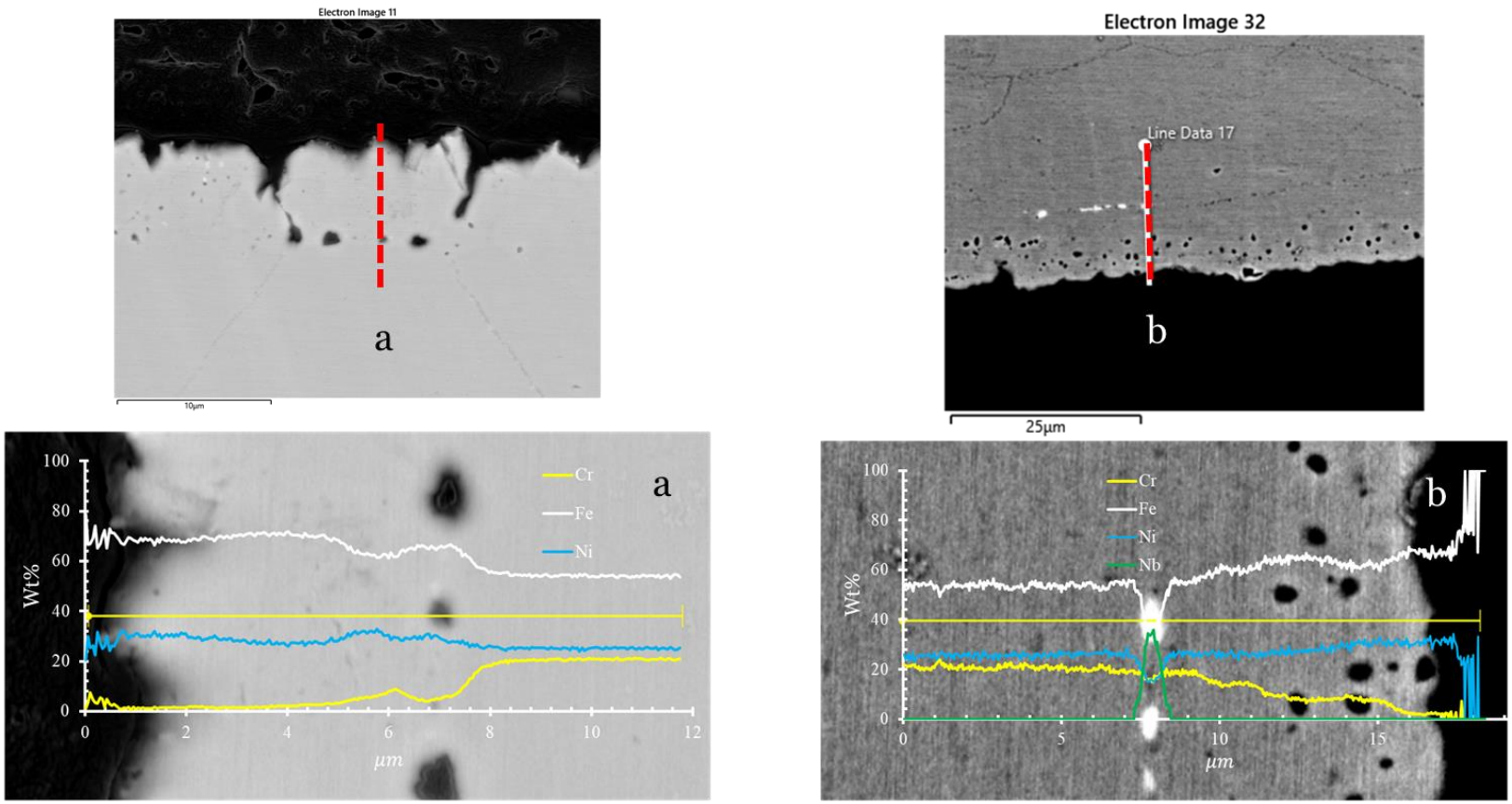

Figure IV-38 EDS line scan data of A709 surface exposed in FCL-100 test. (a) Outer surface facing the flow. (b) Inner surface without flow.

In Figure IV-37 (a), the outer surface geometry reveals clear signs of metal particle removal especially at the end of the grain boundaries. Additionally, the Cr depletion region exhibits a consistent thickness, measuring 10-15 μm for FCL-100-A709-S1, 5-6 μm for FCL-100-A709-S2, and 6-9 μm for FCL-100-A709-S3. To assess the corrosion level of A709 accurately, it is crucial to consider the corrosion occurring on the inner surface as shown in Figure IV-37 (b). Although there are no distinctive observations for the inner surface, they exhibit similar behaviors to FCL-50 and FCL-80. However, special attention must be given to the Cr depletion depth, which is approximately 2-3 times greater than that of the outer surface, as shown in Figure IV-38s. The depth of inner corrosion is measured as 25-30 μm for FCL-100-A709-S1, 20-30 μm for FCL-100-A709-S2, and 14-20 μm for FCL-100-A709-S3. The Cr depletion layer thickness of A709 at both inner and outer surface are summarized in Table IV-7.

Table IV-7 Cr depletion layer thickness of A709 in FCL tests.

Unit μm	MSL-50-S1	MSL-50-S3	MSL-80-S1	MSL-80-S3	MSL-100-S1	MSL-100-S2	MSL-100-S3
In	20-25	24-32	15-20	30-35	25-30	20-30	14-20
Out	2-5	3-10	7-16	25-40	10-15	5-6	6-9

IV.4.3. Flow induced corrosion of alloys in chloride molten salt

In section IV.4.1 and IV.4.2, we present an analysis of the general corrosion behavior of SS316 and A709. Additionally, we have made some intriguing observations regarding the FIC. The surface of the post-test sample of FCL-100 has been characterized using SEM. Figure IV-39 (a)

and Figure IV-40 display the post-test surface images of SS316. Specifically, Figure IV-40 (a) and (b) show the surface SED image, revealing the absence of certain surface particles and the formation of numerous basins with either sharp (a) or gradual (b) edges. The EDS point spectrum analysis of the lower and higher surfaces indicates similar surface compositions, with an average weight percentage of Fe (74%), Ni (22%), Cr (2%), and Mo (2%). Moving to image (c), it displays three distinct zones. The bright region corresponds to the metal region, characterized by very low oxygen levels, which could be attributed to the peeling off loose attached layer such as the oxidation layer during ultrasonic cleaning or potentially formed during the test, considering the surface composition. The high magnification SED image on the right clearly demonstrates surface had been removed. However, the gray and dark regions exhibit an increasing level of oxygen, indicating the formation of Cr_2O_3 in the gray region and Fe_2O_3 in the dark region. It is worth noting that neither Cr_2O_3 nor Fe_2O_3 are observed based on the characteristics of the cross-section, which indicates that the oxide layer is very thin, and they are probably forming in the air instead of in the salt.

Figure IV-39 (b) and (c) illustrate FCL-100-A709 surface SEM images at various magnifications, revealing that the surface geometry is more uniform compared to SS316, without significant areas of large peeled-off surfaces. However, the high magnification images (c) exhibit grooves on the surface, indicating the uniform removal of small particles. Furthermore, the BED images clearly display grain boundaries, which undergo Cr depletion across the entire surface. The average surface composition, determined through EDS point spectrum analysis in weight percentage, consists of Fe (60%), Ni (22%), Cr (3%), Mo (3%), and O (10%).

various FIC phenomena have been observed on the outer layer of the alloys. Figure IV-41 to Figure IV-43 present observations on SS316. In Figure IV-41, unique corrosion structures were identified, distinct from the uniform or impact corrosion layers observed in molten salt static tests. Instead, a severely damaged layer was observed. Figure IV-41(a1) indicates that FIC occurred beneath the surface due to the severe corrosion at the ravine, which is eroded faster by the flow. The different surface height in (a1) further confirms the occurrence of erosion.

In the case of (b1), where the opening is against the flow direction, the gap developed rapidly, leading to Cr depletion occurring on both sides of the gap. The server corrosion causes a loose connection between the small structure and the base alloy, as the structure exhibits porosity. Moving on to image (c1), a porous Ni-Fe strip is shown with one end attached to the alloy, while the opening faces the flow direction. It is noteworthy that the Cr depletion under the Ni-Fe strip is minimal, as the flow salt struggles to penetrate the thin gap in the opposite direction.

Figure IV-42 provides a comprehensive understanding of the corrosion layers and the stages of corrosion in the SS316 case. At a specific spot, three different surfaces were observed, each revealing distinct characteristics of the corrosion process. The lowest surface displayed the fully developed corrosion layer had just been removed, leading to the initiation of Cr depletion. This indicates the lightest Cr depletion at this stage. On the middle surface, the Cr depletion layer was developing, indicating that the outer surface had been removed for a considerable duration. The highest surface exhibited the fully developed corrosion layers, consisting of four major layers. The first layer comprised the outer Ni-Fe residual, which seemed detached from the bulk metal in the cross-section view. However, in a 3D dimension, it likely remained connected to the bulk. The

subsequent layer was the formation of MgO and Cr_2O_3 at the porous Ni-Fe layer. Notably, the MgO layer formed outside the Cr_2O_3 layer. This is attributed to the initial formation of Cr_2O_3, followed by its continuous dissolution in the molten salt. Subsequently, oxygen ions were captured by Mg ions, resulting in the formation of the MgO layer. The C to D region represented the Fe depletion area, where all the Cr had been consumed, further contributing to the corrosion process. Lastly, the outermost layer constituted the Cr depletion layer. It's important to mention that while the corrosion layers are described from the outermost to the innermost layer, the actual formation order follows the opposite direction.

Figure IV-43 presents observed evidence of particle removal on the FCL-100-SS316 sample. A distinctive bump, measuring approximately 20 μm in width and 15 μm in height, was identified. The bottom of the bump exhibits a curved corrosion line, indicating Cr depletion. The corresponding EDS mapping is depicted in Figure IV-47 (a). In addition to the bump, a groove with similar dimensions was observed on the same cross-section. The presence of both the bump and groove provide strong indications of erosion. The correlation between the curved corrosion line at the bottom of the bump and the erosion groove reinforces the hypothesis of erosion as the contributing factor to the partial removal observed in this sample.

Figure IV-44 presents compelling evidence of erosion corrosion on the A709 material. Long-discontinued Ni-Fe strips were observed at various locations, with a measured thickness of approximately 2-5 μm. Upon closer examination using zoomed BED images, a clear separation line was observed between the Ni-Fe strip and the Ni-Fe corrosion layer. Only several spots appeared to be connected under this cross-section view. This line is likely an initial grain boundary

where the material dissolves faster than the material within the grain. When the salt manages to penetrate this grain boundary, Fe dissolution and MgO formation occur, leading to an accumulation of MgO within the grain boundary. As Fe continues to be depleted, the strength of the connection reduces significantly, eventually causing the strip to peel off and roll away from its original location, as depicted in image (c). Notably, it is essential to recognize that besides the long-strip peeling off shown in Figure IV-44, small particles were also observed to peel off simultaneously. This additional evidence can be found in Figure VII-11. Figure IV-45 displays a cross-section of the A709 with rough surfaces. By combining the surface information from Figure IV-39(b) and (c), a robust proof of erosion corrosion is established, supporting the conclusions drawn from the observed evidence.

Based on the provided evidence, the FIC process appears to consist of three stages, as illustrated in Figure IV-46. The first stage resembles static corrosion, where Cr diffuses to the metal surface and reacts, forming either a discontinuous Cr_2O_3 layer (b) or directly dissolving into the molten salt (a). If a discontinued Cr_2O_3 layer is formed, it is unstable in the molten salt environment and can dissolve into the salt, resulting in the formation of Cr^{2+}. The dissolution reactions are represented by Equation IV-27 and Equation IV-28. In the flow-induced condition, the Cr_2O_3 layer is susceptible to peeling off due to the flow, and consequently undergoing the aforementioned dissolution reaction. Throughout this first stage, the Cr depletion layer continues to grow, while the rate of Cr diffusion decreases with the increasing thickness of the depletion layer.

$$Cr_2O_3 \rightarrow 2Cr^{3+} + 3O^{2-}$$ **Equation IV-27**

$$2Cr^{3+} + Cr_{in\ alloy} \rightleftharpoons 3Cr^{2+}$$ **Equation IV-28**

Under flow-induced conditions, the mass transfer of both corrosion products away from the surface and corrosive oxidants towards the surface is significantly increased compared to static conditions. As a result, the reaction rate on the metal surface remains consistently high. As the Cr depletion layer continues to grow and becomes sufficiently thick, the diffused Cr from the bulk to the surface becomes insufficient to react with the corrosive oxidants. This marks the beginning of the second stage, where Fe in the Cr depletion layer starts to be consumed in reaction with the oxidants. During the second stage, the anodic reaction shifts from being primarily driven by the depletion of Cr to the consumption of Fe.

The final stage is the erosion stage, which occurs when a sufficient amount of Fe is depleted, causing the Ni-Fe corrosion layer to become porous and reducing its overall strength. Consequently, the weakened corrosion layer becomes susceptible to peeling off under the influence of the flow. As the Ni-Fe layer becomes thinner due to erosion, the supply of Cr is compromised, leading to the formation of a new Cr depletion layer that extends deeper into the bulk material. This marks the initiation of a repeated corrosion cycle, akin to the first stage.

The continuous erosion and depletion of materials under flow-induced conditions perpetuate the degradation process, contributing to the thinner Cr depletion layer compared to the static scenario.

This phenomenon further highlights the significant impact of flow-induced factors on the corrosion behavior and mechanisms of the material.

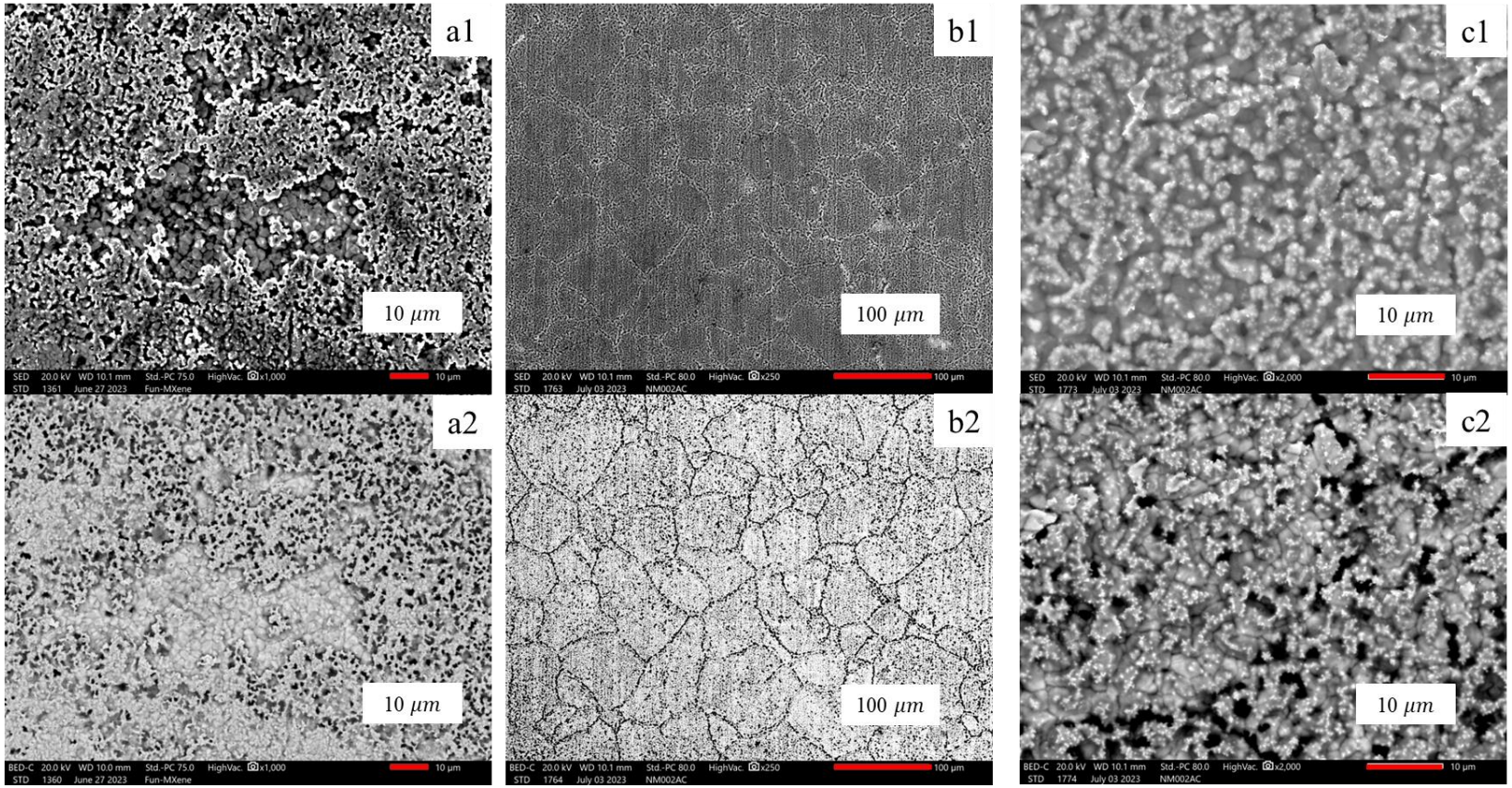

Figure IV-39 BED/SED SEM images of the post-test sample surface. (a1) FCL-100-SS316. (b1) and (c1) different magnifications of FCL-100-A709.

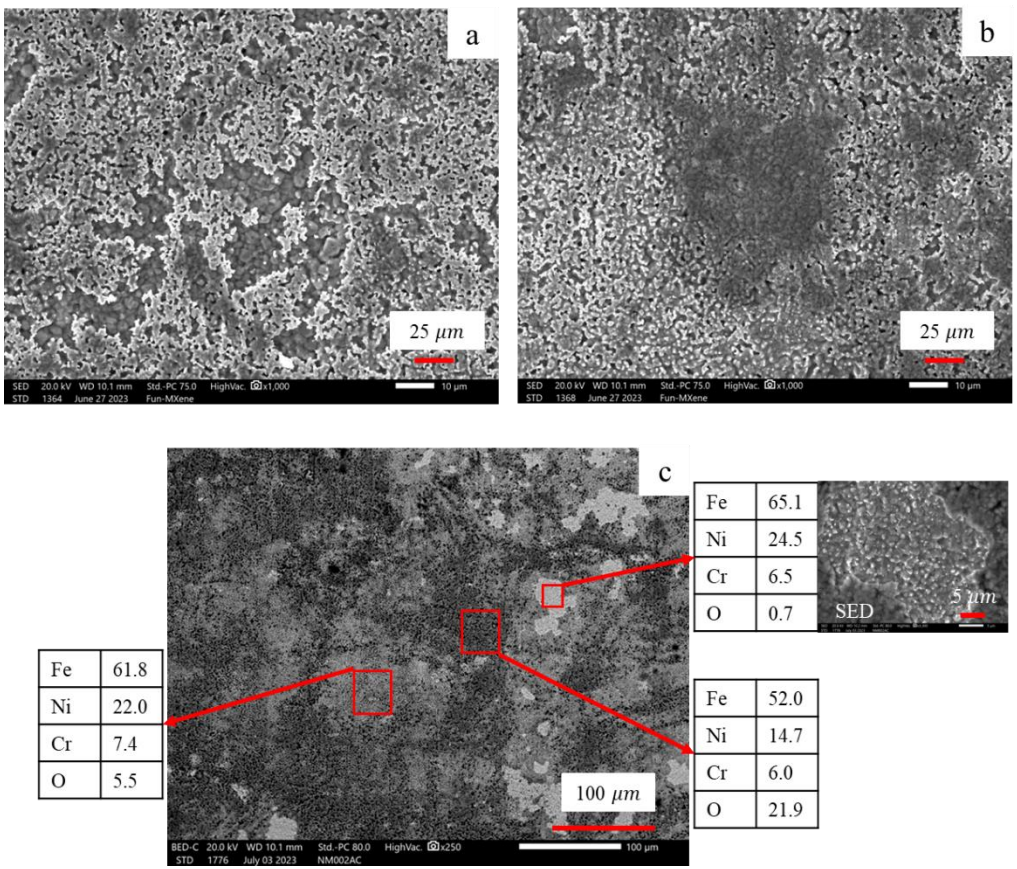

Figure IV-40 SEM images of the FCL-100-SS316 sample surface after testing. (a) and (b) depict SED images taken at different locations. (c) BED images reveal distinct regions with varying oxygen content.

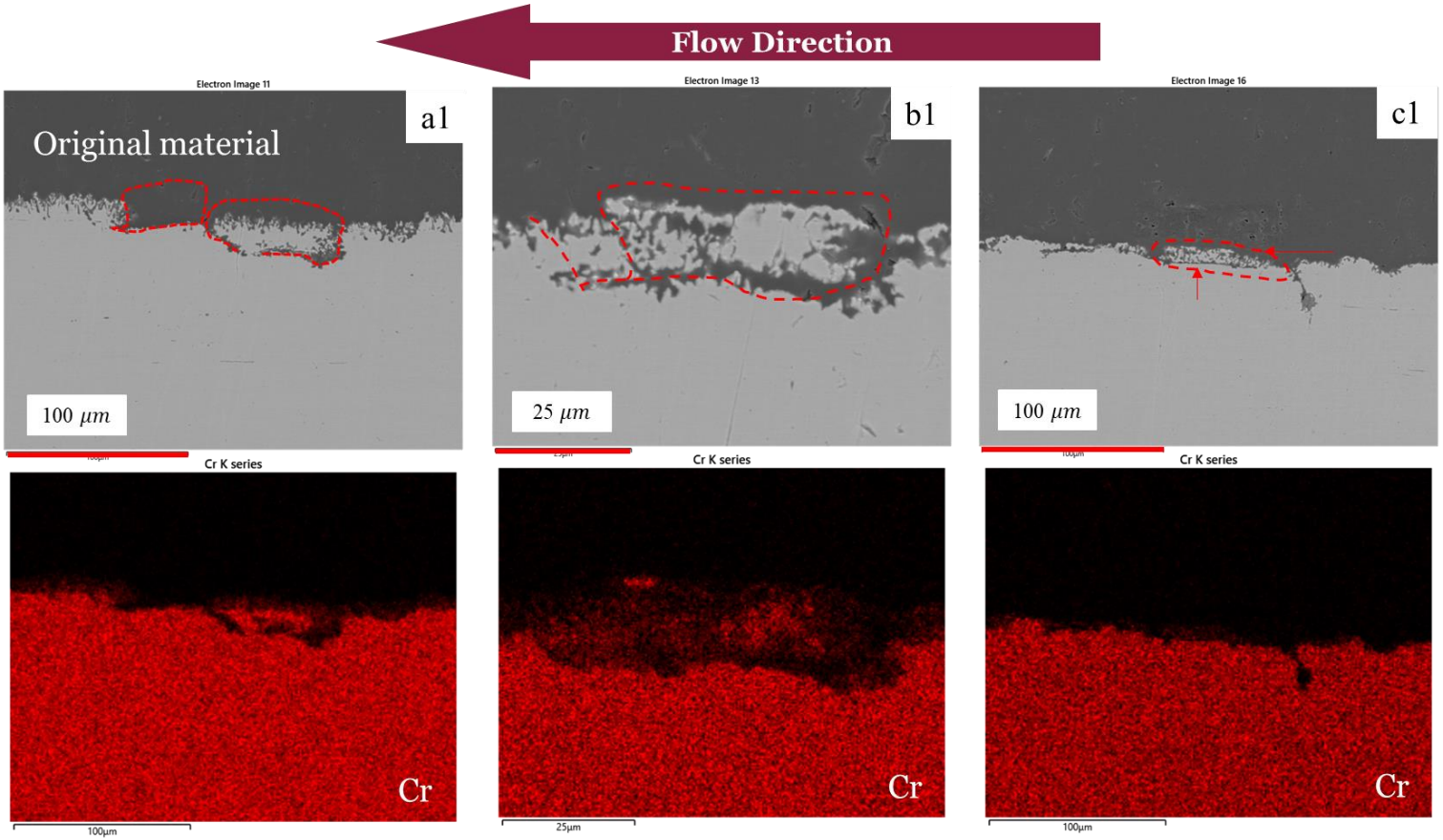

Figure IV-41 Observation of flow induced surface corrosion on FCL-80-SS316, BED images and EDS chromium mapping.

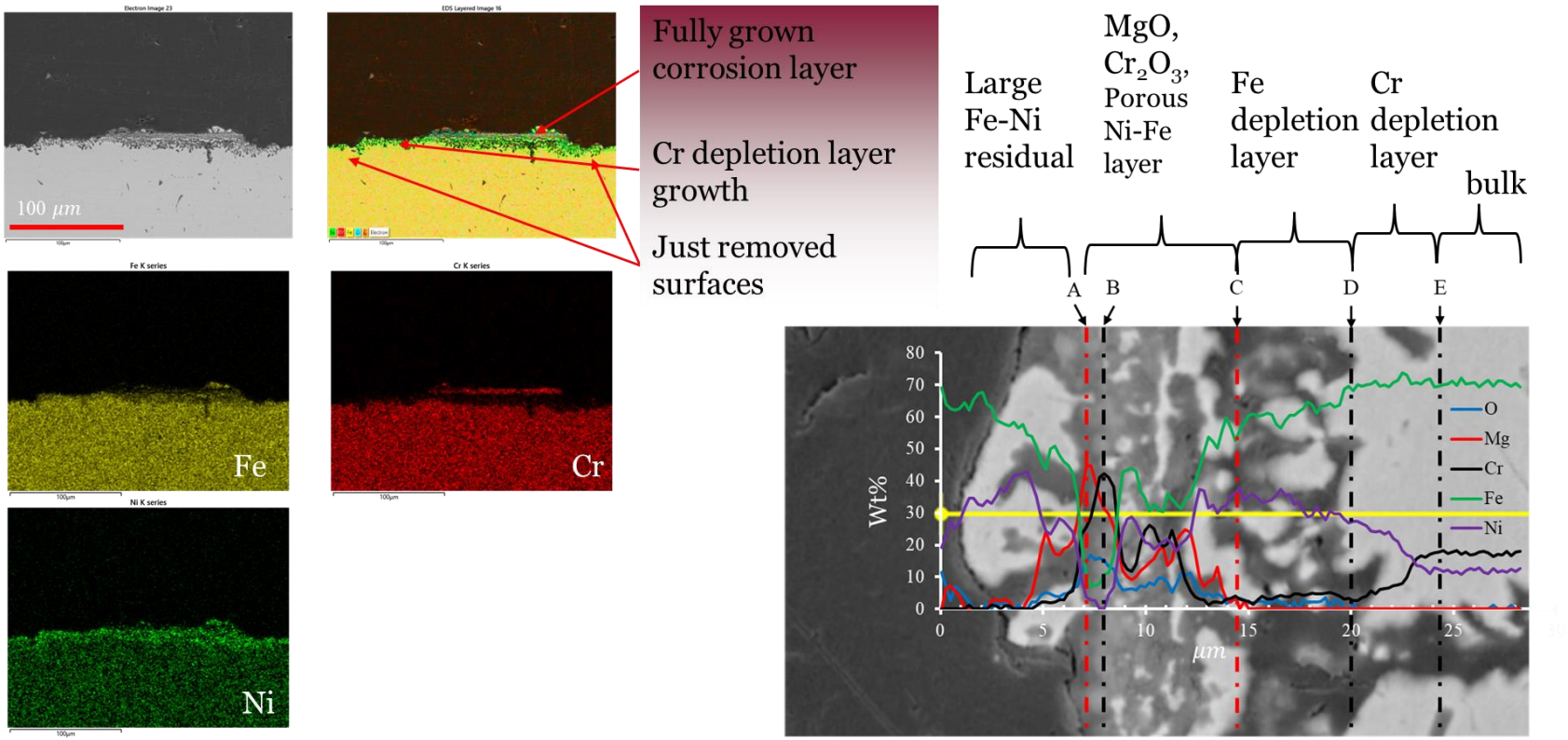

Figure IV-42 Observation of surface removal on FCL-80-SS316, with three different corrosion layers.

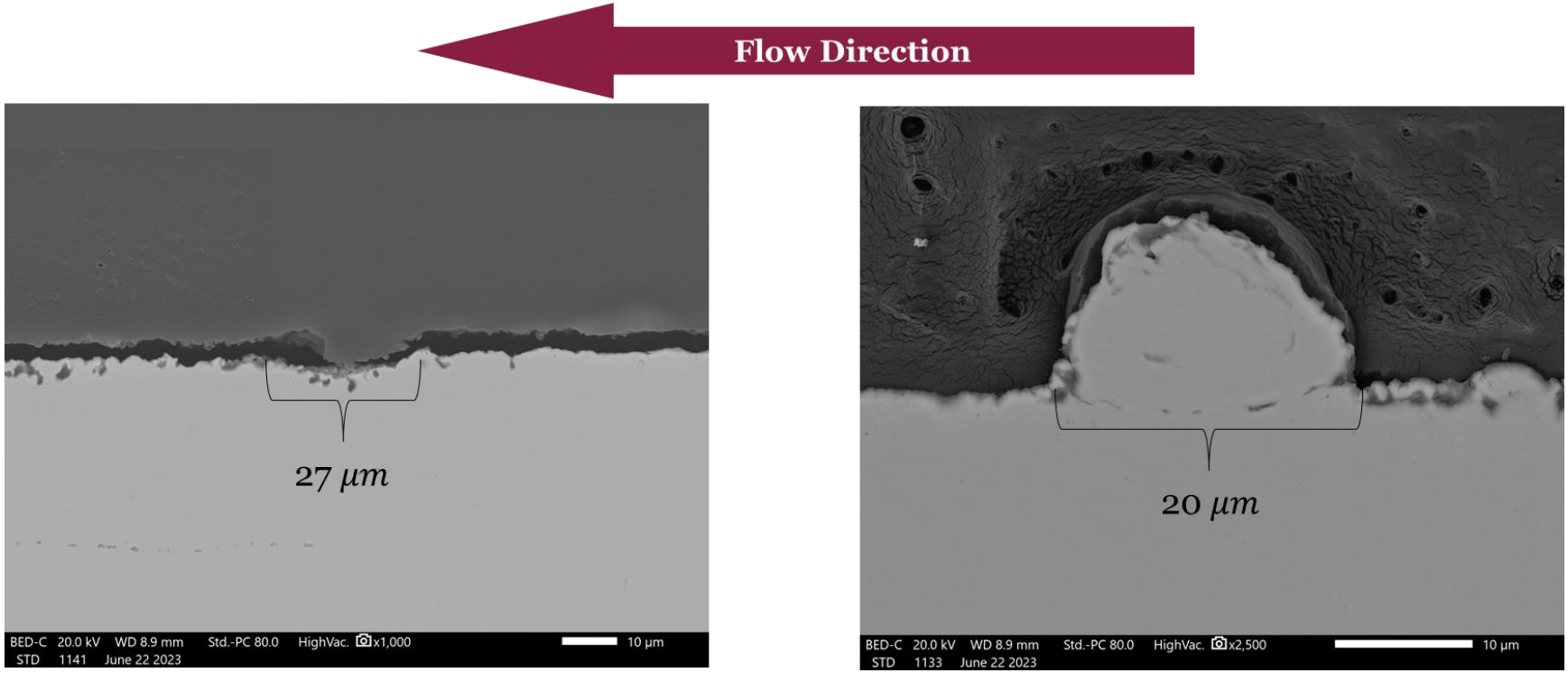

Figure IV-43 Observation of particle removal on FCL-100-SS316.

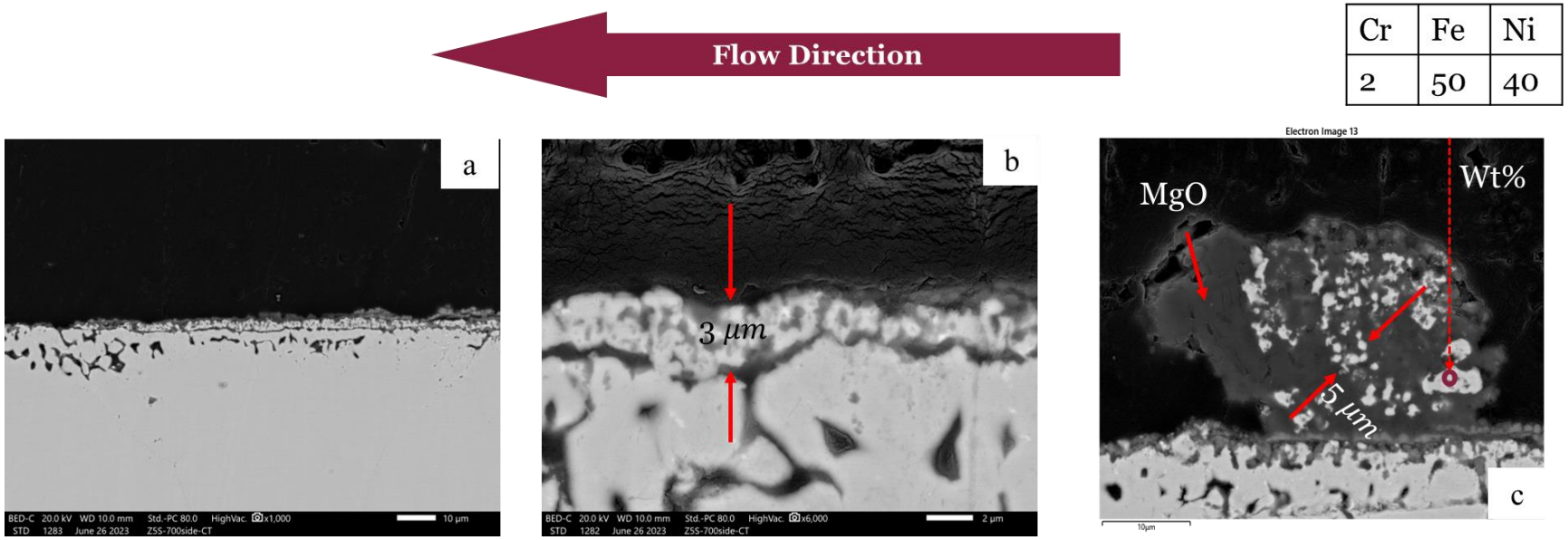

Cr	Fe	Ni
2	50	40

Figure IV-44 Observation of surface removal on FCL-80-A709, with a Ni-Fe strip showing signs of peeling off.

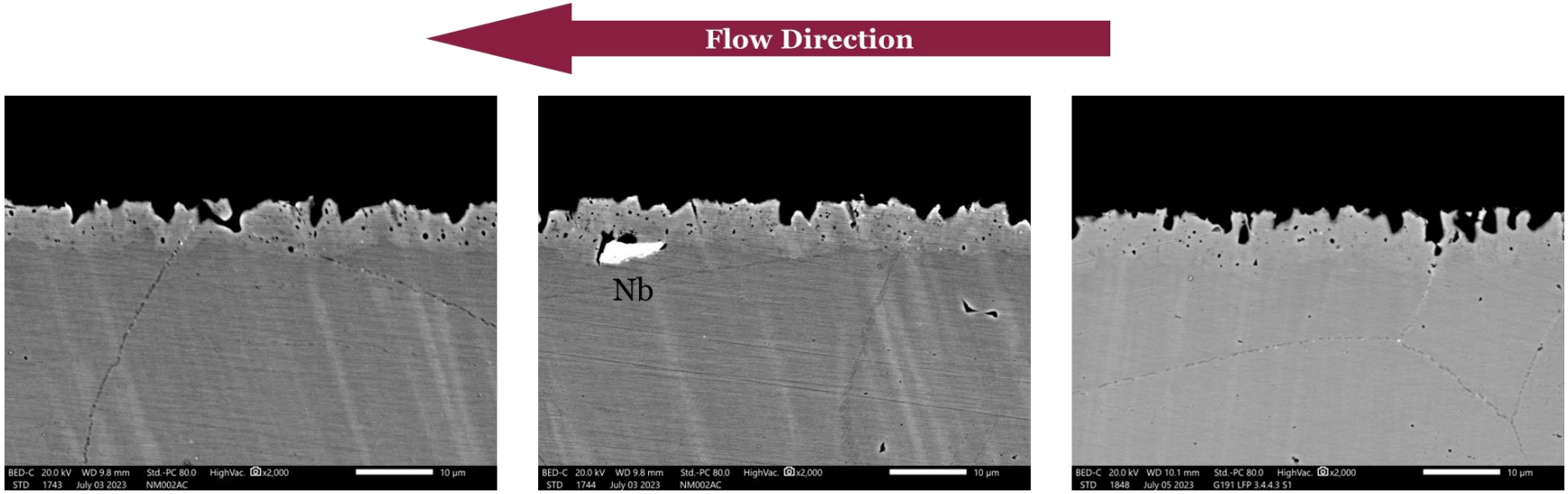

Figure IV-45 Observation of surface erosion on FCL-100-A709.

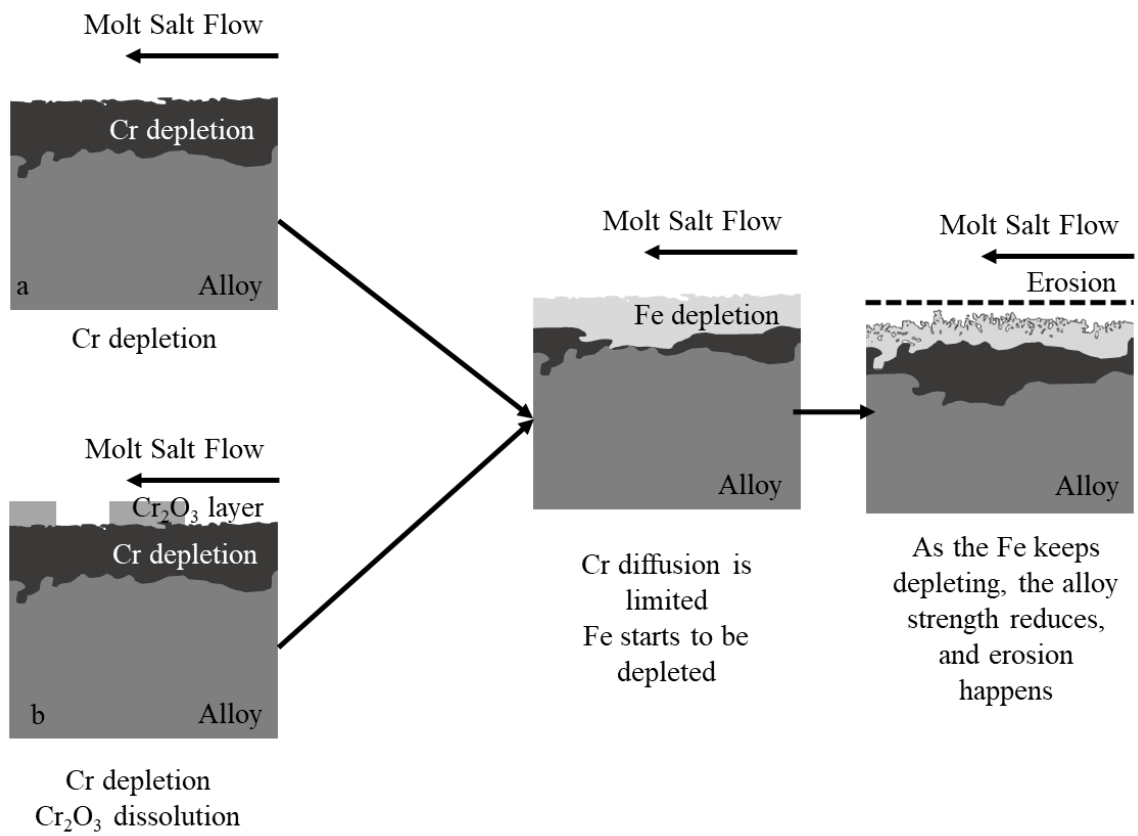

Figure IV-46 Flow induced corrosion mechanism of Fe-based alloy in chloride molten salt.

Based on the developed flow-induced corrosion mechanism, an interesting observation was clarified regarding the corrosion of the bumps in the case of FCL-100. Figure IV 46 displays the EDS mapping of the bumps. However, it challenging to ascertain whether the bumps were caused by machine or erosion. Of particular significance is the observation that the surfaces facing the flow exhibit a thinner layer of Cr depletion compared to the surfaces oriented away from the flow. To understand this phenomenon, calculations were performed considering the aspect ratio of the

flow channel and bump height, along with the overall Reynolds number. The flow over the bump was found to occur under a laminar condition, with a Reynolds number of approximately 50. When the flow impinges on the surface of the bump, the stagnation zone experiences a higher mass transfer rate compared to other locations on the bump. As a result, this region encounters a higher corrosion/erosion rate. This phenomenon explains why the Ni-Fe layer on the front surface (facing the flow) is thinner. This insight provides valuable information regarding the localized corrosion behavior under flow-induced conditions.

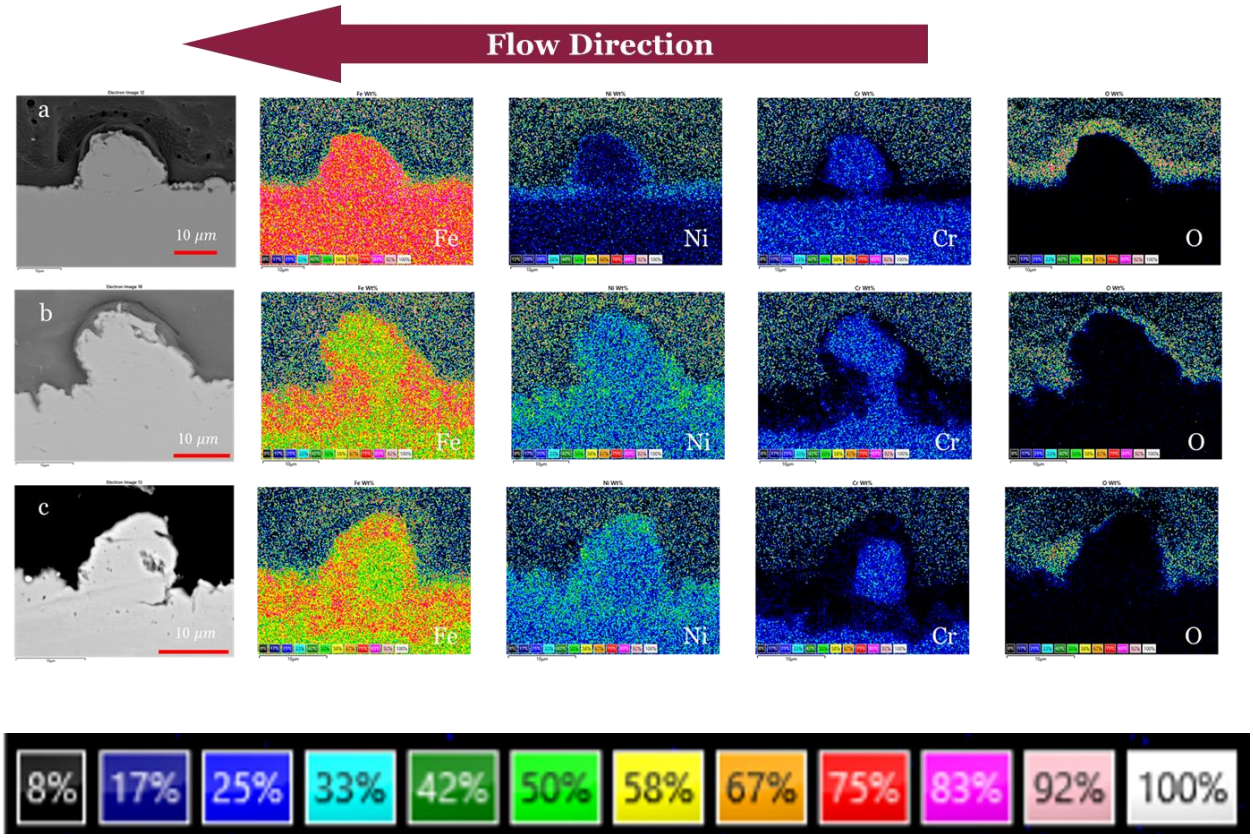

Figure IV-47 Quantitative mapping reveals flow effects in the bump. (a) FCL-100-SS316-S1. (b) and (c) FCL-100-A709-S1.

IV.4.4. Sub-Conclusion

In summary, the successful implementation of the loops to generate FIC has proven to be essential in detecting corrosion at an early stage in molten salt power plants. Through exposure of Type SS316 and A709 alloys to Magnak chloride under turbulent flow conditions at high temperatures for varying durations, it was observed that the Cr depletion layer thickness in FIC is primarily influenced by flow conditions and tends to be thinner compared to static corrosion under similar conditions. This finding highlights the importance of understanding the dynamic nature of FIC in molten salt systems.

The flow-induced corrosion (FIC) results of Fe-based alloys (SS316 and A709) at 650°C under turbulent flow conditions (Re=9225) have been reported. Unexpectedly, static corrosion phenomena were also observed on the inner surfaces, providing a unique opportunity to compare static and dynamic corrosion under identical conditions. The FIC surface typically exhibits a thinner Cr depletion layer but an incomplete surface, suggesting that the FIC process includes erosion. Multiple erosion evidence supports these assumptions.

The FIC mechanism in molten chloride salt for Fe-based alloys has been unveiled. The FIC process is primarily controlled by the cathodic reaction driven by corrosive impurities. Mass transfer rates of corrosion products and corrosive impurities are higher than in static scenarios, especially in turbulent flow conditions. The FIC process comprises three major steps: (1) Cr depletion to balance with the cathodic current, (2) insufficient Cr leads to Fe depletion, and (3) continuous Fe

consumption causes the corrosion layer to become porous and weaker, eventually leading to the removal of the outer corrosion layer.

The FCL tests have provided valuable insights into the FIC mechanism in Magnak chloride salt, which is a significant knowledge gap in the field of molten salt corrosion. However, it is important to note that the current testing methods have limitations, particularly in terms of controlling the salt conditions. Furthermore, the difference in sample size between A709 and SS316 alloys and the simultaneous corrosion at the inner and outer surface of the sample has made it challenging to compare weight loss results or calculate the FIC corrosion rate accurately based on weight changes. As a result, no specific recommendations regarding the suitability of these materials can be provided based on the available data.

Future research on alloy selection and development should prioritize the investigation of the strength and characteristics of the Cr and Fe depletion layer, as it has been identified as a significant factor in the FIC environment. By further exploring these aspects, a more comprehensive understanding of FIC in molten salt systems can be achieved, leading to improved corrosion mitigation strategies and material selection in the future.

Chapter V CONCLUSIONS

In conclusion, this comprehensive study has contributed significant insights into various aspects of corrosion in chloride molten salt environments. The first part of the study focused on the development of chronopotentiometry and potentiodynamic polarization techniques to measure redox potentials using the Ag^+/Ag to Cl_2/Cl^- redox couple in LiCl-KCl eutectic melt. A new correlation of formal potential at X=0.0039 was given as $E^f_{AgCl/Ag} = -1.038 + 0.000264T$ while that at X=0.0145 was expressed as $E^f_{AgCl/Ag} = -1.037 + 0.000244T$, in the temperature range 723 K to 823 K. The calculated activity coefficients of AgCl range from 1.905 to 2.638 and an estimated relationship between temperature and the activity coefficients is also given.

The obtained results were considered reliable and aligned well with previous studies. Then the innovative method was implemented to scope to investigate the redox potentials of $MgCl_2$, $NiCl_2$, and $CrCl_2$ in the temperature range of 873 K to 1073 K. The empirical expression of the formal potential of $NiCl_2$ is given as $E^f_{NiCl_2/Ni} = -1.385 + 6.020 \times 10^{-4}T$ and that of $CrCl_2$ is $E^f_{CrCl_2/Cr} = -2.127 + 7.041 \times 10^{-4}T$ in the tested concentration range. The formal potential of $MgCl_2$ in the salt mixture (X=0.4587) is also given as $E^f_{MgCl_2/Mg} = -3.289 + 7.501 \times 10^{-4}T$. The results highlighted Ni's higher corrosion resistance compared to Cr in Magnak chloride salt. Additionally, the low limited dissolution concentration of $NiCl_2$ and $CrCl_2$ suggested that pure Magnak chloride salt, free from corrosive impurities like moisture, would not corrode Ni and Cr metals.

Moreover, electrochemical corrosion tests were performed at 600-700°C in chemically purified Magnak chloride molten salt on various materials (Fe, Cr, Ni, A709, and SS316). Pure metals displayed lower corrosion potentials than their formation potentials because the presence of fewer corrosion products lowered their Nernst potential., following the corrosion resistance order of Ni > Cr. Notably, SS316 exhibited better corrosion resistance than A709, contrary to expectations. However, SS316's corrosion potential decreased with temperature, while A709's increased. It is possible that at higher temperatures, A709 might exhibit improved corrosion resistance. These tests provided valuable insights into the electrochemical corrosion process in low impurity environments for different materials.

Furthermore, we have addressed the design experience and challenges faced during the development of the test loop components, as well as the operational experiences gained from using the chloride salt loop. Through our operational experience, we have confirmed the advantages of using molten salt as a coolant, which effectively reduces the risk of coolant leaks. The self-sealing properties of the molten salt slow down or even stop leaks at points of rupture. However, it is important to be cautious about the potential electrolysis of the chloride salt, as the current heating source for the test loop is electricity, which may generate hazardous gases. One of the most significant challenges identified during the operation of the molten salt loop for high-temperature applications is the implementation of effective seal techniques for the connections and valves. Given the demanding conditions, ensuring reliable and durable seals remains a crucial aspect that requires careful consideration and innovation.

Finally, the flow-induced corrosion (FIC) results of Fe-based alloys (SS316 and A709) at 650°C under turbulent flow conditions (Re=9225) have been reported. Unexpectedly, static corrosion phenomena were also observed on the inner surfaces, providing a unique opportunity to compare static and dynamic corrosion under identical conditions. The FIC surface typically exhibits a thinner Cr depletion layer but an incomplete surface, suggesting that the FIC process includes erosion. Multiple erosion evidence supports these assumptions.

The FIC mechanism in molten chloride salt for Fe-based alloys has been unveiled. The FIC process is primarily controlled by the cathodic reaction driven by corrosive impurities. Mass transfer rates of corrosion products and corrosive impurities are higher than in static scenarios, especially in turbulent flow conditions. The FIC process comprises three major steps: (1) Cr depletion to balance with the cathodic current, (2) insufficient Cr leads to Fe depletion, and (3) continuous Fe consumption causes the corrosion layer to become porous and weaker, eventually leading to the removal of the outer corrosion layer.

This research work has made significant advancements in understanding the corrosion mechanisms in chloride molten salt for high temperature concentrating solar and nuclear power plants. Firstly, a new and secure electrochemical method for accurately measuring thermodynamic properties in chloride molten salt has been developed. Secondly, the database of thermodynamic properties of corrosion products in Magnak salt has been established for the first time. Thirdly, the corrosion data and behavior of the novel A709 alloy were thoroughly investigated in Magnak salt. Fourthly, this study provides first-hand experience and valuable insights into the design and operation of a

forced convection chloride molten salt corrosion loop. Finally, this research marks the first-ever report on the turbulent flow-induced corrosion mechanism in chloride molten salt.

Future research should focus on conducting corrosion studies on SS316 and A709 at higher temperatures to assess their performance in elevated temperature applications. Additionally, investigating the strength and characteristics of the Cr and Fe depletion layers in flow-induced corrosion (FIC) environments would contribute to a comprehensive understanding of FIC mechanisms. This understanding can aid in the development of improved corrosion mitigation strategies and material selection. It is also important to explore the influence of impurities and assess long-term stability and durability to ensure the reliability of materials in molten salt environments.

Chapter VI Reference

1 Agency, I. E. *Key world energy statistics*. (International Energy Agency Paris, 2007).

2 IEA. Key World Energy Statistics 2021. (2021).

3 Rosenthal, M., Kasten, P. & Briggs, R. Molten-salt reactors—history, status, and potential. *Nuclear Applications and Technology* **8**, 107-117 (1970).

4 Shaffer, J. H. PREPARATION AND HANDLING OF SALT MIXTURES FOR THE MOLTEN SALT REACTOR EXPERIMENT. (Oak Ridge National Lab., Tenn., 1971).

5 Haubenreich, P. N. & Engel, J. Experience with the molten-salt reactor experiment. *Nuclear Applications and technology* **8**, 118-136 (1970).

6 Williams, D. & Britt, P. in *Molten Salt Chemistry Workshop at Oak Ridge National Laboratory.*

7 Mignacca, B. & Locatelli, G. Economics and finance of molten salt reactors. *Progress in Nuclear Energy* **129**, 103503 (2020).

8 Bettis, E. & Robertson, R. C. The design and performance features of a single-fluid molten-salt breeder reactor. *Nuclear applications and technology* **8**, 190-207 (1970).

9 Perry, A. & Bauman, H. Reactor physics and fuel-cycle analyses. *Nuclear Applications and Technology* **8**, 208-219 (1970).

10 Grimes, W. Molten-salt reactor chemistry. *Nuclear Applications and Technology* **8**, 137-155 (1970).

11 Roy, D. M., Roy, R. & Osborn, E. Phase Relations and Structural Phenomena in the Fluoride - Model Systems LiF - BeF2 and NaF - BeF2. *Journal of the American Ceramic Society* **33**, 85-90 (1950).

12 Capelli, E., Beneš, O. & Konings, R. Thermodynamic assessment of the LiF–NaF–BeF2–ThF4–UF4 system. *Journal of Nuclear Materials* **449**, 111-121 (2014).

13 Fukuda, G., Peterson, P., Olander, D. & Prausnitz, J. Thermodynamics of the LiF–NaF–BeF2 system at high temperatures. *Fluid phase equilibria* **255**, 1-10 (2007).

14 He, L.-Y. *et al.* Th–U cycle performance analysis based on molten chloride salt and molten fluoride salt fast reactors. *Nuclear Science and Techniques* **31**, 1-13 (2020).

15 Taube, M. Fast reactors using molten chloride salts as fuel. (INFCE (Switzerland), 1978).

16 Mausolff, Z., DeHart, M. & Goluoglu, S. Design and assessment of a molten chloride fast reactor. *Nuclear Engineering and Design* **379**, 111181 (2021).

17 Glassner, A. The thermochemical properties of the oxides, fluorides, and chlorides to 2500 K. (Argonne National Lab., Lemont, Ill., 1957).

18 Ignat'ev, V., Merzlyakov, A., Subbotin, V., Panov, A. & Golovatov, Y. V. Experimental investigation of the physical properties of salt melts containing sodium and lithium fluorides and beryllium difluoride. *Atomic Energy* **101**, 822-829 (2006).

19 Ignatiev, V. *et al.* Molten-salt reactors: new possibilities, problems and solutions. *Atomic energy* **112**, 157-165 (2012).

20 Zhang, H., Baeyens, J., Degrève, J. & Cacères, G. Concentrated solar power plants: Review and design methodology. *Renewable and sustainable energy reviews* **22**, 466-481 (2013).

21 Pramanik, S. & Ravikrishna, R. A review of concentrated solar power hybrid technologies. *Applied Thermal Engineering* **127**, 602-637 (2017).

22 González-Roubaud, E., Pérez-Osorio, D. & Prieto, C. Review of commercial thermal energy storage in concentrated solar power plants: Steam vs. molten salts. *Renewable and sustainable energy reviews* **80**, 133-148 (2017).

23 Gil, A. *et al.* State of the art on high temperature thermal energy storage for power generation. Part 1—Concepts, materials and modellization. *Renewable and sustainable energy reviews* **14**, 31-55 (2010).

24 Kenisarin, M. M. High-temperature phase change materials for thermal energy storage. *Renewable and sustainable energy reviews* **14**, 955-970 (2010).

25 Bonk, A., Sau, S., Uranga, N., Hernaiz, M. & Bauer, T. Advanced heat transfer fluids for direct molten salt line-focusing CSP plants. *Progress in Energy and Combustion Science* **67**, 69-87 (2018).

26 Kearney, D. *et al.* Assessment of a molten salt heat transfer fluid in a parabolic trough solar field. *J. Sol. Energy Eng.* **125**, 170-176 (2003).

27 Herrmann, U., Kelly, B. & Price, H. Two-tank molten salt storage for parabolic trough solar power plants. *Energy* **29**, 883-893 (2004).

28 Kearney, D. *et al.* Engineering aspects of a molten salt heat transfer fluid in a trough solar field. *Energy* **29**, 861-870 (2004).

29 Olivares, R. I. The thermal stability of molten nitrite/nitrates salt for solar thermal energy storage in different atmospheres. *Solar Energy* **86**, 2576-2583 (2012).

30 Mehos, M. *et al.* Concentrating solar power Gen3 demonstration roadmap. (National Renewable Energy Lab.(NREL), Golden, CO (United States), 2017).

31 Guo, S., Zhang, J., Wu, W. & Zhou, W. Corrosion in the molten fluoride and chloride salts and materials development for nuclear applications. *Progress in Materials Science* **97**, 448-487 (2018).

32 Zhang, J. Impurities in primary coolant salt of FHRs: Chemistry, impact, and removal methods. *Energy Technology* **7**, 1900016 (2019).

33 Zhang, J. *et al.* Redox potential control in molten salt systems for corrosion mitigation. *Corrosion Science* **144**, 44-53 (2018).

34 Singh, P. M. *et al.* Phenomena Identification and Ranking Table (PIRT) study for metallic structural materials for advanced High-Temperature reactor. *Annals of Nuclear Energy* **123**, 222-229 (2019).

35 Zhang, M., Ge, J., Yin, T. & Zhang, J. Redox potential measurements of Cr (II)/Cr Ni (II)/Ni and Mg (II)/Mg in molten MgCl2–KCl–NaCl mixture. *Journal of The Electrochemical Society* **167**, 116505 (2020).

36 Yang, Q., Ge, J. & Zhang, J. Electrochemical study on the kinetic properties of Fe2+/Fe, Ni2+/Ni, Cr2+/Cr and Cr3+/Cr2+ in molten MgCl2-KCl-NaCl salts. *Journal of The Electrochemical Society* **168**, 012504 (2021).

37 Wang, Y., Yang, Q. & Zhang, J. Transport and kinetics properties of LaF3 in FLiNaK molten salt determined by electrochemical methods. *Journal of Fluorine Chemistry* **233**, 109502 (2020).

38 Wang, Y. & Zhang, J. Electrochemical properties of CrF2 in FLiNaK molten salt and the new analytical methods for their determination. *Journal of The Electrochemical Society* **167**, 086503 (2020).

39 Guo, S., Shay, N., Wang, Y., Zhou, W. & Zhang, J. Measurement of europium (III)/europium (II) couple in fluoride molten salt for redox control in a molten salt reactor concept. *Journal of Nuclear Materials* **496**, 197-206 (2017).

40 Manly, W. *et al.* Metallurgical problems in molten fluoride systems. (Oak Ridge National Lab., Tenn., 1958).

41 Wright, R. & Sham, T.-L. Status of metallic structural materials for molten salt reactors. (Idaho National Lab.(INL), Idaho Falls, ID (United States); Argonne National …, 2018).

42 Hu, Z. *et al.* Corrosion behavior and mechanism of 316 stainless steel in NaCl-KCl-ZnCl2 molten salts at high temperature. *Materials Today Communications* **31**, 103297 (2022).

43 Zheng, G. *et al.* Corrosion of 316 stainless steel in high temperature molten Li2BeF4 (FLiBe) salt. *Journal of Nuclear Materials* **461**, 143-150 (2015).

44 Zhu, M., Zeng, S., Zhang, H., Li, J. & Cao, B. Electrochemical study on the corrosion behaviors of 316 SS in HITEC molten salt at different temperatures. *Solar Energy Materials and Solar Cells* **186**, 200-207 (2018).

45 Ren, S. *et al.* Corrosion behavior of carburized 316 stainless steel in molten chloride salts. *Solar Energy* **223**, 1-10 (2021).

46 D'Souza, B., Leong, A., Yang, Q. & Zhang, J. Corrosion behavior of boronized nickel-based alloys in the molten chloride Salt. *Corrosion Science* **182**, 109285 (2021).

47 Raiman, S. S. & Lee, S. Aggregation and data analysis of corrosion studies in molten chloride and fluoride salts. *Journal of Nuclear Materials* **511**, 523-535 (2018).

48 DeVan, J. & Evans III, R. Corrosion behavior of reactor materials in fluoride salt mixtures. (Oak Ridge National Lab., Tenn., 1962).

49 Keiser, J., DeVan, J. & Lawrence, E. Compatibility of molten salts with type 316 stainless steel and lithium. *Journal of Nuclear Materials* **85**, 295-298 (1979).

50 Susskind, H. *et al.* Corrosion studies for a fused salt-liquid metal extraction process for the liquid metal fuel reactor. (Brookhaven National Lab., Upton, NY, 1960).

51 Koger, J. Evaluation of Hastelloy N alloys after nine years exposure to both a molten fluoride salt and air at temperatures from 700 to 560 0 C. (Oak Ridge National Lab., 1972).

52 Sabharwall, P., Ebner, M., Sohal, M. & Sharpe, P. Molten Salts for High Temperature Reactors: University of Wisconsin Molten Salt Corrosion and Flow Loop Experiments--Issues Identified and Path Forward. (Idaho National Lab.(INL), Idaho Falls, ID (United States), 2010).

53 Matsunami, J. *et al.* Coal gasification by CO2 gas bubbling in molten salt for solar/fossil energy hybridization. *Solar Energy* **68**, 257-261 (2000).

54 Yoshida, S. *et al.* Coal/CO2 gasification system using molten carbonate salt for solar/fossil energy hybridization. *Energy & fuels* **13**, 961-964 (1999).

55 Fray, D. J. Emerging molten salt technologies for metals production. *JOM* **53**, 27-31 (2001).

56 Juzeliūnas, E. & Fray, D. J. Silicon electrochemistry in molten salts. *Chemical reviews* **120**, 1690-1709 (2019).

57 Zhang, J. Kinetic model for electrorefining, part I: Model development and validation. *Progress in nuclear energy* **70**, 279-286 (2014).

58 Zhang, J. Electrochemistry of actinides and fission products in molten salts—Data review. *Journal of Nuclear Materials* **447**, 271-284 (2014).

59 Zhang, J. *Nuclear fuel reprocessing and waste management*. Vol. 2 (World Scientific, 2018).

60 Koyama, T. *et al.* Development of pyro-processing fuel cycle technology for closing actinide cycle. *Procedia Chemistry* **7**, 772-778 (2012).

61 Masset, P. & Guidotti, R. A. Thermal activated (thermal) battery technology: Part II. Molten salt electrolytes. *Journal of power sources* **164**, 397-414 (2007).

62 Masset, P., Schoeffert, S., Poinso, J.-Y. & Poignet, J.-C. Retained molten salt electrolytes in thermal batteries. *Journal of power sources* **139**, 356-365 (2005).

63 Leung, P. *et al.* Performance and polarization studies of the magnesium–antimony liquid metal battery with the use of in-situ reference electrode. *RSC advances* **5**, 83096-83105 (2015).

64 Ding, W., Bonk, A. & Bauer, T. in *AIP conference proceedings.* 200014 (AIP Publishing LLC).

65 Wang, X. *Investigation of the Thermal and Transport Properties of NaCl-KCl-MgCl2-CaCl2 Molten Salt for Application as HTF and TES Media in CSP Systems*, The University of Arizona, (2020).

66 Villada, C., Ding, W., Bonk, A. & Bauer, T. Engineering molten MgCl2–KCl–NaCl salt for high-temperature thermal energy storage: Review on salt properties and corrosion control strategies. *Solar Energy Materials and Solar Cells* **232**, 111344 (2021).

67 Vidal, J. C. & Klammer, N. in *AIP Conference Proceedings.* 080006 (AIP Publishing LLC).

68 Ding, W., Bonk, A. & Bauer, T. Corrosion behavior of metallic alloys in molten chloride salts for thermal energy storage in concentrated solar power plants: A review. *Frontiers of Chemical Science and Engineering* **12**, 564-576 (2018).

69 Lantelme, F. & Groult, H. *Molten salts chemistry: from lab to applications*. (Newnes, 2013).

70 Li, Y. *et al.* Survey and evaluation of equations for thermophysical properties of binary/ternary eutectic salts from NaCl, KCl, MgCl2, CaCl2, ZnCl2 for heat transfer and thermal storage fluids in CSP. *Solar Energy* **152**, 57-79 (2017).

71 Vignarooban, K., Xu, X., Arvay, A., Hsu, K. & Kannan, A. M. Heat transfer fluids for concentrating solar power systems–a review. *Applied Energy* **146**, 383-396 (2015).

72 Tian, Y. & Zhao, C.-Y. A review of solar collectors and thermal energy storage in solar thermal applications. *Applied energy* **104**, 538-553 (2013).

73 Yin, H., Wang, Z., Lai, X., Wang, Y. & Tang, Z. Optimum design and key thermal property of NaCl–KCl–CaCl2 eutectic salt for ultra-high-temperature thermal energy storage. *Solar Energy Materials and Solar Cells* **236**, 111541 (2022).

74 Scholich, K. Neues Jahrb. *Mineral. Geol. Palaontol., Beil* **43**, 251-262 (1920).

75 Jänecke, E. Über das Schmelz‐und Erstarrungsbild des doppelt‐ternären Systemes (K2 • Na2 • Mg)(Cl2 • SO4). *Zeitschrift für anorganische Chemie* **261**, 213-225 (1950).

76 Mohan, G., Venkataraman, M., Gomez-Vidal, J. & Coventry, J. Assessment of a novel ternary eutectic chloride salt for next generation high-temperature sensible heat storage. *Energy conversion and management* **167**, 156-164 (2018).

77 Nemecek, J., Simmons, D. & Chubb, T. Demand sensitive energy storage in molten salts. *Solar Energy* **20**, 213-217 (1978).

78 Liu, Q. *et al.* Corrosion behaviour of 316 stainless steel in NaCl-KCl-MgCl2 salt vapour at 700° C. *Corrosion Science* **194**, 109921 (2022).

79 Shi, H. *et al.* Hot corrosion behavior of additively manufactured stainless steel 316L and Inconel 718 in MgCl2/KCl/NaCl chloride salts at 700° C. *Corrosion Science* **207**, 110561 (2022).

80 Ding, W. *et al.* Hot corrosion behavior of commercial alloys in thermal energy storage material of molten MgCl2/KCl/NaCl under inert atmosphere. *Solar Energy Materials and Solar Cells* **184**, 22-30 (2018).

81 Sun, H., Wang, J., Li, Z., Zhang, P. & Su, X. Corrosion behavior of 316SS and Ni-based alloys in a ternary NaCl-KCl-MgCl2 molten salt. *Solar Energy* **171**, 320-329 (2018).

82 Grégoire, B., Oskay, C., Meißner, T. & Galetz, M. Corrosion mechanisms of ferritic-martensitic P91 steel and Inconel 600 nickel-based alloy in molten chlorides. Part II: NaCl-KCl-MgCl2 ternary system. *Solar Energy Materials and Solar Cells* **216**, 110675 (2020).

83 Patel, N. S., Pavlík, V. & Boča, M. High-temperature corrosion behavior of superalloys in molten salts–a review. *Critical Reviews in Solid State and Materials Sciences* **42**, 83-97 (2017).

84 Bell, S., Steinberg, T. & Will, G. Corrosion mechanisms in molten salt thermal energy storage for concentrating solar power. *Renewable and Sustainable Energy Reviews* **114**, 109328 (2019).

85 Dsouza, B. H. *Material Degradation Studies in Molten Halide Salts*, Virginia Tech, (2021).

86 Ding, W. *et al.* Molten chloride salts for next generation concentrated solar power plants: Mitigation strategies against corrosion of structural materials. *Solar Energy Materials and Solar Cells* **193**, 298-313 (2019).

87 Heitz, E. Chemo-mechanical effects of flow on corrosion. *Corrosion* **47**, 135-145 (1991).

88 Zhang, J. & Li, N. Review of the studies on fundamental issues in LBE corrosion. *Journal of nuclear materials* **373**, 351-377 (2008).

89 Sridharan, K. & Allen, T. in *Molten salts chemistry* 241-267 (Elsevier, 2013).

90 Balbaud-Celerier, F. & Barbier, F. Investigation of models to predict the corrosion of steels in flowing liquid lead alloys. *Journal of Nuclear Materials* **289**, 227-242 (2001).

91 G46-94, A. Standard guide for examination and evaluation of pitting corrosion. *ASTM International* (2005).

92 Wang, Y., Liu, H. & Zeng, C. Galvanic corrosion of pure metals in molten fluorides. *Journal of Fluorine Chemistry* **165**, 1-6 (2014).

93 Karlsdottir, S. Corrosion, scaling and material selection in geothermal power production. (2021).

94 Olson, L., Sridharan, K., Anderson, M. & Allen, T. Intergranular corrosion of high temperature alloys in molten fluoride salts. *Materials at High Temperatures* **27**, 145-149 (2010).

95 Gomez-Vidal, J. C. & Tirawat, R. Corrosion of alloys in a chloride molten salt (NaCl-LiCl) for solar thermal technologies. *Solar Energy Materials and Solar Cells* **157**, 234-244 (2016).

96 D'Souza, B., Zhuo, W., Yang, Q., Leong, A. & Zhang, J. Impurity driven corrosion behavior of HAYNES® 230® alloy in molten chloride Salt. *Corrosion Science* **187**, 109483 (2021).

97 Leong, A. *Material Corrosion by Nuclear Reactor Coolants*, Virginia Tech, (2022).

98 Kondo, M. *et al.* Metallurgical study on erosion and corrosion behaviors of steels exposed to liquid lead–bismuth flow. *Journal of Nuclear materials* **343**, 349-359 (2005).

99 Rieger, P. H. *Electrochemistry*. (Springer Science & Business Media, 1993).

100 Yang, L. & Hudson, R. G. Some Investigations of the Ag/AgCl in LiCl - KCl Eutectic Reference Electrode. *Journal of The Electrochemical Society* **106**, 986 (1959).

101 Fusselman, S. *et al.* Thermodynamic properties for rare earths and americium in pyropartitioning process solvents. *Journal of the Electrochemical Society* **146**, 2573 (1999).

102 Masset, P. *et al.* Electrochemistry of uranium in molten LiCl-KCl eutectic. *Journal of The Electrochemical Society* **152**, A1109 (2005).

103 Sakamura, Y. Zirconium behavior in molten LiCl-KCl eutectic. *Journal of the electrochemical society* **151**, C187 (2004).

104 Salstrom, E. J. Thermodynamic Properties of Fused Salt Solutions. VIII. Lead Chloride in Silver Chloride. *Journal of the American Chemical Society* **56**, 1272-1275 (1934).

105 Gruner, A. C. & Thompson, W. T. The Activity of AgCl in AgCl–LiCl–KCl Melts. *Canadian Journal of Chemistry* **53**, 1084-1092 (1975).

106 Panish, M., Blankenship, F., Grimes, W. & Newton, R. Thermodynamic properties of molten and solid solutions of silver chloride and sodium chloride. *The Journal of Physical Chemistry* **62**, 1325-1331 (1958).

107 Moser, Z. & Rzyman, K. Thermodynamic studies on liquid AgCl · KCl · LiCl solutions. *Electrochimica Acta* **25**, 183-187 (1980).

108 Shirai, O., Nagai, T., Uehara, A. & Yamana, H. Electrochemical properties of the Ag+| Ag and other reference electrodes in the LiCl–KCl eutectic melts. *Journal of Alloys and Compounds* **456**, 498-502 (2008).

109 Yoon, D., Baggett, A., Phongikaroon, S., King, J. A. & Marsden, K. Fundamental data acquisition toward silver-silver chloride reference electrode. *Journal of The Electrochemical Society* **166**, E159 (2019).

110 Yang, L. & Hudson, R. G. Some Investigations of the Ag/AgCl in LiCl - KCl Eutectic Reference Electrode. *Journal of The Electrochemical Society* **106**, 986-990 (1959).

111 Yang, L. & Hudson, R. Equilibrium electrode potentials of some metal-chlorine galvanic cells and activities of some metal chlorides in LiCl-KCl eutectic melt. *Trans. Met. Soc. AIME* **215**, 589-601 (1959).

112 Zhang, J. & Guo, S. Rare Earth Electrochemical Property Measurements and Phase Diagram Development in a Complex Molten Salt Mixture for Molten Salt Recycle. (The Ohio State Univ., Columbus, OH (United States), 2018).

113 Bermejo, M., Gomez, J., Martinez, A., Barrado, E. & Castrillejo, Y. Electrochemistry of terbium in the eutectic LiCl–KCl. *Electrochimica Acta* **53**, 5106-5112 (2008).

114 Kim, B. Y., Lee, D. H., Lee, J.-Y. & Yun, J.-I. Electrochemical and spectroscopic investigations of Tb (III) in molten LiCl–KCl eutectic at high temperature. *Electrochemistry communications* **12**, 1005-1008 (2010).

115 Liu, Y. L., Liu, K., Yuan, L. Y., Chai, Z. F. & Shi, W. Q. Estimation of the composition of intermetallic compounds in LiCl–KCl molten salt by cyclic voltammetry. *Faraday discussions* **190**, 387-398 (2016).

116 Zhang, M., Ge, J., Zhang, J. & Liu, L. E. Redox potential measurement of AgCl in molten LiCl-KCl salt using chronopotentiometry and potentiodynamic scan techniques. *Electrochemistry Communications* **105**, 106498 (2019).

117 HOLLAND, R. I. Use of potentiodynamic polarization technique for corrosion testing of dental alloys. *European Journal of Oral Sciences* **99**, 75-85 (1991).

118 Esmailzadeh, S., Aliofkhazraei, M. & Sarlak, H. Interpretation of cyclic potentiodynamic polarization test results for study of corrosion behavior of metals: a review. *Protection of metals and physical chemistry of surfaces* **54**, 976-989 (2018).

119 Yi, Y., Cho, P., Al Zaabi, A., Addad, Y. & Jang, C. Potentiodynamic polarization behaviour of AISI type 316 stainless steel in NaCl solution. *Corrosion Science* **74**, 92-97 (2013).

120 Holland, R. Corrosion testing by potentiodynamic polarization in various electrolytes. *Dental Materials* **8**, 241-245 (1992).

121 Munir, S., Pelletier, M. H. & Walsh, W. R. Potentiodynamic corrosion testing. *JoVE (Journal of Visualized Experiments)*, e54351 (2016).

122 Zhang, X., Jiang, Z. H., Yao, Z. P., Song, Y. & Wu, Z. D. Effects of scan rate on the potentiodynamic polarization curve obtained to determine the Tafel slopes and corrosion current density. *Corrosion science* **51**, 581-587 (2009).

123 Doniger, W. H., Couet, A. & Sridharan, K. Potentiodynamic Polarization of Pure Metals and Alloys in Molten LiF-NaF-KF (FLiNaK) Using the K/K+ Dynamic Reference Electrode. *Journal of The Electrochemical Society* **169**, 071502 (2022).

124 Ghaznavi, T., Persaud, S. Y. & Newman, R. C. Electrochemical corrosion studies in molten chloride salts. *Journal of the Electrochemical Society* **169**, 061502 (2022).

125 Vignarooban, K., Pugazhendhi, P., Tucker, C., Gervasio, D. & Kannan, A. M. Corrosion resistance of Hastelloys in molten metal-chloride heat-transfer fluids for concentrating solar power applications. *Solar Energy* **103**, 62-69 (2014).

126 Zeng, C., Wang, W. & Wu, W. Electrochemical impedance models for molten salt corrosion. *Corrosion science* **43**, 787-801 (2001).

127 Fernández, A. G. & Cabeza, L. F. Corrosion evaluation of eutectic chloride molten salt for new generation of CSP plants. Part 1: Thermal treatment assessment. *Journal of Energy Storage* **27**, 101125 (2020).

128 Encinas-Sánchez, V., de Miguel, M., Lasanta, M., García-Martín, G. & Pérez, F. Electrochemical impedance spectroscopy (EIS): An efficient technique for monitoring corrosion processes in molten salt environments in CSP applications. *Solar energy materials and solar cells* **191**, 157-163 (2019).

129 Serp, J. *et al.* The molten salt reactor (MSR) in generation IV: overview and perspectives. *Progress in Nuclear Energy* **77**, 308-319 (2014).

130 Zhang, D. *et al.* Review of conceptual design and fundamental research of molten salt reactors in China. *International Journal of Energy Research* **42**, 1834-1848 (2018).

131 Ignatiev, V. & Surenkov, A. Alloys compatibility in molten salt fluorides: Kurchatov Institute related experience. *Journal of Nuclear Materials* **441**, 592-603 (2013).

132 Toda, S., Chiba, S., Yuki, K., Omae, M. & Sagara, A. Experimental research on molten salt thermofluid technology using a high-temperature molten salt loop applied for a fusion reactor Flibe blanket. *Fusion engineering and design* **63**, 405-409 (2002).

133 Kelleher, B. C., Gagnon, S. F. & Mitchell, I. G. Thermal gradient mass transport corrosion in NaCl-MgCl2 and MgCl2-NaCl-KCl molten salts. *Materials Today Communications* **33**, 104358 (2022).

134 Raiman, S. S. *et al.* Corrosion of 316H stainless steel in flowing FLiNaK salt. *Journal of Nuclear Materials* **561**, 153551 (2022).

135 Chiba, S.-y. *et al.* Experimental research on heat transfer enhancement for high Prandtl-number fluid. *Fusion science and technology* **47**, 569-573 (2005).

136 Satoh, T., Yuki, K., Chiba, S.-y., Hashizume, H. & Sagara, A. Heat transfer performance for high Prandtl and high temperature molten salt flow in sphere-packed pipes. *Fusion Science and Technology* **52**, 618-624 (2007).

137 Sohal, M. S., Sabharwall, P., Calderoni, P., Wertsching, A. K. & Grover, S. B. Conceptual design of forced convection molten salt heat transfer testing loop. (Idaho National Lab.(INL), Idaho Falls, ID (United States), 2010).

138 Yoder Jr, G. L. *et al.* An experimental test facility to support development of the fluoride-salt-cooled high-temperature reactor. *Annals of Nuclear Energy* **64**, 511-517 (2014).

139 Arora, O., Lancaster, B., Yang, S. R., Vaghetto, R. & Hassan, Y. Advanced flow and temperature measurements in a forced convection molten salt test loop. *Annals of Nuclear Energy* **159**, 108269 (2021).

140 Head, T. L. *et al.* A molten salt test loop for component and instrumentation testing. *Annals of Nuclear Energy* **186**, 109772 (2023).

141 Silverman, D. The rotating cylinder electrode for examining velocity-sensitive corrosion—a review. *Corrosion* **60**, 1003-1023 (2004).

142 Walsh, F., Kear, G., Nahle, A. H., Wharton, J. & Arenas, L. The rotating cylinder electrode for studies of corrosion engineering and protection of metals—An illustrated review. *Corrosion Science* **123**, 1-20 (2017).

143 Silverman, D. Rotating cylinder electrode—geometry relationships for prediction of velocity-sensitive corrosion. *Corrosion* **44**, 42-49 (1988).

144 Efird, K., Wright, E., Boros, J. & Hailey, T. Correlation of steel corrosion in pipe flow with jet impingement and rotating cylinder tests. *Corrosion* **49**, 992-1003 (1993).

145 Kear, G., Barker, B., Stokes, K. & Walsh, F. Corrosion and impressed current cathodic protection of copper-based materials using a bimetallic rotating cylinder electrode (BRCE). *Corrosion science* **47**, 1694-1705 (2005).

146 Feng, Y., Teo, W.-K., Siow, K.-S., Tan, K.-L. & Hsieh, A.-K. The corrosion behaviour of copper in neutral tap water. Part I: corrosion mechanisms. *Corrosion Science* **38**, 369-385 (1996).

147 Townsend, T. & Chidambaram, D. in *Electrochemical Society Meeting Abstracts 242*. 766-766 (The Electrochemical Society, Inc.).

148 Briant, R. C. & Weinberg, A. M. Molten fluorides as power reactor fuels. *Nuclear science and engineering* **2**, 797-803 (1957).

149 Bettis, E. *et al.* The aircraft reactor experiment—design and construction. *Nucl. Sci. Eng* **2**, 804-825 (1957).

150 Bettis, E., Cottrell, W., Mann, E., Meem, J. & Whitman, G. The aircraft reactor experiment—operation. *Nuclear Science and Engineering* **2**, 841-853 (1957).

151 Manly, W. *et al.* AIRCRAFT REACTOR EXPERIMENT--METALLURGICAL ASPECTS. (Oak Ridge National Lab., Tenn., 1958).

152 Crowley, J., McDonald, W. & Clark, D. Design and operation of forced-circulation corrosion testing loops with molten salt. (Oak Ridge National Lab., Tenn., 1963).

153 MacPherson, H. Molten-salt reactor program quarterly progress report for period ending july 31, 1960. (Oak Ridge National Lab., Tenn., 1960).

154 Keiser, J. Compatibility studies of potential molten-salt breeder reactor materials in molten fluoride salts. (Oak Ridge National Lab., 1977).

155 Koger, J. Fluoride salt corrosion and mass transfer in high temperature dynamic systems. *Corrosion* **29**, 115-122 (1973).

156 McNEESE, L. Molten-salt reactor program. Semiannual progress report for period ending August 31, 1974. (Oak Ridge National Lab., Tenn.(USA), 1975).

157 McGonigal, P., Kirshenbaum, A. & Grosse, A. THE LIQUID TEMPERATURE RANGE, DENSITY, AND CRITICAL CONSTANTS OF MAGNESIUM1. *The Journal of Physical Chemistry* **66**, 737-740 (1962).

158 Bohdansky, J. & Schins, H. Surface tension and density of the liquid earth alkaline metals Mg, Ca, Sr, Ba. *Journal of Inorganic and Nuclear Chemistry* **30**, 2331-2337 (1968).

159 Faulkner, L. R. & Bard, A. J. *Electrochemical methods: fundamentals and applications*. (John Wiley and Sons, 2002).

160 Caravaca, C., Laplace, A., Vermeulen, J. & Lacquement, J. Determination of the E-pO2− stability diagram of plutonium in the molten LiCl–KCl eutectic at 450 C. *Journal of nuclear materials* **377**, 340-347 (2008).

161 Ihsan, B. Thermochemical data of pure substances. *and* **934**, 587 (1995).

162 Bard, A. J., Faulkner, L. R., Leddy, J. & Zoski, C. G. *Electrochemical methods: fundamentals and applications*. Vol. 2 (wiley New York, 1980).

163 Barlin, I. Thermochemical Data of Pure Substance. *Part* **1**, 1 (1989).

164 Bagri, P. *Measurement of Thermodynamic Properties of Rare Earth Chlorides in Molten LiCl-KCl Eutectic Salt for Waste Minimization from Pyrochemical Processing of Spent Nuclear Fuel*, The University of Utah, (2017).

165 Neil, D., Clark, H. & Wiswall Jr, R. Thermodynamic Properties of Molten Solutions of MgCl2-KCl, MgCl2-NaCl, and MgCl2-KCl-NaCl. *Journal of Chemical and Engineering Data* **10**, 21-24 (1965).

166 Zhao, Y. & Vidal, J. Potential scalability of a cost-effective purification method for MgCl2-Containing salts for next-generation concentrating solar power technologies. *Solar Energy Materials and Solar Cells* **215**, 110663 (2020).

167 Kanzaki, Y. & Takahashi, M. The hydrogen electrode in fused lithium chloride-potassium chloride eutectic containing hydrogen ion. *Journal of Electroanalytical Chemistry and Interfacial Electrochemistry* **58**, 349-356 (1975).

168 Leslie, N. & Mauzeroll, J. Spatially resolved electrochemical measurements. (2023).

169 de Assis, S. L., Wolynec, S. & Costa, I. Corrosion characterization of titanium alloys by electrochemical techniques. *Electrochimica Acta* **51**, 1815-1819 (2006).

170 Bard, A. J. & Faulkner, L. R. Fundamentals and applications. *Electrochemical methods* **2**, 580-632 (2001).

171 Leong, A., Zhang, J. & Rountree, S. D. Kinetics of Corrosion and Oxidation of Fe-and Ni-Based Alloys by Molten Fluoride Salt. *High Temperature Corrosion of Materials*, 1-23 (2023).

172 D'Souza, B., Leong, A. & Zhang, J. A Method for Inhibiting Corrosion of Type 316L Stainless Steel in High-Temperature Molten Chloride Salt. *Nuclear Science and Engineering*, 1-5 (2023).

173 Lu, P., Liu, Q., Bao, H., Pan, T. & Tang, Z. Effect of FeCl3 in NaCl-MgCl2 molten salts on the corrosion behavior of 316 stainless steel at 600° C. *Corrosion Science* **212**, 110961 (2023).

174 Thorp, J., Skinner, A. & Al-Hawery, A. Magnesiochromite formation and EPR linewidths in Cr/MgO. *Journal of magnetism and magnetic materials* **82**, 277-286 (1989).

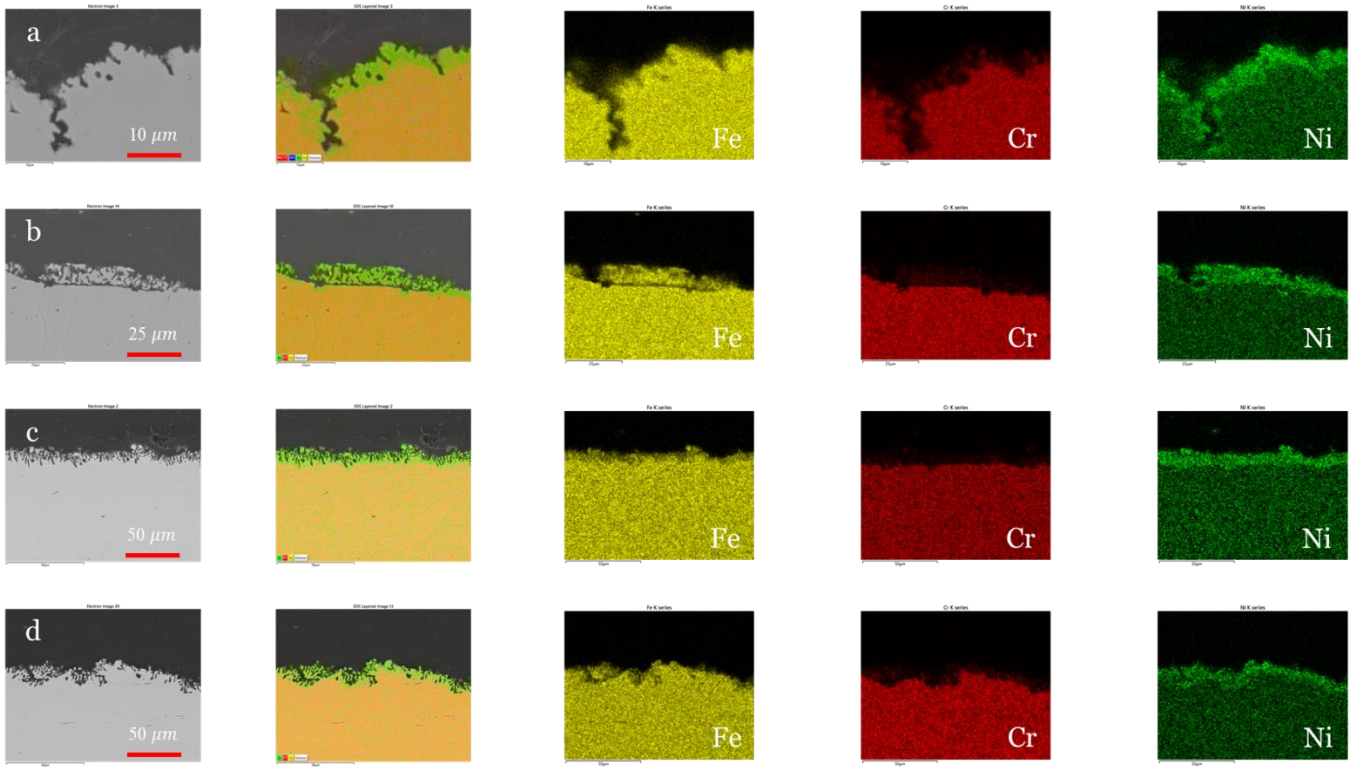

Figure VII-1 BSE/EDS cross-sectional true mapping of SS316 outer (facing to flow) surface exposed in FCL-80 test. (a) & (b) are different locations on FCL-80-SS316-S1. (c)&(d) MSL-80-SS316-S3.

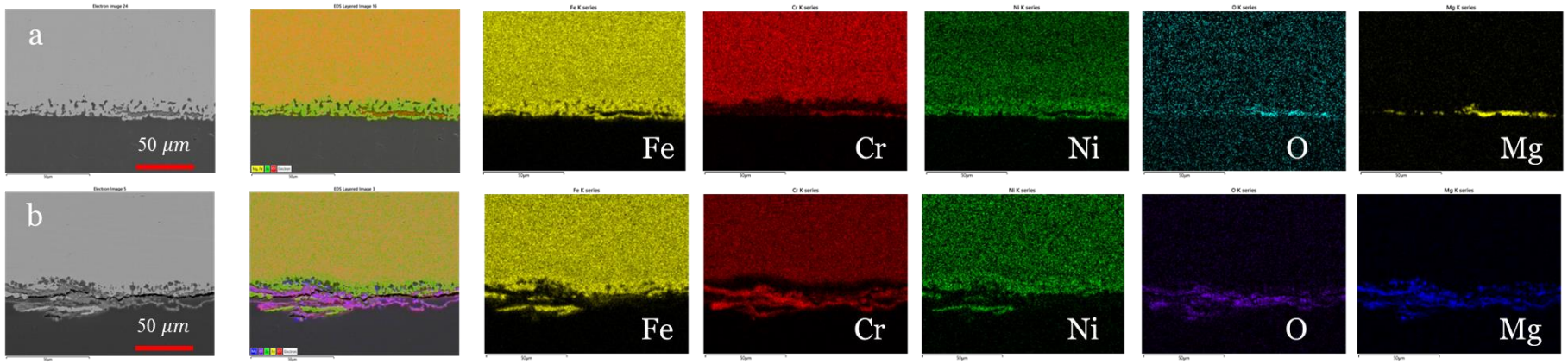

Figure VII-2 BSE/EDS cross-sectional true mapping of SS316 inner (facing to fixture) surface exposed in FCL-80 test. (a) FCL-80-SS316-S1. (b) MSL-80-SS316-S3.

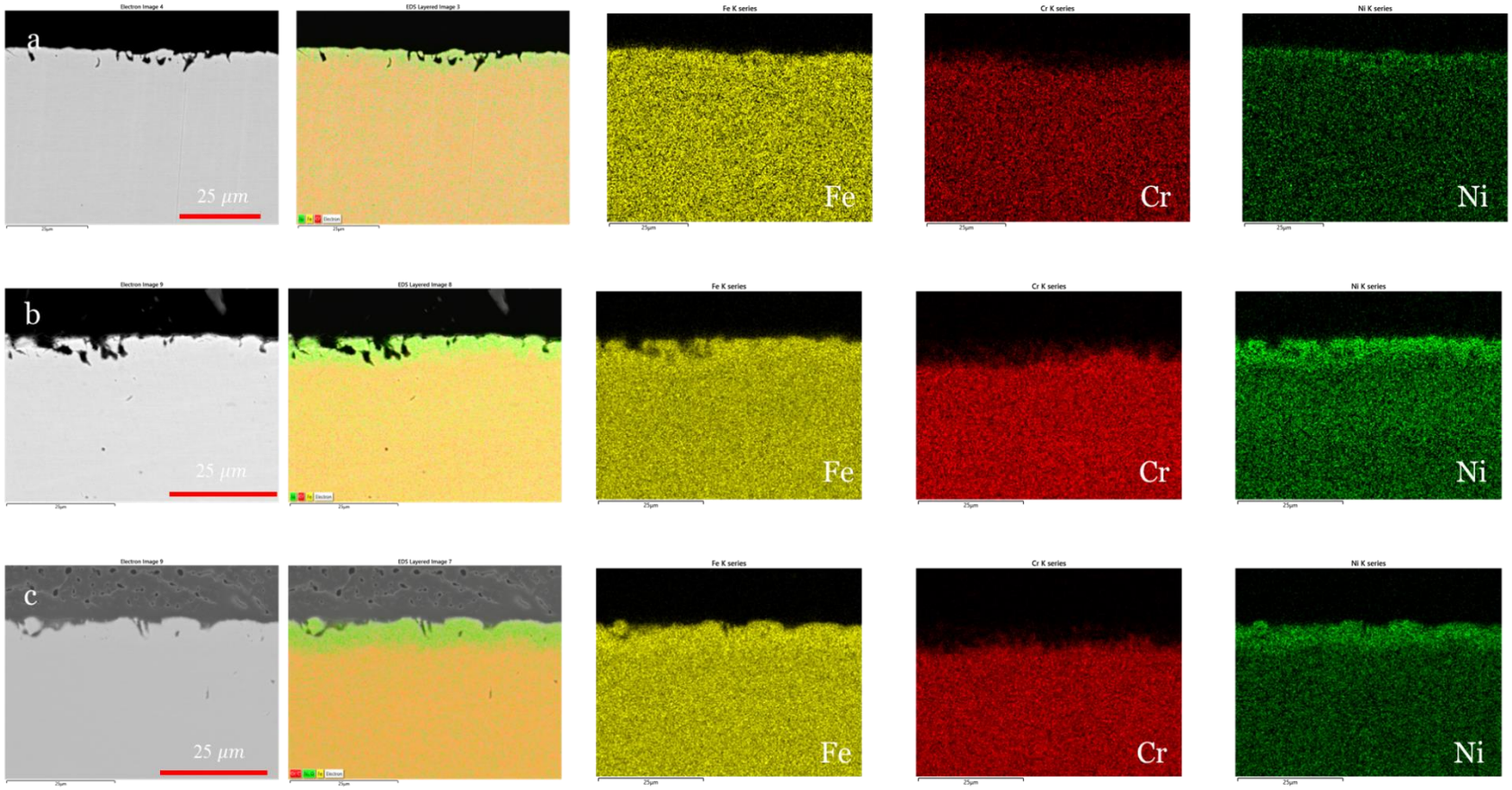

Figure VII-3 BSE/EDS cross-sectional true mapping of SS316 outer (facing to flow) surface exposed in FCL-100 test. (a) FCL-100-SS316-S1. (b) MSL-100-SS316-S2. (c) MSL-100-SS316-S3.

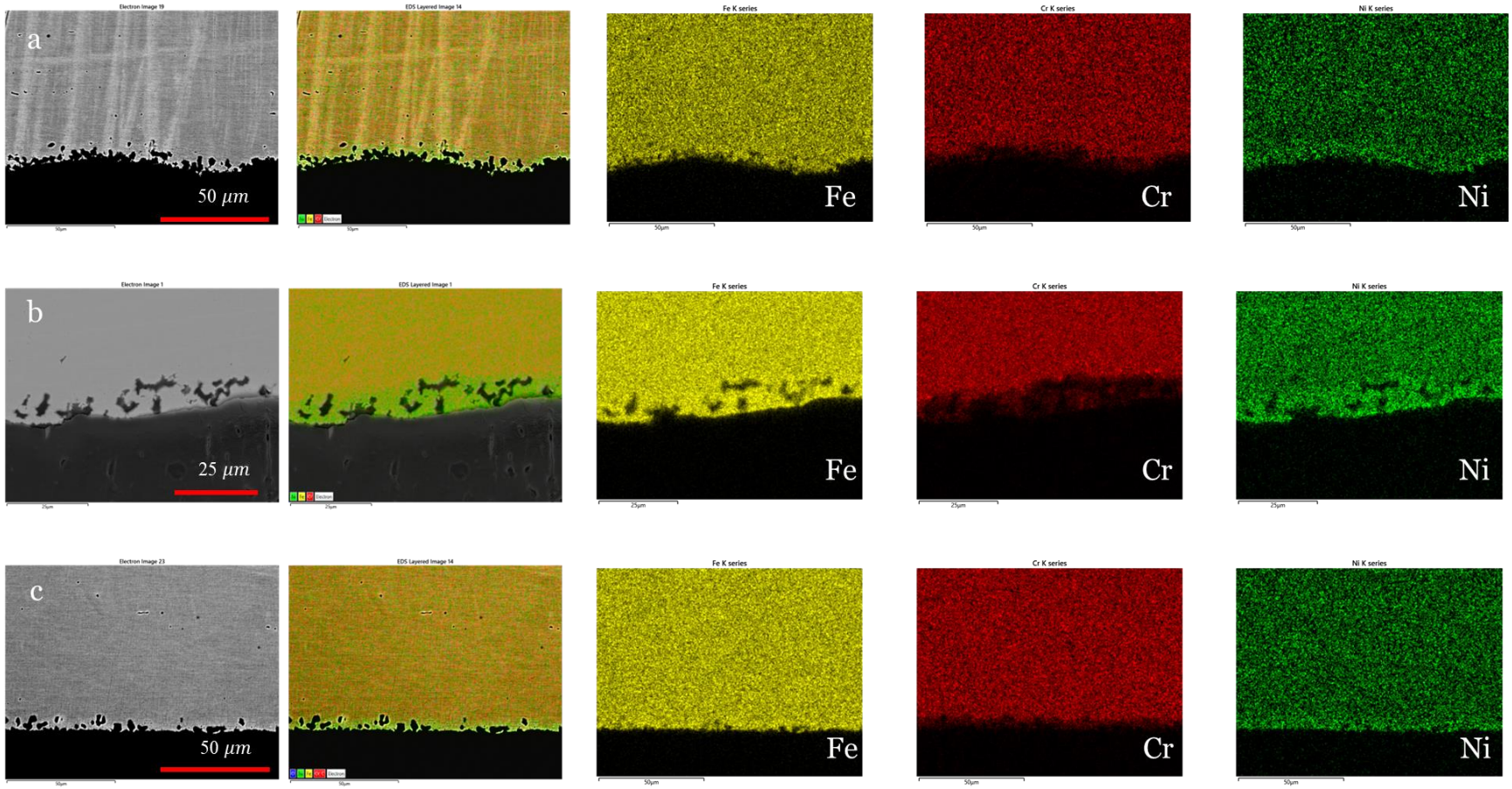

Figure VII-4 BSE/EDS cross-sectional true mapping of SS316 outer (facing to fixture) surface exposed in FCL-100 test. (a) FCL-100-SS316-S1. (b) MSL-100-SS316-S2. (c) MSL-100-SS316-S3.

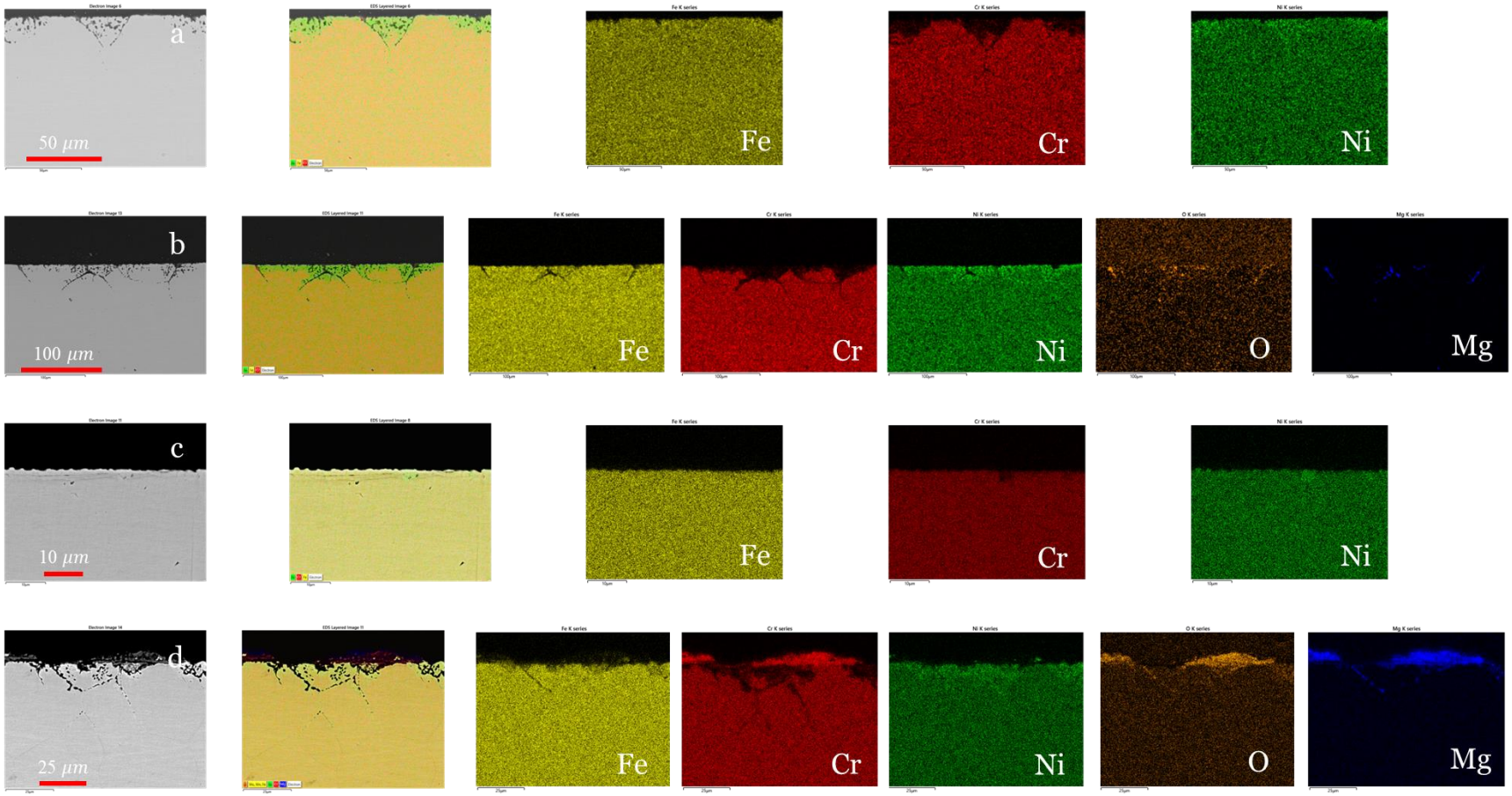

Figure VII-5 BSE/EDS cross-sectional true mapping of A709 outer (facing to flow) surface exposed in FCL-50 test. (a) & (b) are different locations on FCL-50-A709-S1. (c) & (d) MSL-50-A709-S3.

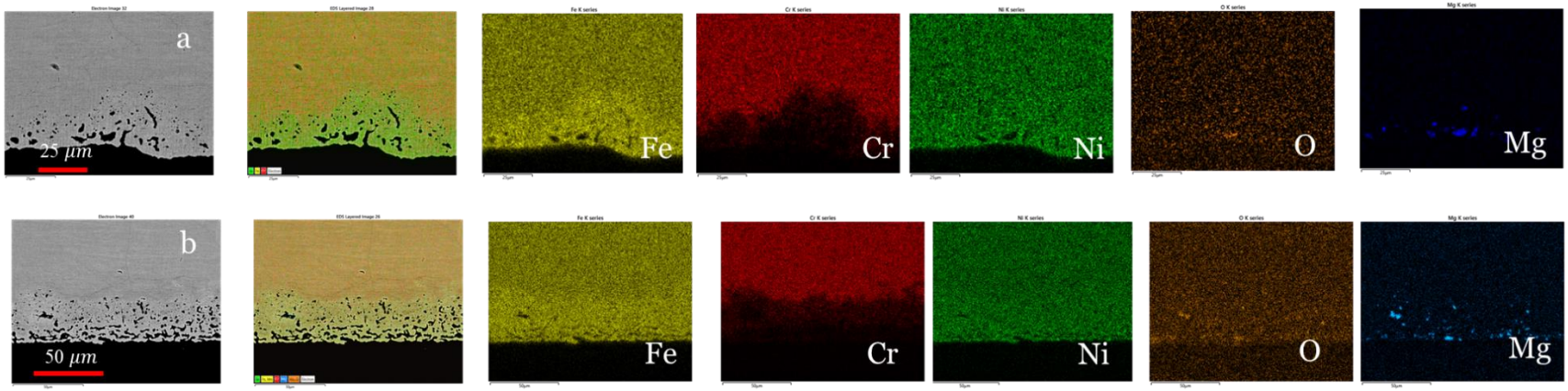

Figure VII-6 BSE/EDS cross-sectional true mapping of A709 inner (facing to fixture) surface exposed in FCL-50 test. (a) FCL-50-A709-S1. (b) MSL-50-A709-S3.

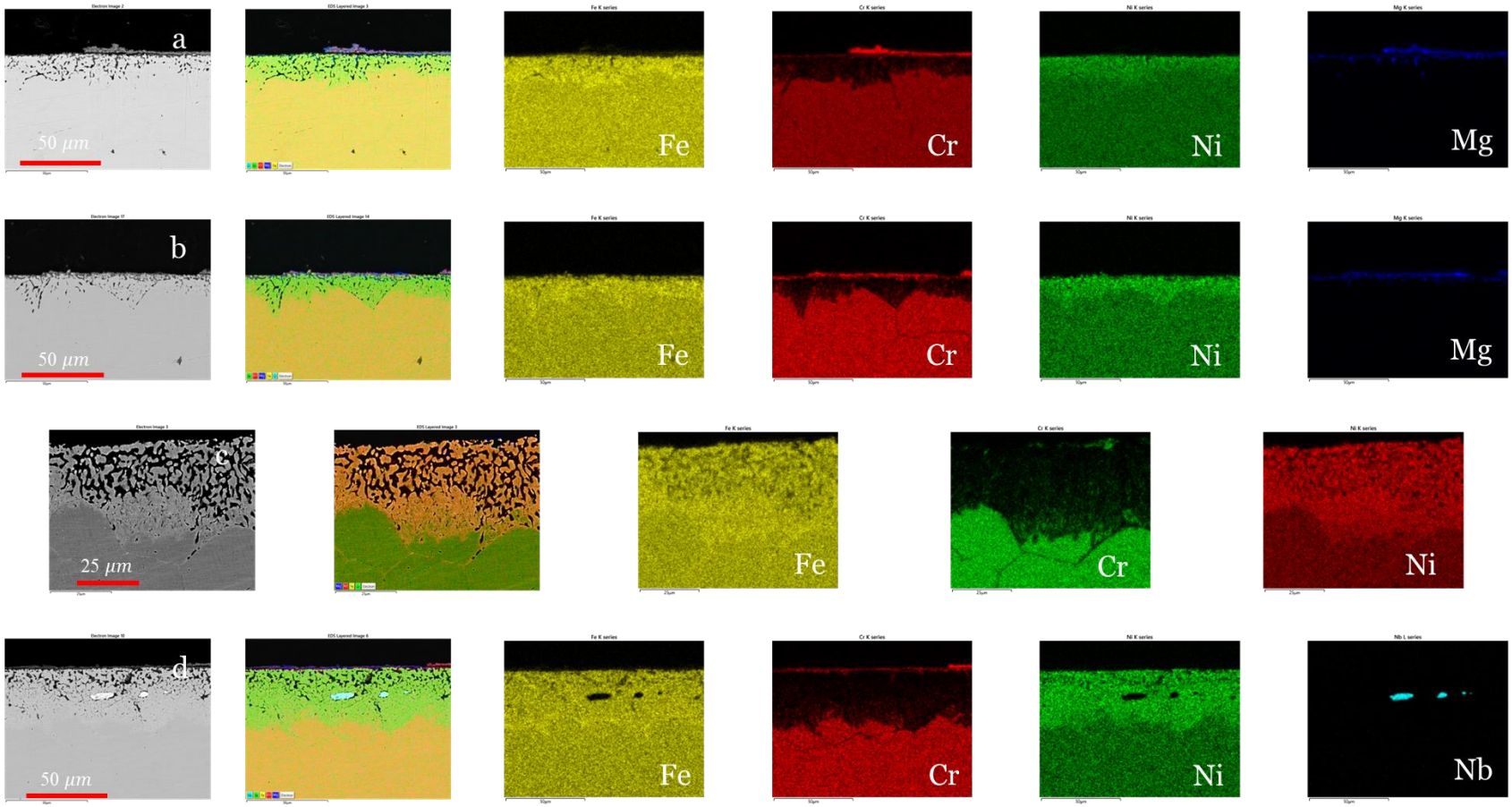

Figure VII-7 BSE/EDS cross-sectional true mapping of A709 outer (facing to flow) surface exposed in FCL-80 test. (a) & (b) are different locations on FCL-80-A709-S1. (c) & (d) MSL-80-A709-S3.

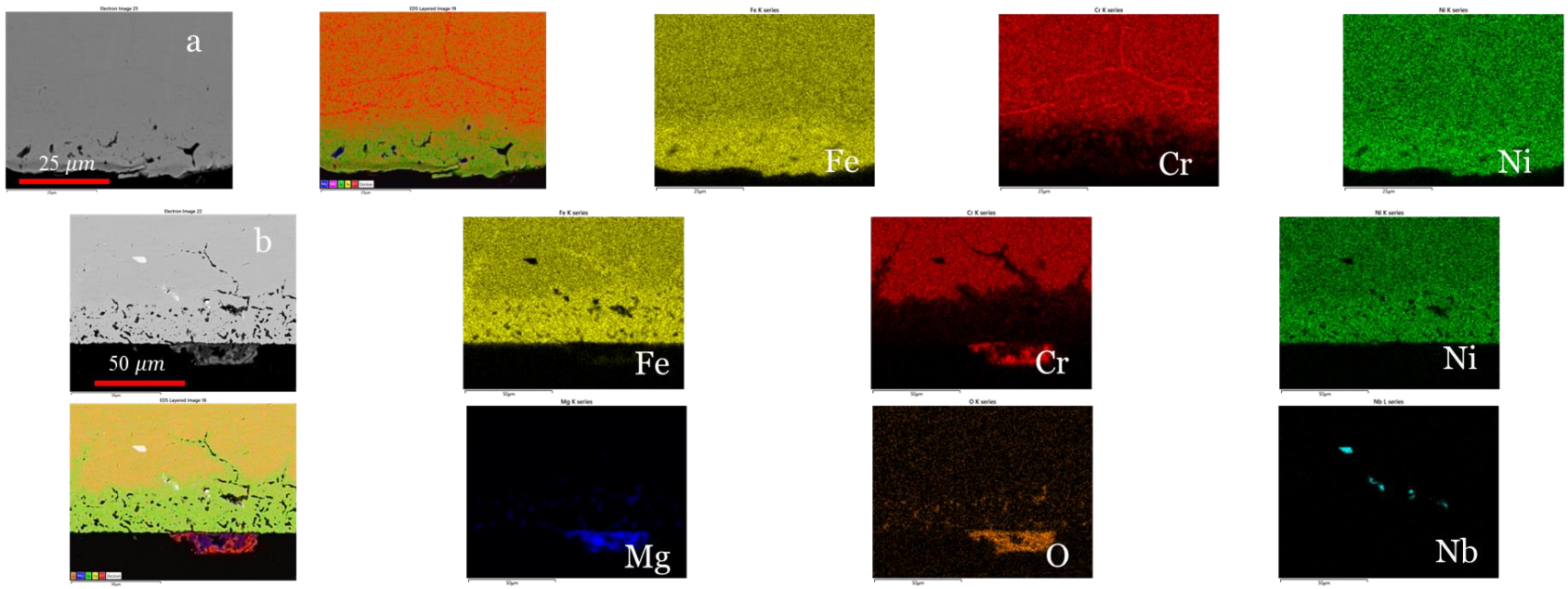

Figure VII-8 BSE/EDS cross-sectional true mapping of A709 inner (facing to fixture) surface exposed in FCL-80 test. (a) FCL-80-A709-S1. (b) MSL-80-A709-S3.

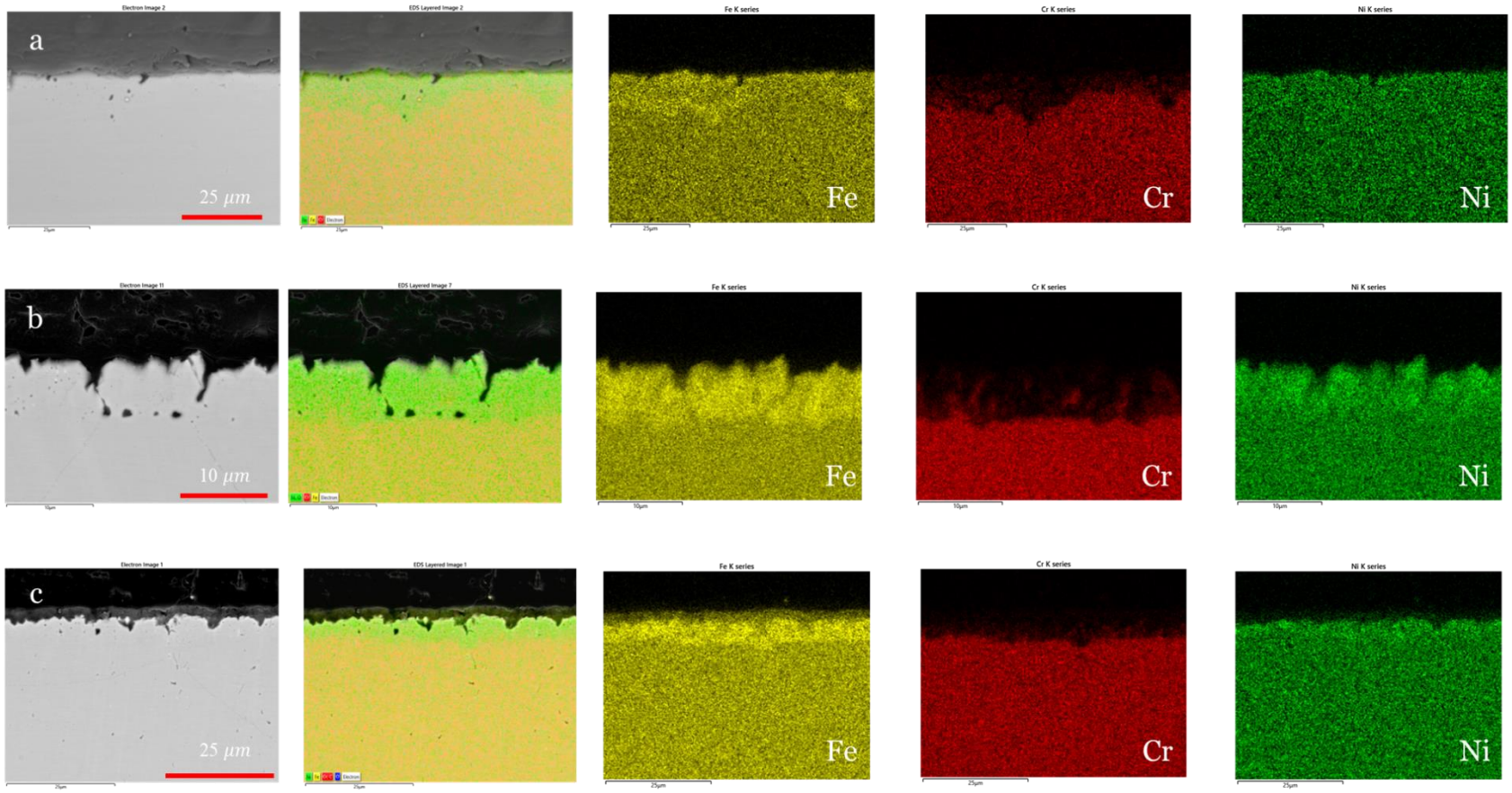

Figure VII-9 BSE/EDS cross-sectional true mapping of A709 outer (facing to flow) surface exposed in FCL-100 test. (a) FCL-100-A709-S1. (b) MSL-100-A709-S2. (c) MSL-100-A709-S3.

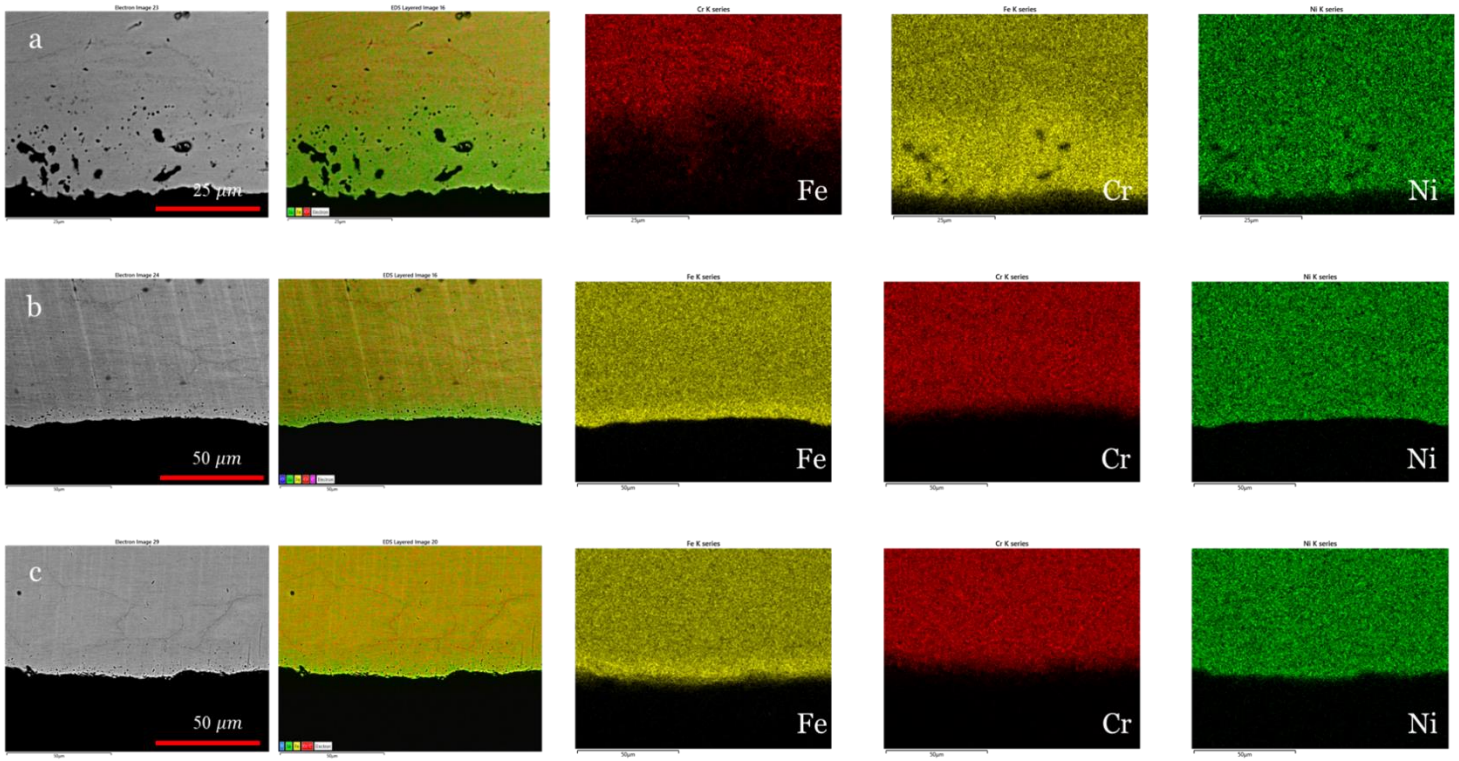

Figure VII-10 BSE/EDS cross-sectional true mapping of A709 outer (facing to fixture) surface exposed in FCL-100 test. (a) FCL-100-A709-S1. (b) MSL-100-A709-S2. (c) MSL-100-A709-S3.

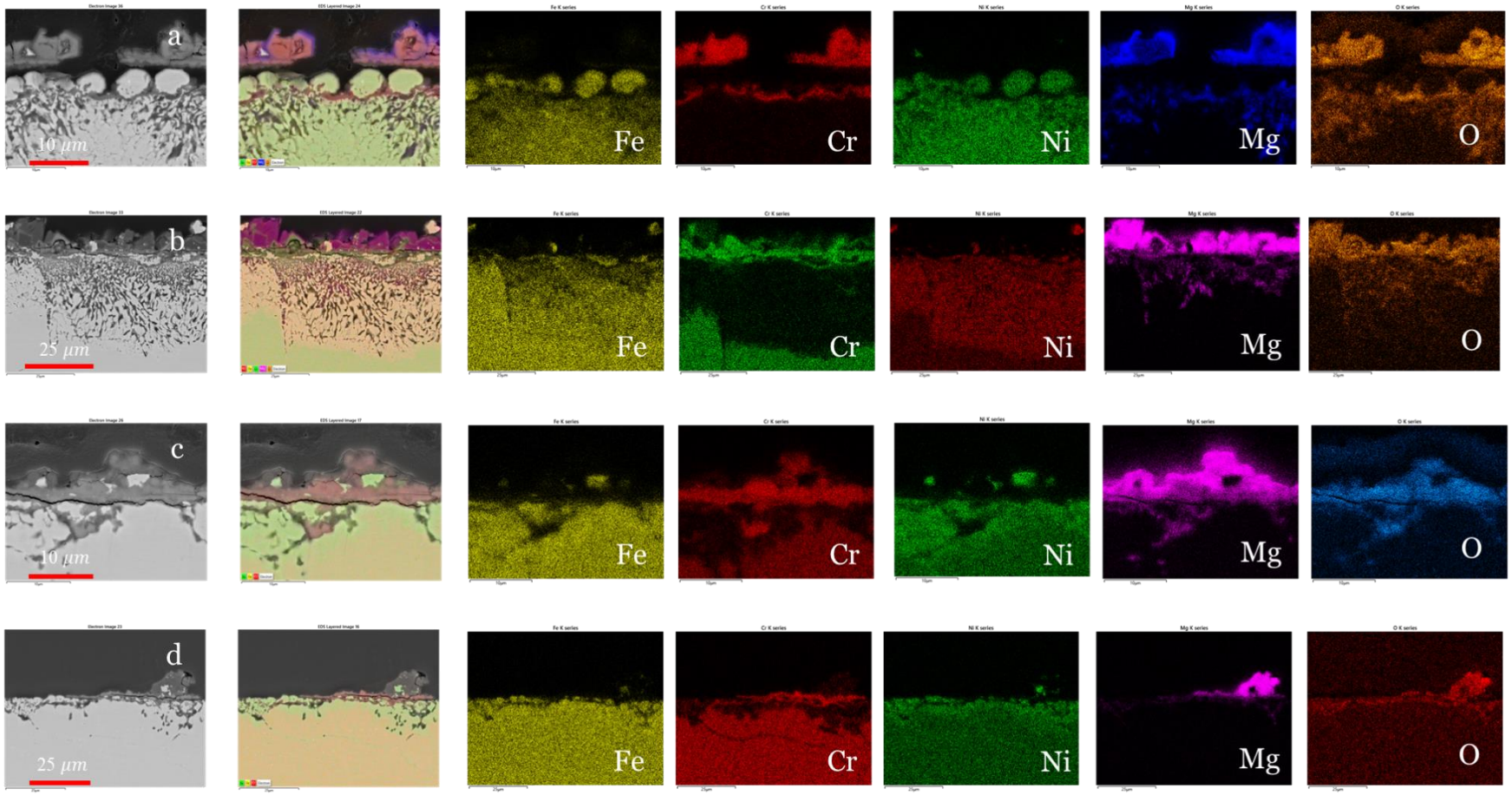
a
10 μm
Fe
Cr
Ni
Mg
O
b
25 μm
Fe
Cr
Ni
Mg
O
c
10 μm
Fe
Cr
Ni
Mg
O
d
25 μm
Fe
Cr
Ni
Mg
O

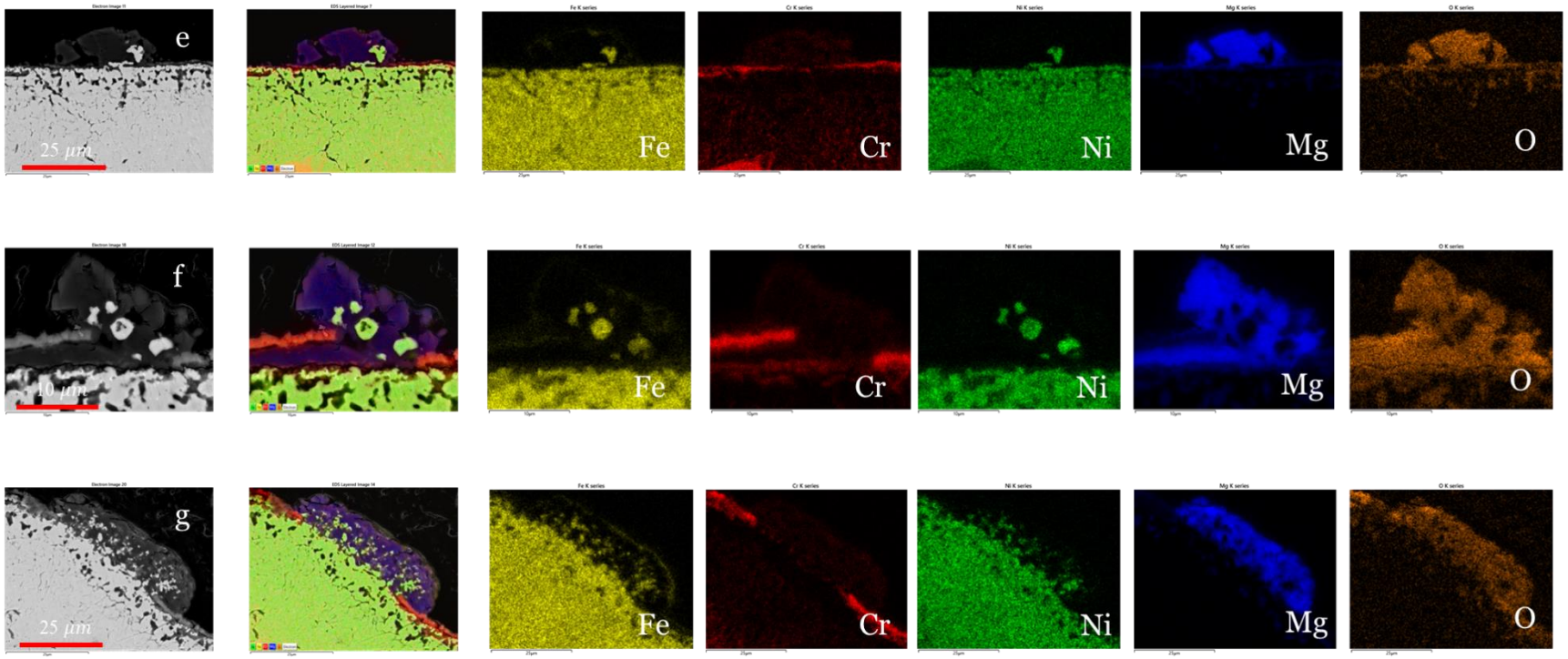
e
25 μm
Fe
Cr
Ni
Mg
O
f
10 μm
Fe
Cr
Ni
Mg
O
g
25 μm
Fe
Cr
Ni
Mg
O

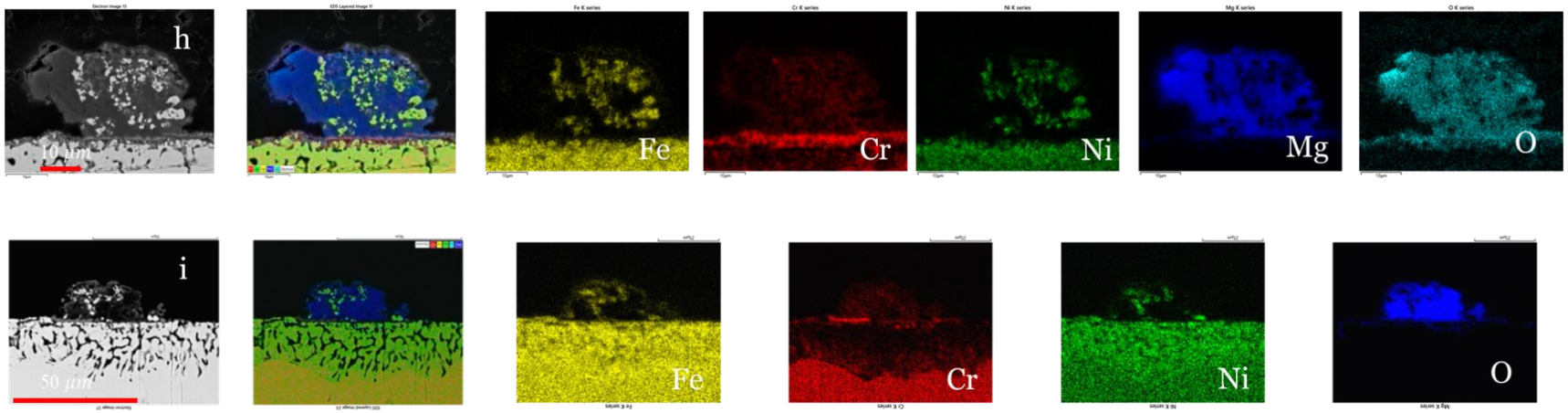

Figure VII-11 Special evidence of MgO effect in FIC in Magnak salt. (a)-(d) FCL-50-A709-S3. (e)-(g) FCL-80-A709 S3. (h) and (i) FCL-80-A709-S1.